Condition monitoring of fibre ropes using machine learning

Shaun Falconer

UiA University of Agder

Doctoral Dissertations at the University of Agder 368

Shaun Falconer

Condition monitoring of fibre ropes using machine learning

Doctoral Dissertation for the Degree Philosophiae Doctor (PhD) at
the Faculty of Engineering and Science, Specialisation in Mechatronics

University of Agder
Faculty of Engineering and Science
2022

Doctoral Dissertations at the University of Agder 368
ISSN: 1504-9272
ISBN: 978-82-8427-078-4

Printed by 07 Media
Kristiansand

Preface

The work presented in this doctoral thesis has been carried out in the time period starting in October 2016 and ended in January 2021 at the University of Agder, Grimstad, Norway. Professor Geir Grasmo from the University of Agder and Dr Ellen Nordgård-Hansen from NORCE Norwegian Research Centre served as supervisors during this project.

The research presented in this thesis has received funding from the Norwegian Research Council, Centre for research-based innovations SFI Offshore Mechatronics, project number 237896.

Acknowledgements

I would like to extend an extra special thanks to both my supervisors Geir Grasmo and Ellen Nordgård-Hansen. To Geir for your guidance, engineering expertise and the interesting insights into both rope splicing and Norwegian culture. To Ellen, not only for stepping up to be my supervisor early in the project, but for your expert insights into data analysis, attention to detail and encouragement to make this research the best it could be. It has truly been a pleasure to work with both of you and I hope you both enjoy reclaiming your Monday nights.

I would also like to thank Peter Krause and Thomas Bäck from divis Intelligent Solutions Gmbh for their collaboration, advice and expert insights into machine learning during my stay in Dortmund. Also thanks to Rune Schlanbusch, Thomas J. J. Meyer, Nadia Saad Noori and Benyamin Akdemir from NORCE Norwegian Research Centre for their support, encouragement and additional discussions during the project. An additional thanks also goes to Espen Oland and Andreas Gromsrud for their collaboration and work at the start of this project.

Thanks also goes to all the great people I have met during my time in Norway. A special mention to Reyn, Andreas K. F., Philipp, Rolf, Saeed, Alfredo, Lorenzo, Bernhard, Rune H., Charly, Simon, Ingvild, Sinziana, Gulshan, Kristoffer, Helle, Saga, Yvonne, Manuel, Martin, Cecilie, Morten R., Sissel, Jannik, Atle, Geir-Arne, Andreas K., Sondre S. T., Daniel, Joacim, Julie, Rune B., Arild, Tord, Sondre N., Gerrit, Luismi, Mahmoud, Verena, Sveinung and the many others I may have forgotten for contributing to an amazing four year journey.

An additional thanks goes to:

My friends in Denmark and my co-workers at NOV Flexibles.

My friends since childhood, Michael and Bonnar for keeping me grounded. Josh for

allowing me to let off some steam about our beloved Celtic. Darren for all the incredible gigs and festivals throughout the years. Also to the rest of the boys from the Saint Andrew's High School, Clydebank days.

My "wee" brother Kieran, I look up to and admire you more than you'll ever know. I am proud of everything you continue to achieve.

Finally, a sincere thanks to my parents, Margaret and John for your unconditional love and support in a journey that has taken me to Scotland, Spain, Norway, Denmark and a few other interesting places along the way. I would never have been where I am today without your encouragement, enthusiasm and the sacrifices you both have made throughout my life.

Shaun Falconer
Copenhagen, Denmark
April 2022

Abstract

The application of fibre ropes in offshore lifting operations has significant potential for further development. With minimum breaking loads (MBL) equivalent to steel wire at similar diameters and almost neutral buoyancy in water, it is in theory possible to reach depths exceeding 3000 m with smaller cranes and vessels, representing substantial savings in not only potential operation costs. However, with fibre ropes there are different requirements and standards to consider with regards to condition monitoring, maintenance and retirement criteria.

Safe and reliable operations are paramount in the offshore sector and any incidents that occur during offshore lifting would not be only significantly damaging financially but could potentially lead to loss of life. Current standards for fibre rope condition monitoring originate in mooring applications, and are based on manual inspection for retirement and re-certification. There is significant room for developments in methods that can aid the inspection process.

To address this problem, computer vision and thermal monitoring methods for fibre ropes are developed and experimentally investigated at the Mechatronics Innovation Lab in Grimstad, Norway. The methods are used to monitor changes in fibre rope condition during cyclic-bend-over-sheave testing and to find relevant condition indicators that give more information regarding the condition and remaining useful life of the fibre rope. In addition, the data recorded is used to form machine learning models that both classify rope condition and predict the remaining life of fibre ropes during CBOS testing. The expected outcome is to use physics-based machine learning methods to improve both condition classification and remaining useful life estimation of fibre ropes used in offshore lifting operations.

In the appended papers at the end of this thesis, the proposed methods have been experimentally investigated and validated through cyclic-bend-over-sheave experiments performed at the Mechatronics Innovation Lab and further data analysis performed at the University of Agder, Norway and at divis in Dortmund, Germany.

Sammendrag

Anvendelse av fibertau i offshore løfteoperasjoner har betydelig potensial for videre utvikling. Med minimum bruddlaster (MBL) tilsvarende ståltråd ved lignende diametre og nesten nøytral oppdrift i vann, er det i teorien mulig å nå dybder over 3000 m med mindre kraner og fartøyer, som representerer betydelige besparelser i ikke bare potensielle driftskostnader. Men med fibertau er det forskjellige re-krav og standarder å vurdere med hensyn til tilstandsovervåking, vedlikehold og pensjonskriterier.

Sikker og pålitelig drift er avgjørende i offshoresektoren og eventuelle hendelser som oppstår under offshoreløfting vil ikke bare være betydelig økonomisk skadelig, men også kan potensielt føre til tap av liv. Gjeldende standarder for tilstandsovervåking av fibertau stammer fra fortøyningsapplikasjoner, og er basert på manuell inspeksjon for pensjonisttilværelse og ny sertifisering. Det er betydelig rom for utvikling i metoder som kan hjelpe denne prosessen.

For å løse dette problemet, datasyn og termiske overvåkingsmetoder for fiber tau er utviklet og eksperimentelt undersøkt ved Mechatronics Innovation Lab i Grimstad, Norge. Metodene brukes til å overvåke endringer i fibertautilstand under syklisk-bøy-over-skive testing og for å finne relevante tilstandsindikatorer som gir mer informasjon om tilstanden og gjenværende brukstid for fibertauet. I tillegg brukes dataene som er registrert for å danne maskinlæringsmodeller som begge klassifiserer tautilstand og forutsi gjenværende levetid for fibertau under CBOS-testing. De forventet resultat er å bruke fysikkbaserte maskinlæringsmetoder for å forbedre begge tilstandsklassifisering og gjenværende levetidsberegning av fibertau brukt i offshore løfteoperasjoner.

Publications

The following listed papers are based on research activities conducted by the author and have been published or submitted for publications in peer-reviewed journals or conference proceedings.

Paper A S. Falconer, A. Gromsrud, E. Oland and G. Grasmo. Preliminary results on condition monitoring of fibre Ropes using automatic width and discrete length measurements. In *Proceedings of the Annual Conference of the Prognostics and Health Management Society 2017, St. Petersburg, FL, USA*, 2017. ISBN: 978-1-936263-26-4.

Paper B S. Falconer, G. Grasmo and E. Nordgård-Hansen. Condition monitoring of HMPE fibre rope using computer vision during CBOS testing. In *Exploring Opportunities - Synthetic/Steel - Proceedings of the OIPEEC Conference 2019, The Hague, The Netherlands*, pp 129-147, 2019. ISBN: 978-1-7336004-0-8.

Paper C S. Falconer, E. Nordgård-Hansen, G. Grasmo. Computer vision and thermal monitoring of HMPE fibre rope condition during CBOS testing. *Journal of Applied Ocean Research*, 102, 102248, 2020. doi: 10.1016/j.apor.2020.102248

Paper D S. Falconer, P. Krause, T. Bäck, E. Nordgård-Hansen, G. Grasmo. Condition Classification of Fibre Ropes during Cyclic Bend over Sheave testing Using Machine Learning. *International Journal of Prognostics and Health Management*, Vol. 13, 1, 2022. doi: 10.36001/ijphm.2022.v13i1.3105

Paper E S. Falconer, E. Nordgård-Hansen, G. Grasmo. Remaining useful life estimation of HMPE rope during CBOS testing through machine learning. *Journal of Ocean Engineering*, 238(1), 2021. doi: 10.1016/j.oceaneng.2021.109617

The following journal and conference proceeding were published during the time of this project, but are not included in the dissertation.

Paper F E. Oland, R. Schlanbusch, S. Falconer. Condition monitoring technologies for synthetic fiber ropes - a review. *International Journal of Prognostics and Health Management*, 2017. ISSN: 2153-2648.

Paper G S. Falconer, E. Nordgård-Hansen and G. Grasmo. Temperature Measurements as a Method for Monitoring Ropes. In *Engineering Assets and Public Infrastructures in the Age of Digitalization: Proceedings of the 13th World Congress on Engineering Asset Management, Stavanger, Norway*, 2020. ISBN: 9783030480202.

Contents

List of Figures

List of Tables

Nomenclature

Abbreviations

AHC	Active heave compensation
AI	Artificial intelligence
CBM	Condition based maintenance
CBOS	Cyclic-bend-over-sheave
CI	Condition indicator
CM	Condition monitoring
CT	Computed tomography
CTR	Close to rupture
DAS	Data acquisition system
DBZ	Double Bend Zone
DL	Deep learning
DT	Decision tree
EPR	Electron Paramagnetic Resonance
FEM	Finite Element Method
FFT	Fast Fourier Transform
fps	Frames per second
HE	Healthy
HMPE	High modulus polyethylene
LOOCV	Leave-one-out cross-validation
MBL	Minimum break load
ML	Machine learning
MLP	Multi-layer perceptron
NDT	Non-destructive testing
NN	Neural network
OTDR	Optical time-domain reflectometry
PHM	Prognostics and health management
ReLU	Rectified Linear Unit
R_f	Remaining Useful Life factor
RF	Random forest
RUL	Remaining useful life
SBZ	Single Bend zone
SEM	Scanning Electron Microscopy
SVM	Support vector machine
SZ	Straight zone

Variables

CTF	Cycles to failure
MAD	Median absolute deviation
SF	Safety Factor
T_{test}	Test tension

Chapter 1

Introduction

1.1 Background and Motivation

Safe and reliable lifting operations are of paramount importance in the offshore industry. Failure of any component in a crane, such as a rope, would not only have significant financial ramifications and operational downtime, but could also lead to fatality and implications for the environment. Therefore, effective condition monitoring methods and robust maintenance schemes are required to avoid these situations. Therefore, effective condition monitoring methods and robust maintenance schemes are required to lower costs and avoid failing situations. A poor and uninformed inspection and maintenance routine could lead to undesirable outcomes. Conversely, a conservative and ultra-cautious inspection and maintenance regime will significantly reduce chances of failure occurring but will contribute to unnecessary early retirement or re-certification. The latter is an ongoing issue in relation to fibre ropes in the marine sector, where there is significant potential for further digitisation of inspection and monitoring methods to aid intelligent prognostics and health management (PHM) methods. Additionally, there is a risk for negative environmental effects from using too much material, and all maintenance contains risks of introducing errors.

It has become more common for subsea lifting operations to be performed at depths exceeding 3000 m, which places limitations on steel wire rope crane capabilities due to rope weight. Therefore there is a motivation to use fibre ropes, as they are an attractive alternative to steel wire ropes for cranes due to advantageous material properties, with some typical fibre rope materials shown to have similar or better mechanical properties to the steel [1, 2, 3, 4, 5]. High-modulus polyethylene (HMPE) has emerged as a leading candidate for this use and exhibits minimum break loads (MBL) similar to those of steel wires at comparable diameters, but is almost neutrally buoyant in water. Potential benefits of this property include: reaching depths that exceed 3000 m with smaller cranes due

to not having to compensate for rope weight; utilising less deck space on vessel; replacing worn sections of the rope through splicing; and making use of smaller vessels to perform similar lifts, potentially reducing carbon footprint.

However, there are associated challenges with the implementation of fibre ropes for offshore lifting operations. To keep a payload at the same depth relative to the seabed during operations, the crane will use active heave compensation (AHC). This will require the rope to be subjected to extended periods of cyclic-bend-over-sheave (CBOS) motion, with the severity being influenced by a combination of payload mass, sea state and local environment. Traditional use of fibre ropes in the marine sector has been in mooring, and retirement criteria is mainly based in experience from this application. Some current standards advocate manual inspection [6], while others detail specific limits in load history [7] or combinations of load, time and temperature for estimated time-to-rupture [8]. It is also specified that fibre rope used in deployment and recovery systems requires their failure mode and material properties to be detailed [9].

Specific guidelines exist that detail a plethora of failure mechanisms and considerations to take in relation to retirement or re-certification of fibre ropes [10, 11, 6], but these still rely heavily on manual visual inspection. Fibre ropes comprise of several smaller sub-structures and their respective interactions add further complexity to condition monitoring (CM). Therefore, this research deals specifically with developing condition indicators (CI) that can be extracted by extending these visual inspections methods through the use of computer vision and thermal monitoring.

The use of fibre ropes in offshore lifting operations is a fairly recent development but fibre ropes have more established use in other marine applications such as mooring, tugging, fishing and sailing. Through these different applications there are a variety of different rope structures and material compositions that can be adapted for specific use cases [12, 13, 14].

There is still a need to develop a means of continuous condition monitoring of fibre ropes for lifting operations, rather than simple re-certification or retirement. There is significant potential in digitisation of manual inspection methods through monitoring of damage with computer vision and thermal monitoring, shifting towards more data-driven artificial intelligence (AI) methods using machine learning (ML) for condition classification and RUL estimation. This shift toward use of intelligent CM methods has been seen in other industries, with many data-driven approaches for both diagnostics and prognostics being specified [15, 16, 17]. An issue in applying this to fibre rope CM is the lack of publicly available datasets that simulate the CBOS motion in AHC lifting operations. Additionally appropriate features to be monitored require further exploration. These are issues that need to be addressed to exploit the full potential of intelligent data-driven

solutions for fibre rope CM and help facilitate their further application for offshore lifting operations.

This dissertation aims to address the problem of developing data-driven fibre rope CM methods and to subsequently propose and develop algorithms for intelligent diagnostics and prognostics. The required data for algorithm development is acquired through a laboratory test set up and a data acquisition system. A CBOS machine is used to test different types of ropes until failure at pre-defined test tensions. The data acquisition system consists of machine vision cameras, a thermal camera and a distance measuring laser, which all monitor changes in the test ropes as the experiments progress. Features are created and derived from the data recorded during experiments and are used to form the datasets required for training and testing for the proposed diagnostic and prognostic algorithms.

1.2 Contributions of the dissertation

The scientific contributions of this dissertation are taken from five research papers published or submitted to scientific conferences and journals. The content of these papers forms the basis of this thesis. Contributions are focused towards developing digitised methods for fibre rope monitoring and deriving CIs for ML application for both diagnostics and prognostics of rope condition.

1.2.1 Paper A: Preliminary results on condition monitoring of fibre ropes using automatic width and discrete length measurements

Summary: A review completed in the early stages of the project concluded that current practice in industry for rope CM was based mainly on manual inspection, and that width measurements received little attention in research [18]. Therefore, it was proposed to extend these manual inspection processes through computer vision application and geometric measurements using image processing methods. Paper A addresses the initial iteration and development of an automatic width and length measurement through computer vision methods used to monitor fibre ropes under tension-tension testing. It was concluded that there was potential in using width and lengths as condition indicators (CI) but this had to be adapted for the CBOS testing case.

Contributions: Development of algorithm based on computer vision and image processing to monitor width and length of fibre ropes during tension-tension testing.

This paper has been published as: S. Falconer, A. Gromsrud, E. Oland and G. Grasmo. Preliminary results on condition monitoring of fibre Ropes using automatic width and discrete length measurements. In *Proceedings of the Annual Conference of the Prognostics and Health Management Society 2017, St. Petersburg, FL, USA*, 2017. ISBN: 978-1-936263-26-4.

1.2.2 Paper B: Condition monitoring of HMPE fibre rope using computer vision during CBOS testing

Summary: Width and length algorithms were adapted to monitor ropes subject to CBOS testing. Furthermore, it was proposed to calculate the roundness of the rope based on the width measurements and assess their suitability as a CI. Different bending zones were also monitored to accurately reflect the differences in deterioration due to bending regime and to provide local measurements. The work found that length was a suitable CI but should be monitored at a local level rather than across the whole rope. The width measurements gave mixed potential as a CI but it was noted there could be further improvements in the methods used for calculation. Conversely, roundness was shown to contribute very little to condition assessment. It was also highlighted that the geometric measurements should be combined with thermal monitoring for the next round of testing.

Contributions: Adaptation of automatic width and length algorithm for fibre ropes based on computer vision and image processing for application to fibre ropes in CBOS testing.

This paper has been published as: S. Falconer, G. Grasmo and E. Nordgård-Hansen. Condition monitoring of HMPE fibre rope using computer vision during CBOS testing. In *Exploring Opportunities - Synthetic/Steel - Proceedings of the OIPEEC Conference 2019, The Hague, The Netherlands*, pp 129-147, 2019. ISBN: 978-1-7336004-0-8.

1.2.3 Paper C: Computer vision and thermal monitoring of HMPE fibre rope condition during CBOS testing

Summary: In this paper, combined results for computer vision and thermal monitoring for fibre ropes during CBOS testing are presented. It is shown that localised strand-level monitoring is required and that length, width and temperature demonstrated changes while the rope deteriorates. New monitoring features such as local length and width through computer vision algorithms are presented. These are combined with surface

thermal monitoring and global elongation measurements, where their effectiveness as CIs is assessed.

Contributions: Validating use of more stable local strand-level width, length and temperature measurements as CIs and developing feature engineering process for future ML application for ropes during CBOS testing.

This paper has been published as: S. Falconer, E. Nordgård-Hansen, G. Grasmo. Computer vision and thermal monitoring of HMPE fibre rope condition during CBOS testing. *Journal of Applied Ocean Research*, 102, 102248, 2020. doi: 10.1016/j.apor.2020.102248

1.2.4 Paper D: Condition classification of HMPE rope during CBOS testing through supervised machine learning Methods

Summary: Fault diagnosis is explored within this work, where ML algorithms for classification are applied to data from two different rope types from CBOS tests at different safety factors. The data is labelled into healthy (HE) or close to rupture (CTR) classes based on measurements from global elongation throughout testing. The study uses local length, width and temperature data as features and classifies data using decision tree (DT), random forest (RF) and support vector machine (SVM). This is validated through leave-one-out cross-validation (LOOCV) with the test data being validated against the other ropes in the data set. The results of these models are presented through confusion matrices, and their effectiveness are assessed through metrics specific to binary classification. The influence of changing feature set, data size and model hyperparameters is also investigated. The results showed that support vector machine using a linear kernel and random forest were the most effective techniques in condition classification of fibre ropes under CBOS testing based on the data in this study.

Contributions: A fault diagnosis scheme for fibre ropes under CBOS testing is detailed. The proposed method performs binary classification of rope condition based on DT, RF and SVM models.

This paper has been published as: S. Falconer, P. Krause, T. Bäck, E. Nordgård-Hansen, G. Grasmo. Condition Classification of Fibre Ropes during Cyclic Bend over Sheave testing Using Machine Learning. *International Journal of Prognostics and Health*

Management, Vol. 13, 1, 2022. doi: 10.36001/ijphm.2022.v13i1.3105

1.2.5 Paper E: Remaining useful life estimation of HMPE rope during CBOS testing through machine learning

Summary: Within this work, the ML approach is further extended for prognostics, where it is adapted to perform RUL predictions for two rope types subject to different CBOS test at different safety factors. This is validated through LOOCV, with the test data being validated against the other ropes in the data set. A target variable based on RUL is predicted through regression using neural networks (NN), SVM and RF and the various approaches are compared to find the best method. The effects of varying algorithm hyperparameters and the use of different feature sets are also investigated. Additionally, the two different data sets are combined and LOOCV is performed to assess the effect and feasibility of using multiple distinct data sets for fibre rope RUL prediction.

Contributions: A prognostics scheme for fibre ropes under CBOS testing is presented. The proposed method applies NN, SVM and RF to predict a target variable based for RUL in fibre ropes based on the amount of cycles to failure, CTF. The study also shows that data from distinct rope types with different safety factors can be combined for training data to enhance RUL prediction.

This paper has been published as: S. Falconer, E. Nordgård-Hansen, G. Grasmo. Remaining useful life estimation of HMPE rope during CBOS testing through machine learning. *Journal of Ocean Engineering*, 238(1), 2021. doi: 10.1016/j.oceaneng.2021.109617

1.3 Outline of the dissertation

The dissertation consists of eight chapters. The introduction chapter gives an overview of the dissertation and a summary of the research conducted. In Chapter 2, the state-of-the-art for fibre rope CM methods, maintenance strategies, diagnostics and prognostics are presented and the research direction is identified. The experiments, equipment and datasets used for developing the data acquisition methods are summarised in Chapter 3. Chapter 4 discusses the computer vision algorithms developed to extract length and width data from rope images and develop features to be used in ML application. Chapter 5 summarises the proposed diagnostics methods developed using ML for damage classification of fibre ropes. A prognostics method for fibre rope developed through a ML framework is given in Chapter 6. Finally, limitations and suggestions for future work

and improvements are presented in Chapter 7 and the conclusions and future work are presented in Chapter 8.

Chapter 2

State-of-the-art

This chapter introduces the state-of-the-art in material property knowledge, industry and maintenance standards, CM techniques, fault diagnostics and prognostics for fibre ropes. This overview provides the basis for the approaches outlined in this dissertation and the research direction taken.

2.1 Fibre rope and damage mechanisms

There are many challenges related to developing effective fibre rope CM methods related to both structural and material concerns. Figure 2.1 displays the sub-structures that comprise a standard fibre rope: the rope, sub-ropes, strands, and filaments. The various interactions between these constituent parts and their material properties have the potential to influence RUL. Fibre ropes can be made from several materials including HMPE, aramid, polyester and natural fibres [1, 19]. HMPE rope has emerged as a leading candidate for offshore lifting application [20] and, therefore the methods applied in this thesis are used on this type of rope. This material has both associated advantages and disadvantages, in addition to degradation mechanisms common to all types of fibre rope.

Fibre rope degradation mechanisms related to mooring and offshore lifting have been summarised and are both relevant in this context [21, 22, 11, 10]. These include but are not limited to: creep, temperature, abrasion, tension fatigue, compression fatigue, and shock. These damage mechanisms and potential failure modes add difficulty in developing an all-encompassing method of monitoring fibre ropes.

Creep in the context of fibre ropes can be classified as the elongation that occurs when a material is subject to extended periods of static loading [23]. Crane payloads may be held in suspension for extended periods, so creep considerations are still relevant for monitoring during lifting operations. A standard creep elongation follows three distinct

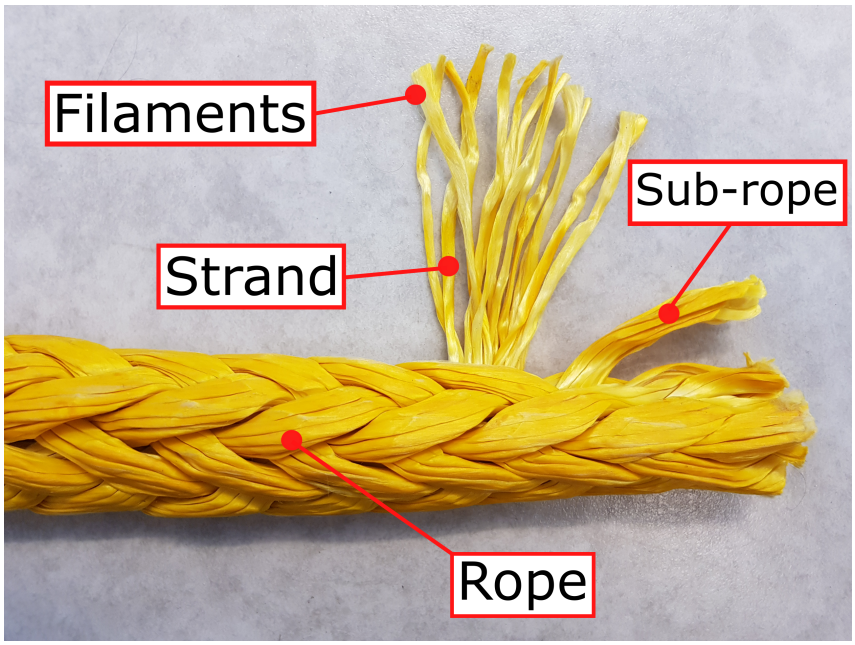

Figure 2.1: Overview of constituent fibre rope sub-structures

stages, namely: Regime I, Regime II and Regime III creep [24]. Regime I is the primary phase where the rope elongation is reversible. Regime II is second phase where rope elongation is irreversible due to plastic deformation caused by sliding of polymer molecular chains. In the third and final stage, Regime III, rope failure is accelerated due to molecular chain breakdown coupled with an increase in local stresses. This indicates that creep must be monitored at a local scale, as well as across the whole rope. Creep is also shown to occur as a result of rearrangement of the various sub-structures highlighted in Figure 2.1 [25]. Creep has been investigated for ropes in tension testing [5, 26, 27, 28] and there have also been attempts to model this phenomena [29, 30, 31, 32].

The fibre rope will be subjected to extended periods of CBOS motion during AHC. Heating and temperature will increase as the rope is driven back and forth over the sheave. The extent of this will be influenced by a combination of payload size, sea state, friction between rope sub-structures and the environment in which the lifting operation occurs [33, 34]. Temperature is a particular concern with HMPE due to its relatively low melting point compared to other rope making materials [1]. HMPE ropes typically have a working temperature at 65°C [35]. Above this working temperature, the rope structure will additionally degrade through thermal means, therefore temperature monitoring is a vital component of a fibre rope monitoring system. Temperature has been monitored using both thermocouples and IR camera to gain insights into rope damage [36, 37], as well as modelling attempts [38].

Abrasion is another concern with fibre ropes in CBOS motion and can lead to reduction in rope strength. Abrasion can occur both internally and externally and is influenced by

a multitude of factors including: the abrasive surface, the rope construction, the severity of the movement over the sheave and the environmental conditions where the operation takes place [39, 40]. Intra-strand abrasion is also a source of heating that causes fibres to fuse together and is also shown to influence RUL more than external abrasion in CBOS tests [41]. Internal abrasion is also known to contribute to tension fatigue observed in fibre ropes that are cyclically loaded at normal working loads [39]. This is also shown to influence other factors such as the dynamic stiffness and elongation of the rope while in use [42]. This effect on rope properties is seen in operational data and can be exacerbated by presence of foreign marine objects within the rope structure [43, 44].

As the rope is driven over the sheave, axial compression will occur in certain portions of the rope as a result of bending and twisting. Compression fatigue can occur over extended periods of usage at low tensions, which lead to formations of kinks in all rope sub-components. The rope can then potentially fail due to buckling at the kinks [39, 45, 46].

It is acknowledged that damage mechanisms observed during CBOS motion interact with each other, which adds further complexity to CM processes [47]. Therefore an effective CM approach would have to encompass technology capable of monitoring the fibre rope from different perspectives and establish relevant condition indicators (CI). A CI gives information regarding the state of the rope and can be extracted from the measurements and signals provided through different CM techniques. In this study, geometric and thermal CIs are chosen to give more insight into the rope degradation process and to be used as relevant features for ML application.

2.2 Industry standards and maintenance strategies

Fibre rope usage in the offshore industry is regulated by several certification societies that provide specific guidance on manufacturing, testing and fitness for use. The standards and recommended practices in this section are used to highlight the main considerations for maintenance and CM of fibre ropes in current industry practice. They may also serve as reference for development of potential intelligent solutions to CM and provide a basis for the strategies undertaken in this work.

A general overview of the standards required for offshore fibre rope implementation is summarised in DNVGL-OS-E303 [7], which uses mooring applications as a basis for the majority of the document. The general fitness for purpose of the rope is determined by material properties, application, operational use and condition maintenance approach. The responsibilities of the manufacturer and end-user are also highlighted. An automated fibre rope CM system would have to be detailed as one of the methods used to comply this industry standard, including instrumentation used and features monitored to determine

condition. A specific criteria mentioned for retirement or re-certification in this standard requires that a rope subjected to greater than 70 % MBL must be retired or re-certified. Other than this requirement, more detailed information regarding specific practices are referenced and discussed further in this section.

ABS-90 [48] provides another perspective on fibre ropes for mooring, with more detailed emphasis on different rope materials. HMPE is particularly interesting as it has gained traction as the material used for lifting applications and its related material properties are discussed. Creep is a prominent issue, and the various stages while the rope is in use require monitoring. Temperature and tension considerations are mentioned which are also echoed in DNVGL-RP-E305 [8].

DNVGL-RP-E304 [6] expands on condition management in more detail and deals with damage assessment for polyester ropes from a mooring perspective. This is still relevant for offshore lifting with other types of rope, such as HMPE, as damage in the structure is described and material propeties are considered. It advocates a thorough manual visual inspection of each constituent substructure for discard or recertification. This is based on the number of damaged sub-ropes as a fraction of the total sub-ropes in the structure. This fraction is then used to calculate the reduction in MBL and give a basic fatigue-life assessment. This judgement is based on inspector opinion and load history documentation quality, with assessments potentially varying depending on respective experience.

DNVGL-RP-E305 deals specifically with design, testing and analysis of offshore ropes, but makes references to condition management [8]. This includes providing a means of assessing rope condition with or without load history and information related to internal abrasion, external damage and temperature response. Mooring is the main document focus but it mentions that combined loading operations such as CBOS in active bend over sheave require temperature monitoring. This is further highlighted by the 3-T parameter which estimates synthetic filament endurance based on three critical parameters "time, tension, temperature", and is used as a rope design criteria. This emphasises the importance of temperature for monitoring and should be considered in combination with visual inspection, which is relevant in particular for HMPE rope for active heave compensated cranes.

DNVGL-ST-E407 [9] provides a more general overview of components to be verified for deployment and lifting system classification and approval for industrial application. Fibre rope usage is considered as a separate case from steel wire ropes, with its own set of specific considerations related to critical performance parameters and failure modes. Critical parameters can be summarised as the local stresses, temperature, time under tension and wear in the rope. The standard also highlights factors arising during bending, such as geometry changes due to strand and yarn rearrangement and concentration of

stresses and twisting at local spots. It is specified that all these aspects and factors must be monitored and given the complexity of their interactions and subsequent effect of RUL estimation, there is significant potential for ML application.

CI 2001-04 [10] is an inspection guide commissioned by the Cordage Institute that provides detailed damage descriptions and images, as well as advice on repair, re-certification and retirement. The mechanisms mentioned can be detected by different forms of automatic visual inspection and the recommended damage and load history logging can be digitised. Decisions on corrective actions to be taken can then be decided by intelligent classification and diagnostic algorithms.

While the standards are thorough in their approach to industry requirements for fibre ropes, there is still potential for improvement in their application to deep sea lifting. Current standards that mention offshore lifting serve as more of a general guide as the technology to harness the application is still under development. Therefore, digitisation of these processes is a possible approach and could allow industry concerns for fibre ropes to be incorporated into intelligent solutions.

2.3 Condition monitoring techniques

Fibre rope CM techniques can be separated into two distinct categories: embedded and non-embedded methods. Embedded methods comprise of sensors or threads distinct from rope fibres that are typically placed or woven into the rope during or after construction. Non-embedded methods refer to sensors that do not interfere or alter the rope structure but monitor through observation or measurement of a physical change. There have been several review papers that detail different technologies applied to fibre ropes. While this study focusses on the use of fibre rope in offshore lifting, it is important to mention those applied in mooring applications due to the greater accumulated experience in that sector. An earlier review on fibre rope CM was provided by Rebel et al [49]. An updated summary of further CM methods focussed on ropes used in lifting operations was given by Oland et al [18].

2.3.1 Embedded approaches

Embedded approaches specifically refer to threads or sensors that are designed into the rope structure that can be monitored during use. There are several different types outlined in literature related to magnetic, electrical, optical and temperature monitoring.

Magnetic monitoring is common in steel wire rope use but the application to fibre ropes requires paramagnetic material properties to be interpreted or magnetic threads to be embedded in the rope. Bryden and Poehler detail an electron paramagnetic resonance

(EPR) method for non-destructive testing (NDT) in polymer materials [50], where fractures in the material can be detected due to variations in magnetic flux. More recently, Huntley et al detailed a patent with a magnetically detectable strength member in the rope, where the amplitudes of magnetic flux leakage and eddy currents would be used as CIs [51]. Additionally, Grabandt et al [52] use a magnetic thread within the rope, where differences between healthy and deteriorated signals detected through magnetism, X-ray, terahertz analysis and capacitive effect are potentially used for rope CM. This is also explored in a paper by Huntley et al [53], where Fast Fourier Transform (FFT) is used to quantify rope condition based on a voltage from a sensor monitoring the magnetic thread. De Sousa Faria proposed hoisting rope construction that incorporates a solid core that allows NDT to be performed through magnetic flux or eddy current monitoring [54]. Ouellette proposed a device that can gauges rope condition through measuring the lay length, breakage and wear of the embedded magnetic element [55]. Finally, Mupende and Zerza also suggest including magnetic measurements as part of a wider monitoring system to determine the state or wear of fibre rope [56].

Electrical conductive threads can also be used in conjunction with magnetic measurements to assess rope condition. Robar et all provide a solution for elevators where the measured electrical resistance in tension members is used to indicate defects [57]. Goldwater et al detail an elongation monitoring method based on an indicator thread in a fibrous structural member [58]. De Angelis also detailed a patent for use in elevators where a fiber rope is embedded with an electrical thread to monitor wear [59]. Furthermore, Schmieder et al [60] show a method where increasing electrical resistance of an embedded sensor can be related to the increasing number of bending cycles in a CBOS test. Additionally, Schneiders has a patent aimed at monitoring the integrity of a splice for fibre ropes through an electrically conductive thread, as an aid to visual inspection [61].

Optical fibres can also be embedded into fibre ropes for monitoring purposes. Brillouin fibre sensing for application in local strain measurement for fibre rope is mentioned by Thévenaz et al [62]. Cortázar et al detected ruptures in kevlar cable strands based on propagations of pulses through a fibre-optic based system [63]. D'Agostino et al have a patent where the stresses and strains in a rope can be monitored by the changes in an embedded fibre optics light transmissive and reflective properties [64]. Barton Smith and Williams performed a study where three types of optical fibre were assessed for mooring rope monitoring, using optical time-domain reflectometry (OTDR) to measure strains in ropes [65]. There have also been other studies into distributed fibre optic systems embedded in ropes as a means of detecting yarn breakages in fibre ropes [66, 67]. A more recent study by Gordelier et al also makes use of optical time-domain reflectometry

(OTDR) to monitor creep in fibre ropes under tensile testing at different strain rates [68].

Temperature can also be monitored using thermocouples embedded inside a rope. Ning et al performed a study where thermocouples were embedded inside a rope during CBOS testing to study failure through thermal mechanism [36]. An earlier patent by De Angelis proposes the inclusion of a thermally conductive thread in a synthetic cable for elevator installations, which can give warnings if critical temperatures are exceeded [69].

Embedded methods are shown to be useful for fibre rope CM, however their implementation requires rope design to be slightly altered to be incorporated. The CBOS motion that occurs during an AHC lifting operation would require the embedded sensors or threads to be thoroughly tested to ensure they can also last the lifetime of the rope. Additionally, with rope lengths exceeding three kilometres in some cases, it would be difficult to implement along the whole length without significant engineering design work. Due to these considerations, it was decided to focus on non-embedded approaches for CM in fibre ropes in this thesis.

2.3.2 Non-embedded approaches

Non-embedded approaches refer to means of monitoring a rope without placing special threads or sensors within the rope. Examples of this include vibration, acoustic, thermal, X-Ray and visual monitoring to determine rope condition.

Vibration and acoustic measurements have shown to be useful in fibre rope inspection. Williams and Lee provided a review on acoustic monitoring methods for both fibre and steel ropes [70]. Williams et al also published a study where they measured the Stress Wave Factor (SWF) and correlated the tension applied to the rope [71]. Kwun and Burkhardt detailed a method in both a paper and patent where transverse impulse vibration method is used to determine flaw locations of a rope in tension [72, 73]. Ferreira et al present a method where the change in dynamic stiffness of the a rope can be used as a condition indicator and monitored though the changes in speed of longitudinal propagation of acoustic waves [74]. Padilla et al detail a patent with a non-contact system consisting of a transmitter and receiver, where changes in rope condition are quantified through changes in an ultrasonic pulse propagated through and around the rope [75]. For mooring ropes, Bashir et al conducted a study where the acoustic signatures from ropes subjected to cyclic tension-tension tests can be potentially used for in-service condition assessment [76].

As temperature is a concern in fibre CM, thermal monitoring through non-embedded methods is also important to consider. Heat is generated through interaction with the sheave but mainly as a results of intra-strand abrasion [20, 41]. Davies et al presented an example of using an IR camera during CBOS testing to monitor temperature changes,

with clear differences between different bending zones visible [41]. Nordgård-Hansen et al also explored the use of chemometrics to assess fibre rope condition through IR camera measurements recorded during CBOS testing on fibre ropes [37].

Computed tomography (CT) and X-ray imaging can also give insight into fibre rope condition. Davies et al produced X-ray images of fibre rope, highlighting strand rearrangement in a sample from before and midway through CBOS testing [41]. The aforementioned study by Huntley et al also uses an X-ray imaging of an embedded yarn that can be used to asses damage during CBOS testing [53]. Toda et al made use of X-ray micro-tomography where it was shown it is possible to assess the effects of internal abrasion and estimate the loss of fibres in the rope cross-section [77]. Schmieder et al performed studies on the use of CT in failure analysis of high-strength fibre ropes during CBOS testing to assess wear behaviour and produce new discard criteria [60, 78]. Terahertz non-destructive testing can also be used to detect contaminants and foreign particles within a rope that can contribute to accelerated wear through internal abrasion as demonstrated by Schecklman et al [79]. Finally, Scanning electron microscopy (SEM) analysis is also shown to be useful in assessing abrasion and penetration of foreign materials inside ropes [80].

Visual inspection remains the most common method of damage assessment as indicated by current industry standards [6]. Computer vision can potentially automate this inspection process with several different methods explored to detect changes in fibre yarns and both steel and fibre ropes [81, 82, 83]. Furthermore, Rudy and Thoresen detailed a patent where an optical system is used to assess both the condition of rope and hoist in cranes [84]. Visual inspection also complements the use of marking schemes which have been adapted for ropes used for elevators, mooring and lifting to determine their condition [85, 86, 60, 6, 87, 88].

Non-embedded methods were chosen as the approach for this thesis, with both visual and thermal monitoring used for data recording. This allows both geometric and thermal data to be used as CIs which are both considered in current industry standards and have potential for ML application.

2.4 Remaining useful life and modelling methods

There are several examples of RUL prediction methods for fibre ropes. RUL methods for fibre ropes have been mainly based on empirical evidence where a number of studies with CBOS testing have been conducted for both steel and fibre ropes of several different diameters [89, 47, 90, 91, 92]. Tension-tension testing is another suitable method for deriving empirical based models for rope lifetime, particularly for ropes used in mooring [30, 27].

Several different modelling approaches have also been adopted to compare to mechanical testing. Feyrer presented a model for determining the remaining useful life for steel wire ropes subject to CBOS motion [93]. Nuttall then presented an adapted version of the Feyrer model for fibre ropes in CBOS motion [94]. Frick et al also detail a modelling approach where viscous deformation of rope is considered combined with fatigue test data [95]. Sloan has also developed a wear-based parameter for fatigue in fibre ropes during CBOS testing and compare it to CBOS data [96]. Lian et al detailed a model based on thermodynamic properties of fibres, yarns and ropes and compared predictions to tensile tests [97]. Beltran and other collaborators have developed models for behaviour and mechanical response of fibre ropes with different types of damage over a number of studies [98, 99, 100, 101]. Vu et al also used finite element method (FEM) to model ropes and compare to tensile tests [102]. Similarly, Davies et al also used FEM to investigate the response of twisting in ropes and compared them to tensile testing [103].

When developing a modelling approach, several parameters and their influence are considered. There have been some patents developed that incorporate discard parameters into a wider fibre rope monitoring system. Examples of this are provided by Mupende and Zerza, who detail similar patents where a discard signal is created from monitoring rope and environmental parameters [104, 105, 56]. Additionally, van der Woude and Zijlmans also advocate the approach of real-time monitoring through several sensors that log data related to use and correlate them to position along the rope [106].

It is shown that RUL approaches for fibre ropes have potential to be further developed, with little research on the topic of combining both better monitoring techniques and ML and DL application. While several different approaches have been detailed in this section, the importance of monitoring specific rope parameters is highlighted. These will be monitored through non-embedded approaches to allow data to be recorded for ML application.

2.5 Machine learning

There have been extensive reviews into the use of ML and DL for diagnostics and prognostics over a number of sectors [16, 107, 108, 15, 17, 109]. Many of the developed approaches are applied to publicly available datasets of data collected from other engineering components such as bearings, motors and other rotating machinery. At the time of writing, there are no publicly available datasets for CBOS testing of fibre ropes that include geometric and thermal monitoring of discrete rope sections.

ML and DL have been applied previously for steel wire ropes. Onur et al used neural networks to predict RUL of steel wire rope in CBOS testing and compared the performance

to Feyrer models at different loads and diameter ratios [110]. Xue et al used support vector machine to classify steel wire rope condition based from vibration monitoring data [111]. Furthermore, Zhou et al used convolutional neural networks (CNN) for classifying faults in balancing tail ropes for mine shaft hoisting operations [112]. Huang also applied a CNN approach and computer vision techniques that detect surface damage in steel wire ropes [113]. Finally, Chung et al detailed a an approach where deep neural networks (DNN) are used to classify faults simulation data of mooring lines [114].

The ML and DL application detailed in this section mainly deal with steel ropes and classification of condition, specifically for mooring or mining purposes. At the time of writing, there is no publicly available research into ML and DL application for fibre ropes intended for lifting operations under CBOS testing in terms of diagnostics or prognostics.

2.6 Research questions and proposed research directions

The research presented in this thesis was conducted as part of the SFI Offshore Mechatronics work package 5, dealing with condition monitoring technologies. The specific subtask 5.3 objective was to develop methods to determine the remaining useful life of large diameter fibre ropes applied for heave compensated operations.

As stated in the previous sections, manual visual inspection is still the main method used to determine the retirement of fibre ropes for offshore use. Even then, these standards are based on ropes used for mooring purposes, instead of lifting operations. There is significant potential in automation of these processes, as well as developing intelligent diagnostics and prognostics methods to aid offshore inspectors in decision making. The following research questions are posed:

1. What condition indicators are best served to indicate the condition of rope during CBOS testing?

2. What combination of sensors will best monitor the condition of fibre ropes used for offshore lifting operations?

3. What is the best approach to predict RUL of a fibre rope based on CBOS experimental data?

This research focusses on proposing condition monitoring methods for RUL estimation of fibre rope during offshore lifting operations . It will specifically focus on increasing the capabilities of visual inspection through computer vision and thermal monitoring and

the algorithms used to acquire the data. The application of ML algorithms for both diagnostics and prognostics as a further aid to decision making on re-certification or retirement of fibre ropes from service will also be explored.

Chapter 3

Design of experiments

This chapter outlines the experiments performed through the course of this project and used in the publications that form this thesis. The details of tension and CBOS testing are summarised in Sections 3.1 and 3.2, respectively. Further details of the rope types used in each experiment are given in Section 4.

3.1 Experiment type 1: Tension testing

The tension tests were performed as part of initial development of data acquisition algorithms and forms the basis of the research presented in Paper A. This thesis focuses on offshore lifting operations, so tension tests under different conditions were performed as a way of testing and validating the computer vision algorithms that monitor the CIs length and width, before future application to CBOS testing.

3.1.1 Equipment

The tests were conducted using a Wolpert tensioner machine, which is capable of delivering a maximum load of 1000 kN. The test setup is shown in Figure 3.1. The ropes were fastened into the machine clamps with two 25 ton (250 kN) rated shackles attached to spliced rope end eye.

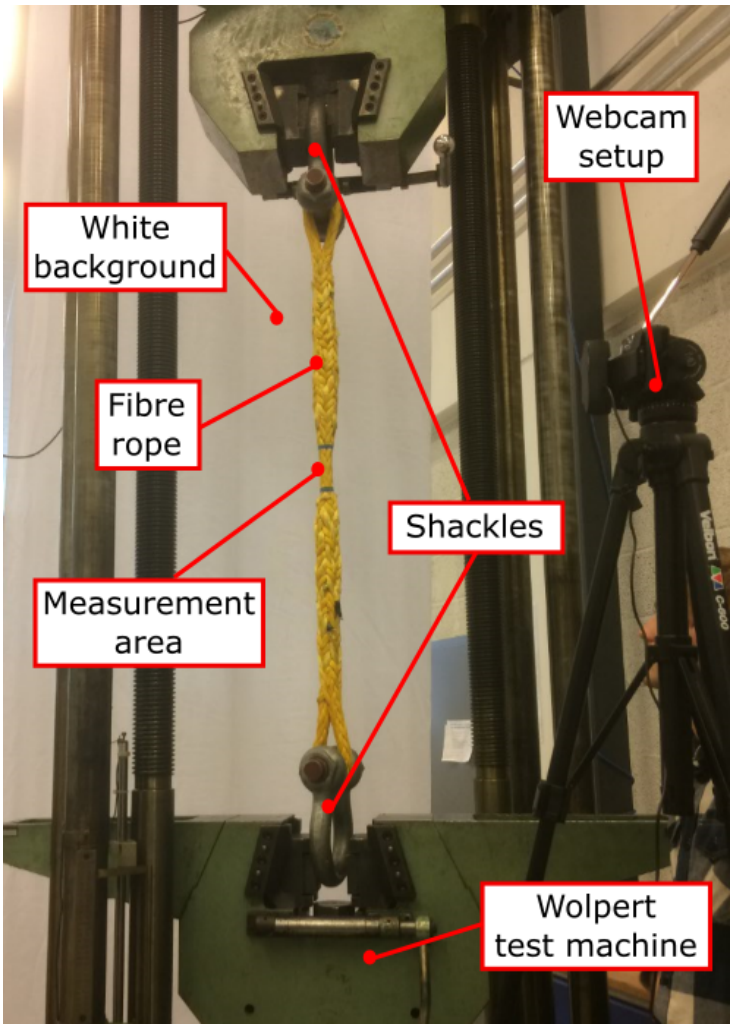

Figure 3.1: Overview of tension test setup with fibre rope in Wolpert tensioner machine for the experiments outlined in Paper A.

Each experiment was recorded using a Logitech C922 1080p web camera with 1920 x 1080 resolution and recording at 30 fps (frames per second). The camera set up is positioned so the measurement area on the rope is within the field of view. A white backdrop was also erected behind the tensioner machine to remove background interference.

3.1.2 Fibre rope and marking scheme

Three samples of 28 mm width, 12 strand, Dextron 12 Plus fibre ropes were used in the experiments. Splicing of the ropes was carried out before the experiments, making use of a modified version of the Tuck-Bury splice [115] to make the eyelets to attach the ropes to the shackles. The measurement section was in between both splice transition zones and was designated using blue electrical tape. Geometrics measurements such as length and width were tested as CIs and therefore a marking scheme was implemented. The markings were a distinct colour from the rope so they could be distinguished easily when

(a) An example of the splice used for the ropes during tension testing.

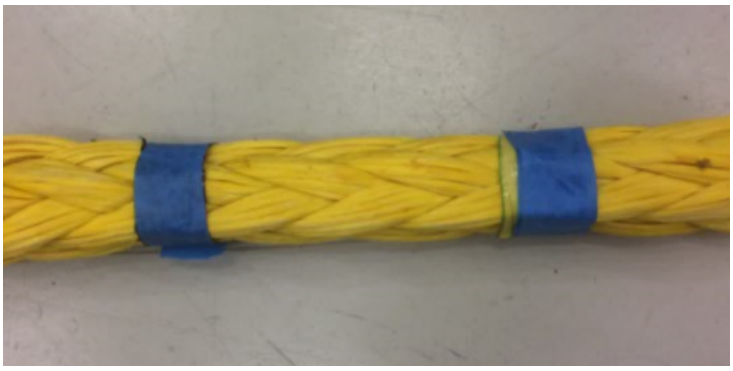

(b) An example of the measurement zone on rope for the tension tests designated by the blue markers.

Figure 3.2: Modifications made to the ropes for tension testing.

the computer vision algorithms measuring length were applied. This was chosen as a temporary solution to allow validation of measurement algorithms until a more robust marking scheme had to be developed for future CBOS testing. It is noted that a black marker pen was used in the first test, but this was replaced by the blue tape in subsequent tests. The splice and measurement area used for the tension tests are shown in Figures 3.2a and 3.2b, respectively.

3.1.3 Test procedures

Three different testing regimes were performed on the samples to assess the marker movement. The details of these different test conditions are summarised below:

1. Pre-load phase where the tensioner initially held the rope at 0.4 kN. The load steadily increased until 338.8 kN before the test was stopped after 160 seconds.

2. Pre-load phase where the tensioner initially held the rope at 0.4 kN. The load was steadily increased over approximately 100 seconds until 310 kN before the test was stopped.

3. Pre-load phase where the tensioner initially held the rope at 1.5 kN. The load was

steadily increased in a step-wise fashion of approximately 20 kN until 290 kN before the test was stopped after 400 seconds.

3.2 Experiment type 2: CBOS testing

The CBOS experiments were performed at the Mechatronics Innovation Lab in Grimstad, Norway and form the basis of the research detailed in Papers B and C. The data sets form the basis of the research detailed in Papers B - E. The CBOS machine was used to emulate deformation process of rope in AHC operations, though under cosntant conditions which is not realistic.

3.2.1 Test machine

The CBOS machine used in this thesis was designed and installed by DEP Engineering (www.dep-engineering.fr). An overview of the machine is shown in Figure 3.3 and a summary of the machine properties is specified in Table 3.1.

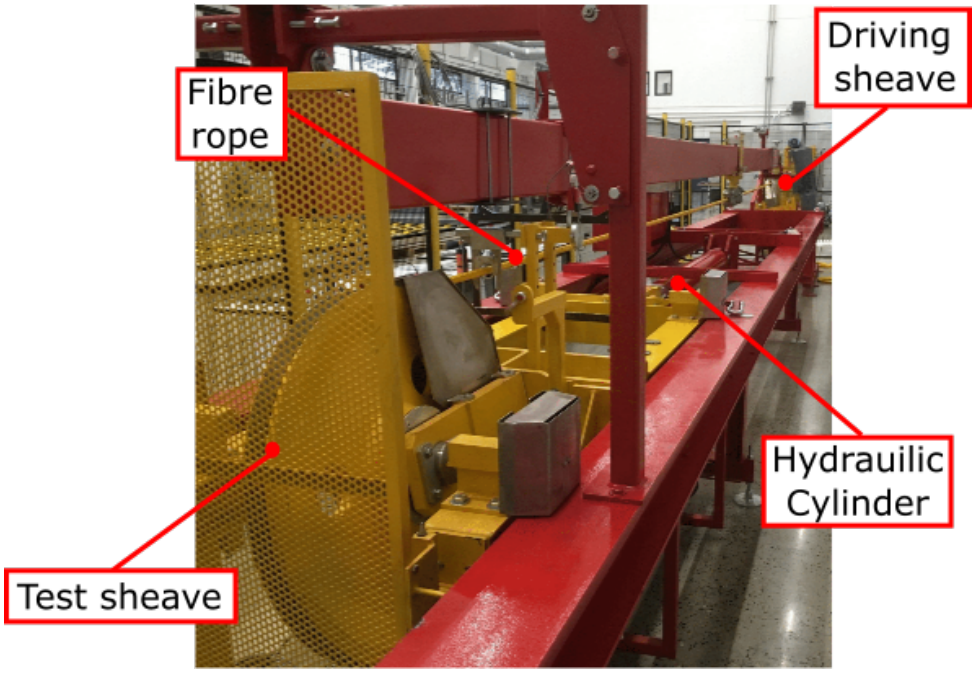

Figure 3.3: Overview of CBOS test machine with fibre rope installed. The view is from behind the test sheave. This was used for the experiments outlined in Papers B - E.

The machine comprises of two different sheaves: a driving sheave and a test sheave. The rotating driving sheave provides the motion of the rope and force the rope to bend over the testing sheave. The test sheave is the smallest sheave, meaning the rope experiences more shear straining on this than on the driving sheave. The rope is held at a pre-defined

Table 3.1: Properties of CBOS machine.

Test sheave diameter (m)	0.8
Driving sheave diameter (m)	1.0
Maximum line pull (kN)	150
Rope diameter range (mm)	20-30
Dimensions (m × m × m)	12 × 1.3 × 2.2

tension throughout testing by a hydraulic cylinder that extends as the rope is elongated (and creeping) throughout the tests.

Either end of the rope is attached into opposite ends of a connector attached to a trolley that moves as the rope is cycled back and forth. In Paper B the mounting was done through a special resin applied to the end of the ropes, held in place by a specially designed fastener similar to [116]. In the subsequent CBOS experiments detailed in Papers C, D and E, the ropes were attached via spliced eye at the ends of the rope, similar to those described in Section 3.1.2. Care was taken to ensure there was minimal twist in the rope when it was installed in the machine.

3.2.2 Instrumentation

The condition monitoring set-up consists of three parts: a computer vision system, a thermal monitoring system, and a laser distance measurement. The computer vision system consisted of five cameras viewing the rope from different angles, each attached into a frame positioned near the testing sheave as shown in Figures 3.4a and 3.4b. As the CBOS tests progress, the rope structure will degrade with ruptured strands and extruded loops. After tension testing it was decided that higher quality machine vision cameras were needed for CBOS testing, therefore the Edmund Optics 13122C Colour USB 3.0, 1.3 MP resolution model with maximum frame rate of 169 fps, was used to record data. Each camera recorded around 2000 images for each recording, which corresponded to 13-15 complete cycles. Depending on the ropes used, periodic recordings for 20 seconds were made every 500 or 1000 cycles of the rope in the CBOS machine.

As highlighted in Section 2.1, thermal monitoring should be incorporated into a fibre rope monitoring system due to the thermal properties of HMPE ropes. A FLIR A6753sc infrared thermal camera was used to record rope surface temperature periodically as the tests progressed. It was placed approximately 50 cm from the rope entrance to the sheave profile, as shown in Figure 3.5. The recording process was set to sample at 100 Hz for 2000 images, resulting in a 20 seconds video for each period, which recorded one full cycle of the CBOS test.

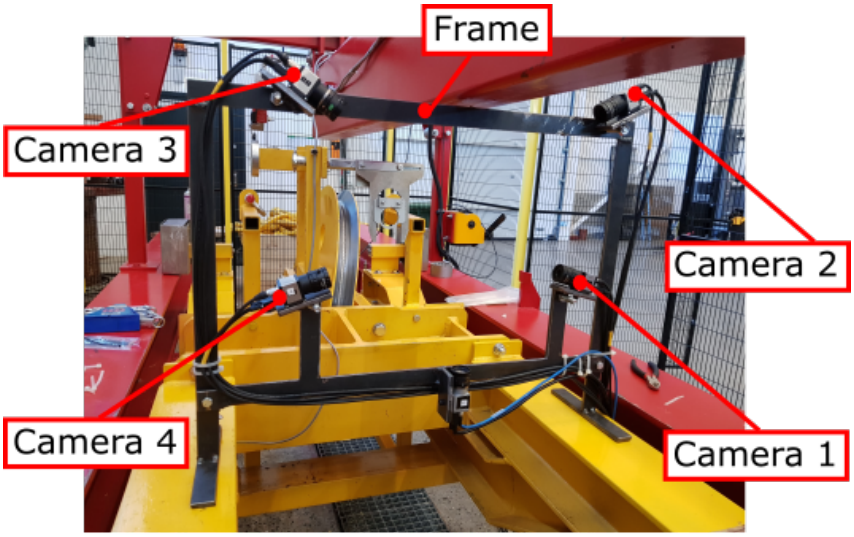

(a) The frame and cameras installed at the testing sheave of the CBOS machine.

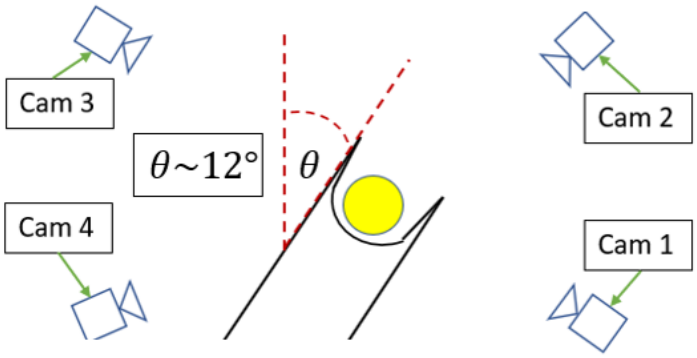

(b) Schematic of how cameras are positioned around the rope.

(c) Edmund optics camera.

Figure 3.4: Overview of computer vision system set-up.

Figure 3.5: View of FLIR A6753sc infrared thermal camera during CBOS testing for steel wire ropes.

A distance measuring laser was used to monitor the extension of the cylinder in the CBOS machine during the CBOS test. This allowed the global elongation of the rope to be recorded. The specific properties of each constituent part of the CM system are available in Section C.9.

3.2.3 Fibre rope and marking scheme

Three different types of fibre ropes were used during CBOS testing. Paper B documents the testing of 28 mm width, 12 strand, Dextron 12 Plus fibre rope and Paper C describes CBOS tests with 12 strand Dyneema DM20 XBO HMPE fibre ropes with nominal diameter of 28 mm. Tests are also carried out on 28 mm Samson Amsteel Blue ropes, which form a part of the data sets used for ML application in Papers D and E.

The rope is subjected to different amounts of bending during one cycle of the CBOS machine. For the purposes of the research discussed in thesis, three general bending zones are defined for data recording, namely the straight zone (SZ), single bend zone (SBZ) and double bend zone (DBZ). SBZ bending can be summarised as the portion of the rope following a straight-bend-straight motion during one cycle, whereas DBZ bending can be defined as straight-bend-bend-straight-bend-bend-straight motion during one cycle. A schematic of these zones is shown in Figure 3.6a. It is noted that this specific example relates to the zones measured for Paper C and that the research presented in Paper B featured only one measurement from the DBZ, as shown in B.1.

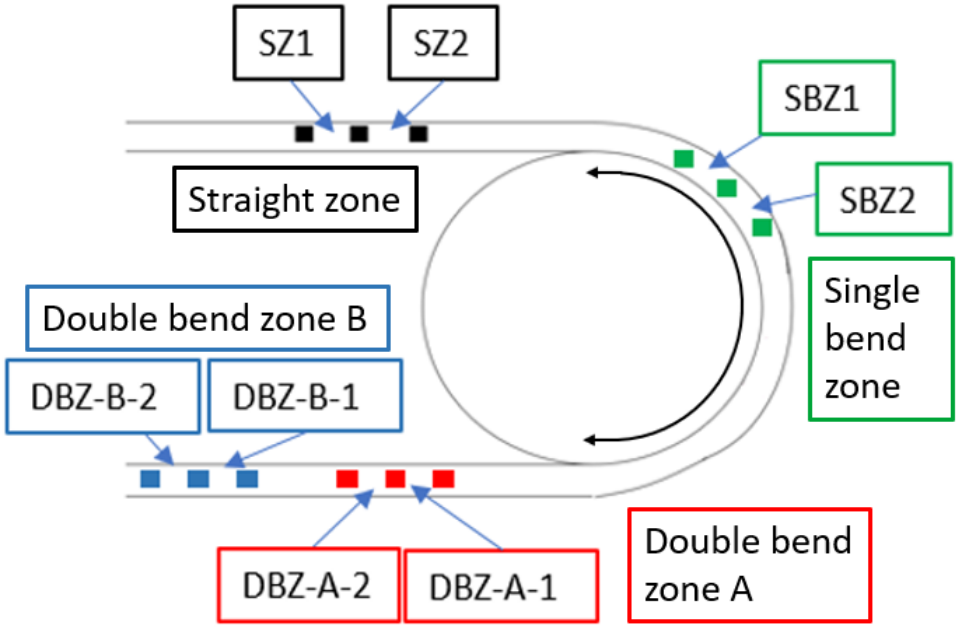

(a) Approximate location of different coloured markings placed on the rope for length and width monitoring based on bending zones.

(b) Example of threads sown into a rope sample to designate a bending zone.

Figure 3.6: Overview of measurement zones on ropes during CBOS testing.

Additionally, based on the findings from the tension tests, a more robust means of defining these measurement areas was implemented. Instead of tape, threads are used to designate each bend zone, as shown in Figure 3.6b. The markers are arranged such that there is half a lay length between each one, with its own label to distinguish it from the neighbouring subsection.

3.2.4 Testing procedure

The ropes were tested until failure. A rope failure was considered to occur when the machine automatically stopped due to substantial loss in tension or when there was a more obvious rupture in the rope.

Additionally different safety factors (SF) were used during testing. The SF is defined using equation 3.1.

$$SF = \frac{MBL_{rope}}{T_{test}} \tag{3.1}$$

where MBL_{rope} is the rope minimum break load as specified by the manufacturer and T_{test} is the test tension exerted by the cylinder in the CBOS machine divided by two. A summary of the SFs used for each rope during CBOS testing is shown in Table 3.2.

Table 3.2: Summary of data sets taken from CBOS testing.

Campaign	Rope	SF	No. of ropes
1	Dextron 12	13.6	3
2	DM20 XBO	11	5
3	Amsteel Blue	8	4

The number of rope samples tested in this project are limited as CBOS testing is both time consuming and costly. However, with the samples provided it was possible to validate the selected condition monitoring methods for condition classification and RUL estimation.

3.2.5 Calibration

Calibration of the visual measurements was performed using the in-built function in MATLAB that uses a chessboard pattern to adjust the images for distortion and give an approximate error in pixel size. Additionally, an object of known size is placed next to the rope to convert the measurement in pixels to millimetres for better comparison between all the cameras.

Calibration of the thermal camera was performed with two different methods for validation. This was performed through a black-body calibration with an attached sample, which was further validated through placing thermocouples embedded in rope samples to find the ropes' emissivity. There is also further auto-calibration implemented in the FLIR software used to record the thermal data.

Chapter 4

Feature extraction

This chapter outlines the methods used to extract features from the data recorded in the experiments outlined in chapter 3 and gives an assessment of their effectiveness for indicating rope state. Local deformations (lengths of sections of strands), global length, local width (of cross sections) and temperature were chosen for investigation as potential condition indicators (CIs) in fibre ropes for both diagnostics and prognostics. The methods of feature extraction are shown in Sections 4.1 and 4.2. All features, with the exception of global elongation, are extracted from videos recorded by the machine vision and thermal cameras.

4.1 Geometric data

The algorithms used for image processing and data analysis were developed in Python using OpenCV [117]. A series of morphological operations are performed to calculate the local length, local width and roundness of the rope. While calculating the same ~~data for~~ CIs, it is noted that there are slight differences between the algorithms applied to calculate rope geometric data in Papers A, B and C.

4.1.1 Global length

The global length is measured using a infrared distance measuring laser outlined in Section 3.2.2. The distance recorded corresponds to the extension of the hydraulic cylinder as the experiment proceeds.

4.1.2 Local length

The algorithm used to calculate the local length is based on locating the different coloured markers, an example of which is shown in Figure 3.6b. Figure 4.1 show the progression

of morphological operations applied to the image that allow the calculation to take place. Firstly the raw image is converted to HSV colour space to make it easier to detect specific colours even at varying brightness. In Figure 4.1, the colour red is detected but the scale can be adjusted to reflect the other colours in the marking scheme in the other bend zones. A colour mask is created from this scale and a binary image is produced where the areas coinciding with the colour are converted to white. A dilation operation is applied to fill in smaller gaps in the white areas to aid finding the centre point. Finally, the centre points of the marker is found through a contouring operation. The Euclidean distance between these centre points is then calculated as the local length.

Where possible, at least ten images of the same subsection in each video recording are used so the median, maximum, minimum and variation as standard deviation of the length from each image form additional features. These distances are monitored for changes as the tests proceed.

Figure 4.1: Morphological operations applied to the image to detect a specific colour for length measurements: (a) original image, (b) binary image created, (c) dilation operation applied and (d) final processed image with centre point of marker visible after contouring operation.

4.1.3 Local width

Rope cross section width is calculated from the perspective of each camera used in each experiment. There are two different methods outlined in the research presented in this thesis. A width algorithm based on detecting the rope colour forms the approaches outlined in Papers A and C, whereas a combination of different filters is applied to images in Paper B.

The approach used in Papers A and C is done in a similar fashion to the length algorithm specified in Section 4.1.2. The raw image is converted to HSV interpretation and the rope colour is used to create the binary image. It is then dilated to fill in any gaps and eroded so the colour mask better coincides with the true edges of the rope. Finally, the ropes are detected with a contouring algorithm. An example of these morphological operations is show in Figure 4.2.

The Paper B approach uses a combination of bilateral filter, Gaussian blur, canny

edge detection, dilation, erosion and contouring to find the outer limits of the ropes in the images.

Both of these approaches share the same final stage, where the lines found through the contouring operations are saved as coordinates. Seven regions of interest (ROI) are defined. The shortest length detected between the top and bottom lines defined by the contour is then saved as the width for that particular ROI (only three ROIs are used in the tension tests in Paper A). From these seven ROIs, the median is saved as the overall width for the subsection in question. Median is used rather than average, since median is a statistical feature less sensitive to outliers. Additionally, the maximum, minimum and standard deviation are also measured as potential features. As the cameras in the CBOS experiments are synchronised, the widths from all four perspectives at the same time and position on the rope can be interpreted.

While both approaches give the same result, the approach outlined in Paper C is less computationally expensive than that outlined in Paper B.

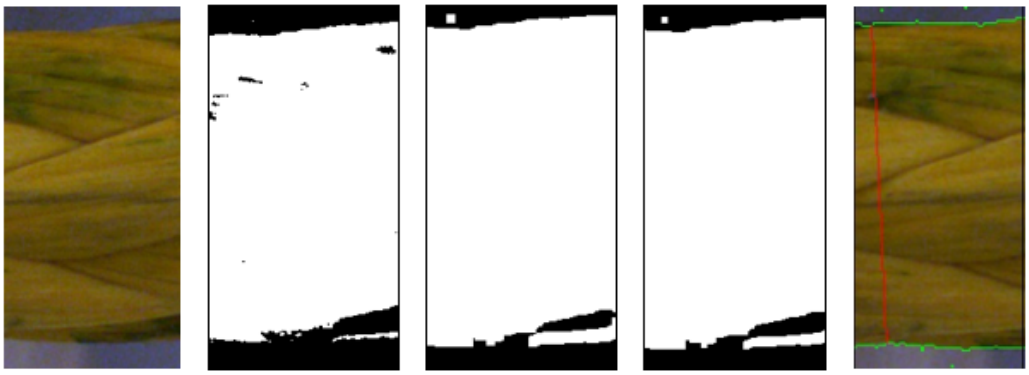

Figure 4.2: Different stages of morphological operations applied to the image to detect the rope and calculate the width: (a) original image, (b) binary image created, (c) dilation operation applied, (d) erosion to reduce edge thickness, (e) contouring to find edges of rope and applied to original image to find the width (red line).

4.1.4 Roundness

As part of the CBOS experiments outlined in Paper B, an estimation for the roundness of the rope was also calculated. The roundness, R is specified in equation 4.1.

$$R = \frac{A_o}{P}\frac{2}{\bar{r}} \tag{4.1}$$

where R is the roundness shape factor, A_o is the cross-sectional area, P is the perimeter and $\bar{r}$ is the average radius. The calculation is based on a circle, where 1 indicates perfect roundness and any decrease is seen as a reduction in roundness.

The roundness R was not used in any research after Paper B as it was not deemed to contribute anything to characterization of the rope state not already seen from the width measures.

4.2 Thermal data

The temperatures from the rope surface are interpreted through FLIR camera software [118]. As shown in Figure 4.3, an ROI is defined on the rope surface, where the average temperature is determined from the pixels within it. The maximum, minimum and standard deviation of the measurements from within this ROI are also recorded. An ROI is defined so it will always contain the rope and no background interference due to slight varying vertical displacements of the rope during CBOS testing.

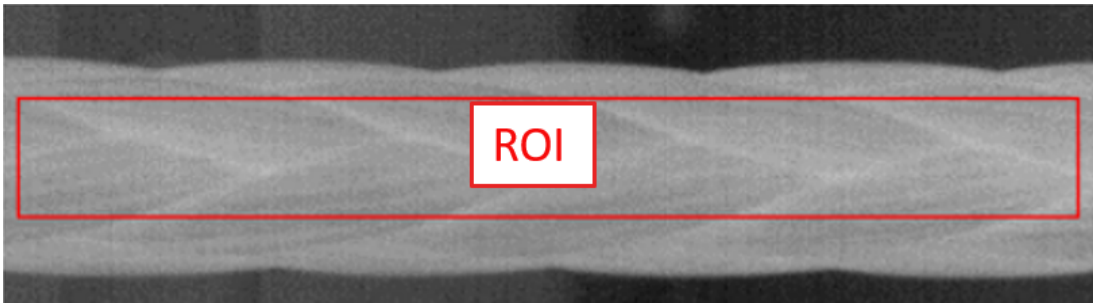

Figure 4.3: Example ROI applied in IR camera software to measure temperature on rope surface.

4.3 Outliers

Outliers in the geometric features are handled through using the median absolute deviation (MAD) as shown in equation 4.2. This is applied to the local length and width data due to these CIs comprising of readings from several images.

$$\text{MAD} = \text{median}(\mid x - \tilde{x} \mid) \tag{4.2}$$

where x is each value and $\tilde{x}$ is the median value for each recording. This is done for both the local length and width measurements, as these operations are performed on the same images. For local length measurements, this is done from the ten length values extracted from the ten images. For the width measurements, this will be based on seventy values comprising seven ROIs from ten images.

The median is known to be more robust than using the average of the measurements, which can be greatly influenced by outliers. The following criteria shown in expression 4.2 is used to eliminate the outliers from the data set.

$$| x - \tilde{x} | \geq 3 \times \text{MAD} \tag{4.3}$$

The median, maximum, minimum and standard deviation of the values that remain after the application of MAD are used as the feature values at each particular time stamp.

Outliers in the thermal data are limited by the conservative ROI applied during recording. The data collected is limited to the rope surface area with no interference from the background in the images. Average temperatures within the ROIs can therefore safely be used as statistical feature here.

4.4 Missing data

After outliers are omitted, linear interpolation is applied to account for missing data. Missing data may occur as a result of intermittent instrumentation failures or the algorithms failing to detect the specific sections of the rope due to degradation of section markers.

4.5 Results

4.5.1 Tension testing

Figure 4.4 shows the results of the length and width algorithms monitoring the tension tests. While the reduction in width and increase in length should be expected given the nature of the test, the monitoring provided by the algorithms show good correlation with the increased load in the tests. It served as validation for the method but also showed that more robust means of marking had to be developed since it was not possible to measure length in experiments 1 and 2. These findings were then brought forward and adapted to the CBOS tests.

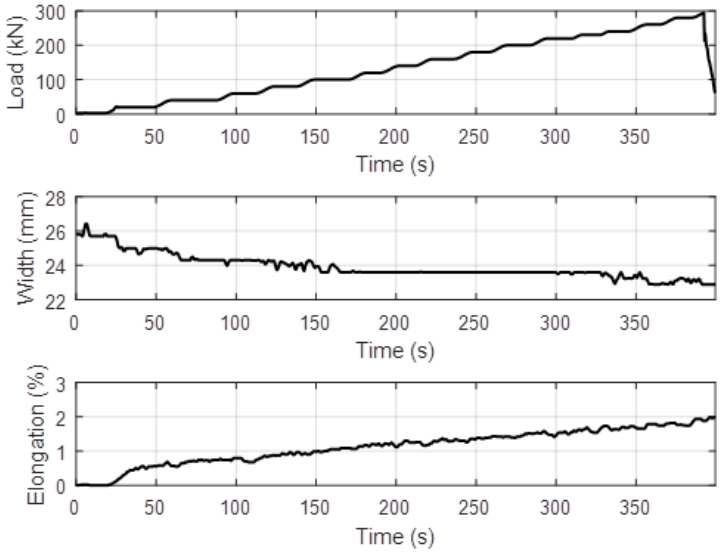

Figure 4.4: Width and length results in experiment 3 from tension testing.

4.5.2 Cyclic-bend-over-sheave testing

4.5.2.1 Observations

Figures 4.5 and 4.6 show typical damage seen in ropes as a result of CBOS testing. Compression damage on the surface is seen in the portion of the rope in contact with the sheave, as shown in top image of Figure 4.5. However, the opposite side of the rope shows both ruptured strands and extruded loops, which progressively develop through the testing period. It is possible to monitor these changes in the rope topography as a CI, in particular through use of the width monitoring algorithm.

This gradual change in the rope can lead to "larger" width measurements as the algorithm detects the extruded loops and ruptured strands. This coincides with increases and decreases in the local length at the measured subsections.

Figure 4.6 shows an example of a rupture in a rope that results in the end of a CBOS test. There is an increase in local stress concentrations, as the ruptures in the rope build up as the CBOS test progresses and causes rearrangement in structure.

The number of cycles counted by the CBOS machine for each rope at failure are summarised in Table 4.1. This details which rope samples were tested in each campaign and the paper where the analysis was presented. All ropes failed at the smaller test sheave with the exceptions of C2R1 and C2R4. These particular two samples failed at the larger driving sheave as a result of unavoidable contact with the splices.

Figure 4.5: Compression damage (top) and extruded loops (bottom).

Figure 4.6: Example of rupture in fibre rope at the end of a CBOS test.

4.5.2.2 Global length

Figure 4.7 shows the global elongation for the ropes tested in campaign 2. It is noted that Ropes C2R1 and C2R4 failed due to degradation in the splice that was partly in contact with the larger driving sheave. The other ropes all failed at the test sheave as intended. Note that the global elongation in all cases was below 1 %, which was in accordance with the manufacturer's rope specification.

Table 4.1: List of cycles at failure during CBOS testing for ropes in Papers B, C and D.

Paper	Rope	No. of cycles at failure	SF
B	C1R1	57,672	13.9
	C1R2	45,944	13.9
	C1R3	44,925	13.9
C	C2R1	75,324	11
	C2R2	122,368	11
	C2R3	120,430	11
	C2R4	87,314	11
	C2R5	143,374	11
D	C3R1	14,948	8
	C3R2	13,883	8
	C3R3	13,901	8
	C3R4	13,998	8

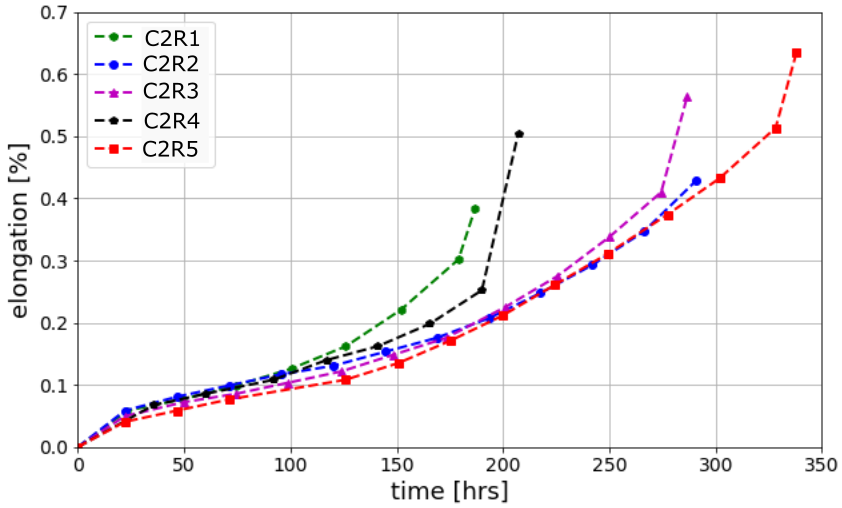

Figure 4.7: Global length progression during testing.

4.5.2.3 Local length

An example of the algorithm working on rope C2R5 is shown in Figure 4.8, local relative distortion of the strand is shown to be +10.8 % in the DBZ-B-2 subsection when comparing the first and final measurements. The overall middle relative distortion equates to -0.6 % across the whole lay length in DBZ-B when the measurement from DBZ-B-1 is taken into account, highlighting the need for sub-lay length measurements.

For all five ropes tested in campaign 2 the sections monitored in the straight zone (SZ) and single bend zone (SBZ), had no strains that exceeded 1 % of the original length. Ropes C2R2, C2R3 and C2R5 ran for significantly more cycles than C2R1 and C2R4, with significant longer elongation detected in the two DBZ sections than the SZ and SBZ sections. This can be attributed to DBZ sections being subjected to twice as many bends over the sheave than SBZ. Figure 4.9 shows the changes detected using the length calculation method throughout each test, with Rope C2R5 displaying the largest changes in the marked DBZ sections. There is observed to be a heterogeneous spread of strain changes in the DBZ sections across all the samples. This was also observed in campaign 3, but there were significantly few cycles than in campaign 2.

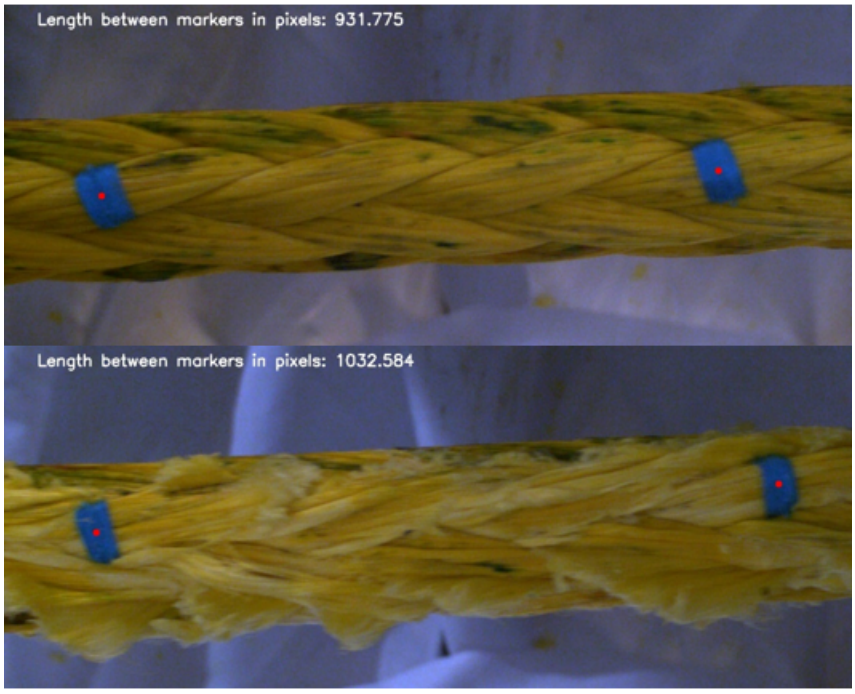

Figure 4.8: Example of increase in local length in the DBZ from the start (top) and end (bottom) of a CBOS test.

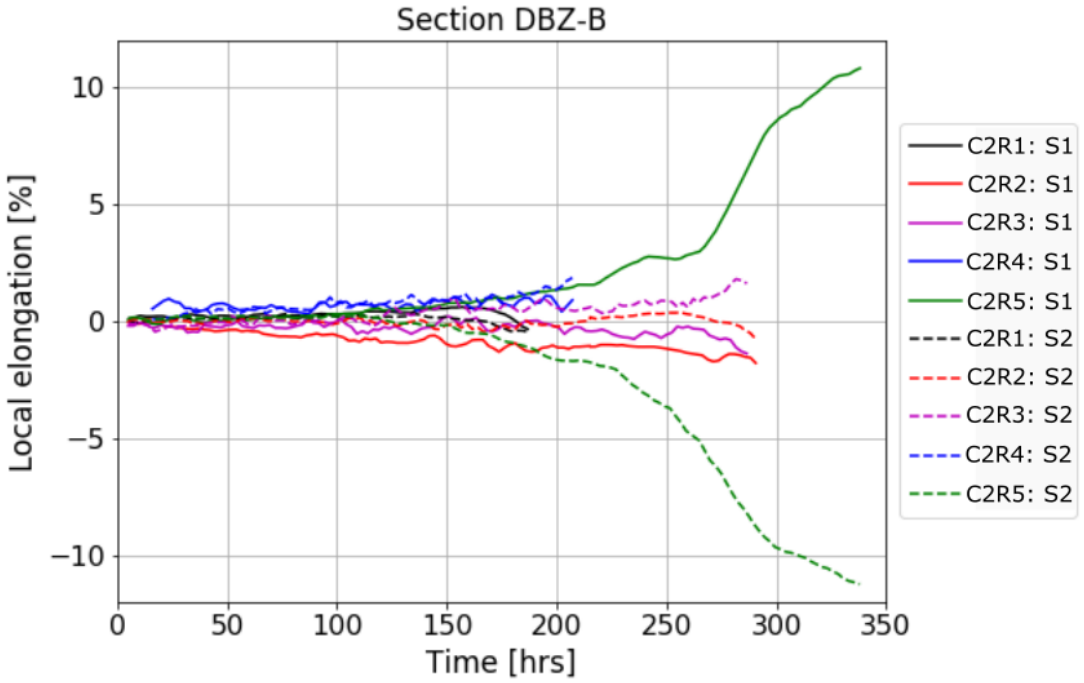

Figure 4.9: Local length changes after bedding in phase in Section DBZ-B for all ropes (R-Rope, S-Subsection).

4.5.2.4 Width

Extruded loops and ruptured strands become more apparent in the DBZ sections due to repeated bending and unbending, which are detected effectively by the visual system and algorithm through the larger relative width change. The structure of the rope rearranges due to repeated deformation. It is noted that generally there are small variations and continuous increase in width despite the elongation of the same sections.

Unlike the local length measurements, there is no evidence of "reciprocal" changes. Each subsection is shown to follow the trend of the neighbouring subsection despite the occurrence of the opposite elongation behaviour in some of the ropes.

Width monitoring is vital as it indicates changes in rope structure, including both in shape or through deterioration such as extruded loops or ruptured strands. The width calculation method applied is adept at monitoring these changes over the testing period, and it also clearly displays the differences in the different bending zones. An example of a processed image is shown in Figure 4.11 from Rope C2R1 as observed from Camera 3. There is visible deterioration in the rope structure with the presence of extruded loops clearly seen before rupture. The width calculation algorithm adapts to this, with the rope edge detection including the extruded loops. In this instance, the shortest distance in the constituent regions of interest will be higher and subsequently produce a larger median value, allowing the changes to be quantified throughout the rope lifetime.

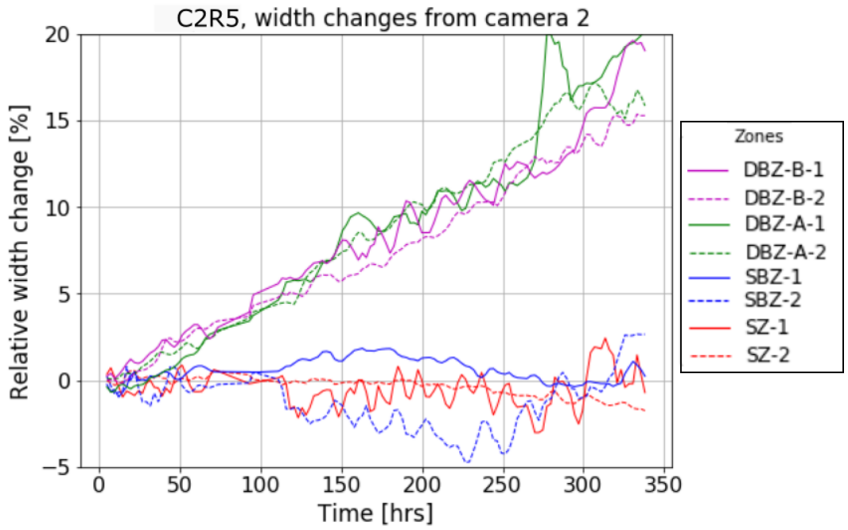

Figure 4.10: Percentage change in width from camera 2 for all zones in Rope C2R5.

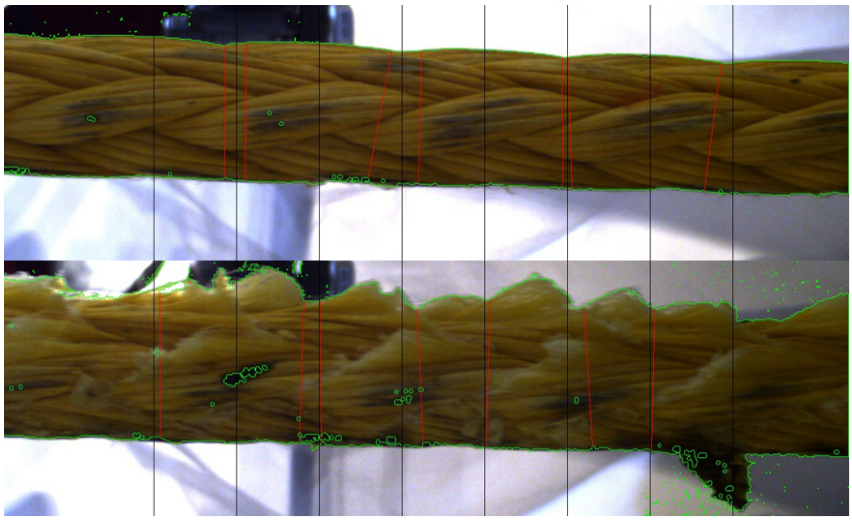

Figure 4.11: Example of differences in a rope sample from the start (top) and showing extruded loops towards the end of CBOS testing (bottom).

4.5.2.5 Temperature

Thermal images are recorded as they indicate frictional and deformation work in the rope. Figure 4.12 shows a distinct temperature measurement curve in each rope. However, within each recording there are distinct zones visible due to temperatures associated with the bending behaviour in each section. The first and second plateaus in the curves are associated with the SBZ and DBZ sections respectively.

After increasing from the beginning of the test, the average temperature in the DBZ section is shown to decrease as the rope heads toward rupture. This also coincides with lower maximum and minimum temperature at the DBZ section at the more advanced

recording times during testing.

The varying temperatures in the sampling areas of the rope surface are given by the standard deviation. This follows the same "plateau" pattern as the temperatures. There are larger deviations recorded in the DBZ sections at the more advanced recording times. Additionally there are large standard deviations recorded in the transfer points between the SZ and DBZ sections in Rope C2R5.

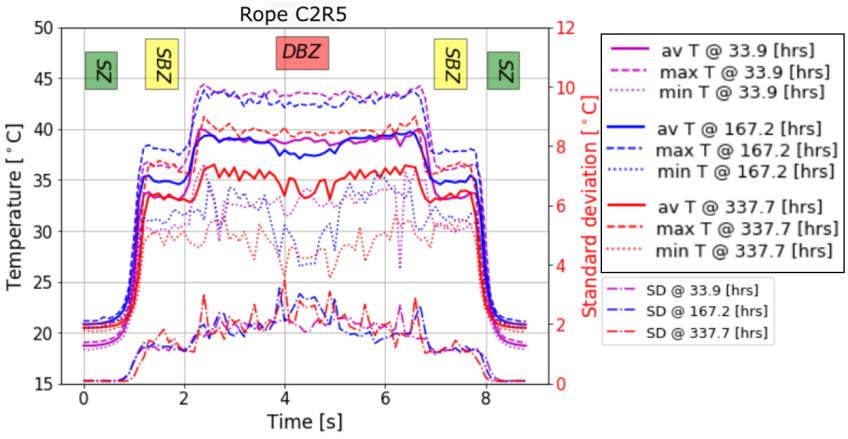

Figure 4.12: Rope C2R5 average, maximum, minimum and standard deviation temperature measurements along the rope for one cycle with respect to the associated test time.

Thermal monitoring using an IR camera brings not only temperature measurements but can provide another useful visual aid to assess the rope surface. The method applied allows each specific bending zone to be scrutinised in detail and monitored over time. Moreover, the results found using the thermal camera in this study allow the physical changes of the rope to be compared concurrently with temperature. Monitoring of the average, maximum, minimum and variation by standard deviation gives information on changes into the physical structure of the rope.

The lower average, maximum and minimum temperatures that coincide with larger standard deviations at more advanced testing stages, particularly in the DBZ section, can be attributed to the increasing presence of structural degradation in the rope. As detected with the width measurement algorithm, the extruded loops and ruptured strands that are visible and more prevalent in the latter stages of testing via the thermal camera can be seen in Figure 4.13. These degradation features are markedly cooler than the main body of the rope and contribute to the spread of measured temperature values.

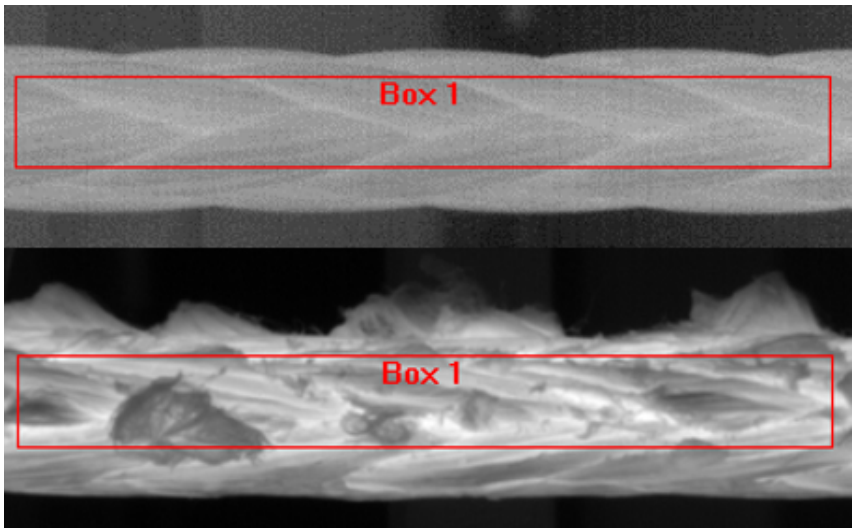

Figure 4.13: Example of differences in temperature in rope sample from start (top) and end (bottom).

Chapter 5

Condition classification

This chapter outlines the application of ML algorithms to the CBOS data sets to classify the condition of the ropes and serves as a summary for the content presented in Paper D. The CIs determined from data recorded through methods outlined in chapter 4 are used to predict fibre rope condition. The methods chosen for classification include: decision trees; random forest; and support vector machine. Each algorithm is compared and assessed for its effectiveness for classification.

5.1 Applied methods

5.1.1 Decision trees

This study applies the decision tree algorithm as detailed in [119], using the implementation in scikit-learn [120]. It comprises a flowchart that assigns each sample to one of two classes based on a condition selected from the features available. The samples are split based on an attribute selection measure, in this case the Gini index, which measures the impurity of a data split with respect to the classes available [121, 122]. This process is performed recursively until all samples are assigned to a class or there are no more features available to make splits. The depth of the trees can also be limited to influence the complexity of the model. For example, a deeper tree can lead to a more accurate result but has the risk of creating an overfitted model due to unrealistic complexity. Since there is a random element involved in the algorithm, each tree configuration is repeated 20 times to assess the spread and confidence in the classification predictions.

5.1.2 Random forest

Random forest is an example of an ensemble learning method comprised of many decision trees. The method is described in detail in [123] and also implemented using sci-kit

learn [120]. A random forest is formed with a defined number of decision trees, where each individual tree is formed on a subset of samples and features created through random sampling with replacement. These multiple predictions are combined in the bagging phase [124], where the a class is assigned based on a majority vote by the individual trees in the random forest. Similar to the decision tree algorithm, the depth of the individual tree can be controlled. The number of trees that make up the forest can also be adjusted. Each configuration is repeated 20 times to assess the variation in the predictions made by the model.

5.1.3 Support vector machine

Support vector machine has also found use for classification problems as defined in [125] and are implemented through scikit-learn [120]. The algorithm works by fitting a hyperplane that divides a set of instances into classes. The optimal solution is separated is defined as where the margin that separates the instances has been maximised, with the instances used for the separation are referred to as "support vectors" [126]. The generalisation to the nonlinear case is achieved by applying the so-called kernel trick, using non-linear kernel functions for transforming the task into a higher-dimensional space, in which the number of possible linearly separating hyperplanes is larger than in the original space. In this study linear (SVM-linear), Sigmoid (SVM-Sigmoid) and radial basis function (SVM-RBF) are applied to alter the hyperplane shape applied to the data. Each configuration is performed once and the performance of the kernels is compared. The variation in performance between each classification with SVM is considered negligible and is therefore performed only once.

5.1.4 Classical statistical methods

The machine learning models detailed previously are compared and assessed along with the classical statistical approaches k-nearest neighbours [127], Naïve-Bayes [128] and logistic regression [129]. These methods are commonly used for classification problems as an alternative to machine learning. As the topic for this research is finding good methods for condition monitoring, classical statistical methods are also investigated to assess if they are sufficiently advanced to achieve good classification results.

5.2 Experimental study

5.2.1 Features

The features used for condition classification are derived from the CBOS data recorded from the experiments and data extraction outlined in Chapters 3 and 4, respectively.

For each of the eight sections defined in Figure 3.6a, one length measurement and four width measurements (one from each of four cameras) are used as features. Each of these measurements are aggregated as average, maximum, minimum and standard deviation. The global length is also measured as a single absolute value.

Temperatures are only available for the lumped zone straight zone (SZ), single-bend zone (SBZ) and double-bend zone (DBZ) and the temperatures values within the rope part of each relevant image are aggregated as average, maximum, minimum, standard deviation and peak-to-peak. The data used for condition classification comes from campaigns 2 and 3, which were tested at different safety factors. A complete list of features used in this study are shown in Tables 5.1 and 5.2.

Table 5.1: List of features created for condition classification.

Data type	Feature (zone)	Statistical parameter type
geo	Local length (eight sections)	Median, max, min, stdev
	Width (eight sections)	Median, max, min, stdev
	Global length	Absolute value
therm	Temperature (three lumped sections)	Average, max, min, stdev, peak-to-peak
	Temperature (SBZ-DBZ)	Ratio

Table 5.2: Data set summary for C2 and C3 ropes.

Data set ID	C2_geo	C2_geo_therm	C3_geo	C3_geo_therm
Data type	geo	geo + therm	geo	geo + therm
Features	65	81	65	81
Ropes	5	5	4	4
Records	509	509	103	103
Manufacturer	Dyneema	Dyneema	Samson	Samson
Rope type	DM20 XBO	DM20 XBO	Amsteel Blue	Amsteel Blue
SF	11	11	8	8

5.2.2 Data pre-processing

The outliers and missing data are dealt with using the steps outlined in Sections 4.3 and 4.4, respectively. After these steps, the raw measurements from the data acquisition phase are scaled by subtracting the mean value and dividing by the standard deviation. This is done for each rope tested to improve comparability between the rope samples and is a standard step to prepare data for machine learning application. An example of a record of standardised values for features used to form the models is shown in Figure 5.3:

Table 5.3: Example of standardised values for the length feature located in the straight zone (SZ).

S1av	S1max	S1min	S1stdev	S2av	S2max	S2min	S2stdev
-0.57	0.27	0.91	0.04	-0.64	0.15	-0.01	0.42

5.2.3 Labelling

To perform classification predictions on the ropes, the records need to be appropriately labelled. This study is a binary classification problem, therefore the ropes can be considered Healthy (HE) or Close To Rupture (CTR). The development of the global length resembles a creep curve with three distinct stages: primary, secondary and tertiary creep. The tertiary creep stage encompasses the accelerated creep phase after the transition point. Fitting the global length development to a polynomial allows a quantitative definition of the transition from secondary to tertiary creep, thereby labelling each sample as "HE" or "CTR", as shown in Figure 5.1. The "CTR" labelled samples equate to the accelerated creep phase. This labelling process allows an automated, quantitative definition of rope condition to be implemented.

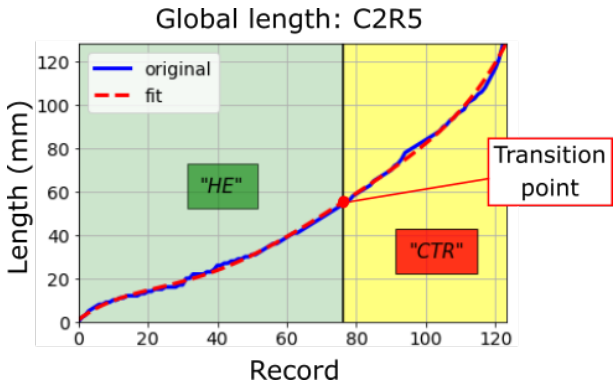

Figure 5.1: Example of labelling process on rope C2R5 with transition point between both classes.

5.2.4 Model training and assessment

Leave one out cross validation (LOOCV) is performed on the CBOS data sets. The steps in the LOOCV process in this study are detailed in Figure 5.2.

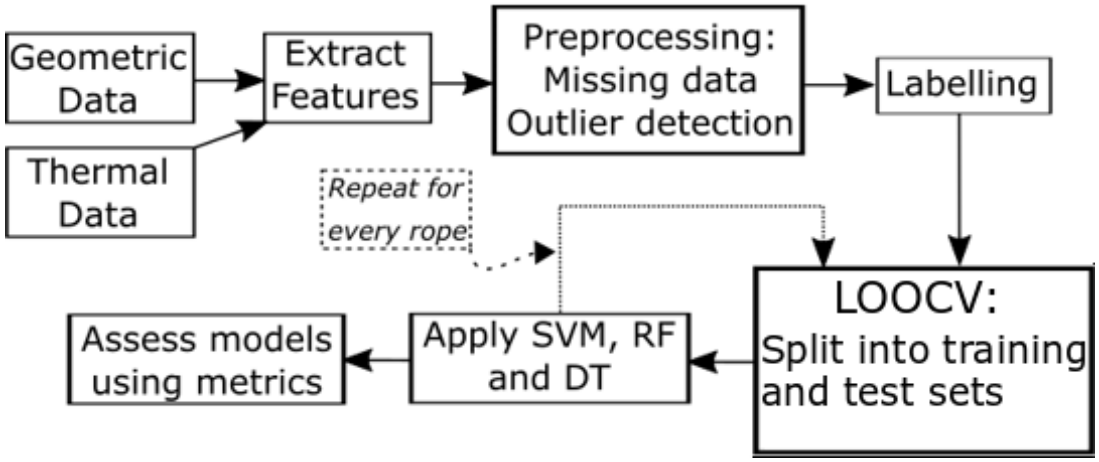

Figure 5.2: Flowchart of operations for fibre rope condition classification.

The results are shown through metrics that are derived from a Confusion matrix description, which is shown in Figure 5.3.

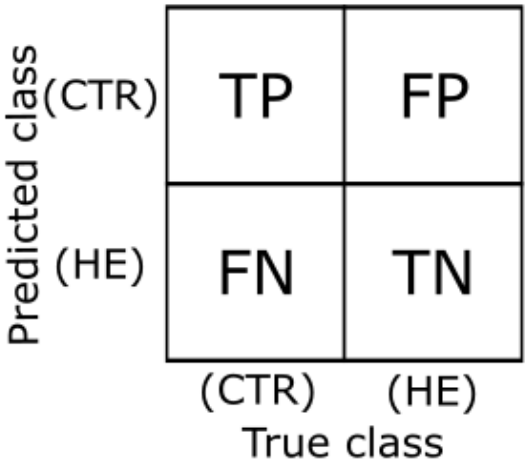

Figure 5.3: Overview of confusion matrix.

The correct predictions can be summarised as true positives (TP) and true negatives (TN) and the incorrect classifications are quantified as false positives (FP) and false negatives (FN). The negative and positive classes coincide with the HE and CTR classes, respectively. The metrics used for model assessment accuracy (ACC), probability of detection (POD), probability of false alarm (PFA) and Matthews correlation coefficient (MCC) are shown in equations 5.1- 5.4:

$$ACC = \frac{TP + TN}{TP + TN + FP + FN} \tag{5.1}$$

$$POD = \frac{TP}{TP + FN} \tag{5.2}$$

$$PFA = \frac{FP}{FP + TN} \tag{5.3}$$

$$MCC = \frac{TP \times TN - FP \times FN}{\sqrt{(TP + FP)(TP + FN)(TN + FP)(TN + FN)}} \tag{5.4}$$

ACC is the most general of the metrics presented in this section and simply takes into account the number of correct predictions across of the whole data set. The closer the value is to 1, the better the model is performing. However, this does not take into account the number of samples present in each class.

POD can be summarised as the likelihood of a CTR being correctly classified. The closer the metric is to 1, the better the model is deemed to have performed in this aspect. A model that fails to detect CTR samples runs the risk of allowing the rope to continue operation until it fails.

PFA is interpreted as the probability of an "HE" sample being mislabelled as "CTR". If a model has a higher tendency to classify samples as CTR when they are HE, it would lead to more false alarms during condition monitoring. This could potentially prove to be costly due to operational stoppages for inspection and therefore a lower value is preferred.

MCC takes into account all four values in the confusion matrix and provides a more balanced assessment regardless of whether one class is disproportionately over or under-represented. A value close to 1 means that both classes are being predicted well and show that true and predicted classes are correlated.

However, none of the metrics give information about what specific samples have been misclassified. A graphical method is therefore applied to assess this aspect. An example is Figure 5.5, which shows an example of the classifications predicted by the models at the various stages of the CBOS test.

Separate results are presented for data sets C2 and C3 and the values of the metrics are averaged over the number of individual ropes in each data set. The algorithms are then ranked and compared based on the predictions made.

5.3 Results

5.3.1 Confusion matrices and classification comparison

Figure 5.4 shows an example of confusion matrix results for the six different techniques applied to rope C2R5. Figure 5.5 shows a qualitative example of the six different techniques applied and the results given for rope C2R5. The true transition point between the HE and CTR classes is highlighted by the vertical blue line.

It is shown that most models identify a too early transition between the classes. There are a substantial number of HE instances classified as CTR before the transition point indicated by the vertical blue line for every different model.

The decision tree is shown to have a particularly poor performance in comparison to the other algorithms. It misclassifies a significant number of both HE and CTR samples. Moreover, when a rope break is imminent it continues to classify the rope as safe for use.

K-nearest gives a lot more false alarms in the earlier parts of the CBOS test than the other algorithms. This could prove costly in terms of operation downtime, as a rope identified as potentially failing requires inspection and remedial actions to ensure continually safe use.

5.3.2 Average metrics

The average results for metrics ACC, POD, PFA and MCC in data set C2 and C3 are shown in Figure 5.6 to 5.9. The best performing configuration of each algorithm is presented and assessed for classification performance.

An ACC value that exceeds 90 % generally indicates a very good performance, as it measures how many correct classifications were made across all samples. Random forest and SVM-linear were shown to be the best performing machine learning algorithms in data sets C2 and C3 respectively.

K-nearest was also shown to have similar scores in data set C2 to random forest, however as shown in Figure 5.5 this can be deceptive due to extensive mislabelling of HE samples as CTR in the earlier portions of the rope test time. These misclassifications are reflected by the higher PFA score, indicating that there is around a 10 % probability of a HE sample being misclassified as CTR. These types of misclassifications could prove costly due to increased down time for inspections.

Similarly, POD above 90 % also indicates a very good performance as this assesses how effective the model at classifying the CTR class. This was shown to drop between data sets C2 and C3, indicating that the data used in C3 was to the detriment of successfully classifying the CTR class.

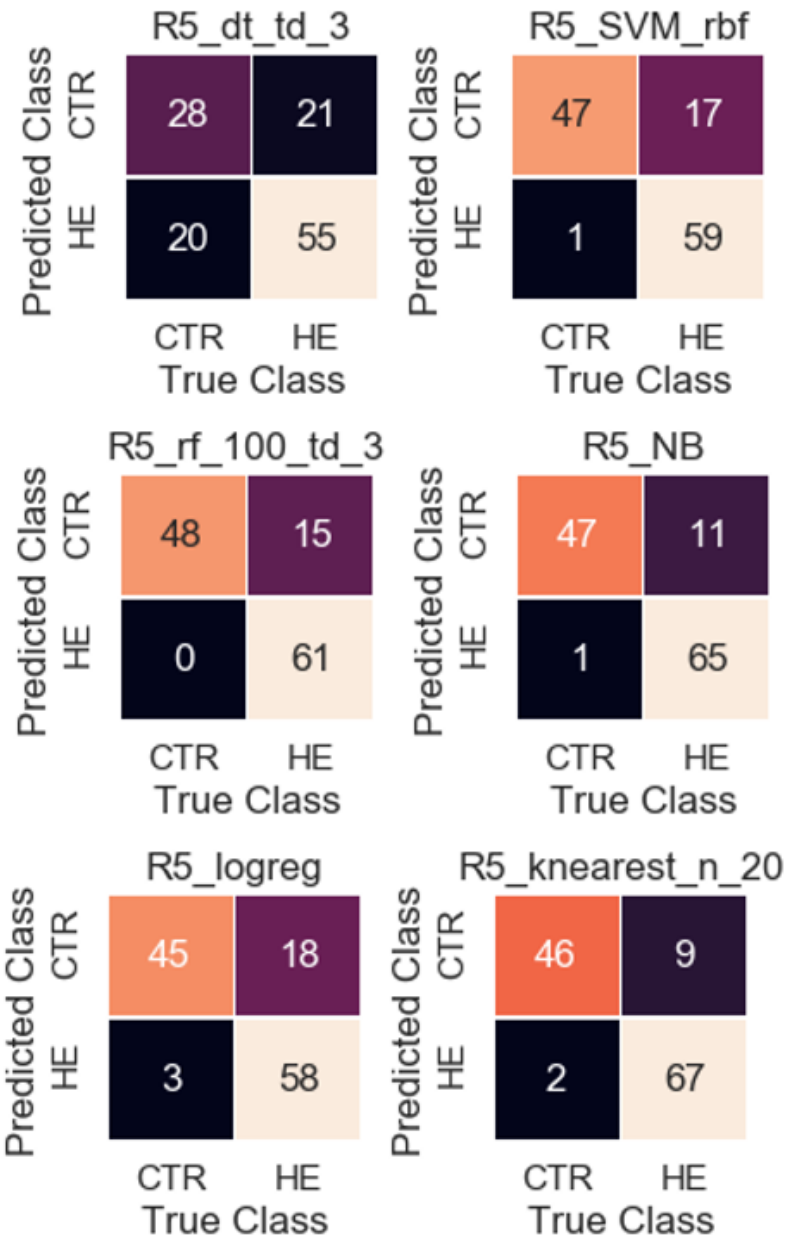

Figure 5.4: Confusion matrices for results on rope C2R5 for six different algorithms. "td" refers to tree depth for both decision tree and random forest. "100" in random forest refers to number of trees in forest.

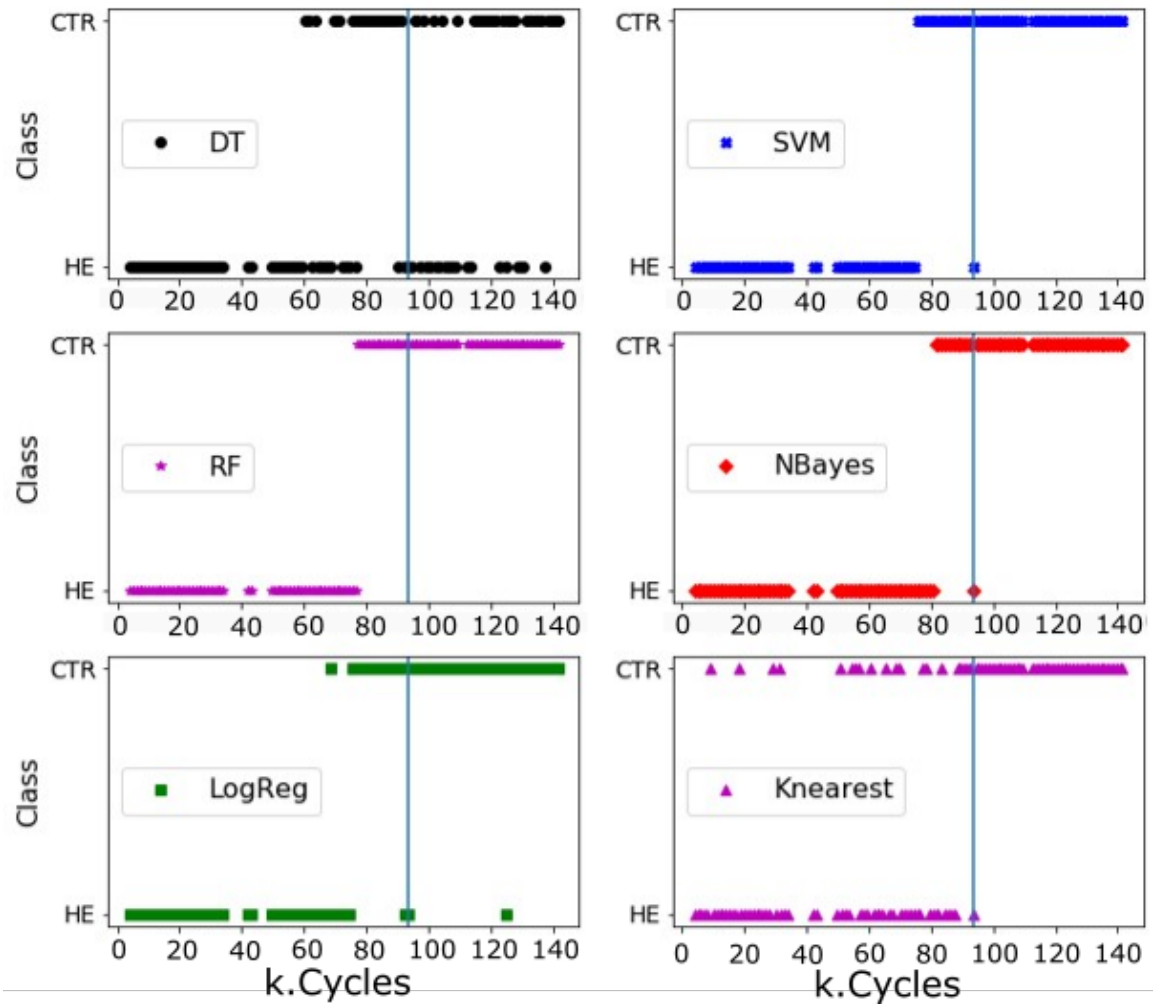

Figure 5.5: Example of classification results on rope C2R5 for six different algorithms.

Generally, a lower PFA score indicates better performance. PFA is shown to decrease dramatically between data set C2 and C3. From the outset a zero PFA score is ideal, however in the case of Naïve-Bayes, random forest and decision tree in data set C3 this indicates the models were biased towards predicting the majority of the samples as HE. There was no misclassification of HE samples as CTR but they failed to identify a number of CTR samples.

SVM linear increases dramatically in performance from C2 to C3. This is reflected in the increase in scores for both MCC and ACC between C2 and C3, indicating that the algorithm was able to better predict both classes with the change in data used.

When only assessing ACC and POD, the best performing algorithms could be interpreted as performing at the same level. However, when considering PFA and MCC scores, there is a clearer separation between the algorithms indicating that these metrics have to be used in combination to properly assess a model.

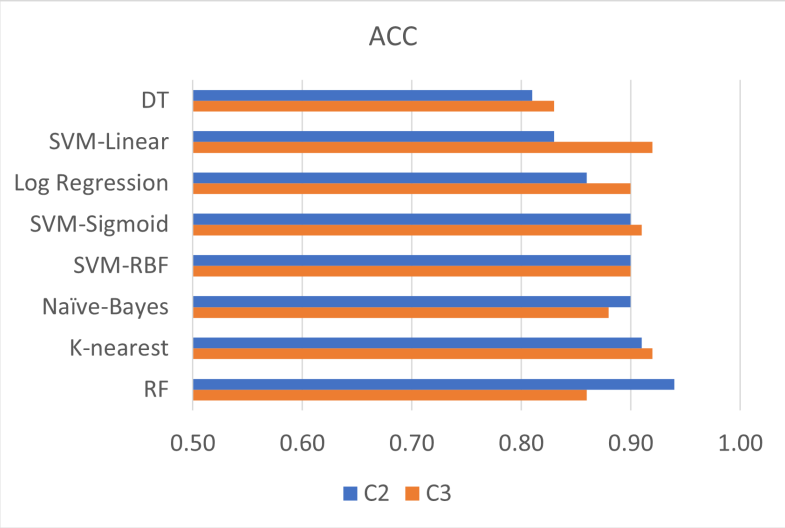

Figure 5.6: ACC results for each algorithm compared between data set C2 and C3.

5.4 Classification method comparison

The performance of each method is assessed and discussed individually in the following sections. Then the performance of the machine learning algorithms against the classical statistical methods is also considered and discussed. Despite discrepancies between the rope lifetimes, it is possible to achieve good condition classification results using both machine learning and statistical approaches with all the viable data from the zones outlined in Figure 3.6a.

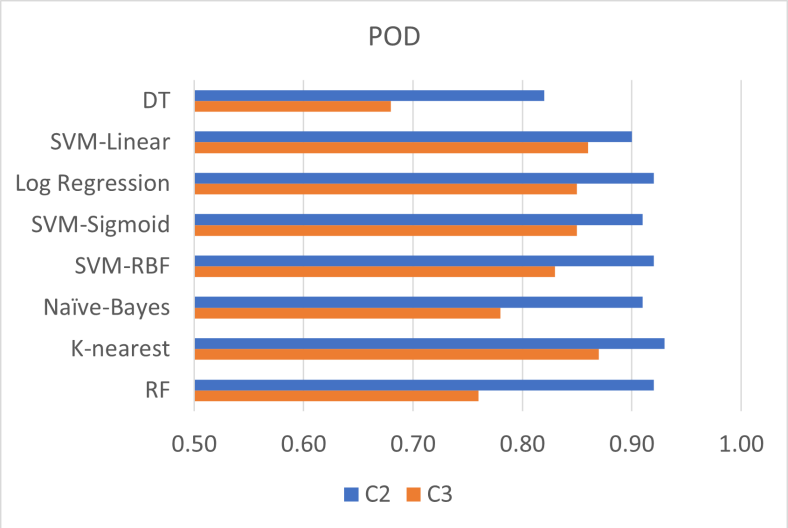

Figure 5.7: POD results for each algorithm compared between data set C2 and C3.

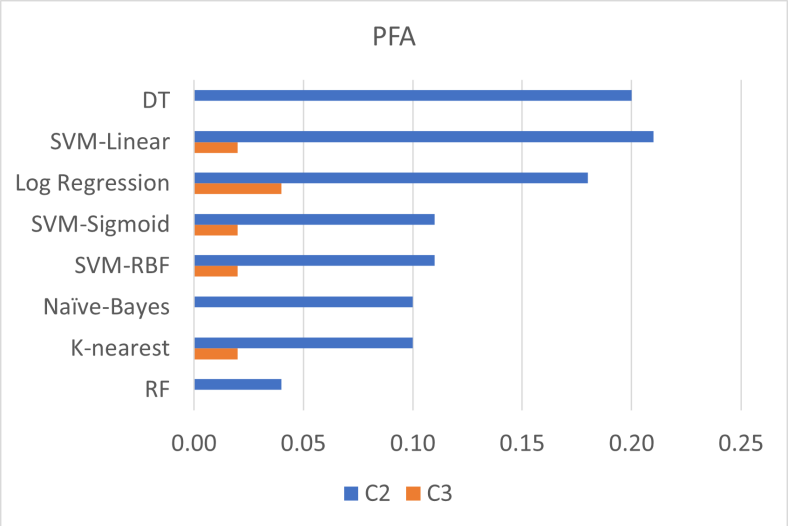

Figure 5.8: PFA results for each algorithm compared between data set C2 and C3.

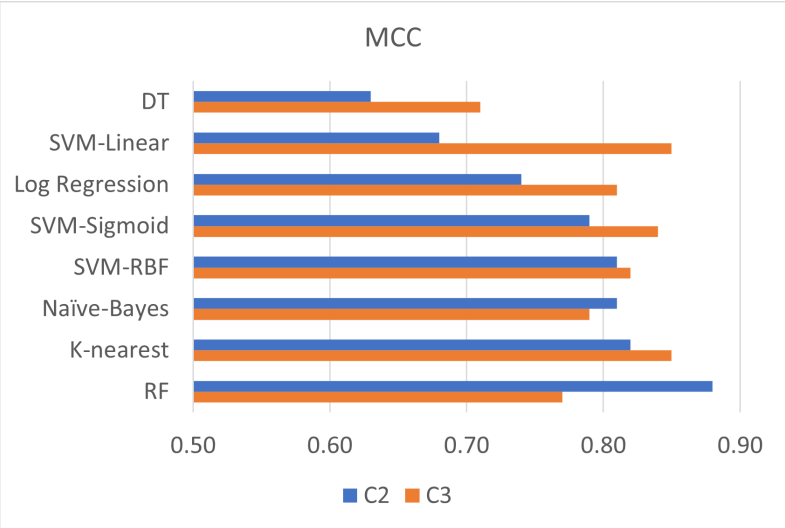

Figure 5.9: MCC results for each algorithm compared between data set C2 and C3.

5.4.1 Decision tree

The decision tree method implemented in this study performed worse than all other algorithms, both machine learning and statistical based. Decision tree is an example of a heuristic algorithm and will classify instances based on the feature that has the lowest Gini index value. This approach causes the results of individual trees to vary, as different features may produce the same "impurity" but the resulting segmentation point could classify samples differently. Unless explicitly programmed to make consistent data splits on the same features, the decision tree will produce variation in results.

The method is however shown to be useful for exploratory analysis of the features best suited to distinguishing between the two classes established in this study. For fibre rope condition monitoring of CBOS testing it highlights that the features derived from the SBZ and DBZ are more relevant than those from the SZ section. This is as expected, since the bending occurs in these zones leading to greater deformation and more variation in width, length and temperature to form data splits. The method should not be used as a stand-alone classification method but can be used as a technique for feature reduction before repeating the modelling process with other machine learning or statistical approaches.

5.4.2 Random forest

Random forest was the most effective method for data set C2 but performed worse than all other algorithms apart from decision tree in data set C3. Data set C3 had less data than data set C2, so therefore the decrease in the amount of data to split the records contributes to the detriment in performance. This is due to the model not being able to achieve the same model complexity at shallow tree depths with fewer samples. This

highlights the importance of having an extensive data set to make predictions when using random forest as indicated in data set C2.

The technique is robust due to the properties of the algorithm, with random sampling with replacement and the majority vote system of trees contributing to more stable predictions. It is also possible to achieve excellent predictions with shallow tree depths, which limits the need for excessive computer capacity. However, substantial and good quality data is required to give the good results achieved through random sampling and the majority vote system.

5.4.3 Support vector machine

The linear kernel was not as effective in data set C2, however was the best performing machine learning algorithm in data set C3. The linear kernel is the simplest implementation of SVM, which puts a straight hyperplane in the higher dimensional space to separate the samples into classes. In data set C2, there is lower temperature variation during the experiment compared to data set C3. Such features with measurements that change little contribute noise to the process of finding the optimal hyperplane. In data set C3, there were larger temperature variations due to greater rope tension, allowing a more optimal split to be found due to more distinctly scaled values.

SVM using both the radial basis function and sigmoid kernels performed to more or less the exact same levels in both data sets, indicating the hyperplane shapes imposed were more adaptable to the differences between data sets C2 and C3. While the linear kernel is limited in the separating hyperplane it can impose for class separation, the other kernels presented here can form a more complex hyperplane that can serve to separate the classes more effectively. Compared to decision tree and random forest, the SVM is a much more adaptable and consistent algorithm as reflected in the results presented.

5.4.4 Machine learning and statistical methods comparison

Both the machine learning and classical statistical approaches were shown to be valid methods for classifying the condition of fibre ropes during CBOS testing. The k-nearest neighbours algorithm was shown to perform just as well or slightly worse than the best performing machine learning algorithm when assessed using only metrics. However, Figure 5.5 demonstrates that there is a possibility that k-nearest neighbours produces a substantial amount of false alarms at earlier stages of testing. The false alarms for random forest occur closer to the transition point between classes and avoid very early stoppages.

Consequently, the results presented in this chapter show that there is merit in applying machine learning for fibre rope condition monitoring. In a machine learning application,

the models created can only perform if there is enough data available. In situations where data is limited a classical statistical approach can suffice, as shown by the robust performance of logistic regression and k-nearest neighbours across both data sets. Logistic regression was also shown to be less hampered by smaller data sets as reflected by the stronger performance in data set C3 than in data set C2. Some machine learning algorithms in this study, such as decision tree and random forest, performed worse in data set C3 than in data set C2 and failed to adapt to the smaller data set.

Chapter 6

Remaining useful life estimation using machine learning

This chapter is a summary of the work in paper E, and further details are found in the corresponding appendix. It outlines the application of ML algorithms to the CBOS data sets for remaining useful life (RUL) estimation of fibre ropes. This builds upon the work outlined in chapter 5, where the algorithms are now developed further to determine how much longer the ropes can be expected to last before failure. While classification is useful to detect patterns that may indicate impeding rope failure, it does not give a continuous variable to serve as indication of time to failure. From an industrial perspective, this would be a more attractive inclusion to a condition monitoring regime for fibre ropes.

The methods chosen for RUL prediction include: neural networks, random forest, and support vector machine. In common with the classification iteration of this analysis, all these methods are compared for effectiveness. Random forest and support vector machine were chosen as they had the most promising performance based on the classification results. Neural networks were introduced as another method to investigated based on application in other areas.

6.1 Applied methods

6.1.1 Target variable - RUL factor

A target variable is required for regression analysis in ML and will act as the value to be predicted based on training data used in the modelling process, unlike in Chapter 5, where only a class is detected. The target variable used in this study is referred to as the RUL factor (R_f), a fraction defined by equation 6.1.

$$Rf = \frac{CTF_t}{CTF_{test}} \tag{6.1}$$

where R_f denotes the RUL factor, CTF_t is the remaining number of cycles to failure at the time of measurement and CTF_{test} is the number of cycles at failure in each individual test where the measurements are made.

The value begins at 1, representing start of life, and ends at 0, representing end of life. Figure 6.1 shows an example of damage progression in a section from a rope (C2R5) at various R_f , with the stages highlighted by decreasing R_f from (a) through to (d). The images show that as R_f decreases the subsection becomes longer and there is more visible wear, as shown by ruptured strands and extruded loops. The prediction errors made by the various approaches will be based on comparison to the true, known R_f .

As the CBOS tests are performed at a constant tension, R_f is related to the accumulated damage d from Palmgren-Miner's rule as shown in equation 6.2.

$$R_f = 1 - d \tag{6.2}$$

As the CBOS tests progress there is accumulated damage in the form of ruptured stands and compromised sub-ropes. The rope is extended further as the true R_f values drop to lower values. Therefore, the reduction in rope residual strength and thereby the retirement criteria in the experiments can be related to the non-linear progression of the global elongation of the rope.

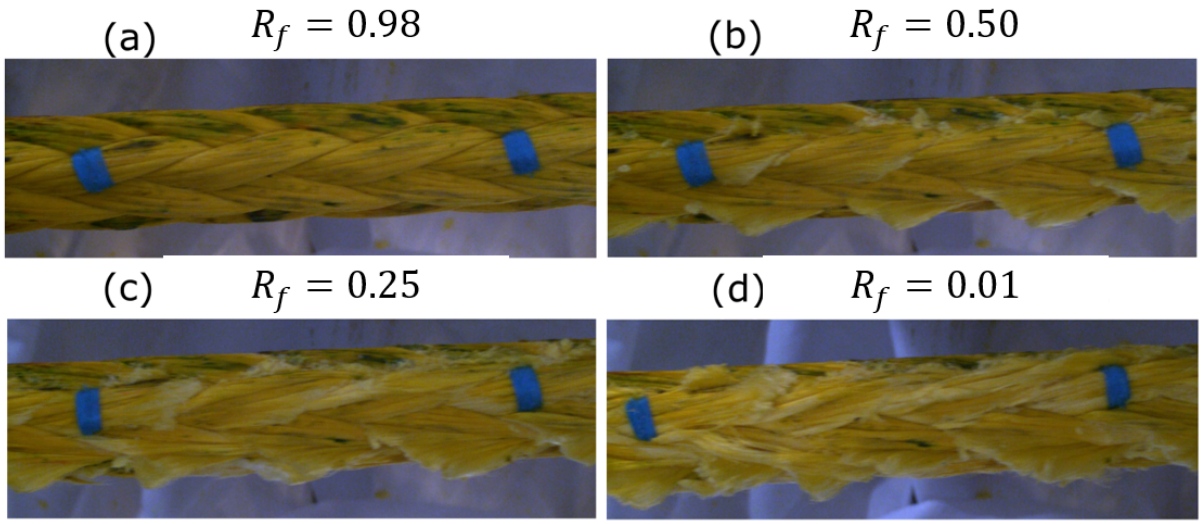

Figure 6.1: Example of degradation in rope C2R5.

6.1.2 Neural networks (NN)

The NN structures, designated as NN1 and NN2, used in this study are detailed in Tables 6.1 and 6.2. These are implemented using the Keras library [130] with a Tensorflow backend [131]. These two architectures are chosen as they are simple to implement for the initial application of machine learning to RUL estimation for fibre ropes. Also one architecture has an additional layer to gauge the influence of using several dense and dropout layers on R_f results.

Dropout layers are used as a regularisation technique, which randomly prevent 20 % of the neuron outputs from proceeding through the network. The final output layer consists of one neuron coupled with a Sigmoid activation function which produces a value between 0 and 1 as a result. This is done to reflect the R_f in Section 6.1.1.

The Adam optimisation function was used for both NN1 and NN2 specified in Tables 6.1 and 6.2 to update the weight values associated with the input features. The inputs are fed forward and backpropagated through the networks for 50 epochs, with the model that produces the lower root mean square error (RMSE) on the test data being saved as the best model used for predictions. The simulations were initially conducted with more epochs, but there was no improvement on results, therefore 50 epochs were used to save on simulation time. Each configuration is simulated 20 times to account for randomness in the weights assigned in the neural network and give a more robust value for model output. The average prediction calculated from these instances is compared to ground truth R_f measured from the CBOS data and a confidence interval is calculated based on the 20 simulations.

Table 6.1: NN architecture 1 (NN1) used to predict R_f .

Layer	Type
1	Input layer, N_{feats} inputs
2	Dense layer, 100 neurons, activation function – 'ReLU'
3	Dropout layer – 20 %
4	Dense layer, 50 neurons, activation function – 'ReLU'
5	Dropout layer – 20 %
6	Output, Dense layer, 1 neuron, activation function – 'Sigmoid'

6.1.3 Support vector machine (SVM)

SVM was first used for classification [125] and was later adapted for regression problems [132]. To predict the R_f in this context, the latter approach is adopted which has also been applied in other studies related to RUL prediction [133]. As for classification, the

Table 6.2: NN architecture 2 (NN2) used to predict R_f .

Layer	Type
1	Input layer, N_{feats} inputs
2	Dense layer, 100 neurons, activation function – 'ReLU'
3	Dropout layer – 20 %
4	Dense layer, 100 neurons, activation function – 'ReLU'
5	Dropout layer – 20 %
6	Dense layer, 50 neurons, activation function – 'ReLU'
7	Dropout layer – 20 %
8	Output, Dense layer, 1 neuron, activation function – 'Sigmoid'

data is separated by a hyperplane in a higher vector space. In regression analysis, the continuous variable is predicted based on distance from this separation plane.

To compare to the performance of the NN, an SVM framework adapted for regression analysis from scikit-learn [120] is chosen. Linear and Gaussian kernels are used due to their simplicity to implement and their previous classification performance. The errors in the predicted R_f values are compared to other methods. The variation in performance between each prediction with SVM is considered negligible and is therefore performed only once.

6.1.4 Random Forest (RF)

RF is an example of an ensemble method which utilises a user-specified number of decision trees created by bootstrapping data from features and data available from a training pool [123, 134]. The models created will assign RUL values to the test samples in each individual tree and an average RUL value will be calculated.

The RF algorithm for regression analysis from scikit-learn [120] is used for R_f prediction. The configurations for RF implementation in each data set are specified in Table 6.3 for data sets C2 and C3. Different tree depths are chosen due to the difference in number of measurements available between the different data sets and to prevent overfitting. Different numbers of trees in the forest are used to assess their performance on convergence to the best performing R_f result. Little improvement was seen after 200 trees, therefore it was limited at this number to save on computation time. Each configuration is repeated 20 times to account for randomness in the split criteria used in each simulation. The differences between the data sets are highlighted in Table 5.2.

Table 6.3: Configurations used for RF to predict R_f for data sets C2 and C3.

Data set C2		Data set C3	
Tree depth	1-4	Tree depth	1-2
Number of trees	50, 100, 200	Number of trees	50, 100, 200

6.2 Flowchart of operations

Figure 6.2 details the flowchart of operations implemented in the ML process from beginning to final output and performance assessment. Specific details related to part (a) test methods and data acquisition were summarised in Chapter 4.

Part (b), the pre-processing techniques applied to the data for RUL estimation are shown in Section 6.2.1. Then in Sections 6.2.2 and 6.2.3 the parts (c) training and RUL estimation stages and (d) model assessment are detailed.

6.2.1 Data pre-processing

The features used for RUL estimation are shown in Table 5.1. The data sets from each type of rope are joined together, therefore the same amount of features are used in each rope type.

The data sets are separated into "geo" and "geo_therm" feature sets based on data type to assess the effect of adding thermal features to the ML model. The data set compositions are summarised in Table 5.2.

Raw measurements from the data acquisition phase are subject to pre-processing, where the data from various features is standardised. The data was scaled using the approach detailed in equation 6.3:

$$z_i = \frac{y_i - \bar{y}}{\sigma_y} \tag{6.3}$$

where z_i is the standardised value, y_i is the raw value, $\bar{y}$ is the average of all raw values for the rope sample feature and σ_y is the standard deviation of all readings for the rope sample feature. This is done for each rope in the data set to increase comparability between the different samples and is a standard pre-processing step to prepare data for ML application.

Similar to Section 5.2.2, the data sets are treated for outliers and missing data to ensure the maximum amount of possible data is available for model simulation.

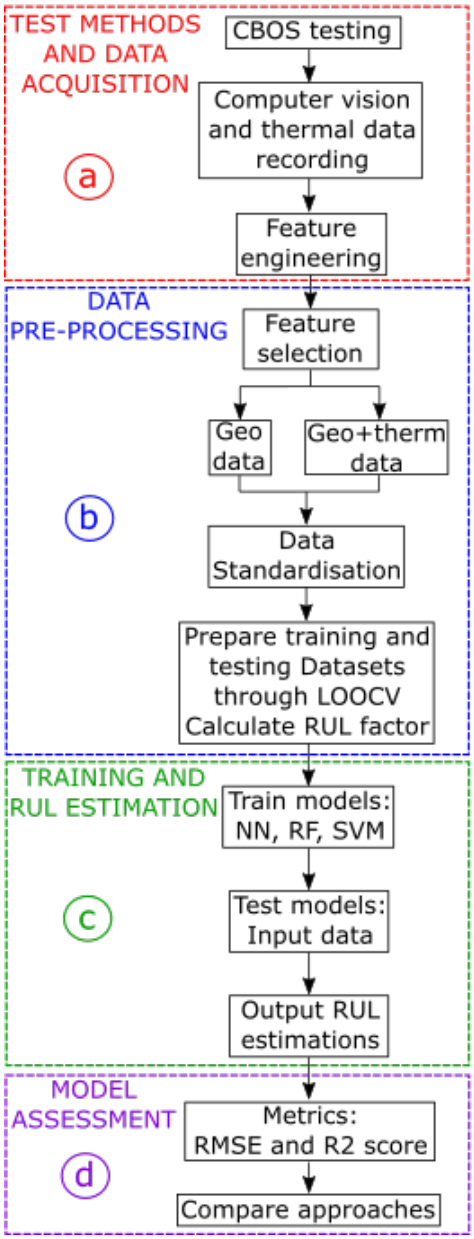

Figure 6.2: Flowchart of operations detailing steps implemented in (a) data acquisition, (b) data pre-processing, (c) training and estimating RUL and (d) model assessment.

6.2.2 Training and RUL estimation

The models are tested through LOOCV, where R_f predictions made on a single rope will be made using models trained with the remaining ropes in the data set. This process is done separately for both rope types in C2 and C3 and as a combined data set with both C2 and C3 together.

In addition to investigating the effect of only geometric and combined geometric and thermal measurements as outlined in Table 5.2, different combinations of features from the various bending zones detailed in Figure 3.6a are also tested. This includes: testing

using all zones; using only SBZ and DBZ measurements; and finally, using only DBZ measurements.

6.2.3 Model assessment

The metrics used for model assessment are root mean square error (RMSE) and R^2 score (R^2), as outlined in expressions 6.4 and 6.5:

$$\text{RMSE} = \sqrt{\frac{1}{N}\sum_{n=1}^{N}(y_i - \hat{y}_i)^2} \tag{6.4}$$

$$R^2 = 1 - \frac{SS_{res}}{SS_{tot}} \tag{6.5}$$

where N is the number of measurements made for each rope sample, y_i is the observed R_f at instance i, $\hat{y}_i$ is the predicted R_f at instance i, SS_{res} is the sum of squares of residuals and SS_{tot} is the total sum of squares.

RMSE in this context will give an insight into how concentrated the R_f predictions are around the R_f ground truth using each algorithm configuration outlined in Section 6.2.2. Additionally, the R^2 score gauges the correlation R_f predictions have with the ground truth R_f using the input variables outlined in Table 5.1.

Model performance is also assessed through the use of R_f graphs and residual analysis. The R_f graphs include the ground truth from the observed experimental measurements and tolerance bounds at $\pm 20\%$ based on this data. The average R_f prediction and a $\pm 95\%$ confidence interval of the repeated simulations of each distinct configuration are compared to the ground truth and tolerance bounds.

The residual values, e are calculated using equation 6.6:

$$e = y_i - \hat{y}_i \tag{6.6}$$

Additional analysis includes plotting residual values against the predicted R_f values, the actual R_f value against the predicted R_f value and finally a histogram analysis accounting for the numerical spread of the residual values. This provides further information about the model ability to predict R_f , potential model bias and where overestimation and underestimation in rope health occurs.

6.3 Results

6.3.1 Average RMSE

A quantitative assessment of R_f prediction is performed by calculating the average $RMSE$ and R^2 scores in each data set using different feature sets. Better performance is reflected by lower and higher values for $RMSE$ and R^2, respectively. The results for different feature combinations are compared for both C2 and C3 rope data sets separately, as well as for the combined data set.

The results for the average RMSE for data sets C2 and C3 are shown in Figures 6.3 and 6.4, respectively. The R^2 scores are shown in the original paper, in Figures E.5 and E.7.

Figure 6.3 gives an overview of each algorithm performance based on different feature sets and training model composition. All available features are used in A, the SBZ and DBZ features are used in B and only the DBZ features are used in C. Both configurations of RF performed best, followed by NN and finally SVM. Introducing thermal features generally either changes nothing or leads to detriment in performance when only C2 ropes are used as training data, which is particularly noticeable in both NN and SVM. When the combined C2 and C3 model is used there is slight improvement in performance when thermal features are introduced for NN when the SBZ+DBZ and DBZ feature sets are considered.

$RMSE$ values for data set C3 are shown in Figure 6.4. Both NN configurations performed best when only C3 data is considered. A noticeable difference in the C3 data from the C2 data is that for both NN and SVM, including the thermal data led to significantly better predictive performance as indicated by lower $RMSE$. Using the combined C2 and C3 data set also improved performance of NN with the exception of the NN2 configuration in the SBZ+DBZ feature set.

6.3.2 RUL graphs

A qualitative assessment of the algorithm performance during LOOCV is given through plotting the predicted R_f against number of cycles in each test. A general assessment of algorithm performance can be gained from the graphs, but they can also reveal at which times in the test both best and worst predictive performance occurs. It is noted that only data sets are combined and not the machine learning methods.

The results of cross validation predictions made only using the single and combined data sets is also considered. Selected RUL prediction results from both C2 and C3 data sets are shown in Figures 6.5 and 6.6. Additional graphs of RF and SVM implementation

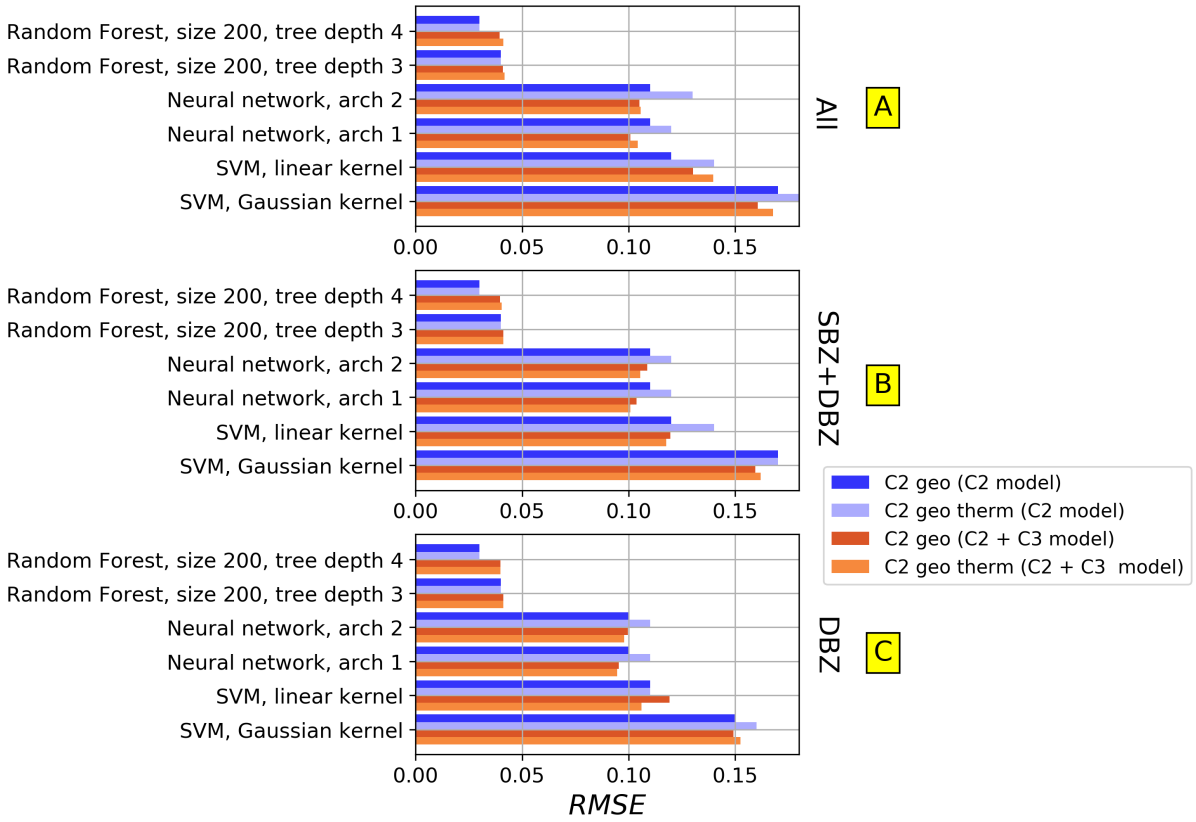

Figure 6.3: Average RMSE values per algorithm for C2 ropes.

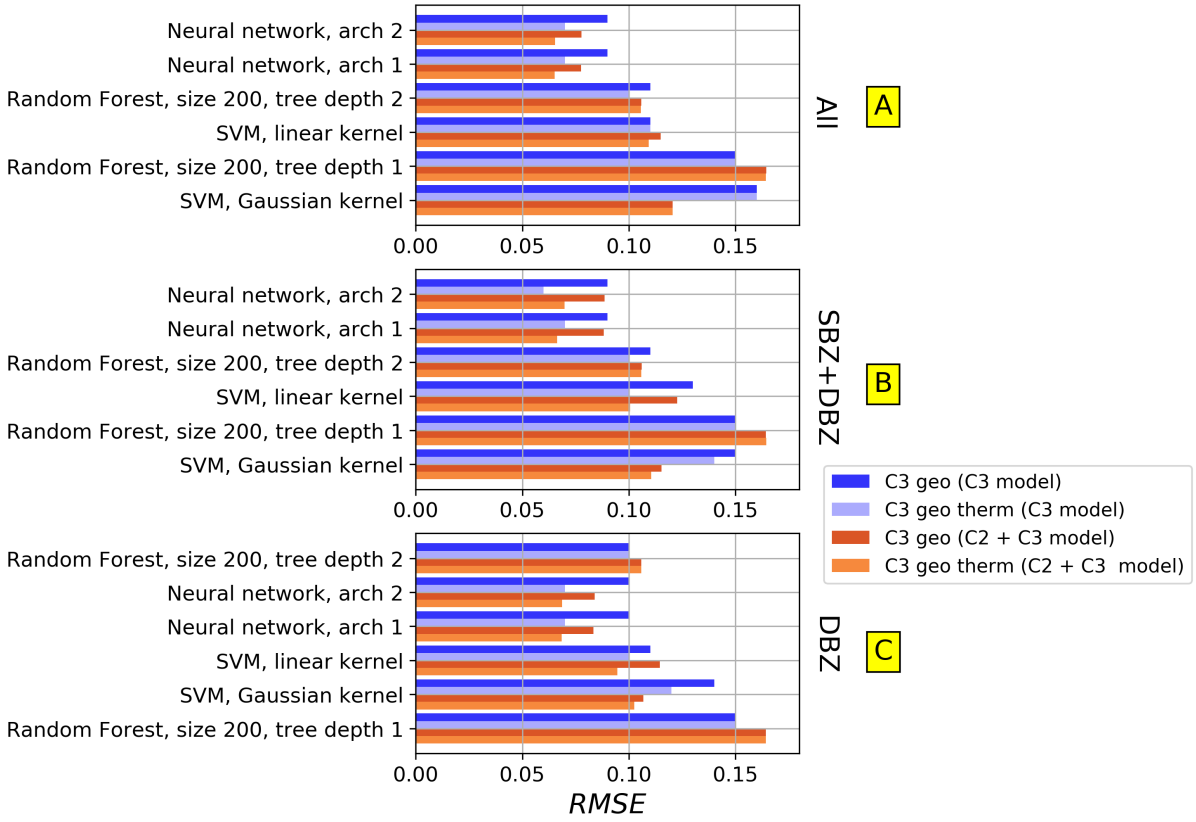

Figure 6.4: Average RMSE values per algorithm for C3 ropes.

are shown in Figures E.9 and E.11.

Figure 6.5 considers the predictions by NN2 on rope C3R2 when both geometric and thermal features from the DBZ are considered. The confidence interval in the prediction is significantly improved when building the model from the combined C2 and C3 data sets and almost totally confined to the tolerance bounds. This is seen at the majority of test times with the exception of between 0 to 4,000 test cycles.

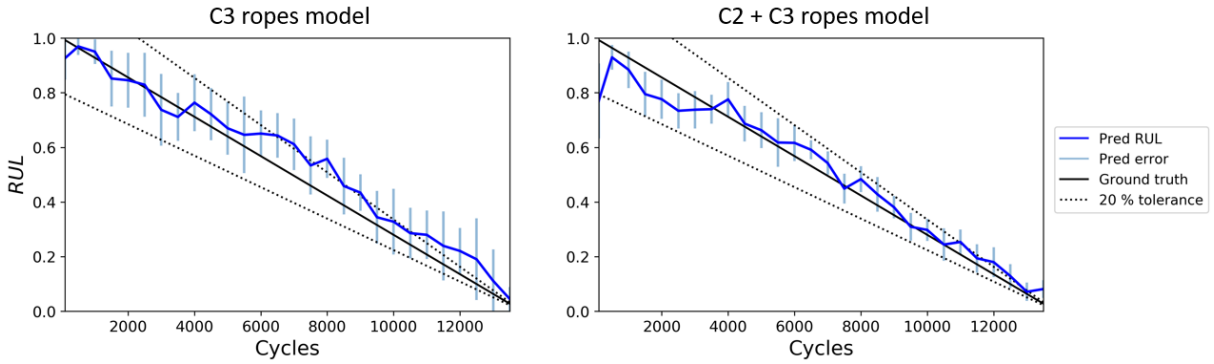

Figure 6.5: R_f prediction using NN2 for rope C3R2, using geometric and thermal features from DBZ.

Figure 6.6 shows the results of R_f prediction using NN2 for geometric features from all bending zones for rope C2R4. It is noted that there was a tear in the rope splice at the driving sheave, instead of the test sheave. This explains why R_f is larger than 0 at the end of the test. By using the combined C2 and C3 data set, the predictions in the first half of the test are shown to be closer to the ground truth, as well as showing a reduction in the "peak" seen in the middle of the C2 ropes model.

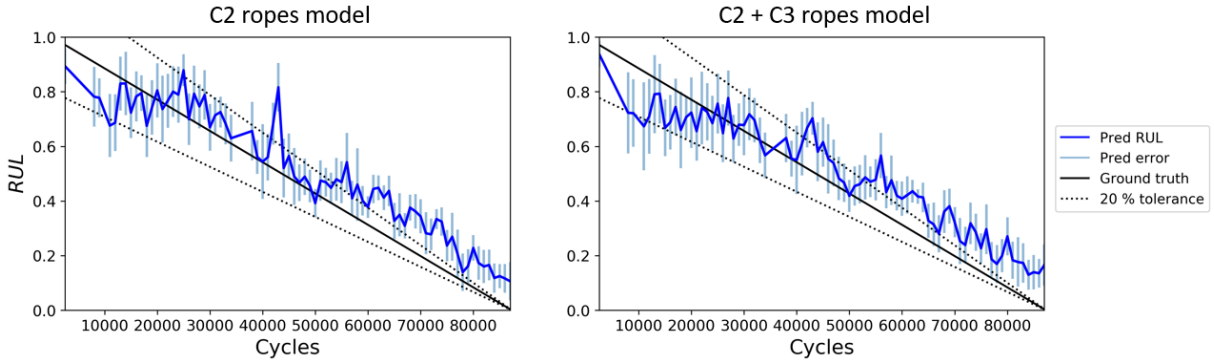

Figure 6.6: R_f prediction using NN2 for rope C2R4, using geometric features from all bend zones.

6.3.3 Residual analysis

A residual analysis is performed to further investigate R_f predictions and to compare the differences in results depending on algorithm, features and training data used.

Figure 6.7 shows the residual analysis comparison of using RF with tree depth 4 and NN2 predictions for rope C2R2 using only geometric features from all bend zones. In this specific case, both models were trained using only the C2 rope data.

The RF model produces low residual values indicating closer agreement with the ground truth, while NN2 prediction are shown to both overestimate and underestimate as indicated by the spread of residual values.

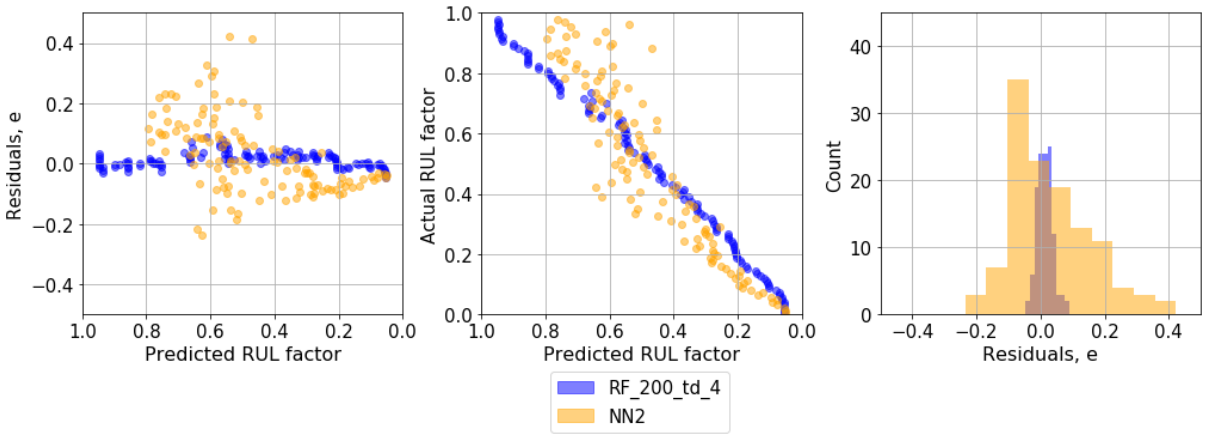

Figure 6.7: Residual analysis and comparison for rope C2R2 predictions made by NN2 and RF, with 200 trees and depth 4 with all features. Both models are trained using only C2 data.

Figure 6.8 provides analysis of improvements made by combining the C2 and C3 rope data sets in model training. This is presented for rope C2R1 with NN2 using combined geometric and thermal data from all bend zones.

An improvement with the combined training set is observed, with magnitude of the outermost outliers being reduced. Rope C2R1 completed the least amount of cycles at failure when compared to the other ropes in the C2 data set and showed poor prediction results in models trained on the C2 data set only.

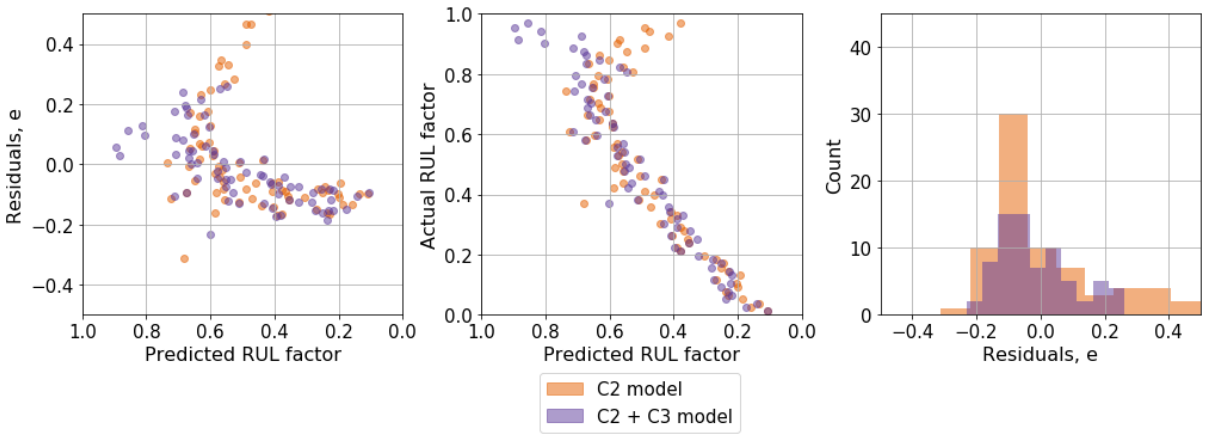

Figure 6.8: Residual analysis and comparison for C2R1 predictions with geo + therm features from all zones by NN2, using models trained with C2 data set and combined C2 + C3 data set.

6.4 Discussion

Model performance varied depending on the algorithm and the data set used. A major difference shown was that RF performs better than NN for campaign C2 but NN performs better than RF in campaign C3. Differences in performance can be explained by the training data used, the size of the data set, and algorithm mechanisms. This will be be discussed in the subsequent subsections.

6.4.1 Recorded data and availability

Two of the ropes in campaign C2, ropes C2R1 and C2R4, broke where the rope splice was bent over the driving sheave. This led to earlier failure than for the other ropes of the campaign, and to failure which was not located where the cameras were, at the test sheave. Still, the failure mechanism was very similar to what caused failure in the other ropes tested in this study. RF frequently identified the global elongation as the most important split variable. In line with this overall sameness of failure mechanism of all ropes tested, this variable showed a similar development for all ropes, including ropes C2R1 and C2R4.

It was chosen to include the ropes in the analysis, a choice that has two positive effects. Excluding them would have lead to even less data for training the machine learning algorithm, and as discussed earlier, CBOS test data are time consuming and expensive to obtain. Secondly, in real life, ropes will not always break where expected. Including ropes C2R1 and C2R4 in the data set makes the models able to handle some such cases, where the deviation from the expectation is not too large.

The model stability is addressed through the 95 % confidence interval for the pre-

dictions. It was found that combining campaigns C2 and C3 in all cases resulted in a narrower confidence interval than from each of the campaigns alone. For unstable models, adding new samples is expected to change the model qualitatively, resulting in wider confidence intervals. Conversely, the present study's narrowing of the confidence intervals indicates a stable model.

6.4.2 Random forest

RF is formed of several individual decision trees, where data is separated based on feature values that give the purest split. The global elongation shows a steady increase during testing, and it will therefore create one of the best splits in the decision trees of the RF. However, this feature will not be available to all trees in the forest, due to feature bagging. Still, the averaging over 200 trees will ensure its contribution to the overall forests. This is shown in the residual analysis performed in Figure E.12, where RF has outperformed NN2. RF was also shown to have a steady balance between slight overestimation and underestimation of predicted R_f compared to the true value.

It is also noted that increasing the tree depth will also lead to a more complex model capable of more accurate predications. In general, increased tree depth increases random forest accuracy, while improvements by increasing forest size tend to plateau. In campaign C3, each rope had fewer records than in C2. Therefore, to avoid overfitting the result was using shallower trees for this campaign, giving less accurate RF results. Since the data is split by random feature sampling in each tree, there would be slightly more variation in the quality of fits due to data splits made on less suitable features. This leads to less accurate R_f as indicated by the higher RMSE and lower R^2 values.

6.4.3 Neural networks

NN algorithms performed better in C3 than C2. All input variables are considered when using NN and a feature that varies very little during CBOS testing only contributes noise to a model and impacts performance negatively. NN struggles to predict RUL in the earlier CBOS test stages in particular for some ropes in the data set. Initially, the various widths, lengths and temperatures monitored will not change until later in the test and therefore NN struggles to predict the distinct R_f values at this testing stage.

Another example is comparing the use of geometric and the combined geometric and thermal feature sets for C2, where thermal features lead to a higher $RMSE$. At the lower test tensions the temperatures do not vary significantly throughout the CBOS tests, but reach a steady temperature until failure, thus contributing noise to a model formulation.

However, the temperatures recorded in C3 are noticeably higher and have more vari-

ation between the SBZ and DBZ in line with the decreasing R_f , therefore improving the model. C3 having more variation in measurements leads to NN finding a better model than developed for C2. Both NN configurations show slight overestimation in the latter stages of the CBOS tests but not to the same extent as SVM.

Generally, it is noted that despite inconsistent numbers of test cycles in campaign C2, it is still possible to achieve acceptable results within the range of ± 20 % of the RUL ground truth.

6.4.4 Support vector machine

SVM performed poorly compared to the other algorithms applied in the RUL prediction study. If the hyperplane fit to the data is poor and non-representative, it will in turn have a detrimental impact on R_f prediction using the algorithm.

As with NN, the presence of noise via lack of variation in certain features will negatively influence this fit. This is particularly prevalent in C2, while it is noticed that SVM performed slightly better in C3 due to the greater variation in values measured. It is shown that the fit created by the linear kernel suits this rope test data set better than the Gaussian kernel. The SVM is also shown to overestimate rope health towards the later stages of the CBOS tests, giving an unrealistic estimation of RUL which would be dangerous in operation.

Improvements to RUL predictions using SVM could be achieved by hyperparameter optimisation for both linear and Gaussian kernels. Finally, other kernel types could also be considered, to further experiment with hyperplane fits to the data set.

6.4.5 Feature selection

Creating models from feature sets consisting of the different bending zones features also influences algorithm performance. During CBOS testing, the SBZ and DBZ are subject to all the bending, whereas there is none present in the SZ. Therefore, in line with what was previously stated about NN, measurements from the SZ essentially contribute noise in the modelling process. As only the features that give the best splits in the data are considered from the random subsets in RF, the likelihood that features from SZ will be consistently picked as splitting criteria in individual trees is extremely low, hence minimal effect on both $RMSE$ and R^2 values.

However, as expected limiting the features used to only those from the DBZ is shown to improve algorithm performance for both NN and SVM. There was very little difference between the results from models that used all features and the combination of SBZ and DBZ features but the most accurate results for SVM were achieved by reducing to only

training with DBZ features. More frequent repeated bending will cause more accumulated damage and variation in these features will relate better to the associated RUL value.

The residual analysis performed in Figure E.13 also shows the advantage of combining both geometric and thermal features as training data. The higher temperatures in campaign C3 contribute features with greater variation and therefore improve the prediction capabilities of the NN2 model used in this example.

6.4.6 Combining data sets

Combining the two data sets for predictions based on cross validation had either a positive or a negative impact depending on the algorithm considered. The main benefactors of this approach were the NN configurations, as shown by improved results in average $RMSE$ and R^2 for both the C2 and C3 ropes. Introducing thermal features for C2 rope predictions led to decreased performance when only considering the C2 data set, but improved for the cases where SBZ+DBZ and DBZ features are used with models trained using the C2 and C3 ropes. This can be attributed to the different thermal behaviour in each data set, with the thermal information from the C3 ropes contributing to better predictions. From a C3 ropes prediction perspective, combining the C2 and C3 data sets creates a larger training data set and improves estimations from both NN and SVM. This suggests that simply increasing the amount of training data with slightly different feature behaviours will benefit model fitting in these cases. The observations support the finding from this study that unique rope types subject to different relative test tensions can be combined to produce more accurate results.

The residual analysis performed in Figure 6.8 also shows the advantage of combining the separate test campaigns. In campaign C2, the thermal data varied very little due to the lower test tension applied contributed noise to the modelling process. The introduction of campaign C3, improved the models due to both the presence of similar global elongation trends and thermal features with more varied temperatures.

6.5 Recommended approach for RUL estimation

The algorithms in this study are capable of predicting R_f for ropes using features derived from an experimental set-up that uses computer vision and thermal monitoring.

For data set C2, RF showed the most promise as a RUL prediction method, while NN was the best performing algorithm in data set C3. The benefit of combining data from different types of ropes for training data for RUL prediction is also demonstrated for NN and SVM. RF has been shown to be the most effective in this study, particularly

in cases where larger amounts of data are available, allowing a suitably complex model to be developed based on features selected by the algorithm.

NN is also shown to be useful, but slightly less effective compared to RF. If large amounts of data are not available, then NN application with more focus on including only relevant features is a useful fall-back solution.

Chapter 7

Discussion

This chapter provides discussion of the methods and analyses outlined in Chapters 3-6. It will also examine the validity of the aforementioned approaches and their potential future adaptation for field application.

7.1 Experimental methods and instrumentation

This section addresses the testing methods and instrumentation applied during the experiments performed as part of this research. The effect of these methods and instrumentation choices with respect to individual CI behaviour and machine learning approaches are discussed in later sections in this chapter.

The testing methods presented encompass both tension-tension and CBOS methods. They represent a progression in the thesis that allowed suitable CM methods to be developed and have the closest similarity to offshore loads in a laboratory setting. The first tests using the tension-tension methods allowed the first iterations of the length and width monitoring algorithms to be implemented. It used a relatively simple set-up and was much less time consuming compared to the CBOS testing phase. It also provided an opportunity to gain familiarity with rope handling generally and techniques to be used later in the project such as splicing and instrumentation set-up. Additionally, it highlighted some signs of rope damage to monitor, such as ruptured strands which influences width measurements and could be potentially related to rope lifetime. This affirmed that a computer vision set-up was a valid condition monitoring method to track changes in the rope as the tests progressed.

While the tension-tension testing phase gave useful contributions initially, it highlighted some limitations in both testing and instrumentation that needed to be addressed moving forward to the CBOS case. The tests themselves were limited in the types of damage being monitored as it provided no bending deformation of the rope. Rope used

for offshore lifting will experience tension from payloads, however it will experience twisting and bending that are heavily influenced by sea states and payload mass. The ropes in this testing phase were simply elongated until failure at slightly different tensions and therefore lacked the load variation that would be seen offshore. Overall, it highlighted that more robust instrumentation, algorithms, and rope marking schemes were required if certain sections of the rope were to be monitored accurately throughout testing.

These findings were then taken forward through installing several machine vision cameras that could monitor the rope from different perspectives instead of a simple webcam. It was also shown that an adequate lighting system around the rope at the CBOS machine had to be designed to aid measurements. Also, the morphological operations in the algorithms were reviewed and edited to ensure that the boundaries of the rope were properly captured to allow optimum length and width monitoring.

The CBOS tests were conducted in three different campaigns that made use of different types of HMPE rope to verify that the length, width and eventually, thermal monitoring was applicable. The first campaign revealed the need for monitoring different bending zones more closely, rather than placing the detectable markers in general areas. This applied in particular to the SBZ and DBZ, where greater deformation occurred. The length algorithms also highlighted the need for monitoring at a local level due the presence of both elongation and compression between the markers applied to the rope, indicating there was gliding of strands in both directions. The widths also indicated that clearly visible damage such as extruded loops and ruptured strands could be tracked and that the "increased" widths were in fact the presence of these damage mechanisms.

However, it was shown that using just one image from a recorded video was not sufficient to accurately calculate the lengths and widths as the tests progressed. Therefore the widths and lengths algorithms were revised so that it would produce a median, maximum, minimum and standard deviation based on ten images or the maximum available after eliminating outliers through measuring the median absolute deviation. Additionally, given the temperature limitations of HMPE, it was decided that thermal monitoring would be incorporated into the following campaigns to assess the temperature behaviour during CBOS motion and potentially gain further insight into rope condition.

The second and third campaigns incorporated thermal monitoring at the sheave. The different bending zones were clearly distinguishable by the produced temperature patterns from the FLIR software, and measurements including average, maximum, minimum and standard deviation (representing variation within the field of view) could be easily extracted and aligned with the length and width data in similar locations along the rope length. However, the splicing method used ultimately resulted in some discrepancies between the number of cycles performed, due to the splice running over the driving sheave

of the CBOS machine. This resulted in greater care being taken to measure this length before the third testing campaign. Additionally, since the third campaign was conducted at a higher test tension resulting in earlier ruptures, it was decided there would be more frequent recording to compensate for the drop in data when only recording every 1000 cycles.

Similar to the tension-tension campaign, there were also limiting factors with the CBOS testing method. While the method did introduce bending motion, it is still a test to failure at a stationary amplitude of motion. The offshore cases will have alternating stresses as a result of both varying payloads and sea state. Additionally, the CBOS machine testing takes place at room temperature indoors which will not accurately simulate environmental factors influenced by operation location. Slight differences in marker placement and their degradation also will slightly influence the measurements taken for local length.

7.2 Condition indicators

7.2.1 Local length

The results presented in the project indicated that there was a clear need to monitor length at a local scale, as the change in length across the whole length of the rope was little in comparison to local occurrences. This was particularly evident in the measurements taken from the SBZ and DBZ in the rope samples, where the deformation caused by bending lead to relative distortion by gliding of strands. The trends displayed for local length measurement showed that the computer vision methods were effective at tracking these changes. It also provided further insight into the non-uniform deformation of the rope at a local scale. There were examples of "reciprocal" changes, where a sub-section was shown to increase in length, while its neighbouring sub-section was shown to decrease. With the aid of this monitoring method, it was possible to establish that both extruded loops and ruptured strands were contributing to the structural rearrangement of the rope and taking part in these measured length changes.

However, there were limitations to the local length monitoring method implemented in this project. While a robust marking system was developed to distinguish the different bending zones, it is noted that there is a slight discrepancy in the placement of the tracked sections between each rope sample. The markers are placed in the "general vicinity" of the bending zones and therefore there would be slight differences in measurements as they are not the exact same points on the rope. The markers were also shown to degrade as the experiments progressed. This made them both harder to detect by computer vision

and influencing the measurements taken, hence the need for interpolation to account for missing data. Additionally, the measurements are derived from statistical parameters collected from ten images. In some occurrences where ten images were not available this would lead to some slight increase in the uncertainty in the measurements.

7.2.2 Global length

The global length measurement was shown to give insight into the condition of the ropes during the CBOS tests. While an increase in global length was to be expected due to the extension of the hydraulic cylinder throughout the test, the monitoring method revealed this was not a linear increase. It was revealed that the rope increased in length in a similar fashion to a creep curve with three distinctive zones. The initial bedding in of the rope of was observed, followed by slower steady increase, and then an accelerated increase in length towards failure. While the overall global length measurements are not as significant as the local length measurements throughout testing, a rapid change indicates that failure is likely to occur. The global length also greatly contributed to improving machine learning predictions as discussed in Section 7.3.2.

The global length measurement has limitations in the context of CBOS testing. The CBOS machine tests until failure with the extension of the cylinder, whereas in actual operation the rope will not be in constant use. As a result, hysteresis of rope global length will occur through a rearrangement of strands and sub-ropes when the rope is not in use. Further investigation of this effect would provide knowledge of the permanent elongation of the rope which could be changed with the effects seen at a local scale.

7.2.3 Width

The width monitoring method was effective at measuring the cross section of the rope from different perspectives. This was particularly adept at detecting damage such as extruded loops and ruptured strands in the form of increased width measurements evident in the SBZ and DBZ. Similar to the length measurements, this highlighted the need for monitoring at a local scale. The rope shape changes as the test progresses and depending on the perspective used, it is possible to observe the flattening of the rope surface against the sheave, as well as the previously mentioned visible damage. The statistical measurements also provided further insight, as the greater difference between the maximum and minimum values observed in a subsection can highlight where damage is particularly prominent in the rope.

The width monitoring method was shown to have some limitations. The expected thinning of the rope during testing was not detect due to the visible damage accumulated.

Therefore, the reading calculated did not reflect the true shape of the rope. This led to the ineffectiveness of the attempted roundness measurements. The rope was also shown to twist slightly during testing, which would have had an influence on the measurements taken. Additionally, the lighting conditions and rope colour were also shown to change as the test progressed. This affected the ability of the algorithm to find the boundary of the rope that is used to calculate width. Manual adjustments had to be continually made when post-processing data to get an accurate reading, which was also shown too time consuming in its current iteration and has potential to be automated.

7.2.4 Temperature

Thermal monitoring was introduced due to concerns over thermal degradation in HMPE. The methods applied showed that each distinct bending zone had its own temperature signature during CBOS motion. The SBZ and DBZ temperatures were shown to increase and reach a steady-state value as the tests progressed. However, the average temperature measurement was shown to decrease slightly towards the end of the tests. This decrease in temperature is a result of the average value being calculated from both a warmer compressed core and the noticeably cooler damage areas such as the extruded loops and ruptures. This was also reflected by the higher standard deviation values and the increased range between the maximum and minimum temperature values measured in the area of interest. This indicates that thermal monitoring is also a useful way to detect damage along with the local length and width measurements. Additionally, thermal monitoring revealed that there was a noticeable change in structure of the rope due to the repeated bending and temperature increase. This stiffer structure takes more effort to bend and had higher thermal conductivity compared to unused rope. The method also demonstrated that there were higher temperatures in test campaign three compared to test campaign two, due to the higher applied test tension at a comparatively lower safety factor. This indicated that this change would have to be monitored in conjunction with changing loads over time when implemented into a rope condition monitoring system.

The thermal monitoring method in a laboratory setting is shown to have some limitations. The test was conducted at room temperature, with no further cooling effects or abrasive particles introduced to the rope. Therefore, the measurements taken are for a specific set of circumstances, rather than the field application, which will be influenced by outside temperatures and the presence of potentially abrasive particles. Additionally, the method is limited to only the surface of the rope and the values inside the rope are not represented. It has been clearly demonstrated that there is structural rearrangement and gliding of strands with the CBOS motion, which would contribute to increased temperatures. The temperature here would also have to be monitored to ensure that maximum

working temperatures are never exceeded.

7.3 Machine learning

Machine learning was chosen as the approach in this thesis as it has seen success in condition monitoring of other types of engineering components. The experiments make use data recorded from several different physical parameters, which is ideal for machine learning application. Therefore a machine learning approach on a physics-based model was shown to be promising approach. The same data can be used in conjunction with classical statistical methods and therefore machine learning has potential to be used as an alternative method.

7.3.1 Condition classification

The initial application of machine learning in the project was a condition classification framework. The condition indicators outlined in previous sections were adapted into features that were used to form the models that made the classifications. The samples were divided into two separate classes that were represented as healthy (HE) and close to rupture (CTR) based on the global elongation. This was shown to be a reasonable assumption to make, as the CTR-labelled samples coincided with a period of accelerated global elongation before eventual failure. Decision trees, random forest and SVMs were chosen as the approaches to perform the condition classifications. These methods were chosen based on their previous application to other condition classification problems on other engineering components. Based on the analysis performed, the decision tree was shown to be the worst performing out of all the methods, due to the model lacking the complexity required for the data used. The random forest is an extension of this method that makes use of several trees to make a decision on classification was shown to be more robust and accurate. Additionally, the SVM was shown to be adaptable to the problem, with a changeable kernel that can give a different fit to the data.

However, there was shown to be some limits to the condition classification methods applied in this research. The method only classifies between two general conditions, that are heavily reliant on the changes in global length as the CBOS tests progress. This is advantageous when predicting the condition of the a rope that is due to fail in a CBOS test but it could prove difficult to monitor in an applied industrial setting. Additionally, the models are also limited by the amount of data available from the instrumentation installed. As previously stated, CBOS tests are expensive and time consuming, so therefore the data pool is limited to five and four ropes in campaigns two and three, respectively. Another

alternative would be to increase the sampling rate of the instrumentation used to have more data from the ropes tested, allowing more data samples to be used in model training.

7.3.2 RUL prediction

The experience from forming the condition classification problem was carried forward to the development of the RUL prediction framework. Neural networks were also implemented in addition to random forest and SVM, while the decision tree algorithm was left out. Several different approaches to training the models were also introduced to the RUL prediction. This included combining both types of ropes tested into the same training model despite differences in test tensions, to increase the overall data pool. Additionally, limiting the number of features used for training to create more relevant data with more variation was also attempted. Both random forest and neural networks were shown to be very effective at RUL prediction in the rope data sets. Combining the data from campaigns C2 and C3 also contributed to improved performance for the neural networks. This was apparent for campaign C2, where the increased variation in the thermal data recorded from C3 allowed for more accurate prediction of the continuous variable introduced to represent RUL. This was also the case with campaign C3, which benefited from in the significantly increased amount of data included from campaign C2.

The RUL prediction implementation indicated a significant improvement and fine tuning of methods from the condition classification phase of the project, but there were some limitations to the methods applied in RUL prediction. Despite the combination of data sets for RUL prediction, the training models are still limited. The improvement shown indicates that further testing should be performed to increase the data pool and potentially achieve further improvements on accuracy. Methods such as neural networks can also have further tuning to improve upon the accuracy of predictions. Only two relatively simple networks were considered in this study but other architectures could also be implemented that could potentially improve upon the results implemented. In addition, random forest also relies heavily on the global length measurement for its good performance, which could be potentially difficult to measure in a rope several kilometres long. In this instance more focus should be put on using features with greater variation as seen in the SBZ and DBZ in the CBOS tests.

7.4 Validity

The data recording methods are subject to variation and therefore their validity has to be verified. This is paramount as the data recorded is then used for condition classification and RUL prediction using machine learning. This is relevant for the machine vision

cameras and thermal cameras. The machine vision cameras are subject to a calibration process before every test. This is performed using a chessboard pattern target with several images taken from different angles. As a result of this, the distortion in the image can be quantified. The relative distortion in the pixel values were shown to have a negligible effect on measurements. Furthermore, the thermal camera was calibrated for the emissivity of the rope before the tests started, using thermocouples. In addition, black-body calibrations were performed before each campaign. During the recordings, automatic calibrations were also perfomred by the IR camera.

The estimated variation in the measurements taken by the machine vision and thermal cameras were based on the values taken from the straight zone (SZ), where there was no bending throughout testing. It was shown that based on calculating the width of the 95 % confidence interval as a percentage of the average readings during the experiment for the local length, width and temperature values, it is possible to give an indication of noise in the measurements.

For the local length and width measurements, this was shown to be around 0.3 % and 2 % respectively, indicating that the values recorded without bending of the rope were very close to their average values. This is similarly calculated for the temperature measurements, where there is shown to be an approximate variation of under 10 %. The FLIR camera guide indicates that there is accuracy of $\pm$ 2 °C, therefore the variation seen in the CBOS experiments coincides with this value, showing confidence in measurements taken.

Table 7.1 shows the 95 % confidence interval half-width in percent of the confidence interval centre average value for the straight zone (SZ) compared to the double-bed zone (DBZ) for length, width, and temperature 3 in test campaign 2. It is seen that the double-bend zone variations are much larger than the noise estimated from the straight zone. Consequently, the variations observed in the double-bend zone can be interpreted as real variations, and not as noise.

Table 7.1: 95 % confidence interval half-width in % of confidence interval centre value for all ropes in Campaign 2

	Length	Width	Temperature
SZ	0.34	1.22	9.08
DBZ	0.96	5.37	14.20

The machine learning models were assessed through several different performance measures as explained in previous sections. This was performed for both the classification and RUL prediction algorithms, where the general accuracy and bias of the algorithms was

given. This allowed the best performing algorithms to be properly selected against others. Additionally, a 95 % confidence interval was included for the RUL prediction which allows the reliability of the machine learning algorithms to be seen. This was also used to demonstrate the improvements in algorithm performance when joining the campaign 2 and 3 test data together.

7.5 Adaptation to field application

The initial stage of adaptation to the field application would be the development of the condition monitoring system outlined in the CBOS experiments to an offshore crane. This presents several challenges for sensors and measurements due to the conditions in the offshore environment.

The monitoring set up can potentially be placed next to one of the main sheaves on the crane, allowing the computer vision and thermal monitoring set up to observe the rope during use. These sensors could be incorporated into an enclosure which surrounds the rope. This enclosed structure would allow light conditions to be controlled more easily, as well as protecting sensors from the spray and damage from the surrounding marine environment. Furthermore, this sensor package would also have to satisfy the various considerations and industry standards such as ATEX and IP ratings to be safely incorporated into an operational environment. To maintain reliability of the system, consideration should also be given to continuous calibration and redundancy in case of sensor failure.

The issue of measuring the global elongation of the entire rope could prove difficult to implement. Fibre ropes used in offshore cranes can be up to several kilometres long and would require an extensive marking system to distinguish the different rope sections. In real practice, it will be different sections of the rope that will be subject to bending depending on deployment depth and sea state during operations. Therefore the position and coinciding measurements will have to be properly tracked throughout use. Careful and thorough data acquisition will ensure smooth adaptation of machine learning to the condition monitoring process.

However, there is further work required to fully adapt a machine learning approach usage in offshore construction cranes. Firstly, CBOS testing is an example of a run-to-failure test where a constant tension is applied at the same rope sections. Other factors such as payload size, the temperature at the lift location and the operation time will also influence rope longevity. Data from potential lifting campaigns would have to be recorded as part of a wider rope condition monitoring system, where data is continually added to form a model with historical data. This would create a model that specifically pertains to

fibre rope use for offshore lifting, rather than relying on more commonly used S–N curves for these specific types of ropes. The findings from this study of different ropes at different relative test tensions show there is potential in using data from a fleet of fibre rope cranes performing different lifting operations to validate the condition of an individual fibre rope crane.

Chapter 8

Concluding remarks

8.1 Conclusions

The project focuses on developing condition monitoring methods for fibre rope applied in cranes for deep sea lifting operations. The research is motivated by the potential use of fibre ropes instead of steel wire in cranes that could allow lifting operations at depths exceeding 3000 m with smaller vessels. Within the project framework, three research problems were identified related to:

1. What condition indicators are best served to indicate the condition of rope during CBOS testing?

2. What combination of sensors will best monitor the condition of fibre ropes used for offshore lifting operations?

3. What is the best approach to predict RUL of a fibre rope based on CBOS experimental data?

The first research problem was explored through both tension-tension testing and cyclic-bend-over-sheave testing, as described in Papers A and B. This showed the length and width measurements were suitable condition indicators for fibre rope condition monitoring. The first iterations of developing algorithms that measure local deformation are explored in Paper A, where the length and width changes were monitored through image processing techniques during tension-tension testing. It was concluded they showed promising direction to continue with in the project. The distinct changes in both length and width could be effectively tracked until the rope samples ruptured. Furthermore in Paper B, the length and width measurement algorithms were adapted for cyclic-bend-over-sheave testing experiments. Changes at a local scale, especially length, were shown

to give insight into rope condition. However, the width measurements gave mixed results, but had sufficient potential to be effectively used as a condition indicator fibre rope condition monitoring.

The second research problem focussed on the combination of sensors to be used to effectively monitor the ropes during cyclic-bend-over-sheave testing. It was shown that by combining the length and width condition indicators from computer vision with thermal measurements from a thermal camera, it was possible to gain informed insight into fibre rope condition. The work in Paper C built upon the methods outlined in Paper B, with slight adaptations made to the length and width algorithms that made them more effective at monitoring condition indicators. This cyclic-bend-over-sheave testing campaign also included the introduction of thermal monitoring, due to the limited temperature working range of high modulus polyethylene fibre ropes. The combination of both the computer vision and thermal cameras gave multiple insights into rope condition and both were shown to produce useful condition indicators. It also highlighted the need for monitoring at a local scale as opposed to a global scale, due to different amounts of bending occurring in the distinct zones in contact with the sheave. It was shown that monitoring at local scale allowed detailed observation of local deformation such as the relative glide of strands, ruptures and extruded loops.

The third research question related to finding the best method for remaining useful life prediction of fibre ropes based on experimental data was performed in two stages. They both showed that machine learning can be applied successfully to both classify rope condition and estimate remaining useful life. The first stage of applying machine learning was for condition classification and was the subject of Paper D. The features were extracted from the condition indicators monitored in the previous stages of the project. It was shown that binary classification of the rope was possible with methods such as random forest, decision tree and support vector machine and that it was possible to outperform classical statistical approaches. In paper E, a framework for remaining useful life prediction using random forest, support vector machine and neural networks was developed. This allowed determination of a continuous variable that indicated the estimated rope lifetime left. Additionally, it was shown that different types of rope data could be combined to improve on predictions and algorithms performance. In particular, random forest was shown to perform best overall with neural networks being a useful back-up solution.

Overall, the project resulted in methods for feature extraction, condition classification and remaining useful life prediction for fibre ropes. The results of the research confirm that machine learning is an effective method to classify the condition and predict the remaining useful life of fibre ropes in cyclic-bend-over-sheave testing, where condition

indicators can be taken from sensors and instrumentation that are easily applicable in the field. The format proposed would provide a useful aid to both crane operators and inspectors in the field in determining when to retire a rope from use.

8.2 Further work

The experiments and machine learning methods applied in this research have potential for further work. To maximise the possibilities in a laboratory setting, there has to be expansion of the cyclic-bend-over-sheave testing set-up detailed previously, but with other parameters considered.

Firstly, elevated temperature testing conducted as the thermal limits of fibre rope are key to their use. Lifting operations in warmer climates such offshore Brazil, West Africa or Persian Gulf would place extra demands on the rope in use, therefore learning how temperature damage influences rope condition or remaining useful life is advantageous. Additionally, making use of larger diameter ropes during testing would more accurately reflect the real application of the rope for lifting operations. This can also be further expanded to testing at different safety factors to increase the overall data pool for future machine learning application. Finally, the cyclic-bend-over-sheave machine used for the experiments could also be upgraded with improvements that incorporate alternate stresses to better replicate heave compensation in real operation. Rather than testing straight to failure, it would give opportunities to assess accumulated damage under more severe offshore environments. Further tests can be performed with these conditions, which can be simply used to produce more data for machine learning application. There is also the option of testing at five- or three-sheave cyclic-bend-over-sheave machines, which will allow the rope to be assessed at different lifetime intervals in one test.

The data acquisition methods can also be further developed to improve the presented models. The current method does not account for the internal degradation for the rope, which would provide another perspective to assess damage in fibre rope. This could be done through embedded sensors that could account for changes in internal temperature or further exploration of localised strain. Additionally, as the structure of the rope fuses with the test progression, acoustic sensors could be placed on the sheave or internally to monitor changes in the micro-structure of the rope.

Machine learning applied to condition monitoring of fibre ropes also has further potential for expansion. From the perspective of condition classification, this can be further expanded to identify specific types of damage such as ruptured strands, compression damage or extruded loops, rather than a simple binary classification. This would require extensive manual labelling of each damage type and convolutional neural network archi-

tectures could be exploited to make these classifications direct from images, rather than physical measurements. If the progression in these damage mechanisms can be quantified, this then could be adapted for remaining useful life estimation.

References

[1] H A McKenna, J W S Hearle, and N O'Hear. Ropemaking materials. In H A McKenna, J W S Hearle, and N O'Hear, editors, Handbook of Fibre Rope Technology, Woodhead Publishing Series in Textiles, chapter 2, pages 35–74. Woodhead Publishing, 2004.

[2] G. P. Foster. Advantages of Fiber Rope Over Wire Rope. Journal of Industrial Textiles, 32(1):67–75, 2002.

[3] G Rebel, R Verreet, and I.M.L Ridge. Lightweight ropes for lifting applications. In OIPEEC Conference Proceedings 2006, pages 33–54, Athens, 2006.

[4] William Fronzaglia and Rigo Bosman. Working at depth: Less work with synthetic ropes and cables. In OCEANS 2016 MTS/IEEE Monterey, pages 1–6, Monterey, CA, 2016.

[5] Sam Weller, Peter Davies, Lars Johanning, and Stephen Banfield. Guidance on the use of synthetic fibre ropes for marine energy devices. Technical report, 2013.

[6] DNVGL. DNVGL-RP-E304: Damage Assessment of Fibre Ropes for Offshore Mooring. 2017.

[7] DNVGL. DNVGL-OS-E303: Offshore fibre ropes. 2018.

[8] DNVGL. DNVGL-RP-E305: Design, testing and analysis of offshore fibre ropes. 2015.

[9] DNVGL. DNVGL-ST-E407: Rope based deployment and recovery systems for designated service. 2016.

[10] CI 2001-04: Fiber Rope Inspection and Retirement Criteria. (2004), 2004.

[11] H A McKenna, J W S Hearle, and N O'Hear. Inspection and retirement. In H A McKenna, J W S Hearle, and N O'Hear, editors, Handbook of Fibre Rope Technology, Woodhead Publishing Series in Textiles, chapter 9, pages 269–299. Woodhead Publishing, 2004.

[12] H. A. McKenna, J. W. S. Hearle, and N. O'Hear. Use of rope. In H A McKenna, J W S Hearle, and N O'Hear, editors, Handbook of Fibre Rope Technology, Woodhead Publishing Series in Textiles, chapter 8, pages 237–268. Woodhead Publishing, 2004.

[13] H. A. McKenna, J. W. S. Hearle, and N. O'Hear. Rope structures. In H A McKenna, J W S Hearle, and N O'Hear, editors, Handbook of Fibre Rope Technology, Woodhead Publishing Series in Textiles, chapter 3, pages 75–100. Woodhead Publishing, 2004.

[14] John F. Flory. The past, present and future of synthetic fiber ropes. In OIPEEC Proceedings 2017, pages 1–14, La Rochelle, 2017.

[15] Alberto Diez-Olivan, Javier Del Ser, Diego Galar, and Basilio Sierra. Data fusion and machine learning for industrial prognosis : Trends and perspectives towards Industry 4.0. Information Fusion, 50(July 2018):92–111, 2019.

[16] Van Duc Nguyen, Marios Kefalas, Kaifeng Yang, Asteris Apostolidis, Markus Olhofer, Steffen Limmer, and Thomas Bck. A Review: Prognostics and Health Management in Automotive and Aerospace. International Journal of Prognostics and Health Management, 10:1–35, 2019.

[17] Thamo Sutharssan, Stoyan Stoyanov, Chris Bailey, and Chunyan Yin. Prognostic and health management for engineering systems: a review of the data-driven approach and algorithms. The Journal of Engineering, 2015(7):215–222, 2015.

[18] Espen Oland, Rune Schlanbusch, and Shaun Falconer. Condition monitoring technologies for synthetic fiber ropes - a review. International Journal of Prognostics and Health Management, 8(2), 2017.

[19] Peter Davies, Yvan Reaud, Loic Dussud, and Patrice Woerther. Mechanical behaviour of HMPE and aramid fibre ropes for deep sea handling operations. Ocean Engineering, 38(17-18):2208–2214, 2011.

[20] R. Törnqvist, M. Strande, D. Cannell, P. Gledhill, P. Smeets, and J. Gilmore. Deployment of Subsea Equipment: Qualification of Large Diameter Fibre Rope for Deepwater Construction Applications. In Offshore Technology Conference, Houston, TX, USA, 2011.

[21] S. D. Weller, L. Johanning, P. Davies, and S. J. Banfield. Synthetic mooring ropes for marine renewable energy applications. Renewable Energy, 83(November):1268–1278, 2015.

[22] R. P. Faria, R. Bosman, M. Crawford, S. Leite, and J Boesten. Enabling ultra-deep-water deployment and recovery operations by safe usage of fibre rope. In OIPEEC Proceedings 2017, pages 53–70, La Rochelle, 2017.

[23] Samson Rope Technologies. Samson Technical Bulletin. Understanding Creep, 2019.

[24] M. P. Vlasblom and R. L. M Bosman. Predicting the creep lifetime of HMPE mooring rope applications. In Oceans 2006, Boston, MA, USA, 2006.

[25] F Flory John, P Banfield Stephen, and J Petruska David. Defining, Measuring, and Calculating the Properties of Fiber Rope Deepwater Mooring Lines. Proceedings of Offshore Technology Conference (OTC), (16151-MS), 2004.

[26] Peter Davies, Sam D Weller, Lars Johanning, and Stephen J Banfield. A review of synthetic fiber moorings for marine energy applications. In 5th International Conference on Ocean Energy, pages 1–6, 2014.

[27] Deoraj Asane, Alexander Schmitz, Yushi Wang, and Shigeki Sugano. A Study on the Elongation Behaviour of Synthetic Fibre Ropes under Cyclic Loading. In 2020 IEEE/RSJ International Conference on Intelligent Robots and Systems (IROS), pages 6326–6331, Las Vegas, NV, USA, 2020.

[28] Martin Vlasblom, Tom Engels, and Corentin Humeau. Tension endurance of HMPE fiber ropes. In OCEANS 2017 - Aberdeen, pages 1–8, Aberdeen, UK, 2017.

[29] H. S. Da Costa Mattos and F. E G Chimisso. Modelling creep tests in HMPE fibres used in ultra-deep-sea mooring ropes. International Journal of Solids and Structures, 48(1):144–152, 2011.

[30] C. Humeau, P. Davies, P. Smeets, T. A.P. Engels, L. E. Govaert, M. Vlasblom, and F. Jacquemin. Tension fatigue failure prediction for HMPE fibre ropes. Polymer Testing, 65(October 2017):497–504, 2018.

[31] Yushun Lian, Jinhai Zheng, Haixiao Liu, Pengfei Xu, and Linlu Gan. A study of the creep-rupture behavior of HMPE ropes using viscoelastic-viscoplastic-viscodamage modeling. Ocean Engineering, 162(May):43–54, 2018.

[32] Jefferson Morais Gautério, Leonardo Cofferri, Antonio Henrique Monteiro da Fonseca Thomé da Silva, and Felipe Tempel Stumpf. Lifetime prediction of high-modulus polyethylene yarns subjected to creep using the Larson–Miller methodology. Polymers and Polymer Composites, 27(7):400–406, 2019.

[33] M. Vlasblom, R. Bosman, J. Canedo, and P. Davies. Designing HMPE fiber ropes on durability. In OCEANS 2019 - Marseille, pages 1–7, Marseille, France, 2019.

[34] Bamdad Pourladian and John Groce. A proposal for the numerical and experimental evaluation of temperature rise in synthetic and hybrid ropes used in AHC systems and methods of lessening the effect. In Proceedings of the ASME/USCG 2017, pages 44–50, Washington, DC, USA, 2017.

[35] Cortland Company. Plasma 12 strand tech sheet, 2020.

[36] Fanggang Ning, Xiaoru Li, Nick O Hear, and Rong Zhou. Thermal failure mechanism of fiber ropes when bent over sheaves. Textile Research Journal, 2018.

[37] Ellen Nordgård-Hansen, Håkon Jarle Hassel, and Rune Schlanbusch. Chemometrics as a Tool to Gain Insight into Fiber Rope Aging from Infrared Images. In Proceedings of the Annual Conference of the PHM Society 2019, pages 1–13, Scottsdale, AZ, USA, 2019.

[38] E Oland, E Bossolini, O W Nielsen, and C T Veje. Modelling the thermal properties of large diameter fibre ropes. In OIPEEC Conference Proceedings 2017, pages 1–10, La Rochelle, France, 2017.

[39] H A McKenna, J W S Hearle, and N O'Hear. Properties of rope. In H A McKenna, J W S Hearle, and N O'Hear, editors, Handbook of Fibre Rope Technology, Woodhead Publishing Series in Textiles, chapter 4, pages 101–140. Woodhead Publishing, 2004.

[40] Manuel Herduin, Stephen Banfield, Sam D. Weller, Philipp R. Thies, and Lars Johanning. Abrasion process between a fibre mooring line and a corroded steel element during the transit and commissioning of a marine renewable energy device. Engineering Failure Analysis, 60:137–154, 2016.

[41] P. Davies, N. Lacotte, G. Kibsgaard, R. Craig, D. Cannell, S. Francois, O. Lodeho, K. Konate, S. Mills, M. François, A-L. Defoy, D. Durville, D. Vu, J. Gilmore, and D. Sherman. Bend Over Sheave Durability of Fibre Ropes for Deep Sea Handling Operations. In Proceedings of the ASME 2013 32nd International conference on Ocean, Offshore and Arctic Engineering, pages 1–8, 2013.

[42] Haixiao Liu, Wei Huang, Yushun Lian, and Linan Li. An experimental investigation on nonlinear behaviors of synthetic fiber ropes for deepwater moorings under cyclic loading. Applied Ocean Research, 45:22–32, 2014.

[43] S. D. Weller, P. Davies, A. W. Vickers, and L. Johanning. Synthetic rope responses in the context of load history: Operational performance. Ocean Engineering, 83:111–124, 2014.

[44] S. D. Weller, P. Davies, A. W. Vickers, and L. Johanning. Synthetic rope responses in the context of load history: The influence of aging. Ocean Engineering, 96:192–204, 2015.

[45] R. E. Hobbs, M. S. Overington, J. W.S. Hearle, and S. J. Banfield. Buckling of fibres and yarns within ropes and other fibre assemblies. Journal of the Textile Institute, 91(3):335–358, 2000.

[46]

[47] P. Davies, M. François, N. Lacotte, T. D. Vu, and D. Durville. An empirical model to predict the lifetime of braided HMPE handling ropes under cyclic bend over sheave (CBOS) loading. Ocean Engineering, 97:74–81, 2015.

[48] ABS. ABS-90: Guidance notes on the Application of Synthetic Ropes for Offshore Mooring. 2011.

[49] G. Rebel, C. R. Chaplin, C. Groves-Kirkby, and I. M L Ridge. Condition monitoring techniques for fibre mooring ropes. Insight: Non-Destructive Testing and Condition Monitoring, 42(6):384–390, 2000.

[50] W. A. Bryden and T. O. Poehler. NDE of Polymer Composites Using Magnetic Resonance Techniques. In D.O. Thompson and D.E. Chimenti, editors, Review of Progress in Quantitative Nondestructive Evaluation, pages 441–447. Springer, Boston, MA, 1987.

[51] E. W. Huntley, M. B. Huntley, and A. S. Whitehill. Patent US 9,075,022 B2: Synthetic rope, fibre optic cable and method for non-destructive testing thereof, 2015.

[52] O. Grabandt, B. Van Berkel, F. Oosterhuis, T. Mathew, and P. G. Akker. Patent US 2015/0225894 A1: Method for non-destructive testing of synthetic ropes and rope suitable for use therein, 2015.

[53] E. W. Huntley, O. Grabandt, and R. Graetan. Non-Destructive Test Methods for High-Performance Synthetic Rope. In OIPEEC Proceedings 2015, pages 191–197, 2015.

[54] Rui Pedro De Sousa Faria. Patent US 2019/0301089 A1: Hoisting Rope, 2019.

[55] Sylvain Ouellette. Patent US 10,352,683 B2: Device for analysis of synthetic rope or cable, and method of use, 2019.

[56] Ilaka Mupende and Horst Zerza. Patent US 10,214,396 B2: Device for determining the replacement state or wear of a rope during use in lifting gear, 2019.

[57] T. M Robar, W. A. Veronesi, P. A. Stucky, and J. F. Gieras. Patent US 7,123,030 B2: Method and apparatus for detecting elevator rope degradation using electrical resistance., 2006.

[58] Dan Goldwater, Saul Griffith, Eric Wilhelm, and Colin Bulthaup. Patent US 7,516,605 B2: Electronic elongation-sensing rope, 2009.

[59] Claudio De Angelis. Patent US 7,665,289 B2: Synthetic fiber rope, 2010.

[60] Annett Schmieder, Thorsten Heinze, and Markus Michael. Failure Analysis of High-Strength Fiber Ropes. Materials Science Forum, 825-826:891–898, 2015.

[61] Hans Schneiders. Patent US 2020/0087856 A1: Spliced Rope System, 2020.

[62] Luc Thévenaz, Marc Niklès, Alexandre Fellay, Massimo Facchini, and Philippe Robert. Applications of distributed Brillouin fibre sensing. In Proceedings of the International Conference on Applied Optical Metrology, pages 374–381, Balatonfüred, Hungary, 1998.

[63] O. D. Cortázar, F. G. Tomasel, and P. A. A. Laura. Monitoring the structural health of kevlar cables by means of fiber-optic technology. Journal of Sound and Vibration, 214:576–579, 1998.

[64] William L. D'Agostino, Michael D. Barrick, and Glen R. Williams. Patent US 5,182,779: DEVICE, SYSTEM AND PROCESS FOR DETECTING TENSILE LOADS ON A ROPE HAVING AN OPTICAL FIBER INCORPORATED THEREIN, 1993.

[65] D. Barton Smith and J. G. Williams. Direct Measurement of Large Strains in Synthetic Fiber Mooring Ropes Using Polymeric Optical Fibers. In Proceedings of Offshore Technology Conference (OTC), number 14242-MS, Houston, TX, USA, 2002.

[66] B. P. Ludden, J. E. Carroll, and C. J. Burgoyne. A distributed optical fibre sensor for offshore applications. In IEE Colloquium on Optical Techniques for Structural Monitoring, London, UK, 1995.

[67] P. A. Robertson and B. P. Ludden. A fibre optic distributed sensor system for condition monitoring of synthetic ropes. In Proceedings of the IEE Colloquium on Optical Techniques for Smart Structures and Structural Monitoring, London, UK, 1997.

[68] Tessa Gordelier, Phillip Rudolph Thies, Giovanni Rinaldi, and Lars Johanning. Investigating Polymer Fibre Optics for Condition Monitoring of Synthetic Mooring Lines. Journal of Marine Science and Engineering, 8(2):103, 2020.

[69] A. De Angelis. Patent US 6,392,551: Synthetic fiber cable with temperature sensor, 2002.

[70] J.H. Williams and S.S. Lee. Acoustic emission/rupture load characterisations of double braided nylon rope. Marine Technology, 19(3):268 – 271, 1982.

[71] James H Williams, John Hainsworth, and Samson S Lee. Acoustic-Ultrasonic Nondestructive Evaluation of Double-Braided Nylon Ropes Using the Stress Wave Factor. Fibre Science And Technology, 21:169–180, 1984.

[72] H Kwun and G L Burkhardt. Non-dustructive testing of ropes using the transverse impulse method. Review of Progress in Quantitative Nondestructive Evaluation, pages 1053–1060, 1989.

[73] H. Kwun and G. L. Burkhardt. Patent US 4,979,125: Non-destructive evaluation of ropes by using transverse impulse vibrational wave method, 1990.

[74] M. Ferreira, T. M. Lam, V. Koncar, and Y. Delvael. Non-Destructive Testing of Polyaramide Cables by Longitudinal Wave Propagation: Study of the Dynamic Modulus. Polymer Engineering and Science, 40(7):1628–1634, 2000.

[75] L. S. Padilla, P. Bull, R. L. Royer, and S. E. Owens. Patent US 8,958,994 B2: Non-contact acoustic signal propagation property evaluation of synthetic fiber rope, 2015.

[76] Imran Bashir, Jodi Walsh, Philipp R. Thies, Sam D. Weller, Philippe Blondel, and Lars Johanning. Underwater acoustic emission monitoring – Experimental investigations and acoustic signature recognition of synthetic mooring ropes. Applied Acoustics, 121:95–103, 2017.

[77] Marta Toda, Katarzyna E Grabowska, and Izabela L Ciesielska-Wrobel. Micro-CT supporting structural analysis and modelling of ropes made of natural fibers. Textile Research Journal, 86(12):1280–1293, 2016.

[78] Annett Schmieder, Thorsten Heinze, and Markus Michael. Computer-assisted tomography analysis of high-strength fiber ropes. In Proceedings of the 6th Conference on Industrial Computed Tomography, Wels, Austria, 2016.

[79] Scott Schecklman, Gabriel P. Kniffin, and Lisa M. Zurk. Terahertz Non-destructive Evaluation of Textile Ropes and Slings. In 2014 International Symposium on Optomechatronic Technologies, pages 86–90, Seattle, WA, USA, 2014.

[80] Jeff Nichols, Stephen Banfield, and John Flory. Forensic techniques for investigating the causes of fiber rope failures. In OCEANS 2007, Vancouver, 2007.

[81] J.W.S. Hearle, I. Overington, and M. S. Overington. Non-contact strain and deformation measurement in yarns, ropes and fabrics. In IFAI Expo, 2001.

[82] R Söhnchen. Securing safety of ropes with a visual rope inspection system. In OIPEEC Proceedings 2015, number March, pages 199–208, 2015.

[83] Gregor Novak. Camera-based Visual Rope Inspection. innotrac, 1:55–63, 2020.

[84] John R. Rudy and Matthew Thoresen. Patent US 10,717,631 B2: Optical detection and analysis of crane hoist and rope, 2020.

[85] Claudio De Angelis. Patent US 6,247,359 B1: Apparatus for the identification of need to replace synthetic fiber ropes, 2001.

[86] Douglas E. Logan, Leroy H. Favrow, Robert J. Haas, Paul A. Stucky, and Neil R. Baldwin. Patent US 7,117,981 B2: Load bearning member for use in an elevator system having external markings for indicating a condition of the assembly, 2006.

[87] Davide Rossini and Giuliano Ambroset. Patent US 10,690,482 B2: Device for measuring parameters of a rope, 2020.

[88] Ilaka Mupende, Ulrich Hamme, and Hans-Dieter Willim. Patent US 10,822,742 B2: Apparatus for recognizing the replacement state of a high-strength fiber rope for lifting gear, 2020.

[89] Olav Vennemann, Rikard Törnqvist, Björn Ernst, Sven Winter, and Ian Frazer. Bending fatigue tests using a suitable NDT method to determine lifetime of large diameter wire ropes for offshore lifting applications. In Proceedings of the International Conference on Offshore Mechanics and Arctic Engineering - OMAE, pages 155–161, 2008.

[90] G. Novak, M. Wehr, and K-H Wehking. Lifetime calculation of high-modulus fibre ropes. In OIPEEC Proceedings 2017, pages 85–93, La Rochelle, 2017.

[91] Atsushi Horigome and Gen Endo. Investigation of Repetitive Bending Durability of Synthetic Fiber Ropes. IEEE Robotics and Automation Letters, 3(3):1779–1786, 2018.

[92] Annett Schmieder and Markus Golder. Investigating the Lifetime of Fibre Ropes. innotrac, 1:1–8, 2020.

[93] Klaus Feyrer. Wire Ropes, Tension, Endurance, Reliability. Springer-Verlag Berlin Heidelberg, Berlin, 2007.

[94] Ashley Nuttall. Service life of synthetic fibre ropes in deepwater lifting operations. In The 15th North Sea Offshore Cranes & Lifting Conference, 2010.

[95] A. Frick, W. Frick, and G. Novak. On the assessment of the residual service life of fiber ropes in use. In OIPEEC Proceedings 2019, pages 35–50, The Hague, 2019.

[96] F. Sloan. Wear-based parameter for CBOS fatigue in fiber ropes. In OIPEEC Proceedings 2019, pages 25–34, The Hague, 2019.

[97] Yushun Lian, Haixiao Liu, Wei Huang, and Linan Li. A creep-rupture model of synthetic fiber ropes for deepwater moorings based on thermodynamics. Applied Ocean Research, 52:234–244, 2015.

[98] Juan Felipe Beltran and Eric B. Williamson. Degradation of rope properties under increasing monotonic load. Ocean Engineering, 32(7 SPEC. ISS.):826–844, 2005.

[99] Juan Felipe Beltrán and Eric B. Williamson. Numerical procedure for the analysis of damaged polyester ropes. Engineering Structures, 33(5):1698–1709, 2011.

[100] Juan Felipe Beltrán and Enzo De Vico. Assessment of static rope behavior with asymmetric damage distribution. Engineering Structures, 86:84–98, 2015.

[101] Juan Felipe Beltrán, Nicolás Ramírez, and Eric Williamson. Simplified analysis of the influence of strain localization and asymmetric damage distribution on static damaged polyester rope behavior. Ocean Engineering, 145(September):237–249, 2017.

[102] T. D. Vu, D. Durville, and P. Davies. Finite element simulation of the mechanical behavior of synthetic braided ropes and validation on a tensile test. International Journal of Solids and Structures, 58(April):106–116, 2015.

[103] Peter Davies, Damien Durville, and Thanh Do Vu. The influence of torsion on braided rope performance, modelling and tests. Applied Ocean Research, 59:417–423, 2016.

[104] Ilaka Mupende and H. Zerza. Patent US 2014/0027401 A1: Apparatus for recognizing the discard state of a high-strength fiber rope in use in lifting gear, 2014.

[105] Ilaka Mupende and Horst Zerza. Patent US 9873597 B2: Device for detecting the replacement state of wear of a high-strength fibre rope use in lifting gear, 2018.

[106] Frederik Benjamin van der Woude and Jurgen Arjan Zijlmans. Patent US 2017/0045493 A1: Real-time rope monitoring, 2017.

[107] Olga Fink, Qin Wang, Markus Svensén, Pierre Dersin, Wan-Jui Lee, and Melanie Ducoffe. Potential, challenges and future directions for deep learning in prognostics and health management applications. Engineering Applications of Artificial Intelligence, 92(January):103678, 2020.

[108] Yaguo Lei, Naipeng Li, Liang Guo, Ningbo Li, Tao Yan, and Jing Lin. Machinery health prognostics: A systematic review from data acquisition to RUL prediction. Mechanical Systems and Signal Processing, 104:799–834, 2018.

[109] Samir Khan and Takehisa Yairi. A review on the application of deep learning in system health management. Mechanical Systems and Signal Processing, 107:241–265, 2018.

[110] Yusuf Aytaç Onur, Cevat Erdem İmrak, and Tuğba Özge Onur. Discarding lifetime investigation of a rotation resistant rope subjected to bending over sheave fatigue. Measurement: Journal of the International Measurement Confederation, 142:163–169, 2019.

[111] Shaohua Xue, Jianping Tan, Lixiang Shi, and Jiwei Deng. Rope tension fault diagnosis in hoisting systems based on vibration signals using EEMD, improved permutation entropy, and PSO-SVM. Entropy, 22(2), 2020.

[112] Ping Zhou, Gongbo Zhou, Zhencai Zhu, Chaoquan Tang, Zhenzhi He, Wei Li, and Fan Jiang. Health Monitoring for Balancing Tail Ropes of a Hoisting System Using a Convolutional Neural Network. Applied Sciences, 8(8):1346, 2018.

[113] Xinyuan Huang, Zhiliang Liu, Xinyu Zhang, Jinlong Kang, Mian Zhang, and Yongliang Guo. Surface damage detection for steel wire ropes using deep learning and computer vision techniques. Measurement, 161(April):107843, 2020.

[114] Minwoong Chung, Seungjun Kim, Kanghyeok Lee, and Do Hyoung Shin. Detection of damaged mooring line based on deep neural networks. Ocean Engineering, 209(February):107522, 2020.

[115] Samson Rope Technologies. 12-Strand Class II Tuck-Bury Eye Splice, 2017.

[116] Ridge I.M.L. Teissier, J.M. and J.M. Dodd. In Depth Analysis of the Socket Termination, and Proposal for a New Rope Termination Method. In OIPEEC Proceedings 2019, pages 25–34, The Hague, 2019.

[117] G. Bradski. The OpenCV Library. Dr. Dobb's Journal of Software Tools, 2000.

[118] FLIR. ResearchIR 4. FLIR Systems, Inc., Wilsonville, OR, 2015.

[119] L Breiman, L. H Friedman, R. A Olshen, and C. J Stone. Classification and Regression Trees. Wadsworth Interantional Group, Belmont, CA, 1984.

[120] F. Pedregosa, G. Varoquaux, A. Gramfort, V. Michel, B. Thirion, O. Grisel, M. Blondel, P. Prettenhofer, R. Weiss, V. Dubourg, J. Vanderplas, A. Passos, D. Cournapeau, M. Brucher, M. Perrot, and E. Duchesnay. Scikit-learn: Machine Learning in Python. Journal of Machine Learning Research, 12(1):2825–2830, 2011.

[121] L Rokach and O Maimon. Decision Trees. In O Maimon and L Rokach, editors, Data Mining and Knowledge Discovery Handbook, chapter 9, pages 165–192. Springer, Boston, MA, 2005.

[122] John Mingers. An Empirical Comparison of Selection Measures for Decision-Tree Induction. Machine Learning, 3(4):319–342, 1989.

[123] L Breiman. Random Forests. Machine Learning, 45(1):5–32, 2001.

[124] L Breiman. Bagging predictors. Machine Learning, 24(2):123–140, 1996.

[125] Corinna Cortes and Vladimir Vapnik. Support-Vector Networks. Machine Learning, 20(3):273–297, 1995.

[126] Armin Shmilovici. Support Vector Machines. In O Maimon and L Rokach, editors, Data Mining and Knowledge Discovery Handbook, chapter 12, pages 257–276. Springer, Boston, MA, 2005.

[127] N. S. Altman. An Introduction to Kernel and Nearest-Neighbor Nonparametric Regression. The American Statistician, 46(3):175–185, 1992.

[128] Irina Rish. An Empirical Study of the Naïve Bayes Classifier. IJCAI 2001 workshop on empirical methods in artificial intelligence, 3(2001):41–46, 2014.

[129] J.S. Cramer. The Origins of Logistic Regression. Tinbergen Institute Working Paper No. 2002-119/4, 2002.

[130] F Chollet. Keras, 2015.

[131] Martín Abadi, Paul Barham, Jianmin Chen, Zhifeng Chen, Andy Davis, Jeffrey Dean, Matthieu Devin, Sanjay Ghemawat, Geoffrey Irving, Michael Isard, Manjunath Kudlur, Josh Levenberg, Rajat Monga, Sherry Moore, Derek G. Murray, Benoit Steiner, Paul Tucker, Vijay Vasudevan, Pete Warden, Martin Wicke, Yuan Yu, and Xiaoqiang Zheng. Tensorflow: A system for large-scale machine learning. In 12th USENIX Symposium on Operating Systems Design and Implementation (OSDI '16), pages 265–283, 2016.

[132] Vladimir Vapnik, Steven E. Golowich, and Alex Smola. Support vector method for function approximation, regression estimation, and signal processing. Advances in Neural Information Processing Systems, 9:281–287, 1997.

[133] P. J. García Nieto, E. García-Gonzalo, F. Sánchez Lasheras, and F. J. De Cos Juez. Hybrid PSO-SVM-based method for forecasting of the remaining useful life for aircraft engines and evaluation of its reliability. Reliability Engineering and System Safety, 138:219–231, 2015.

[134] Pradeep Kundu, Ashish K. Darpe, and Makarand S. Kulkarni. An ensemble decision tree methodology for remaining useful life prediction of spur gears under natural pitting progression. Structural Health Monitoring, 19(3):854–872, 2020.

[135] Det Norske Veritas. Damage Assessment of Fibre Ropes for Offshore Mooring. Computer, (April), 2005.

[136] F. Van Der Woude and J. Zijlmans. Patent WO 2015160254 A1: Real-time rope monitoring, 2015.

[137] Tadhg Brosnan and Da Wen Sun. Inspection and grading of agricultural and food products by computer vision systems - A review. Computers and Electronics in Agriculture, 36(2-3):193–213, 2002.

[138] Thomas B Moeslund. Introduction to video and image processing: Building real systems and app Springer Science & Business Media, 2012.

[139] Satoshi Suzuki and Keiichi Abe. Topological structural analysis of digitized binary images by border following. Computer Vision, Graphics and Image Processing, 30(1):32–46, 1985.

[140] Dustin Heins, Greg Mozsgai, and Angelo Tanzarella. Inspection criteria for HMPE rope. OCEANS 2013 MTS/IEEE Bergen: The Challenges of the Northern Dimension, 2013.

[141] Shaun Falconer, Andreas Gromsrud, Espen Oland, and Geir Grasmo. Preliminary Results on Condition Monitoring of Fiber Ropes using Automatic Width and Discrete Length Measurements. In Annual Conference of the Prognostics and Health Managemet Society 2017, 2017.

[142] R Tomasi, C. Manduchi. Bilateral Filtering for Gray and Color Images. In Proceedings ofthe 1998 IEEE International Conference on Computer Vision, 1998.

[143] John F Canny. A Computational Approach to Edge Detection. IEEE TRANSACTIONS ON PATTERN ANALYSIS AND MACHINE INTELLIGENCE, 8(6):679–698, 1986.

[144] Seyed Reza Ghoreishi, Peter Davies, Patrice Cartraud, and Tanguy Messager. Analytical modeling of synthetic fiber ropes. Part II: A linear elastic model for 1 + 6 fibrous structures. International Journal of Solids and Structures, 44(9):2943–2960, 2007.

[145] Orhan Yaman and Mehmet Karakose. Auto correlation based elevator rope monitoring and fault detection approach with image processing. In IDAP 2017 - International Artificial Intelligence and Data Processing Symposium, 2017.

[146] Björn Ernst, Erich Rührnössl, Rudolf Kirth, Peter Baldinger, Robert Traxl, and Gunter Kaiser. US 2018/0363241 A1: METHOD FOR DETERMINING THE REPLACEMENT STATE OF WEAR OF A ROPE MADE OF A TEXTILE FIBRE MATERIAL, 2018.

[147] Chih-Wen Chang, Hau-Wei Lee, and Chein-Hung Liu. A Review of Artificial Intelligence Algorithms Used for Smart Machine Tools. Inventions, 3(3):41, 2018.

[148] Shaun Falconer, Geir Grasmo, and Ellen Nordgård-Hansen. Condition monitoring of HMPE fibre rope using computer vision during CBOS testing. In OIPEEC Proceedings 2019, pages 129–147, The Hague, 2019.

[149] Shaun Falconer, Ellen Nordgård-Hansen, and Geir Grasmo. Computer vision and thermal monitoring of HMPE fibre rope condition during CBOS testing. Applied Ocean Research, 102:102248, 2020.

[150] Shaun Falconer, Peter Krause, Thomas Bäck, Ellen Nordgård-Hansen, and Geir Grasmo. Condition classification of HMPE rope during CBOS testing using Supervised Machine Learning Methods. Engineering Applications of Artificial Intelligence [submitted for review].

Appendices

Paper A

Preliminary results on condition monitoring of fibre Ropes using automatic width and discrete length measurements

Shaun Falconer, Andreas Gromsrud, Espen Oland and Geir Grasmo

This paper has been published as:

S. Falconer, A. Gromsrud, E. Oland and G. Grasmo. Preliminary results on condition monitoring of fibre Ropes using automatic width and discrete length measurements. In *Proceedings of the Annual Conference of the Prognostics and Health Management Society 2017, St. Petersburg, FL, USA*, 2017. ISBN: 978-1-936263-26-4.

Preliminary Results on Condition Monitoring of Fiber Ropes using Automatic Width and Discrete Length Measurements

Shaun Falconer*, Andreas Gromsrud*, Espen Oland**, Geir Grasmo*

*Department of Engineering Sciences
University of Agder
NO-4876 Grimstad, Norway

**Teknova AS
NO-4612 Kristiansand, Norway

Abstract – As the offshore sector move to deeper waters, fiber ropes have the potential to replace more traditional solutions such as steel wire ropes for deep sea lifting and heave-compensated operations. While steel wire ropes must account for their own weight when determining the maximum depth that a payload can be deployed, fiber ropes such as high modulus polyethylene (HMPE), are more buoyant than their steel counterparts, enabling payloads to be deployed at deeper depths using smaller cranes. For this reason, companies are actively developing fiber rope cranes to be used in industry. The inherent issue with these designs is monitoring the condition of the fiber rope due the multitude of damage mechanisms and condition indicators that exist, therefore determining the time to rupture remains an unsolved problem. To this end, this paper considers the use of computer vision to monitor the width at discrete length sections and use that as a potential condition indicator. Furthermore, the paper describes in detail how OpenCV is applied to detect the contour of the rope to find the width, how the experiment has been performed, as well as other practical experiences from testing a 28mm Dyneema® fiber rope. The experimental results show that an exponential relationship between the applied tension and the reduction in width (which was reduced by more than 10% before rupture), and it is believed that if the width can be monitored at discrete sections along the rope over time, the width itself will prove to be a good condition indicator.

A.1 Introduction

Fiber ropes have been used in a offshore context for a variety of purposes including mooring and general sailing. While the use of fiber ropes in the marine sector is not a novel concept, the need to develop technology to adequately monitor their condition is of paramount importance and has substantial potential for progression. A particularly

interesting alternative to steel wire ropes in offshore construction cranes that is gaining increasing popularity, is that of fiber ropes. There are already existing designs for fiber rope cranes by MacGregor, National Oilwell Varco and Rolls Royce. The greater buoyancy of HMPE fiber rope allows for smaller cranes to be used while potentially reaching water depths between 3000-4000m. Additionally this presents a saving in terms of mass and vessel deck space required for offshore operations when compared to steel wire rope designs. The inherent issue with this however is the effect of heave compensation on the fiber rope, which causes heat build up as it moves over the sheaves to keep the payload at the same depth relative to the ocean floor. This heat generation can lead the to the ultimate degradation of the rope through creep, therefore a suitable means of monitoring the condition must be developed to judge the remaining useful life (RUL).

In terms of industry standards, it is recommended by [135] that visual inspection of fiber rope is used to gauge its condition. While this is accepted practice there is still the distinct possibility for premature disposal of the rope due to conservative limits on their use. The natural extension of a visual inspection routine is the use of computer vision for monitoring purposes. Computer vision algorithms could be developed in order to automatically detect changes in the width and elongation of fiber rope and could serve as a valid condition indicator and lead to better understanding of the RUL of fiber rope used in offshore operations. Width and elongation measurements were chosen as the condition indicator based on recommendation from industry expert Nick O'Hear. Contributing factors towards inconsistent diameter measurement in fiber ropes include cut strands, compression damage, pulled strands and heavy internal/external abrasion which can be seen in Figure D.1. In a recent patent [136] propose to correlate physical measurements related to rope diameter, rope shape, elongation, creep, bending, tension and temperature to specific positions along the rope to indication its current condition. Additionally another patent by [**?**] makes use of a clamp and roller set up attached to springs to measure rope diameter. The lower set of spring rollers in this device have rotary axle where the measured diameter is transferred to a position sensor. As a result, cross sectional changes can be monitored to assess rope condition.

In general for condition monitoring of fiber ropes can be separated into two different types; embedded and non-embedded technologies. An example of embedded technology would be the inclusion of a foreign material into the rope. Using this approach it is possible to use magnetism, X-ray or terahertz analysis to assess the rope condition as was demonstrated in a patent by [52].

However for the purposes of this article only non-embedded technologies will be considered. It is proposed that computer vision will automatically monitor the changing width and elongation through an algorithm formulated in OpenCV. In terms of previous work in

Figure A.1: Different kinds of rope damages. Cut strands (top left), compression damage (top right), inconsistent diameter (middle left) and pulled strands (middle right), heavy abrasion (bottom left) and melted fibers (bottom right). Reproduced with permission from Samson Rope Technologies.

this field, computer vision for condition monitoring has been researched using markings to detect the length of wire. An example of this is a patent by [86] where markings on load bearing members in elevators are used for condition monitoring. The elongation between the markers is measured but there is no mention of the width. [86] also suggest the use of cameras as sensors for measuring the elongation between the markers. There has been little research into the use of monitoring the width of rope using computer vision.

This work will document the application and results of an OpenCV algorithm to detect the width and length changes in a 28mm Dyneema® fiber rope when subject to tension-tension testing. The conclusions from these tests will be discussed and potential steps for future research to progress condition monitoring of fiber ropes will be discussed.

A.2 Computer Vision

Computer vision can be described as a computer understanding the world in the same way as humans do through vision. Through the use of digital images and videos, the digital signals can be processed through algorithms and interpreted as useful information. Computer vision contributes to a number of industries including manufacturing, medical diagnosis and robot guidance. An example of computer vision being used for condition monitoring purposes is in the agricultural industry. In their work, [137] used computer vision in the inspection of fruit and berries to classify their grade and quality.

The algorithm developed for this paper is based on color interpretation, therefore the main concepts are discussed in the following sections.

A.2.1 Software

The algorithm for width and elongation measurements was developed using OpenCV with Python chosen as the programming language. The versions used were OpenCV 3.2 and Python 3.6.

A.2.2 Color and Grayscale Representation

The outgoing digital signal from each pixel in an image is usually represented by 8-bit of information for each sensor in the pixel. If only one sensor is present in the pixel then the signal is represented by 256 different values specified on a scale where 0 is black and 255 is white. The computer interprets these different shades of gray as a designated numerical value for each pixel. In the case of color cameras, each pixel has three sensors with one to represent each of the primary colors (blue, green, red), known as "RGB representation". Incoming light to the camera is split into three different colours using optical filters and mirrors, where each of the primary colours will be represented by a scale with values from 0 to 255. This is equivalent to the possibility of $256^3 = 16{,}777{,}214$ different colors that can be assigned to each pixel. Eq. (A.1) is the formula used by OpenCV when converting from color to grayscale:

$$Y = 0.299 \cdot Red + 0.587 \cdot Green + 0.114 \cdot Blue \tag{A.1}$$

where Y is the optimised grayscale value in relation to human perception of colours with regards to luminance [138]. This will be used to turn the image of the fiber rope into grayscale representation before further processing.

A.2.3 Thresholding

Thersholding is used to separate background noise from the object of interest. In thresholding a value T between 0 and 255 is set, which will convert all pixel values under the threshold to 0 and those that are over to 255. This relationship is shown in Eq. (D.2) and Eq. (D.3):

$$\text{if } f(x,y) \leq T \text{ then } g(x,y) = 0 \tag{A.2}$$

$$\text{if } f(x,y) > T \text{ then } g(x,y) = 0 \tag{A.3}$$

where $f(x,y)$ and $g(x,y)$ are a specific pixel on an image before and after the thresholding operation respectively.

A.2.4 Hue, Saturation, Value (HSV)

Hue, Saturation, Value (HSV) is another method of representing colors in an image. Hue is the pure color represented by the dominant wavelength in the perceived light with a given value between 0 and 360 degrees, for example red, green and blue all have Hue values of 0, 120 and 240 degrees respectively. The Saturation and Value parameters represent the brightness and darkness of the colors used respectively, both of which can be denoted by a value between 0 and 255. HSV representation makes focusing on a specific color (i.e the color of the fiber rope) easier. As a default, OpenCV makes use of Blue, Green, Red (BGR) representation and must be converted to HSV representation. Conversion from RGB to HSV is performed by Eqs. (D.4), (D.5) and (A.6).

$$V = max(R, G, B) \tag{A.4}$$

$$S = \begin{cases} \frac{V - min(R,G,B)}{V} & \text{if } V \neq 0 \\ 0 & \text{otherwise} \end{cases} \tag{A.5}$$

$$H = \begin{cases} 60(G-B)/(V - min(R,G,B)) & \text{if } V = R \\ 120 + 60(B-R)/(V - min(R,G,B)) & \text{if } V = G \\ 240 + 60(R-G)/(V - min(R,G,B)) & \text{if } V = B \end{cases} \tag{A.6}$$

A.2.5 Border method

In order to follow the outline of the fiber rope in the image, a border following algorithm is employed. OpenCV makes use of a contour finding method specified in work by [139], where a raster scan is applied to an input binary image. Essentially the algorithm follows pixels of the same intensity or colour to find the contour of the fiber rope in the image.

A.2.6 Green's Theorem

Green's Theorem is applied in OpenCV to the find the moment of the enclosed area made by the contour. It describes the relation between the line integral around the closed curve C, and the double integral over the plane D which C has enclosed. If L and M have continuous first order partial derivatives on D and the path of integration is anticlockwise, then this can be represented as the mathematical expression shown in Eq. (A.7):

$$\oint_C (Ldx + Mdy) = \int\int_D (\frac{\partial M}{\partial x} - \frac{\partial L}{\partial y}) dxdy. \tag{A.7}$$

A.3 Experimental Set-up

The experiment consisted of multiple tension-tension tests on different HMPE fiber rope specimens. The tests were recorded and the video data was analysed using the OpenCV algorithm to detect width and length changes in the fiber rope specimens.

Figure A.2: Example of splice and eyelet at the end of a fiber rope speicmen.

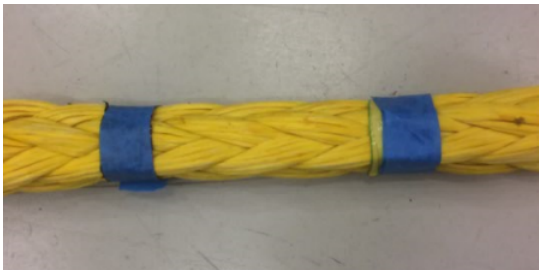

Figure A.3: The area where width and length measurements were taken

A.3.1 Equipment

The tension-tension testing was performed using a Wolport tensioner machine, which is capable of delivering a maximum load of 1000 kN. The fiber rope was secured into the machine using two 25 ton rated shackles attached to eyelets located at either end of the rope.

A 28mm Dyneema® fiber rope consisting of 12 strands each with 14 yarns was used. Eyelets for securing the rope into the tensioner were made through splicing performed in house at the University of Agder. The splice chosen was a modified version of the Tuck-Bury eye splice in order to make the rope specimen short enough to fit into the tensioner. It is worth note that if this type of splicing is performed correctly, the areas were the unspliced rope meets the spliced portion will experience a 5-15% reduction in strength. As this is a modified version of the splice, it is expected that this strength reduction will be at least 15% or higher in this splice transition zone. An example of the splice is shown in Figure A.2.

The area where the width and length measurements will take place is the portion of the rope between both splice transition zones highlighted in Figure A.3. Blue markers are placed on this portion at roughly 100 mm apart for purposes of detecting length measurement in the OpenCV algorithm. Creep is a behaviour that occurs locally, therefore discrete measurements at different portions of the rope will be of interest.

The experiments were recorded using a Logitech C922 1080p web camera with a 1920x1080 resolution. Additionally the camera was full HD and recorded at 30 frames per second (fps). The camera was mounted so that it focused on the area of interest where measurement occurred. This video was then analyzed by the OpenCV algorithm.

A white backdrop was erected behind the tensioner rope in order to distinguish the colors of the rope and markers from background interference. The experimental set up is shown in Figure A.4.

Figure A.4: Experimental set up. Here a fiber rope is secured into the tensioner.

A.3.2 OpenCV Algorithm

A.3.2.1 Length Measurements

The markers were applied to the rope in the area to be tracked by the OpenCV algorithm. Blue was chosen as it contrasts the colors of the yellow rope and white background. The algorithm was programmed to measure the distance between these two markers.

To detect the blue markers every frame of the video is converted from RGB to HSV colour representation. The formula for the transformation process for each pixel is highlighted by Eqs (4), (5) and (6).

Once converted, a suitable search band has to be adjusted for the algorithm to detect the color blue. OpenCV uses a slightly different scale for the Hue portion of HSV representation as previously highlighted. OpenCV uses a scale of 0 to 179 for Hue, with blue to be equivalent to 120 in this range. Therefore the search band values (including Saturation and Value) are set with a lower band [90, 50, 50] and an upper band [150, 255, 255].

The contour is then detected around the marker sections using the border method in the black and white binary image. In order to avoid noise from smaller contours on the edge of the markers, a threshold is applied so that only the large blue areas in the range are detected. The area of interest in the rope along with the binary image after this process is shown in Figure 5.

The image detected essentially works as a coordinate system. The centre point of both markers are found and given as points (x_1, y_1) and (x_2, y_2) for points 1 and 2 respectively. The distance between these points is used for the length measurements, which are highlighted in Figure 6.

A.3.2.2 Width Measurements

The width measurements took place in the area between the two markers. Three separate width readings were taken from this area and were denoted as regions of interest (ROI).

The same conversion from RGB to HSV conversation occurs, however in this instance the color of the rope is used. As the rope is yellow the search bands for HSV thresholding are set as a lower band

Figure A.5: Area with markers (left) and the binary image after HSV conversion and thresholding (right).

Figure A.6: Measurement area with mid points of markers. The distance between these points are used for length measurements.

Figure A.7: Areas with markers (left) and the binary image after HSV conversion and thresholding (right).

[0, 50, 50] and [50, 255, 255]. The measurement area in the rope along with the binary image after this process is shown in Figure 7.

The contour is then found through the border method used for the length calculation. The green contour is then applied to the white portions of the binary image. Each pixel in the contour around the rope has an assigned coordinate. For each frame, the coordinates of each point in the contour are stored in two separate arrays for the left and right sides of the rope. This is performed for all three ROIs. The

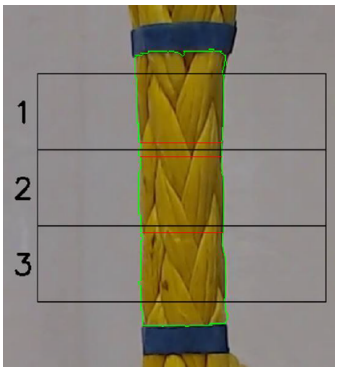

Figure A.8: Measurement area with the three separate ROIs highlighted. The red line in each section denotes the shortest width measured during each frame.

distance between each point on the left and each point on the right is calculated and the shortest distance is returned. This shortest distance represents the smallest width recorded in each frame and is show as a red line in Figure 8.

A.3.3 Method

Three different tests on separate rope specimens were performed with width and length measurements taken in the area between the markers applied to the rope. For all experiments the markers were applied at approximately 100mm apart. The common aim in each test was to stretch the rope in the tensioner until failure. Differences in terms of the markers used and loads applied are detailed in the following sections.

Experiment 1: A permanent marker pen is used to draw markers on the rope to be evaluated by the OpenCV algorithm. There was a pre-load phase were the tensioner holds the rope at 0.4kN and was steadily increased until 338.8kN before stopping the test.

Experiment 2: Blue markers were used for length measurements and to denote the area for the ROIs for width measurements. There was a pre-load phase were the tensioner holds the rope at 0.4kN and was steadily increased until 310kN before stopping the test.

Experiment 3: Blue markers were used for length measurements and to denote the area for the ROIs for width measurements. There was pre-load phase were the tensioner holds the rope at 1.5kN and was steadily increased until 290kN before stopping the test.

A.4 Results

Three different experiments were performed using the described setup. In the following results, a moving average filter with window-size 50 has been used to smooth the width measurements, while the length measurement is smoothed using a filter with window size of 200.

In the first experiment the load was applied linearly from a pre-tension up to 338kN from where the rope ruptured in the splice above the region of interest. Figure 9 shows the experimental results, where it is evident that the width of the rope goes from 25.6mm down to 22.9mm at 150 seconds.

In the second experiment, the load is applied over a shorter time (100 seconds). Figure 10 shows the experimental results, where the width goes from 26.5mm down to 22.9mm right before rupture (from 140

Table A.1: Comparison of results.

Time	**Exp 1**	**Exp 2**	**Exp 3**
Load at rupture	338kN	310kN	295kN
Width reduction	10.5%	13.6%	11.2%
Length increase	N/A	N/A	1.9%

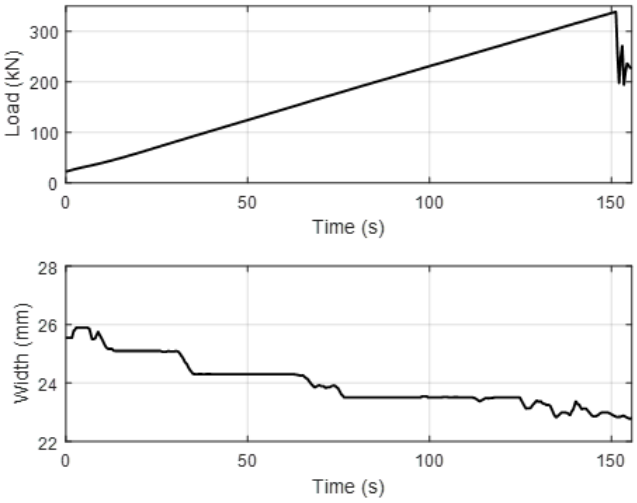

Figure A.9: The first experiment where the load was increased linearly until rupture.

seconds the width decreases linearly, which might be the initial stage of rupture). Pay special attention to the exponential shape of the reduction in width, which become apparent from this experiment. Going back to Figure 1, the same exponential relationship can be observed, but with a much larger time-constant.

While the intention for the two first experiments was to also measure the length using external markers, this proved to be somewhat more challenging than anticipated as the marker moved relative to the rope during the experiments. In the third experiment, this issue was remedied and these results therefore also contain the increase in length during the experiment. Further, the load is here increased in a step-wise manner up to 295kN, instead of linear increase, and over a much longer time. Figure 11 shows the applied load, the width of the rope together with the increase in length at the region of interest. In this experiment, the width goes from 25.8mm to 22.9mm, while the discrete length increases from 100mm to 101.9mm right before rupture. The increase in length is measured by fixing two markers placed 100mm from each-other. This means that the discrete length increases by 1.9%.

Table A.1 shows a summary of the three experiments where it can be observed that the width of the rope decreases in the range of 10.5 - 13.6% before rupture, while the length in the third scenario increases by 1.9%. It is evident that the width and length of the rope changes during use, and as such can be good condition indicators. All three test-samples ruptured at 22.9mm, such that by monitoring the width and defining a minimum value might serve as a way forward. The differences in width reduction from the three experiments are due to sensor-noise and the fact that ropes are slightly different based on tension, temperature, construction, etc. This means that it is the change in diameter that should serve as a condition indicator, and not an absolute value based on the defined diameter of the rope.

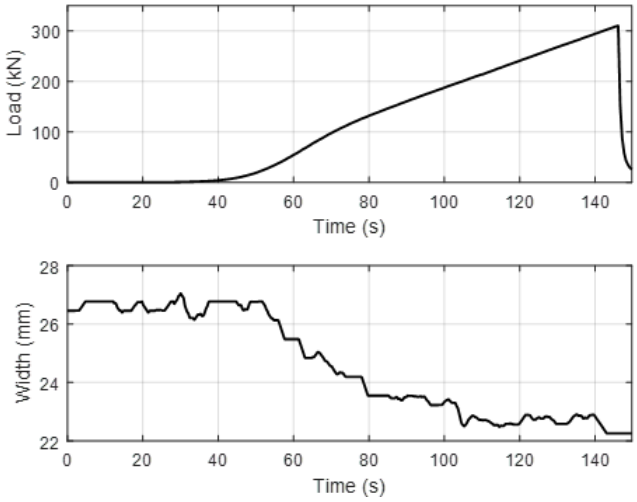

Figure A.10: The second experiment where the load was applied (almost) linearly with a shorter duration than the first experiment.

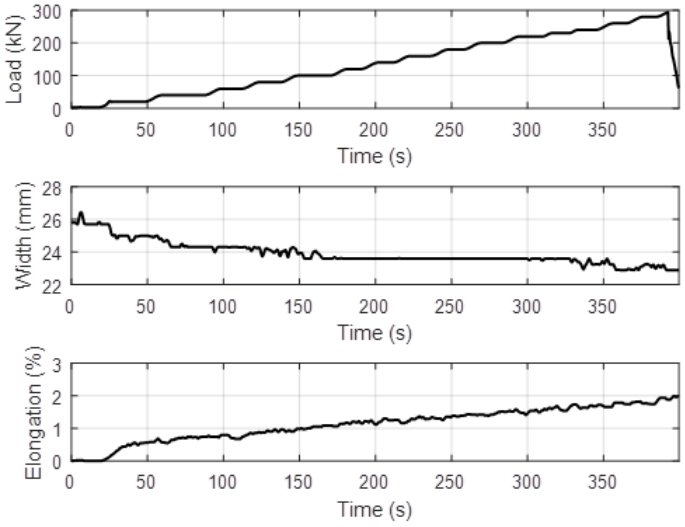

Figure A.11: The third experiment with a step-wise load curve and a longer time-period.

A.5 Discussion

In all three experiments there was an exponential decrease in the width measured as each load was increased. It is also worth note that the separate fiber rope specimens used all ruptured at a width of 22.9mm. Additionally the width measurements across all three experiments vary as there are different starting widths from slight differences in each rope preparation routine. When each fiber rope specimen is prepared, a splicing process takes place and no two routines will be exactly the same, causing discrepancy in the measurements between each test. The ruptures that occurred during testing all came at the splice due to the reduction of the strength in this portion of the rope. In addition to this, as creep is a local phenomenon and will not act the same across the whole length of the rope contributing to varying results. The results do indicate that computer vision is a valid method of tracking the width of fiber rope during tension-tension tests. However in terms of length measurements a new method of attaching markers to the rope has to be found as the previous method led to invalid results from the first two experiments.

The length measurements from the third experiment indicate that it is possible to monitor the length but an improved method is required.

A.6 Conclusion

The overall results indicate that it is possible to monitor the width and length measurements of a fiber rope under tension-tension testing. They also indicate that there is potential in using these measurements as condition indicators to evaluate the state of a fiber rope. However, the application that is of most concern is the effect of heave compensation on fiber rope. In the future, it is proposed thats this technology is applied to fiber rope undergoing a cyclic-bend-over-sheave (CBOS) regime to simulate the effects of offshore lifting operations. Additionally, it is desirable to combine this with other technologies such a thermography, CT scanning and embedded conductive threads in the rope to monitor the condition of the rope and improve estimates of RUL.

A.7 Acknowledgment

The research presented in this paper has received funding from the Norwegian Research Council, SFI Offshore Mechatronics, project number 237896. The authors would also like to extend a special thanks to Cecilie Ødegård for her assistance during the experiments performed through this work.

Paper B

Condition monitoring of HMPE fibre rope using computer vision during CBOS testing

Shaun Falconer, Geir Grasmo and Ellen Nordgård-Hansen

This paper has been published as:

S. Falconer, G. Grasmo and E. Nordgård-Hansen. Condition monitoring of HMPE fibre rope using computer vision during CBOS testing. In *Exploring Opportunities - Synthetic/Steel - Proceedings of the OIPEEC Conference 2019, The Hague, The Netherlands*, pp 129-147, 2019. ISBN: 978-1-7336004-0-8.

Condition monitoring of HMPE fibre rope using computer vision during CBOS testing

Shaun Falconer*, Geir Grasmo*, Ellen Nordgård-Hansen**

*Department of Engineering Sciences
University of Agder
NO-4876 Grimstad, Norway

**NORCE Norwegian Research Centre AS
NO-4876 Grimstad, Norway

Abstract – The paper details the results of recent cyclic-bend-over-sheave (CBOS) experiments performed at the Mechatronics Innovation Lab (MIL) located at the University of Agder, Norway. A method for measuring diameter and elongation of discrete sections of fibre rope using computer vision is detailed. Estimations of the change in roundness of the rope are also explored based on the diameter measurements. These measurements are then assessed for their suitability as condition indicators.

B.1 Introduction

Fibre ropes are increasingly finding use for deep sea lifting operations in the offshore sector due to their similar mechanical properties when compared to steel wire ropes at equivalent diameters. However, due to the lighter weight and almost neutral buoyancy of HMPE fibre rope, they can theoretically be used to reach greater depths than steel wire which must support for its own weight subsea. Additional benefits of HMPE fibre rope use include potential use of smaller cranes and vessels due to their greater ease of handling and lighter weight. The main problem with HMPE fibre rope used for deep sea lifting operations is the conservative retirement criteria used when deciding on replacement.

Current standards provided by DNV-GL related to the retirement criteria of fibre ropes used in the offshore sector are predominately centred around mooring of vessels and platforms with only minor mentions of fibre rope used under CBOS regimes. In DNV-RP-E304 [6], detailed methods for damage assessment in fibre ropes used in offshore mooring are specified, which take close inspection of the various constituent substructures in a rope into account when deciding upon any potential recertification or retirement. Similarly, the standard CI 2001-04 [10] developed by the Cordage Institute, provides a comprehensive guide to visual inspection of fibre ropes and additional considerations to take in terms of retirement criteria. A natural extension of visual inspection of fibre ropes is the application of computer vision to perform the assessment currently done by offshore inspectors or as part of a built-in monitoring system for a crane. Additionally, DNV-GL-OS-E303 [7] specifies that if a rope is subjected to a tension level exceeding 70 % MBS (maximum break strength) it has to be recertified or removed from use. As such, DNV-GL-ST-E407 [9] states that the constituent fibre rope used in a deployment and recovery system must have a detailed overview of its physical properties, as well as failure modes, in order to be certified.

In terms of HMPE rope visual inspections, Heins et al [140] provide a detailed summary of the damage mechanisms that can occur in a sample of HMPE rope. They also provide a scale of abrasion as

a condition indicator, which they then attempt to link to the residual life of the rope.

In terms of CBOS testing of fibre ropes, experiments have been performed recently on smaller ropes used as tendons for cable-driven parallel robots up to the much larger scale tests for rope to be used in cranes. Davies et al [47] propose a model based on experimental CBOS testing of ropes to failure that is used to derive an expression to estimate the lifetime of a fibre rope subjected to cyclic loading. Horigome and Endo [91] investigate the repetitive bending behaviour of fibre ropes at a smaller scale and compare their lifetime results to those of stainless steel wire.

With respect to investigation of diameter measurements, elongation and rope shape there have been some recent patents submitted incorporating these properties. Van Der Woude and Zijlmans [136] proposed correlating the physical measurements along the length of rope, including an example that the measured diameter of a steel wire rope can be related to position along a rope. Additionally, another patent by Ilaka and Zerza [104] makes use of a clamping roller set up that transfers the measured diameter to a position sensor via rotary axle and lever. The rope is classified in different sections where user-defined discard criteria is established that will result in warnings being sent to operators if the limits are breached. Position sensors are also included to measure changes in length of the rope along with diameter changes.

This work is an extension of previous experiments performed using computer vision to monitor tension-tension tests [141] but adapted to monitor a fibre rope subjected to CBOS motion. Computer vision algorithms are used to detect the diameter and elongation changes of discrete sections of a fibre rope. The diameter changes are then used to estimate how the shape of the rope changes through the course of the CBOS regime. The elongation and diameter changes are interpreted as strain and relatives changes respectively, which are then investigated for their suitability as condition indicators.

B.2 Experiment Set Up

B.2.1 Equipment

The following subsections outline the equipment used in the experiment along with their main features and properties.

B.2.1.1 CBOS test machine

The CBOS test machine used to perform the experiments was installed and commissioned by DEP Engineering in 2017 and is located at the Mechatronics Innovation Lab, Grimstad, Norway. The main features of the machine are detailed in Table B.1.

Table B.1: General properties of CBOS machine.

Test sheave diameter (mm)	800
Driving sheave diameter (mm)	1000
Maximum line pull (kN)	150
Rope diameter range (mm)	20-30
Dimensions (m)	12 x 1.3 x 2.2
Cycle speed (m/s)	1

Tension in the rope is maintained by a hydraulic cylinder that adjusts the position of the test sheave as the rope elongates through the testing regime. The rope is attached via two clamps at a trolley that is cycled back and forth due to the motion of the driving sheave. This motion is maintained until failure occurs in the rope.

B.2.1.2 Machine vision cameras

The machine vision set-up comprised of five cameras in total. Five cameras were used to give a detailed in any potential changes in shape from different perspectives around the rope. Four of these cameras were the Edmund Optics EO-13122C Colour USB 3.0 model and the final was the Basler acA1300-200uc Colour USB 3.0 model. The specifications for the EO and Basler models are listed in Table B.2. The cameras were placed in an asymmetric fashion around the rope, with varying distances from the rope. The ratios applied to each camera measurement to convert form pixels to millimetres was achieved by calibrating the image with a same-sized object.

Table B.2: The Basler acA1300-200uc Colour USB 3.0 and EO-13122C Colour USB 3.0 camera specification.

Manufacturer	Basler	EO
Model	acA1300-200uc Colour USB 3.0	13122C Colour USB 3.0
Maximum frame rate (fps)	203	169
Resolution (MP)	1.3	1.3
Pixels (H x V)	1280 x 1024	1280 x 1024
Pixel size (μm)	4.8 x 4.8	4.8 x 4.8

B.2.1.3 Distance measuring laser

A Fluke 414D Distance Measuring Laser was used to monitor the position of the cylinder on the CBOS test machine as it compensated for the change in rope length as the test progressed. The basic specification is detailed in Table B.3.

Table B.3: Fluke 414D specification.

Typical measuring tolerance	$\pm$2.0 mm
Typical range	40 m

B.2.1.4 Webcam

A Logitech C922 Pro Stream Webcam was implemented to count the cycles of the CBOS machine based on the movement of the trolley to act as a trigger for the machine vision to start the recording process. A Texas Instruments MSP439F5529 USB Launchpad MCU was used to start the recording process on the five machine vision cameras based on the cycles counted due to trolley movement from the webcam.

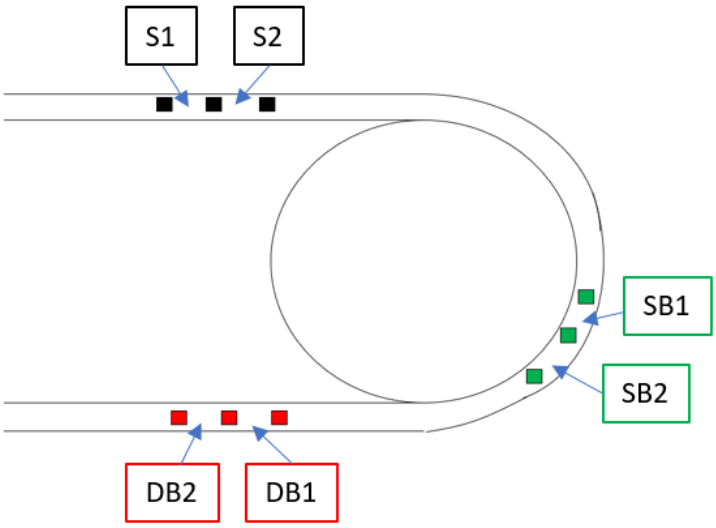

Figure B.1: Simple schematic of rope marking system on the rope with respect to the sheave.

B.2.2 Method

B.2.2.1 Rope sample and experimental conditions

The five cameras were set up around the rope to record video data of the rope as the test progresses. The rope is recorded at approximately every 1000 cycles for 2000 frames. This equates to recording between 12 and 13 cycles for during each sampling period.

The machine was configured to apply approximately 50 kN line pull on the rope through the test, which is equivalent to approximately 6.6 % of the rope MBS.

The rope type tested during the experimental run was a 28 mm diameter, 12 strand HMPE fibre rope.

B.2.2.2 Rope markings

The fibre rope is marked with three positions along the length of the rope to be tracked during testing. Each specific sub-section is the equivalent of a half lay-length, both of which are combined to estimate the whole lay-length. From the recordings, these specific sections are monitored such that any changes can be detected in the image processing phase performed after the data has been recorded as outlined in Section B.3.

The parameters S1 and S2, SB1 and SB2 and DB1 and DB2 represent the constituent subsections of the black, green and red markers respectively, see Figure B.1 for a schematic of the marking system. The black subsections were not subject to any bending whereas the green and red sections were situated approximately in the single and double bend zones respectively.

B.3 Image Processing

The image processing phase is performed using algorithms developed in Python 3.6.4 with OpenCV version 3.4.2. Figure B.2 shows an example of the combined diameter and elongation detection algorithm

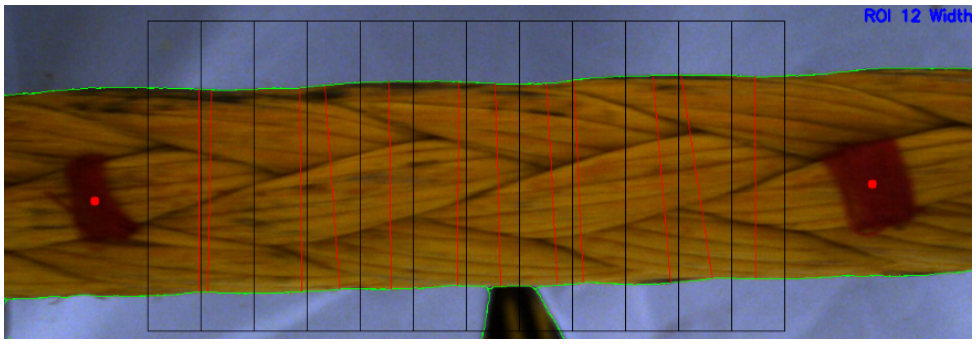

Figure B.2: Example image of the rope with both elongation and diameter algorithms implemented.

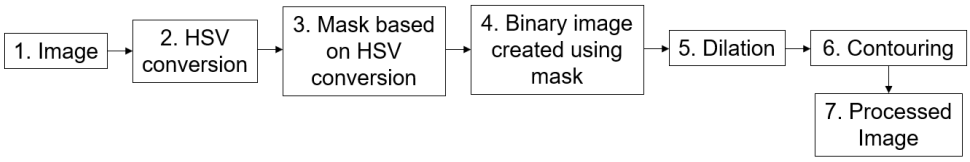

Figure B.3: Elongation calculation pre-processing flowchart.

implemented onto an image of the rope. The following subsections highlight the various steps in each algorithm, including background theory.

B.3.1 Elongation calculation

The elongation of the discrete section of the rope is found by recognition of the markers sewed into the rope at half lay length intervals. The process of detecting the length change is as follows: HSV colour conversion, a mask is found based on colour, mask applied to HSV image to create binary image, dilation of section, contours found in sections, centre points found using Green's theorem and finally distance between points found. A general overview of each morphological operation applied to the image is summarised in Figure B.3. One frame is selected from each recording and is used to calculate the elongation.

Python OpenCV makes use of Blue, Green, Red (BGR) as a default colour representation and is converted to Hue, Saturation, Value (HSV) colour representation to apply the thresholding algorithm to produce the binary image. In BGR representation, each pixel is a discrete value of 0 to 255, which are modified to produce different colours based on these combinations. In HSV, the Hue parameter is pure colour represented by the dominant wavelength with a value between 0 and 360 degrees, for example 0, 120 and 240 degrees represent the Hue values for red, green and blue respectively. This colour conversion is chosen for ease of creating colour search bands to find the different coloured markers sown into the rope.

Once HSV colour conversion is completed, a binary image is created based on the colour mask the algorithm is modified to search for. An example of what the detected marker looks like after this operation is shown in Figure B.4(b). Converting the original image to a binary image based on colour will mean there are two clear areas representing the markers in the image that can be easily found when detecting their centre points later in the algorithm. The white area of this image is the detected marker, which is shown to have some smaller undetected portions. These small portions are then then filled in using

Figure B.4: Elongation algorithm process (left to right): (a) original image, (b) binary image based on colour mask, (c) dilation and (d) processed image with centre point found based on contouring.

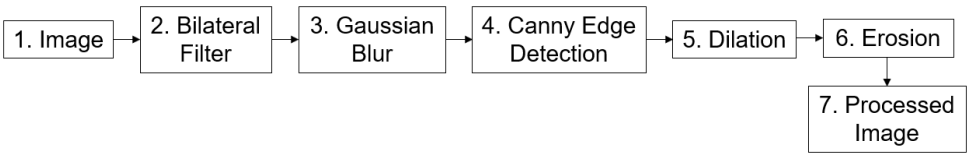

Figure B.5: Diameter detection pre-processing flowchart.

the dilation to create a solid as shown in Figure B.4(c), to ensure that there is a solid area to detect its centre point.

Contours are then found around the dilated area representing the marker, which is done through a built-in function in OpenCV via the Border Method as specified by Suzuki and Abe [139]. This is selected for its ease of finding the contour around the white areas, that form the enclosed curve required for Green's theorem to be applied in the next step.

After the contours are found, OpenCV makes use of Green's Theorem to find the moment of the enclosed area by the contour. This was chosen as it is a simple method of finding the centre point of the marker that will be used in the elongation measurements.

The result of applying this sequence of morphological operations is shown in Figure B.1(d), where the centre point of the area is shown. The distance between these two centre points on the rope as shown in Figure B.2 is used to monitor the elongation in a specific subsection.

B.3.2 Diameter calculation

The algorithm for detecting the diameter of the rope is performed through the application of several filters to identify the rope. The pre-processing stages of the rope images are shown in Figure B.5: a bilateral filter, Gaussian blurring, Canny edge detection, dilation and erosion.

The edges of the rope are found using a combination of the image smoothing filters built in to OpenCV. These functions are particularly useful in edge detection. Firstly, a bilateral filter is applied to the original image. The bilateral filter is described in detail by Tomasi and Manduchi [142] but it can be summarised as a method for smoothing images through replacing the intensity of a single pixel in the image with a weighted value from the nearby pixels, therefore allowing detection of the rope shape against a different coloured background. There is a white background behind the rope, therefor this contrasts significantly with the yellow coloured rope, which means the line should be detected with ease and made more prominent. The result of this operation in shown in Figure B.6(b).

Another form of filtering used for edge detection is Gaussian blur. In this method however only, a neighbourhood of pixels are taken into consideration (i.e defined by the kernel size), where they are

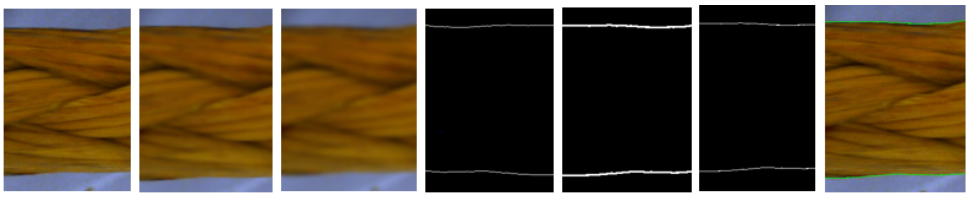

Figure B.6: Diameter calculation algorithm process (left to right): (a) original image, (b) bilateral filter, (c) Gaussian blur, (d) Canny edge detection, (e) dilation (f) erosion and (g) processed image with edges detected on original image.

weighted based on a Gaussian function and based on the output. As the rope is made up of strands, the bilateral filter may count these as lines, therefore a Gaussian filter is applied to generalise the image more so that the rope shape is more prominent.

This image is then put through a Canny edge detection built into OpenCV, which is described in detail by Canny [143], to mark out the lines that constitute the edges of the rope as shown by Figure B.6(d). This is then followed by a dilation of the image in Figure B.6(e), where these lines are made bolder then followed by an erosion operation to form the final line to be processed in the diameter algorithm as shown in Figures B.6(f) and B.6(g) respectively.

The top and bottom lines of the processed image are saved as a series of coordinates which are separated in twelve separate regions of interest. Within each area of interest, the shortest distance between each edge is found. The average of these values is the used as the diameter measurement in this specific section.

B.3.3 Roundness calculation

The roundness of the rope is estimated through the combination of diameter measurements from five different perspectives to serve as a basic geometric estimate of the rope shape. Five points are taken initially and reflected in the y-axis to create ten points. These ten points are then reflected in the x-axis to create ten coordinates that are used as the boundary to calculate the roundness of the rope. An example of the progression of the method is shown in Figure B.7.

Using the coordinates based on the diameter measurements, both the perimeter and the area of the formed shape are calculated-along with the average radius based on the length between the coordinates to the origin. Using these parameters, the roundness can be estimated with the following equation.

$$R = \frac{A_o}{P}\frac{2}{\bar{r}} \tag{B.1}$$

Where R is the roundness shape factor, A_o is the cross-sectional area, P is the perimeter and $\bar{r}$ is the average radius. The calculation is based on a circle, where 1 indicates perfects roundness and any decrease is seen as a reduction in roundness.

B.4 Results

B.4.1 Rope breakage

The three rope specimens failed after the following amounts of cycles detailed in Table B.4.

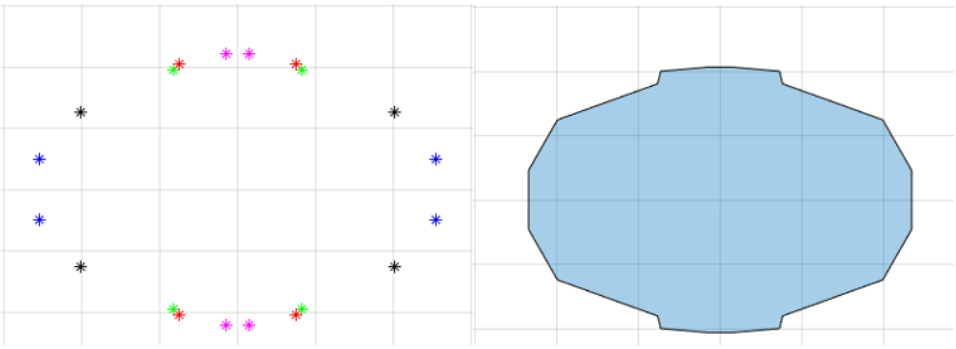

Figure B.7: A collection of coordinates that form the outer shape of the rope (left) and the polygon which is used to calculate the perimeter and cross-sectional area for the roundness shape factor.

Table B.4: Number of cycles to failure in each test.

Rope number	Number of cycles to failure
1	57,672
2	45,944
3	44,925

B.4.2 Elongation

Figure B.7 displays the strain measurements for each subsection in Rope 1, Rope 2 and Rope 3. The strain is calculated using the following expression for calculating strain based on length changes:

$$\epsilon = \frac{\Delta L}{L_o} \tag{B.2}$$

Where ϵ is engineering strain, ΔL is change in length and L_o is the original length after set-up. The results are displayed as percentages based on the observations of the changes at each specific section from the computer vision system. The original lengths of each subsection across the three rope specimens are detailed in Table B.5.

Table B.5: Original measurements of length (mm) in each subsection for Ropes 1, 2 and 3 .

Rope	S1	S2	S_{LL}	SB1	SB2	SB_{LL}	DS1	DS2	DS_{LL}
1	94	95	189	99	92	191	93	94	187
2	96	96	192	93	95	188	95	100	195
3	98	92	190	97	97	194	97	96	193

It is worth note the final readings displayed in Figure B.9 vary slightly from the final rope failure values denoted in Table B.5 due to discrepancies in the recording system.

The measurements displayed for Rope 1 in Figure B.8 (top chart) were taken at approximately 57,000 cycles.

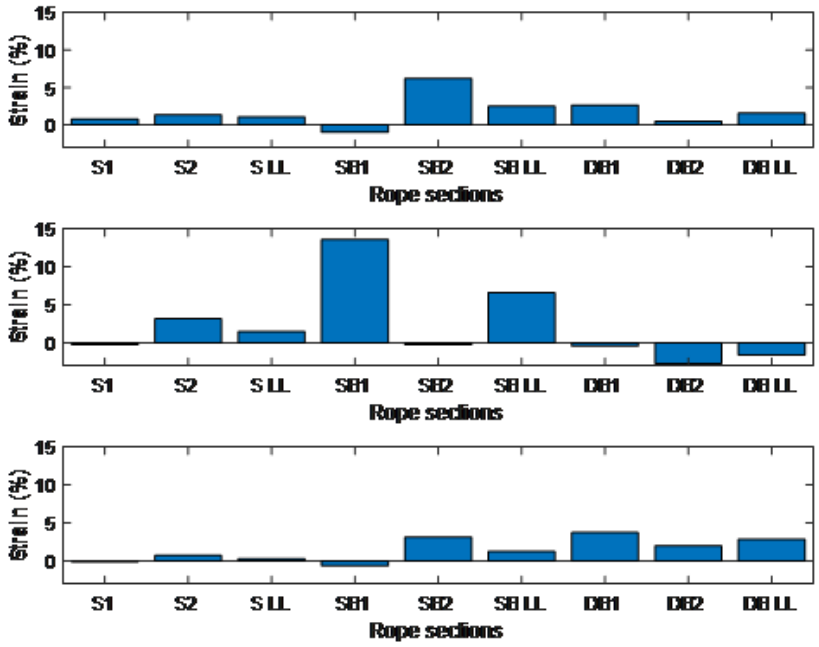

Figure B.8: Strain measurements based on differences between first and final elongation in Rope 1 (top), Rope 2 (middle) and Rope 3 (bottom).

The measurements in Rope 2 in Figure B.8 (middle chart) for positions S1, S2, SLL, SB1, SB2, SBLL were taken at approximately 45,000 cycles. The final elongation reading in Rope 2 for sections DB1, DB2 and DBLL was taken from the second last recording due to the abrasion on the rope making the markers undetectable by the elongation algorithm.

The measurements in Rope 3 in Figure B.8 (bottom chart) were taken at approximately 33,000 cycles. No more readings were taken after this point until failure due to malfunctioning recording equipment during this phase of the test run.

B.4.3 Diameter

Figures B.10, B.11 and B.12 display the relative changes in diameter size as a percentage at each subsection across the three rope specimens between the start and end readings in the test.

Figure B.13 shows a timeseries of the change in relative size of diameter for Rope 1.

B.4.4 Roundness shape factor

The roundness measured for Rope 1 as the test progresses is shown in Figure B.14.

B.4.5 Cylinder extension

Figure B.15 shows the change in extension of the cylinder from the start to the end of the test over the three ropes used in the experiments.

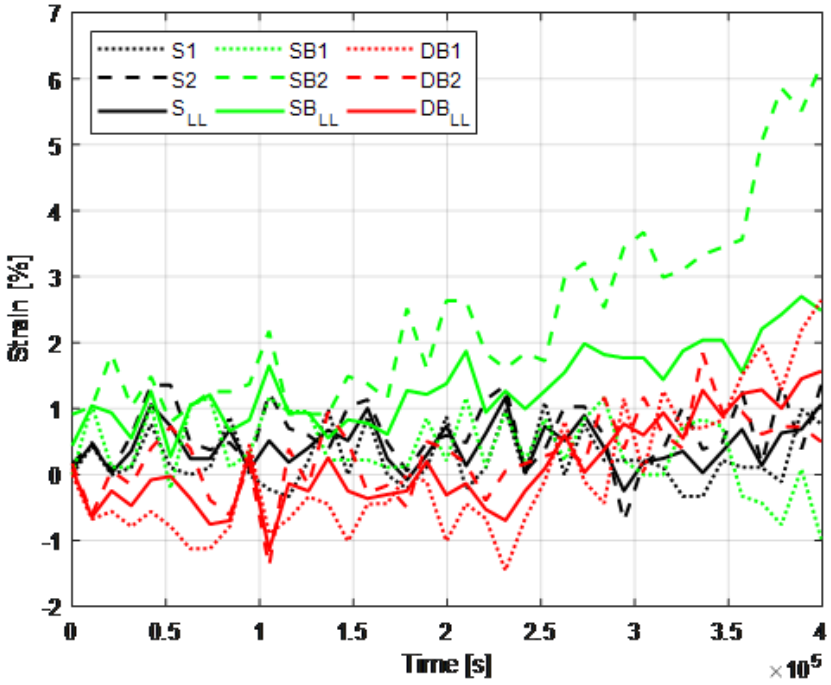

Figure B.9: Strain measurement due to elongation progression in Rope 1.

B.5 Discussion

B.5.1 Elongation

It is clear from the strain readings due to elongation in Figure B.8 that there have been heterogenous changes across all the sections monitored in the rope. Given the different readings across all sections each of the three rope specimens, the elongation occurring in the rope during testing is assumed to be localised rather than uniform throughout the rope. While the sections pertaining to the different colours are not located at the same positions along the length of the rope, they are placed in similar general vicinities and subjected to similar bending regimes on the sheave.

The original measurements for the length between the markers in each respective subsection are outlined in Table B.5.

The black subsections, S1 and S2, are closer to the trolley where the rope is attached in the machine and is not subjected to any bend on the sheave. The length of these two subsections sees consistent small changes across all three rope specimens apart from subsection S1 in Ropes 2 and 3, which see slight reductions in length. However, the overall lay length increases across all three rope specimens.

Similarly, the lay length that is a combination of SB1 and SB2 shows an increase over all three rope specimens, but some negative strain is shown in the SB1 readings in Ropes 1 and 3 and SB2 in Rope 2. The first and second largest strains calculated in an individual subsection occur at SB1 in Rope 2 and SB2 in Rope 1 respectively. This section of the rope contacts the sheave and is subjected to more bending than the black section.

Finally, the red section sees an increase in the overall lay length of the section in Ropes 1 and 3 but is shown to decrease in Rope 2.

The uncertainty is calculated at approximately between 2 and 3 mm based on the initial measurement

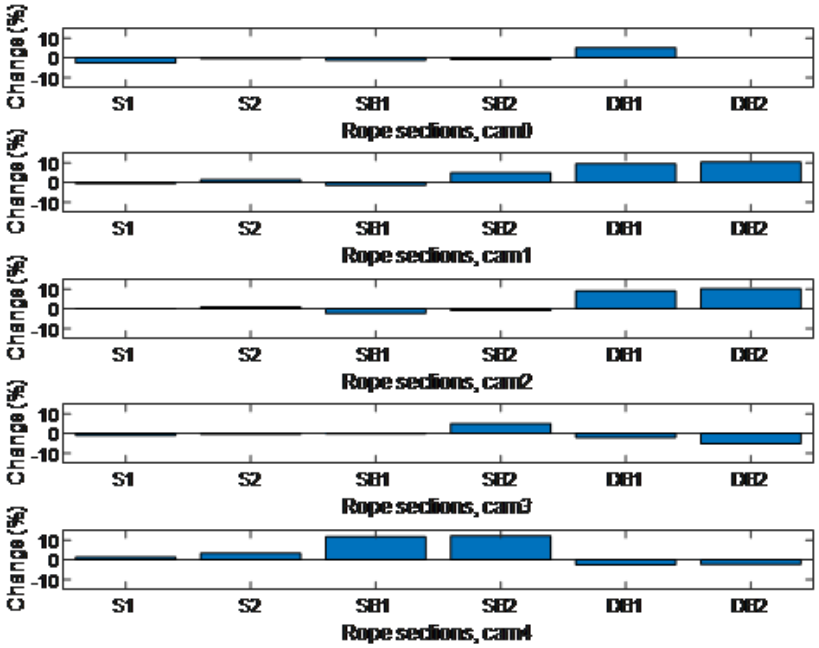

Figure B.10: Rope 1 relative change in diameter readings from the start and the third last recording (around 54,000 cycles) according to all five cameras.

of the lay length distances using callipers and the conversion between pixels to millimetres. Any change detected above this range can be assumed to be significant.

Figure B.9 shows how the strain measurements change across all subsections in Rope 1 as the test progresses. The highest increases in elongation are shown in subsection SB2 were the increase exceeds 6 % when compared the original measurement for the subsection. Increases are seen across all strain measurements when comparing the start and end measurements apart from subsection SB1, where a slight decrease in length is shown to occur. Much like the results shown in Figure B.8, there are differences in the strain to time series measurements. In all the ropes, there has been increases in the lay length measured in the green section, whereas in the red section there was little change in the Rope 2 compared to the other specimens. As the sections are not at the same positions, only in the same general areas, this could contribute to some differences in the measured values.

The areas in contact with the sheave show greater changes in measured strain. In all specimens the rupture occurred in areas of the rope that were in contact with the sheave, which can be seen from the measurements in the green and red sections. While strain measurements do have potential as a condition indicator in fibre rope condition monitoring, there is some discrepancy in what amount of strain can be experienced consistently before rupture in the rope. For example, in subsection SB1 in Rope 2, a strain reading exceeding 10 % is measured at approximately 100 cycles before failure, whereas in a similar section in Rope 1, the value just before failure is shown to be around 5 %.

Figure B.15 shows the elongation of the cylinder from the start until the end of the test in all three rope. Across all tests there is a steady extension of the cylinder, indicating that there is an overall increase in the length of each respective rope. Rope 2 shows a slightly larger increase overall compared to Ropes 1 and 3 but these differences are minute when the whole length of the rope is taken into consideration.

Other potential influences on the measurement of elongation using this method include the degra-

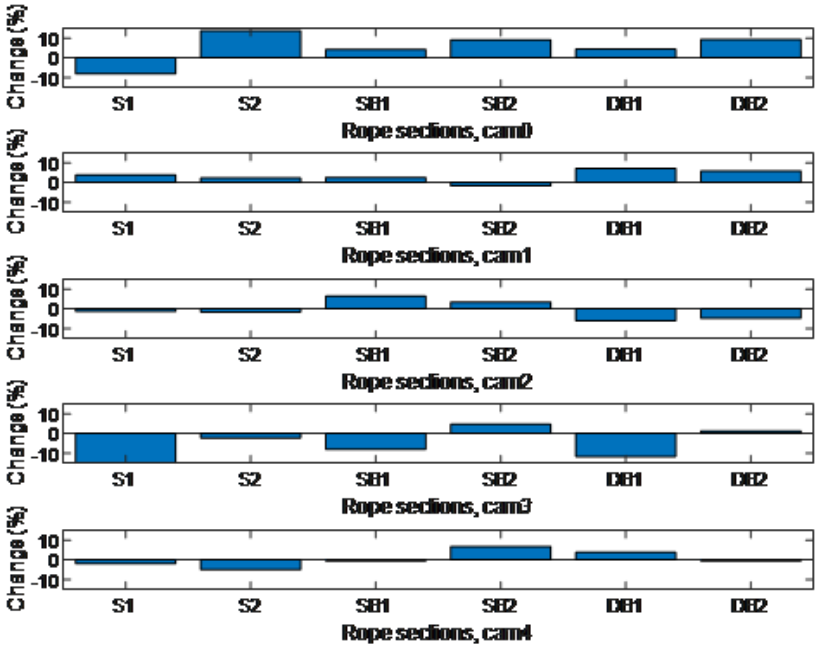

Figure B.11: Rope 2 relative change in diameter readings from the start and finish according to all five cameras.

dation of the markers sewed into the rope. As the algorithm relies on finding the centre point of this different coloured material on the surface of the rope, any potential damage to the marker could result in slightly different centre points being detected, altering the length calculated. Additionally, as the rope deteriorates through the test, it is noticed that the rope's position with respect to the camera changes marginally, also impacting the measurements detected by the camera. While such behaviour would decrease the accuracy of the measurements, any significant unexpected alterations in measurement would serve as a sign that the rope must be inspected. These factors would influence the measurements, meaning some of the observed heterogeneous results would be due to these uncertainties in the method.

B.5.2 Diameter

Figures B.10, B.11 and B.12 show the relative diameter changes as a percentage between the first and last measurements in Rope 1, Rope 2 and Rope 3 respectively. Initial observations suggest that the spread is heterogenous with equivalent subsections across the three rope specimens measuring varying increases or decreases in diameter.

The increases and decreases in diameter can be attributed to two factors throughout the progression of the experiment. Firstly, the groove shape would have an impact in combination with the tension applied by the cylinder which would have significant influence on the shape of the rope, which may increase or decrease the diameter depending on which perspective the camera is viewing the rope. Additionally, the sheave used in the experiments has also been used in CBOS testing for steel wire ropes, from which it has accumulated dents that could cause further damage to the fibre rope. The second factor that influences the diameter detected is due to how the diameter measuring algorithm detects the rope when there is progressive damage done to the rope via several damage mechanisms such abrasion against the

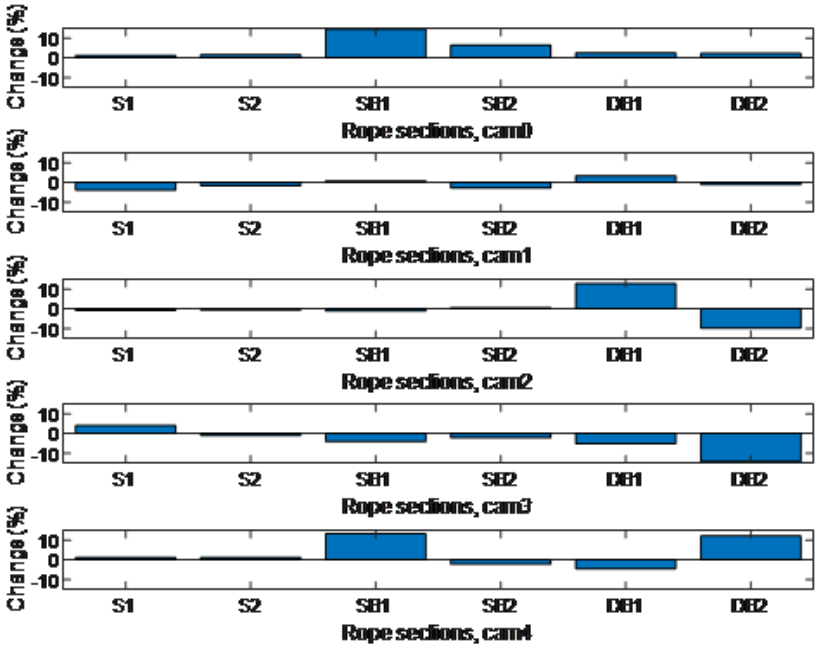

Figure B.12: Rope 3 relative change in diameter readings from the start and finish according to all five cameras.

sheave, the internal friction due to bending in the rope and continuous stress from line pull exerted by the cylinder. As the test progresses there is an abundance of extruded loops as the individual rope strands are damaged but also changes in the appearance of the rope, meaning that the algorithm could detect both larger and smaller diameters than exists in the rope.

Figure B.13 shows a time series from the start to finish of the test with the diameter readings from all five cameras situated around Rope 1. Cameras 1 and 2 show an increase in relative diameter when compared between the start and finish of the test and a decrease is shown in cameras 3 and 4. The readings from camera 0 are shown to be erratic with significantly fluctuating values throughout the test. Given the position of the camera directly under the rope and facing the part of the rope in direct contact with the sheave, an increase in diameter should be expected due to the compression of the rope against the sheave. However, as damage occurs in the rope, the algorithm begins to pick up both shorter lengths in this cross section due to changes in the "look" of the rope, affecting the overall average diameter detected in the subsection. The abrasion damage in the rope also creates extruded loops which are picked in the algorithm and contribute to more inaccuracies in the readings. There are also issues with the lighting used on the rope, as some of the images were darker, particularly as the test was run overnight, making some outlines of the rope difficult to detect.

There is mixed potential in using diameter measurements as a condition indicator when using this specific algorithm as the damage incurred in the rope creates fluctuating values. However, while the algorithm shows a significant "increase" in diameter for some subsections of the rope when there is no increase, can serve as a warning for extruded loops occurring due to strand damage due to abrasion accumulated through use. The algorithm could be modified to ignore certain lengths if they are shown to be a significantly larger value than the measurements previously recorded.

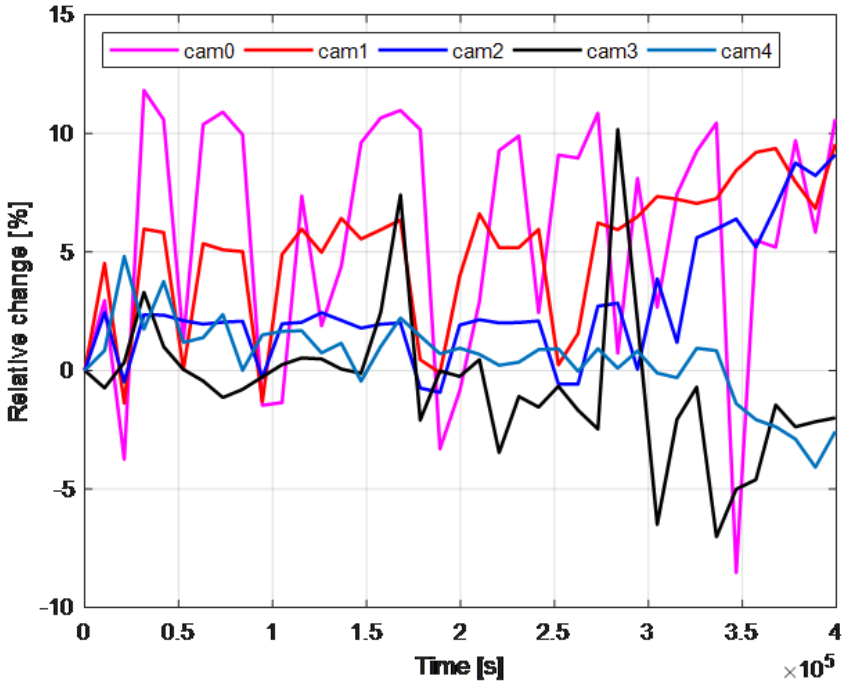

Figure B.13: Relative diameter change in Rope 1 at each position across the test timespan.

B.5.3 Roundness shape factor

Figure B.14 shows the estimated roundness detected of the specific subsections in Rope 1 throughout the test. The top graph represents readings in the black section, which do not come into contact with the sheave groove. The measurements in this section are shown to be more stable than in the other subsections despite the fluctuations in the diameter measurements as highlighted in the previous section.

Measuring the shape via the use of polygons made up from the coordinates provides a general idea of how the rope changes shape through the test. An ellipsis cannot be applied given the variation in spread of the points.

There is shown to be a decrease between the initial and final roundness measurements shown in the green and red sections which are displayed in middle and bottom graphs in Figure B.14, respectively. The readings here are more erratic compared to the top graph for the black section. Both the green and red sections are in contact with the sheave during the cycling motion in the test machine. These sections are heavily affected by the bending cycle, which could be due to a multitude of damage mechanisms such as the stress exerted through the line pull, abrasion against the dented sheave and heating from friction in bending. As these measurements are based ultimately on the average radius measurements affected by the issues outlined in Section 5.2, there will be slight fluctuations in the readings.

Additionally, when compared to diameter, the shape factor has less value as an indicator. It is shown to have a low sensitivity to variation and does not change drastically through the tests.

Much like the diameter measurements, the roundness could be used to indicate that there is a deterioration in the structure of the rope due to the presence of extruded loops or worn out strands. As an example, the black area which does not contact the sheave has a distinctly more stable reading and does not have the same levels of damage progression through the test as the green and red sections. The fluctuation in these readings could serve as a warning that the rope must be at least visual inspected for damage.

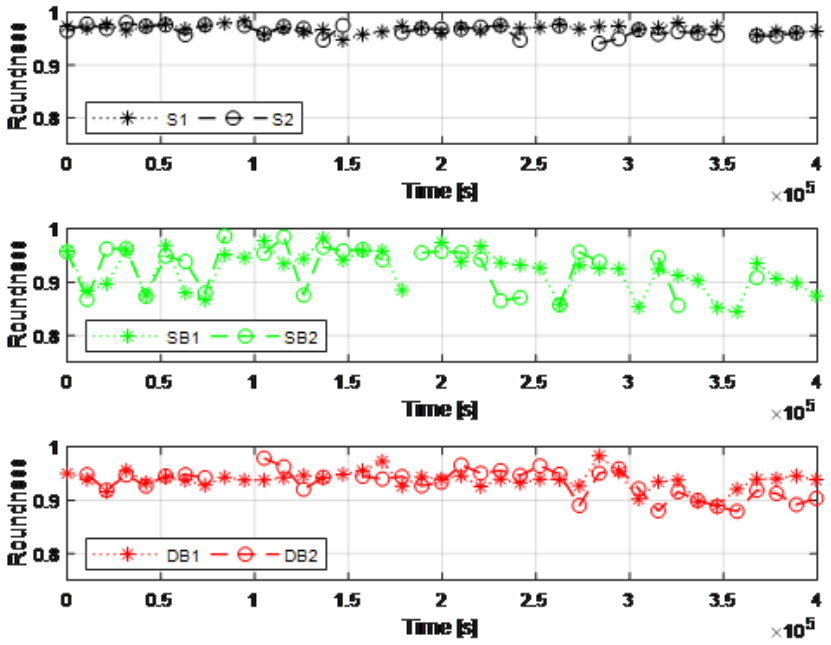

Figure B.14: Roundness estimates in Rope 1 with respect in the S1 and S2 regions (top), SB1 and SB2 regions (middle) and the DB1 and DB2 regions (bottom).

B.6 Future Work

Future testing will also include the use of thermal camera recordings of the rope in conjunction with the computer vision system. With a combination of the elongation measurements, thermal measurements and a modified algorithm to detect the damage incurred by the sheave (i.e worn strands and extruded loops), it may be possible to implement into a deep learning model that can be used to predict the remaining useful life of the rope subjected to the CBOS regime in the machine.

Also, other type of rope will be tested to develop a general model and to validify the method on a different subject. Finally, different cycling regimes could be used in testing machine. Parameters such as the line pull exerted by the cylinder in the machine could be modified and the tests could be paused at different intervals to see if the rope benefits from cooling or the rest from motion.

B.7 Conclusion

There is potential in the use of computer vision for condition monitoring of fibre ropes as it is shown that elongation can be easily detected using a marking system of a different colour to that of the rope. Elongation has shown potential as a condition indicator for the fibre rope as the subsections monitored in this round of testing show significant changes as it progressed towards failure. The diameter and the roundness measurements based on the diameter have been shown to have mixed potential as a good condition indicator based on the current algorithm.

In general, computer vision can be used to detect all these different parameters but given that the changes are unevenly distributed along the rope, they are quite challenging to use for maintenance.

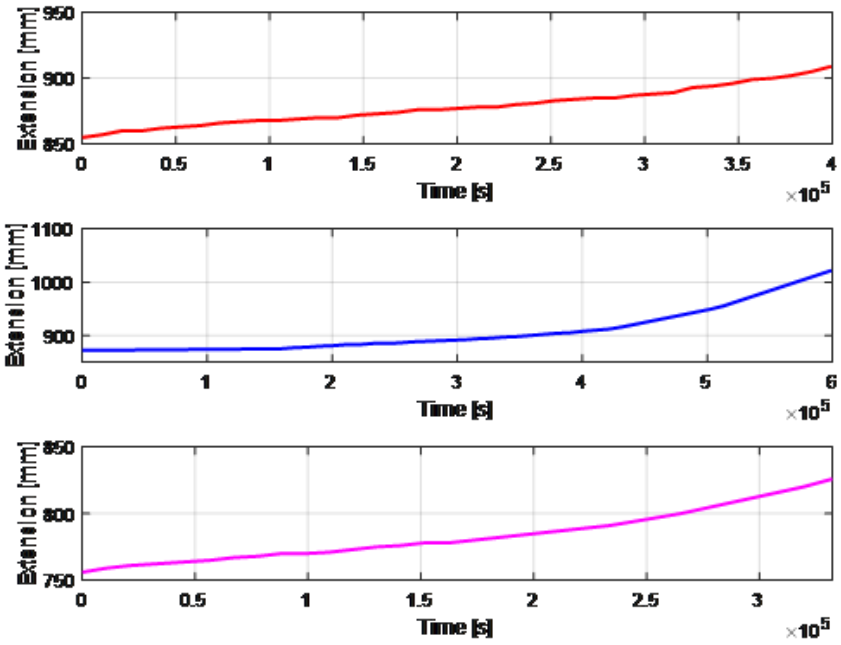

Figure B.15: Cylinder extension in Rope 1 (top), Rope 2 (middle) and Rope 3 (bottom).

B.8 Acknowledgements

The research presented in this paper has received funding from the Norwegian Research Council, SFI Offshore Mechatronics, project number 237896. The authors would also like to extend an extra special thanks to Benyamin Akdemir for his assistance in creating the experiment set up and his insight into the use of machine vision cameras.

Paper C

Computer vision and thermal monitoring of HMPE fibre rope condition during CBOS testing

Shaun Falconer, Ellen Nordgård-Hansen and Geir Grasmo

This paper has been published as:

S. Falconer, E. Nordgård-Hansen, G. Grasmo. Computer vision and thermal monitoring of HMPE fibre rope condition during CBOS testing. *Journal of Applied Ocean Research*, 102, 102248, 2020. doi: 10.1016/j.apor.2020.102248

Computer vision and thermal monitoring of HMPE fibre rope condition during CBOS testing

Shaun Falconer*, Ellen Nordgård-Hansen**, Geir Grasmo*

*University of Agder
Department of Engineering Sciences
Jon Lilletunsvei 9, NO-4876 Grimstad, Norway

**NORCE Norwegian Research Centre AS
Jon Lilletuns vei 9 H, NO-4876 Grimstad, Norway

Abstract – Fibre rope usage in deep sea lifting operations is gaining more prominence in recent times. With rope minimum break loads (MBL) comparable to that of their steel wire counterparts, the use of high modulus polyethylene (HMPE) ropes is seen as a viable option for use in subsea construction cranes. The ropes are worn out during use and visual inspection remains one of the main methods of determining whether a fibre rope is to be retired from use, therefore a natural extension is condition monitoring through computer vision. Creep and temperature are constraining with HMPE ropes and should be monitored continuously, particularly when the rope is cyclically bent over sheaves. Additionally, interpreting the thermal history of the rope during use could give insight into deterioration. In this paper, a condition monitoring system based on combined computer vision and thermal monitoring is used during cyclic bend over sheave tests performed on 560 kN break load of 12 strand braided HMPE ropes. New monitoring features such as local length and width through computer vision algorithms combined with surface thermal monitoring and global elongation are presented and their effectiveness as condition monitoring features is assessed.

C.1 Introduction

Fibre ropes are increasingly gaining recognition as a viable alternative to steel ropes for use in deep sea lifting operations. High Modulus Polyethylene (HMPE) ropes have been shown to have about same mechanical properties to those of steel ropes, but with other potential benefits and contraints. Due to its lighter weight and almost neutral buoyancy, HMPE ropes can be used in subsea construction cranes to exceed the depth limits imposed by steel rope usage. Additionally with their greater ease of handling and lighter weight, there is potential to use smaller cranes and vessels in lifting and subsea deployment operations.

The first issue with HMPE from an endurance perspective is failure by creep. The three main parameters that effect creep in HMPE ropes are a combination of the load, temperature and time of usage. Depending on the size of payload, type of lifting operation and environment where the lift takes place, the extent at which creep influences deformation behaviour in ropes can vary greatly. HMPE rope typically has a maximum working temperature of 65 °C, on which exceeding this limit will lead to deterioration of the material through temperature alone.

The second issue is failure through wear. Offshore lifting operations involve periods where active heave compensation occurs when deploying a payload subsea. The rope will be subject to cyclic bend over sheaves (CBOS), where it is continually driven back and forth over sheaves, the severity of which will be influenced by load size and sea state. In addition to heat generation from bending deformation, friction from both inter-strand motion and sheave contact will contribute to heat generation during operation. Due to the plethora of potential damage mechanisms that have potential to influence the remaining useful life (RUL) of the rope, condition monitoring for this regime requires particular attention through a combination of methods.

Fibre rope for usage in maritime operations is not a novel concept but their application to deep sea lifting operations is a fairly recent development. Applications in vessel and offshore structure mooring are detailed in current standards set by industry, however their application in lifting operations and associated discard criteria is mentioned briefly. DNV-RP-E304 [6] details how the damage of the fibre rope must be assessed, where each constituent substructure (i.e filament, strand, sub-rope, etc) has to be checked by manual inspection and then re-classified or discarded based on inspector judgement. CI 2001-04 [10] provides a thorough guide of fibre rope damage types and mechanisms for inspectors. DNVGL-OS-E303 [7] states that if a rope has been subjected to 70 % of its minimum break load (MBL), then the rope has to be retired or re-certified. DNV-GL-ST-E407 [9] requires that fibre rope used in deployment and recovery systems must have all its physical properties detailed, including potential failure modes, to be certified. Finally, the 3-T parameter developed by DNV-GL [8] is used to obtain a linear relationship between tension and time-to-rupture by evaluating the logarithmic time-to-rupture as a function of tension at a given temperature. However to investigate if longer RUL for deepsea lifting fibre rope is possible, a continuous means of monitoring with thorough data interpretation must be developed, rather than a simple re-classification or re-certification.

Extensive CBOS testing is beneficial to explore RUL. Davies et al [47] presented the results of testing on HMPE braided rope of 19 mm nominal diameter from which an empirical model for RUL was derived, though it is acknowledged that further testing is required on ropes of larger diameters to qualify their method for lifting operations.

Given that visual inspection is common for fibre rope, use of computer vision can potentially replace manual inspection. Hearle et al [81] used a webcam to monitor the strains in yarns during testing. Since machine vision technology has improved after their work, there were obvious limitations in the equipment used, but they showed the possible application of computer vision and image processing for fibre rope monitoring. Additionally, Ghoreishi et al [144] used computer vision and image processing as one of their three independent measuring systems for extensometry during tension-torsion testing to validate their analytical model of rope behaviour. For steel wire ropes, Söhnchen [82] details a system for visual inspection of ropeways and mining shafts from four different perspectives to analyse lay length, diameter, and wire breaks. Yaman and Karakose [145] proposed image processing for monitoring steel rope in elevator systems, where fault detection was performed by analysing the auto-correlation signals of pixels in the rope images to detect wire breaks.

Assessment of rope geometric parameters has been used in other fibre rope monitoring systems. For example, Mupende and Zerza [**?**] made a patent where the diameter of the rope for lifting operations is monitored using clamping roller set up and position sensor with a warning activated at a user-defined discard criteria, along with length change estimations. Van der Woude and Zijlmans [106] proposed as monitoring system for offshore lifting operations (using steel rope as an example), where the device can take cross-sectional area measurements and log its position along the rope. Ernst et al [146] also detail embedded methods for monitoring of elongation of discrete sections of fibre rope where bending occurs

in operation and replacing the rope subject to exceeding a pre-set limit.

Additionally, it is important to distinguish between the sections being monitored via some form of marking system throughout the length of the rope and monitor them for changes. De Angelis [85] proposes a system to replace fibre rope based on the deterioration of markers and evaluate them by visual inspection. In addition to this, Logan et al [86] detailed a patent for having markers on load bearing members for elevators such as rope, with the spaces between these markers being monitored for strain and fatigue.

Temperature measurement of fibre rope for lifting operations is of paramount importance due to material limitations in maximum temperature. Active heave compensation in offshore construction cranes will cause heat generation in the rope if a payload is held at the same depth subsea for extended periods of time. In terms of thermal monitoring of fibre rope, Törnqvist et al [20] analysed rope samples during CBOS testing with embedded thermocouples and an IR camera. However, both are mainly used to observe the effects of water cooling on the rope samples, in order to ensure that they do not reach critical temperature. In addition to this, Davies et al [41] include some results from IR camera during CBOS testing to try to couple rope properties and temperature changes, however references are only made regarding the change in temperature in ropes during dry and wet tests. Additionally, Nordgård-Hansen et al [37] explored the use of chemometrics as method for quantifying aging in fibre ropes based on infrared images recorded using some of the ropes tested as part of the campaigns outlined in this paper, including providing extensive review of possible explanations for observed changes as the rope deteriorates. De Angelis [69] proposed using a conductive thermal element and provides a warning to the user if a critical temperature is exceeded. More recently, Ning et al [36] used embedded thermocouples inside and outside of several different rope samples during CBOS testing by evaluating thermal damage through varying test conditions and its subsequent influence.

Manual inspection of rope without thorough knowledge of its use history has significant potential for waste through premature retirement. Deterioration in fibre ropes through CBOS deformations results in length, width and temperature changes that require monitoring throughout use. This paper builds upon previous work [141] performed at the University of Agder, where computer vision techniques were used to monitor rope width and length in tension-tension tests.

Improved monitoring systems are the first steps in developing more informed RUL estimations and subsequently avoiding fibre rope waste. Still, there is currently no single detailed study of a combined computer vision and thermal monitoring method for fibre ropes under a CBOS regime. In the present work, data is extracted through image processing algorithms to monitor changes in local length and width for fibre ropes. It has been confirmed that there is local motion of strands during usage, and the methods applied allow the continuous monitoring of this movement. The geometric data is combined with temperature measurements, which show corresponding changes over time. This work may therefore serve as the basis for a potential monitoring system to be implemented in an offshore crane.

Test details are given in Section C.2, and the algorithms from previous work have been modified, as presented in Section C.3. These algorithms are then applied to data recorded during CBOS testing. The results of local length, width and temperature monitoring in different bending zones in five ropes during CBOS testing are presented in Section E.4, and their effectiveness with regards to rope condition is discussed in Section C.5, before further work is considered and conclusions offered.

Figure C.1: CBOS test machine as located the MIL, Norway. View is from just behind the test sheave with the driving sheave visible at the far end of the test frame.

C.2 Monitoring methods and materials

The condition monitoring set-up and feature selection were evaluated on ropes during CBOS testing. The test machine used was installed by DEP Engineering at the Mechatronics Innovation Lab (MIL) in Grimstad, Norway, see Figure C.1. The machine is capable of testing both steel and fibre ropes between 20 and 30 mm diameters and can deliver a maximum line pull of 150 kN. The tension is kept constant by a hydraulic cylinder that extends as the test progresses to compensate for creep. The test and driving sheaves have diameters of 0.8 m and 1.0 m respectively. The test sheave is made from 42CrNiMo4 steel and has a U-profile.

The condition monitoring set-up consists of three parts. A computer vision system with four cameras asymmetrically positioned around the rope, was used to record videos of the rope next to the test sheave end approximately every 1000 cycles. Each camera recorded 2000 images in each video recording, which corresponds to 13-15 complete cycles. As seen in Figure C.2, the rope is not centered in the camera frame, due to the testing sheave being slightly angled.

A FLIR A6753sc infrared thermal camera recorded rope surface temperature periodically as the tests progressed. It was placed approximately 50 cm from the rope entrance to the sheave profile. The recording process was set to sample at 100 Hz for 2000 images, resulting in a 20 seconds video for each period. This was sufficient to record at least one full cycle in the CBOS test. The data was then interpreted using FLIR ResearchIR Max 4 software and then converted to CSV format.

Finally, an infra-red distance sensor monitored the increase in length of the CBOS machine hydraulic load cylinder over the duration of the test.

Further details regarding the specification of the optical cameras, thermal camera and distance mea-

suring laser are available in Appendix **??**.

The sections of the rope that never reach the sheave, thus never bends, is called the straight zone (SZ), while the rope section that touches the sheave and bends only once before the sheave changes direction is called the single bend zone (SBZ). Finally, the rope section that bends across the sheave and is straightened again below the sheave before the sheave turns, is called the double bend zone (DBZ). Colour coded markers were sewn into each of these zones, see Figure C.3. These markers were used to monitor the changes in local length at these positions, in addition to the widths. The thermal measurements were also taken from these zones.

The procedure was to guide the rope over both the driving and test sheave with the ends attached to opposite sides of the trolley that moves along the test bench between the sheaves. The spliced eye loops were placed over 56 mm diameter steel pins in the connector attached to the trolley to hold the rope in place. Care was taken to ensure there was minimal twist in the rope. The first 1500 cycles were used to bed in and as a "calibration" phase for the camera set-up, in which camera parameters where adjusted for lighting conditions and to ensure that good quality data was recorded automatically. After this phase, the test was run until failure. A failure was considered to occur when there was a substantial loss of tension on the cylinder, causing the test to stop automatically or when there was a more obvious rupture.

The ropes used were 12 strand Dyneema®DM20 XBO HMPE fibre ropes with nominal diameter of 28 mm and the minimum break load (MBL) was 560 kN. They were approximately 22.2 m long, spliced at each end over a 2.2 m length with eye loops, and tested on a constant 50 kN line pull over approximately 4.2 m stroke length.

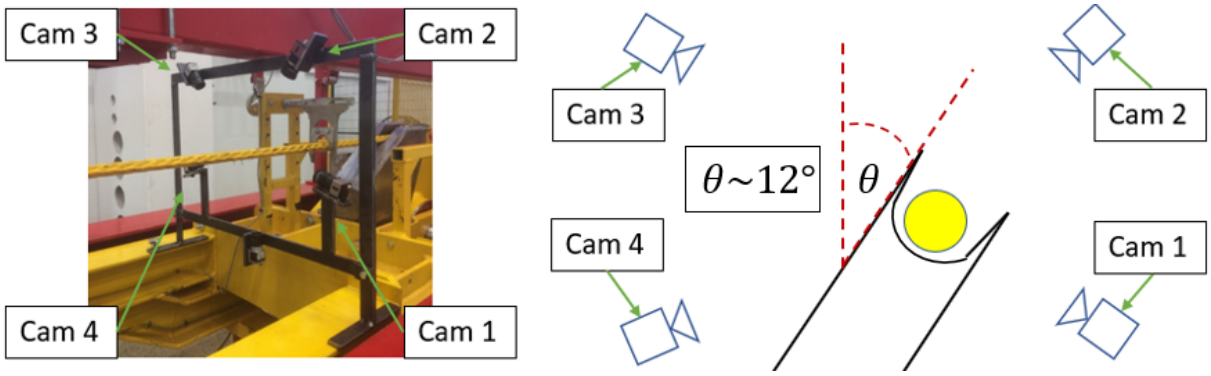

Figure C.2: The computer vision set up with the four cameras used positioned around the rope. The accompanying schematic shows the designated camera labels for each position and roughly how they are positioned with respect to the rope and sheave access.

C.3 Theory and data interpretation

C.3.1 Computer vision system and image processing

The algorithms used for image processing and data analysis were developed in Python using the OpenCV library [117]. The data is interpreted from videos recorded during each CBOS test. During a post-processing phase, a series of morphological operations were performed to calculate the local length and width of the rope.

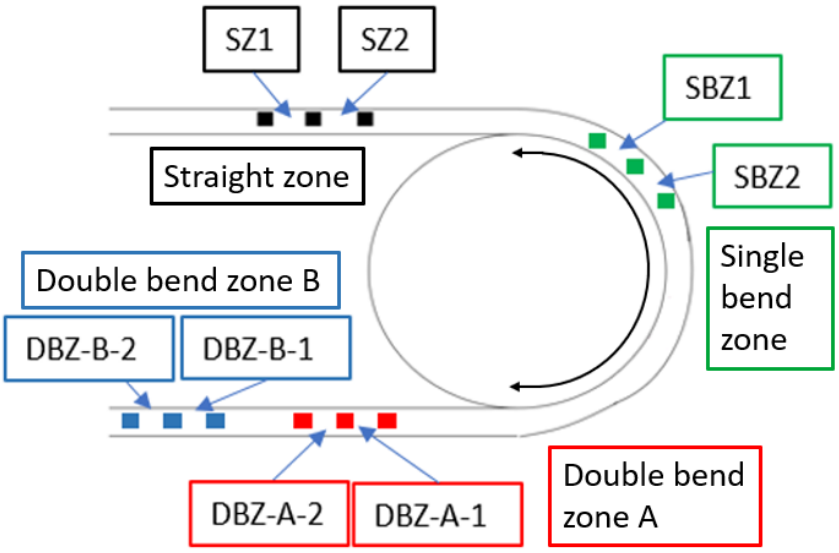

Figure C.3: The approximate location of the colour-coded markers placed on the rope for localised length and width monitoring.

C.3.1.1 Local length of rope sections

The local length of each subsection is calculated by locating the different coloured markers sewn into the rope. The image is converted to HSV colour scaling for ease of detecting colours at varying levels of brightness. A specific colour is selected using this colour regime ("red" in the case of the operations shown in Figure C.4). This scale is modified in the algorithm to detect the other colours coinciding with the other zones of interest on the rope. A binary image is created, where the sections of the image that coincide with the colour mask are converted to white. A dilation operation is performed to fill in the gaps in the colour mask and the marker centre points are found using a contouring operation. The Euclidean distance between centre points of both markers is then calculated. The operations are summarised in Figure C.4.

Figure C.4: Different stages and effects of morphological operations applied to the image to detect a specific colour for length measurements: (a) original image, (b) binary image created, (c) dilation operation applied and (d) final processed image with centre point of marker visible after contouring operation.

It is attempted to find at least ten images of each subsection in each video recording. The median, maximum, minimum and variation as standard deviation of the length across these images is calculated and are used as the values to represent the strain of the rope at that specific time stamp. These distances

are monitored for changes as the test proceeded.

C.3.1.2 Rope widths

Rope cross section width was calculated from the perspective of all four cameras. The width calculation works in a similar fashion to the length algorithm, except it is the rope colour that is detected in the processing stage. The widths along the whole length of rope visible in the computer vision system are calculated at the SZ, SBZ and DBZ sections.

As with the local length calculation process, the image is converted to HSV representation, however the colour of the rope is searched to distinguish it from the background and the different coloured markers. The image is then dilated to fill in any gaps that may be present and eroded to better coincide with the edges of the rope. Finally, the edges of the rope are detected using a contouring operation which is then applied to the original image. Images of selected operations are shown in Figure C.5.

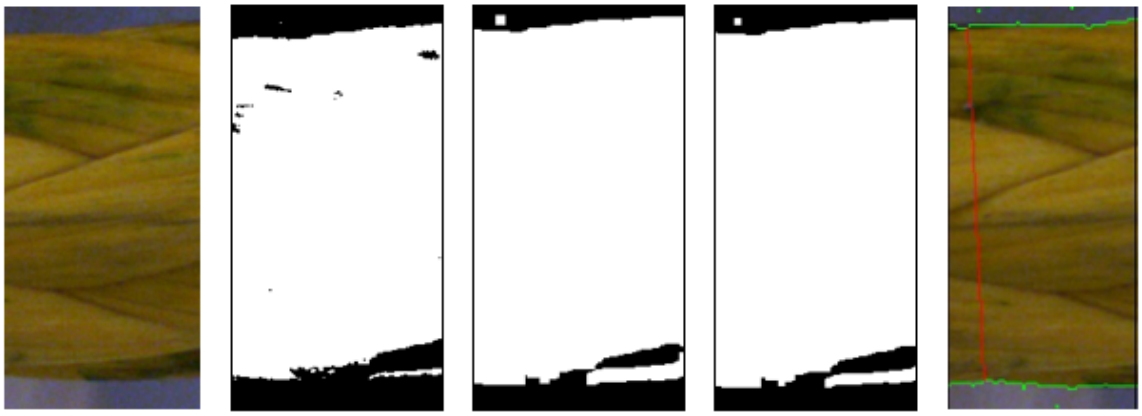

Figure C.5: Different stages and effects of morphological operations applied to the image to detect the rope and calculate the width: (a) original image, (b) binary image created, (c) dilation operation applied, (d) erosion to reduce edge thickness, (e) contouring to find edges of rope and applied to original image to find the width (red line).

The curves that are detected in the vicinity of the rope edges are saved as coordinates. Seven regions of interest are defined for each image, and within these specific areas the shortest distance from the top line to the bottom line to be saved as the view width. The median of the resulting seven values is defined as the width measurement of this section length. The maximum, minimum and standard deviation of these seven measurements are also measured. Figure C.6 shows an example of this fully processed image with complete widths found in each specific region of interest.

The cameras are synchronised, therefore allowing the widths from all four perspectives to be directly compared at the same time and point along the rope.

C.3.1.3 Unit conversion

The cameras are asymmetrically placed around the rope at different distances. Since Python OpenCV's default measurement is in pixels, the cameras readings have to be scaled. The estimation for this conversion is made by placing a metre reference next to the rope at the beginning of each test.

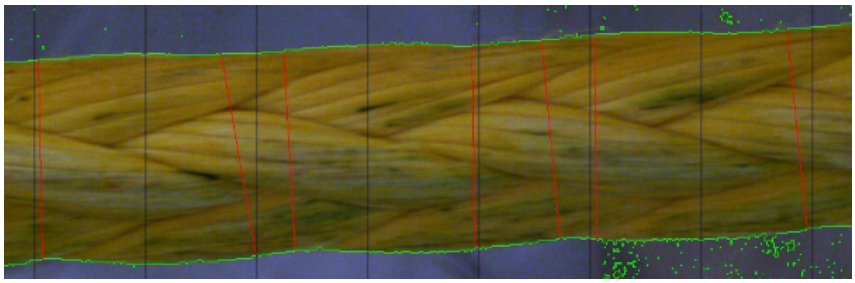

Figure C.6: Example of a processed image with the seven regions of interest applied and widths detected.

C.3.2 Thermal imaging of rope surface

Figure C.7 shows an example of a screen shot from the FLIR software. In this particular example the rope has already been subject to CBOS motion and the various levels of temperature are shown, with the light and dark sections representing the higher and lower temperatures respectively. A region of interest (ROI) is defined, where the average temperature is determined from the pixels located within it. This particular region is chosen so it will always contain only rope and no background during the slight varying vertical displacements of the rope.

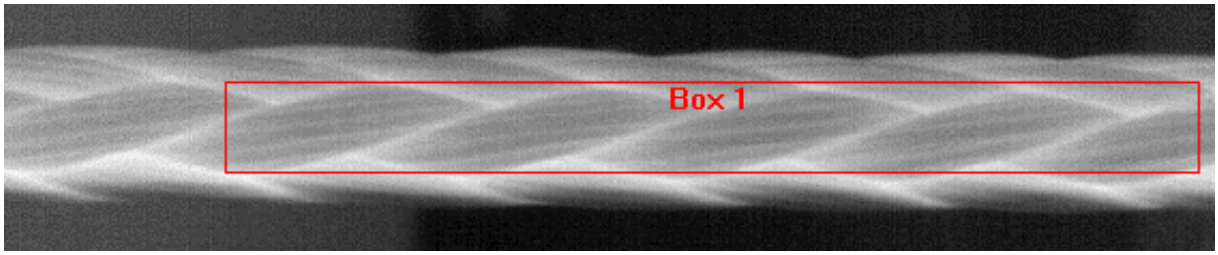

Figure C.7: Screen shot from FLIR ResearchIR Max 4 software with the ROI defined for average temperature calculation.

C.3.2.1 Outliers

Outliers in the geometric features are handled through using the median absolute deviation (MAD) as shown in equation C.1. This is applied to the local length and width data due to these measurements comprising of readings from several images of the same sections at each time stamp.

$$\text{MAD} = \text{median}(\mid x - \tilde{x} \mid) \tag{C.1}$$

Where x is each value and $\tilde{x}$ is the median value of the recorded data set.

This approach is chosen since it is more robust to outliers than using the average of the measurements. It is possible to eliminate these outliers from the data set based on a defined limit:

$$\mid x - \tilde{x} \mid \geq 3 \times \text{MAD} \tag{C.2}$$

The median, maximum, minimum and standard deviation of the values that remain after the application of MAD are used as the feature values at each particular time stamp.

Outliers in the thermal data are limited by the conservative ROI applied during recording. The data collected is limited to the rope surface area with no interference from the background in the images.

C.3.2.2 Missing data

Once outliers are omitted, the data set is treated for missing data. Missing data may occur as a result of instrumentation failures or the algorithms failing to detect the specific sections of the rope due to degradation of section markers.

Imputation via linear interpolation is implemented, replacing the missing data through interpolation in each respective feature over the whole test time of each individual rope. A rolling mean of 3 steps is applied before presenting the local length and width results to maintain the general trend of the measurements throughout the monitoring period.

C.3.2.3 Summary of recorded data

Table C.1 gives a summary of the data are recorded for each step by the condition monitoring system.

Table C.1: Data recorded by condition monitoring system

Length	Width 1	Width 2	Width 3	Width 4	Temperature
SZ-1	SZ-1	SZ-1	SZ-1	SZ-1	SZ
SZ-2	SZ-2	SZ-2	SZ-2	SZ-2	SBZ
SBZ-1	SBZ-1	SBZ-1	SBZ-1	SBZ-1	DBZ
SBZ-2	SBZ-2	SBZ-2	SBZ-2	SBZ-2	
DBZ-A-1	DBZ-A-1	DBZ-A-1	DBZ-A-1	DBZ-A-1	
DBZ-A-2	DBZ-A-2	DBZ-A-2	DBZ-A-2	DBZ-A-2	
DBZ-B-1	DBZ-B-1	DBZ-B-1	DBZ-B-1	DBZ-B-1	
DBZ-B-2	DBZ-B-2	DBZ-B-2	DBZ-B-2	DBZ-B-2	

C.4 Results

C.4.1 Initial observations

Table C.2 shows the number of cycles each rope sample reached before failure in the CBOS machine tests. These numbers are thus the number of cycles to failure (CTF). All the ropes are the same type. (Rope no. 1 and no. 2 were used for different process and test developments and results are thus excluded.)

Table C.2: Number of cycles to failure (CTF)

Rope no.	3	4	5	6	7
CTF	75,324	122,368	120,430	87,314	143,374

Figure C.8 shows images of the typical state of the rope after each testing phase and removal from the CBOS machine. The top image is an example of the surface compression damage done to the rope

through contact with the sheave. The bottom image is the other side of the rope that did not get in contact with the sheave. From this view, the ruptured strands and extruded loops are visible. These become more apparent as the rope degrades during the test.

Figure C.8: Compression damage (top) and extruded loops (bottom).

Figure C.9 shows the global elongation for the ropes tested. The extension of the rope is based on the changes in length of the hydraulic cylinder keeping tension on the rope as measured by the IR laser. This extension is then interpreted as general rope elongation using the ropes' original length as starting point.

It is noted that Ropes 3 and 6 failed due to degradation in the splice that was partly running over the larger driving sheave. The other ropes all failed at the test sheave as intended. Note that the global elongation in all cases is below 1 %, which is in accordance with the manufacturer's rope specification.

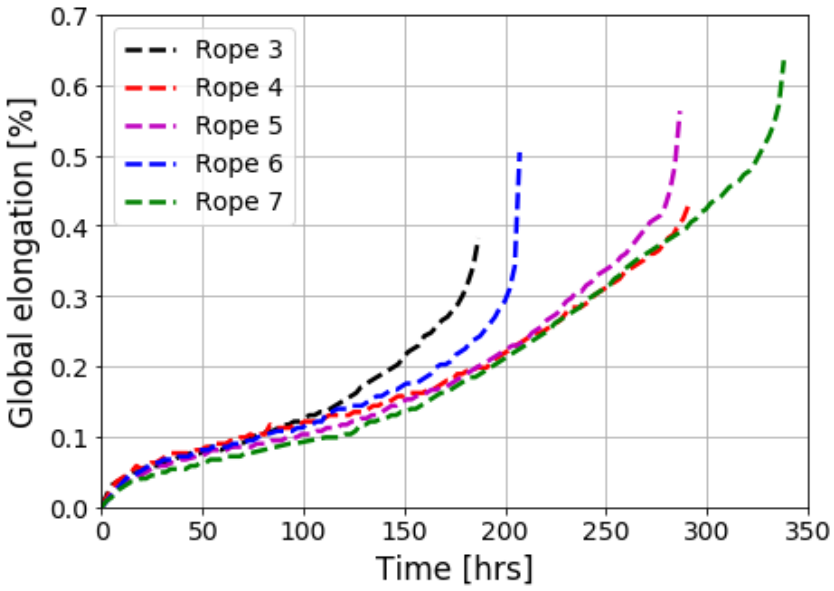

Figure C.9: Global elongation of the ropes after bedding in.

C.4.2 Computer vision system and image processing

C.4.2.1 Local length

Figures C.10 and C.11 show the results of the relative local nominal length for Ropes 3 to 7, in sections DBZ-A and DBZ-B respectively. In each figure, the elongation changes (local strains) as detected by the algorithm for each rope are shown and compared. These are shown against the time, starting from just after the initial bedding in phase until just before failure occurred in the rope specimen. The % local length measurements are based on the changes from the original length of each respective subsection from the end of the bedding in phase. The changes for the SZ and SBZ sections are not presented as they were negligible in comparison to the DBZ-A and DBZ-B sections.

From Figures C.10 and C.11 it is seen that local distances between the markers vary and increase over time. Overall the strands are shown to heterogeneously displaced in the DBZ sections. However in Ropes 4, 5 and 7 there are reciprocal changes in the DBZ, where a decrease in one subsection is accompanied by an increase in adjacent subsection. Rope 7 in particular shows the largest changes in local distance compared to the other rope samples.

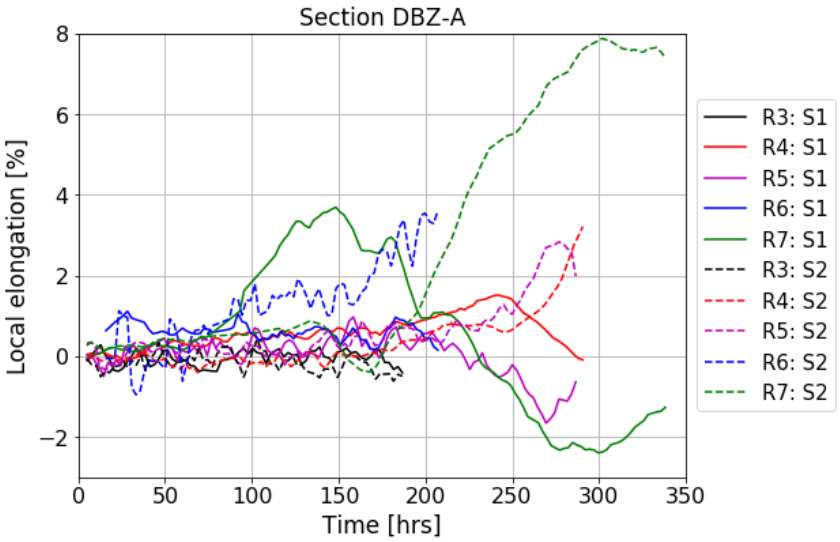

Figure C.10: Local length changes after bedding in phase in Section DBZ-A for all ropes (R-Rope, S-Subsection).

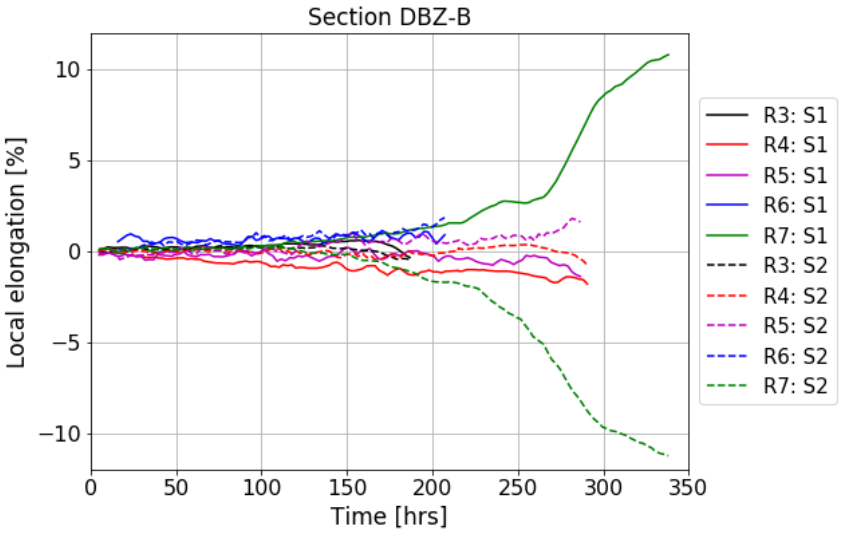

Figure C.11: Local length changes after bedding in phase in Section DBZ-B for all ropes (R-Rope, S-Subsection).

C.4.2.2 Width

The % change in relative width measurements are based on the changes from the original width of each respective subsection. Figure C.12 shows the relative change in width at DBZ-A-1 subsection across all five ropes against time from after the initial bedding in phase until rupture. It also shows that the smallest total relative width changes, when comparing initial and just-before-rupture values, occurred in Ropes 3 and 6, which ran for shortest duration. Substantial varying measurements compared to the other ropes were also observed for this subsection in Rope 4. Camera 2 coincides with viewing from above the rope directly along the sheave axis. Views from the other cameras showed the same tendency of increased width as a function of time, but to a lesser degree.

Examples of relative width change from camera 2 across all sections with respect to time are shown in Figures C.13 and C.14 for Ropes 5 and 7 respectively. The other ropes showed a similar separation between SZ and SBZ showing minor changes, and DBZ sections showing increasing width measurements with the progression of testing. In the SZ section in both examples there is slightly reduced width due to rope elongation. This similarly occurs in the SBZ section in both examples, however there are increases in the width detected in some subsections towards the end of the monitoring period.

In general, width changes in the SZ and SBZ sections do not exceed 5 %, whereas the DBZ section width changes are shown to have reached 10 % and more.

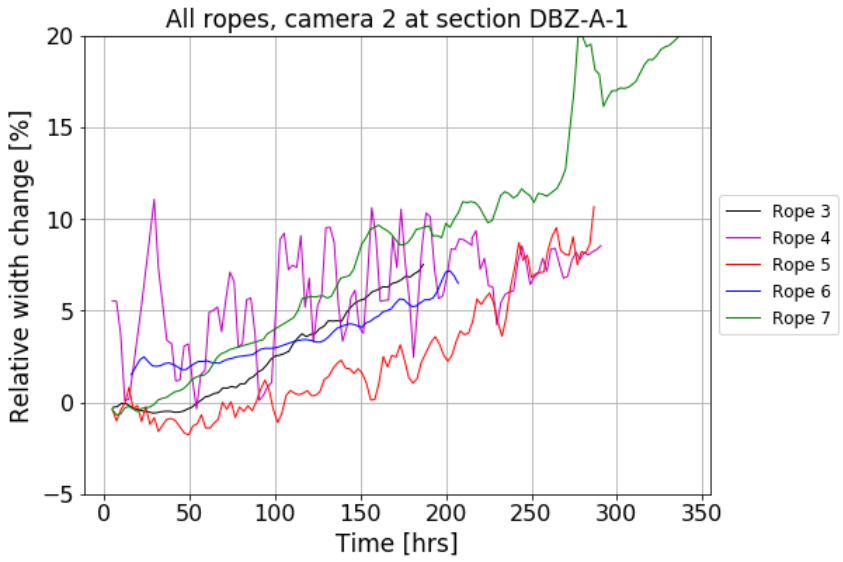

Figure C.12: Percentage change in width from camera 2, perpendicular to sheave axis, at position DBZ-A-1 for all ropes.

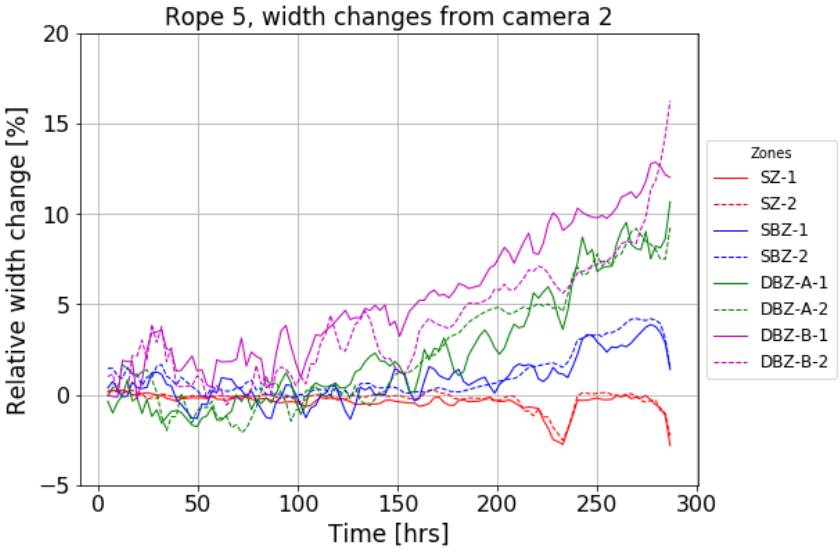

Figure C.13: Percentage change in width from camera 2 for all zones in Rope 5.

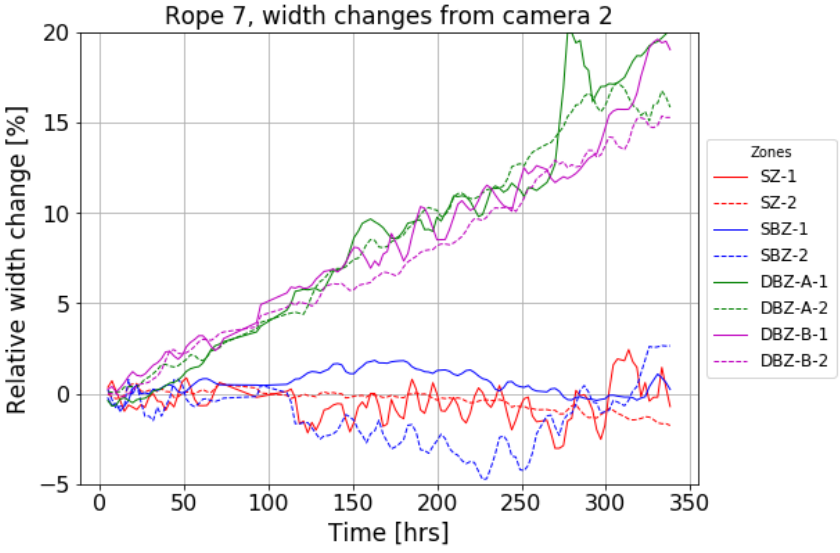

Figure C.14: Percentage change in width from camera 2 for all zones in Rope 7.

C.4.3 Thermal imaging

Figures C.15 to C.16 show the results for the average, maximum, minimum and standard deviation of the temperatures measured in the ROI defined in Figure C.7 for Ropes 4 and 7 respectively at different times during testing.

Each curve represents the temperature measurements of the rope sections visible to the thermal camera as it is cycled back and forth over the sheave. The measurement starts in the SZ section, with the mid point in the DBZ section, then cycles back to the SZ section.

In Rope 4, the average temperature in both the SBZ and DBZ sections measured at 289 hours has decreased in comparison to the temperatures at 162 and 192 hours. Additionally, the DBZ section is shown to have a lower maximum temperature and minimum temperature compared to the measurements at 162 and 192 hours.

Similarly in Rope 7, the average, maximum and minimum temperatures in the DBZ section measured at 338 hours are lower in comparison to the measurements at 34 and 167 hours. The SBZ average, maximum and minimum temperatures at 34 and 338 hours are observed to be similar values. This behaviour is discussed later.

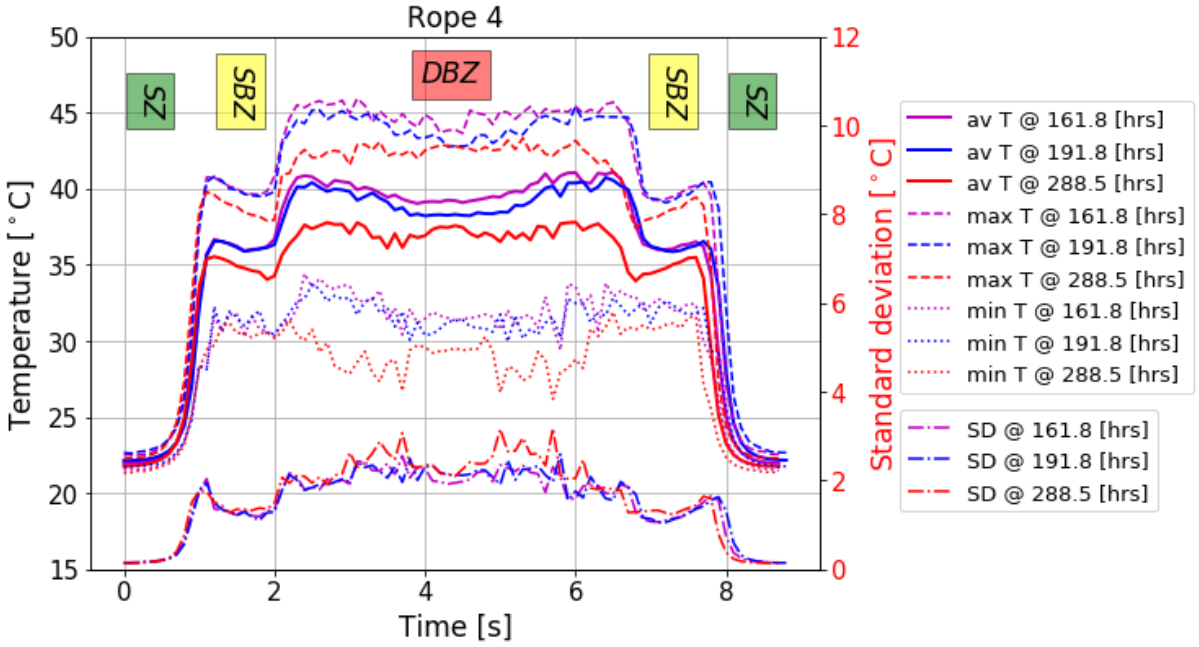

Figure C.15: Rope 4 average, maximum, minimum and standard deviation temperature measurements along the rope for one cycle with respect to the associated test time.

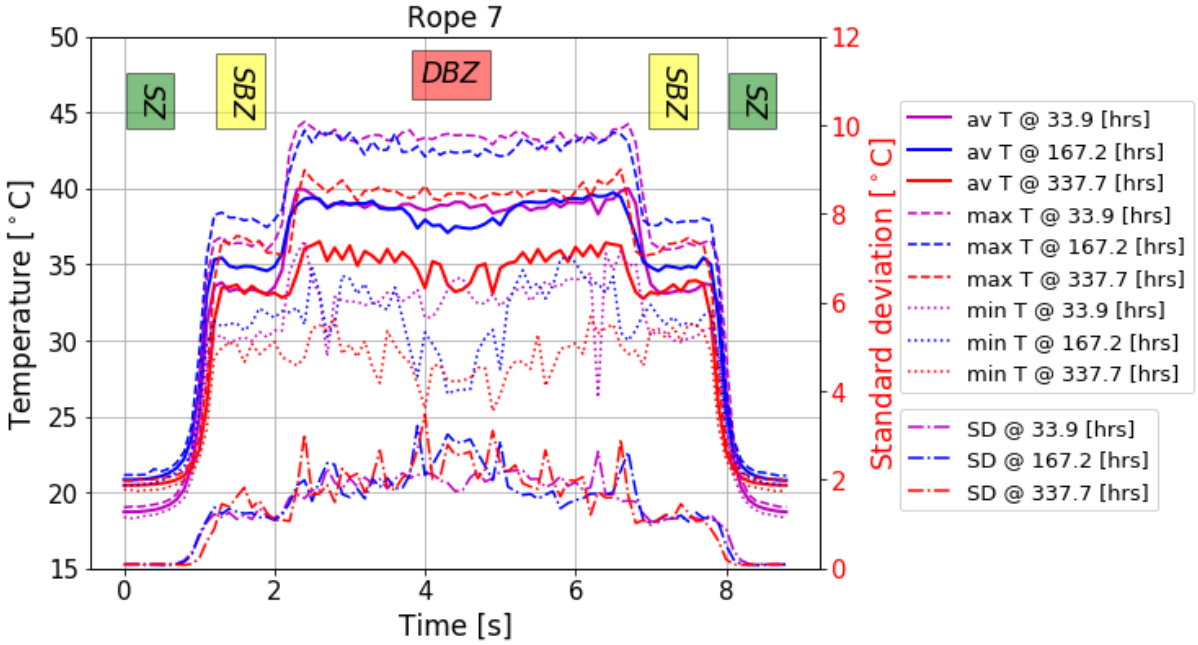

Figure C.16: Rope 7 average, maximum, minimum and standard deviation temperature measurements along the rope for one cycle with respect to the associated test time.

C.5 Discussion

In order to monitor the rope state, CBOS testing is used as it can represent rope use during offshore lifting operations. Focus is put on evaluating adequate monitoring methods that can potentially be applied for field use.

C.5.1 Local length

C.5.1.1 Findings

For all five ropes tested the sections monitored in the straight zone (SZ) and single bend zone (SBZ), there were no strains that exceeded 1 % of the original length. Ropes 4, 5 and 7 ran for significantly more cycles than Ropes 3 and 6, with significant longer elongation detected in the two DBZ sections than the SZ and SBZ sections. This can be attributed to DBZ sections being subjected to twice as many bends over the sheave than SBZ.

Figures C.10 and C.11 show the changes detected using the length calculation method throughout each test, with Rope 7 displaying the largest changes in the marked DBZ sections. There is observed to be a heterogeneous spread of strain changes in the DBZ sections across all the samples, most severe for DBZ-A in Rope 7.

Local length changes are attributed to rope structure rearrangement as the test progresses as well as to actual fibre creep. Extruded loops occur as strands are bunched together with the flexing-unflexing movement during bending, pulling portions of the sub-rope through the whole structure, resulting in length changes at the local scale. The strands also rupture and fuse, contributing to rearrangement of the rope morphology.

Figures C.17 and C.18 are examples taken from the processed data and show the significant changes in both length and rope structure from the first to the final length measurements. There are instances of "reciprocal" changes where one subsection increases or decreases in length and the corresponding opposite behaviour occurs in the continual subsection. The subsections show strands move between each other and give rise to heterogeneous displacement of markers.

C.5.1.2 Uncertainties and error sources

The markers used for detection are not guaranteed to be placed at the exact same position relative to the test sheave on each rope, contributing to variations in the measurement results.

The deterioration of the rope condition causes displacement in the position of the rope with respect to the camera position, for example in Rope 5 where there was pronounced twist before failure. Such displacements of the rope will contribute to variation in the local length and width measurements.

The algorithm relies on finding the centre point of each marker. The wear on these markers while testing progresses can have an effect on the lengths measured. It is acknowledged than any reduction in size of these markers is insignificant compared to the change in length of the subsection. The number of tests conducted are too few to quantify the errors so far.

C.5.1.3 Application to condition monitoring

The heterogeneous local length changes observed between ropes, across the DBZ sections in particular, indicate that rope condition monitoring must be addressed at strand level. What the rope experiences during CBOS motion defines what the system must be capable of monitoring. The present method is

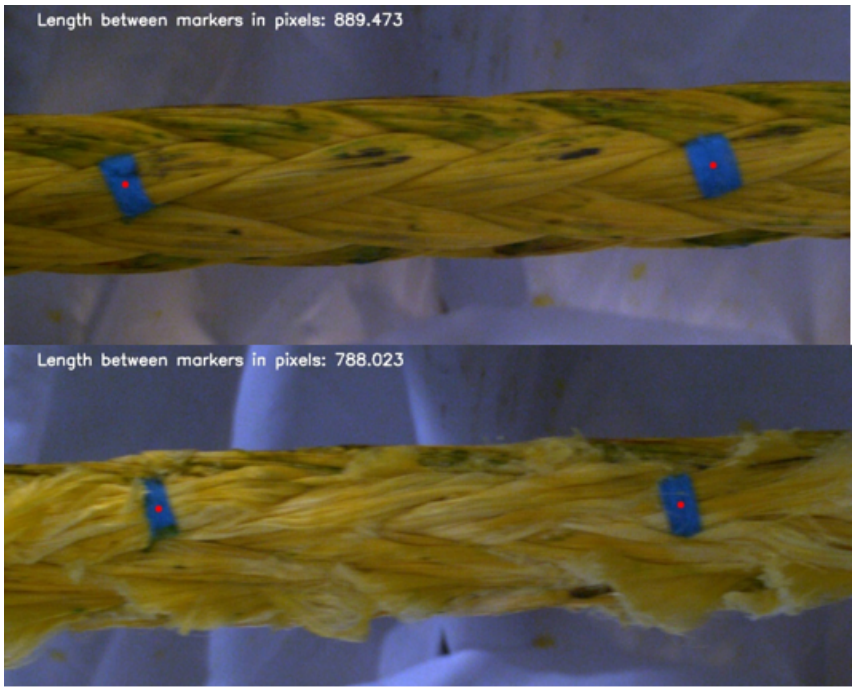

Figure C.17: Subsection DBZ-B-1 in Rope 7 at the beginning of the test (top) and just before rupture (bottom).

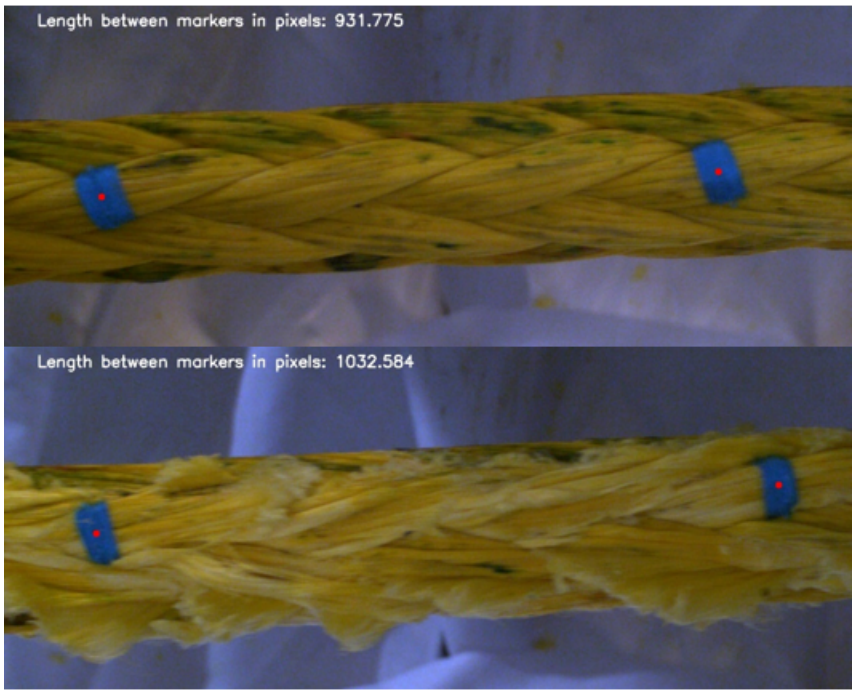

Figure C.18: Subsection DBZ-B-2 in Rope 7 at the beginning of the test (top) and just before rupture (bottom).

shown to be able to reliably track the changes in local length during testing, allowing local length to be properly mapped during rope lifetime.

The majority of local length changes over 1 % came after half the rope lifetime, thus this could serve

as warning and call for further inspection when the total for subsection length exceeds this value, as well as an aid to subsequent decision making.

In Figures C.17 and C.18, local relative distortion of the strand is shown to be -11.4 % and +10.8 % in the DBZ-B-1 and DBZ-B-2 subsections respectively when comparing the first and final measurements. The overall middle relative distortion equates to -0.6 % across the whole lay length in DBZ-B, highlighting the need for sub-lay length measurements.

The presented method is effective at monitoring the local length changes and also provides a useful visual aid to rope deterioration and how the related subsections interact with each other at strand level.

C.5.2 Width

C.5.2.1 Findings

Extruded loops and ruptured strands become more apparent in the DBZ sections due to repeated bending and unbending, which are detected effectively by the visual system and algorithm through the larger relative width change. The structure of the rope rearranges due to repeated deformation. It is noted that generally there are small variations and continuous increase in width despite the elongation of the same sections.

Unlike the local length measurements, there is no evidence of "reciprocal" changes. Each subsection is shown to follow the trend of the neighbouring subsection despite the occurrence of the opposite elongation behaviour in some of the ropes.

After inspection of the processed images from Rope 4, there is visible evidence of substantial twist in the rope, explaining the observation of varying widths for Rope 4 in section DBZ-A-1.

C.5.2.2 Uncertainties and error sources

The rope will not maintain the exact same perspective to the camera due to slight rotation while testing. Since several hours pass between each recording, it is possible that the portion of the rope in contact with the sheave changes.

The rope colour also changed slightly during degradation, meaning that edge detection created from applied binary image created through the colour mask may not resemble the "true" edge of the rope.

Imputation is used to compensate for missing data and can add uncertainty as it is just an interpolation. However the rolling mean smoothing process helps to show the "general trend" in width change with these values included.

C.5.2.3 Application to condition monitoring

Width monitoring is vital as it indicates changes in rope structure, including both in shape or through deterioration such as extruded loops or ruptured strands. The width calculation method applied is adept at monitoring these changes over the testing period, but it also clearly displays the differences in the different bending zones.

An example of a processed image is shown in Figure C.19 from Rope 3 as observed from Camera 3. There is visible deterioration in the rope structure with the presence of extruded loops clearly seen before rupture. The width calculation algorithm adapts to this, with the rope edge detection including the extruded loops. In this instance, the shortest distance in the constituent regions of interest will be

higher and subsequently produce a larger median value, allowing the changes to be quantified throughout the rope lifetime.

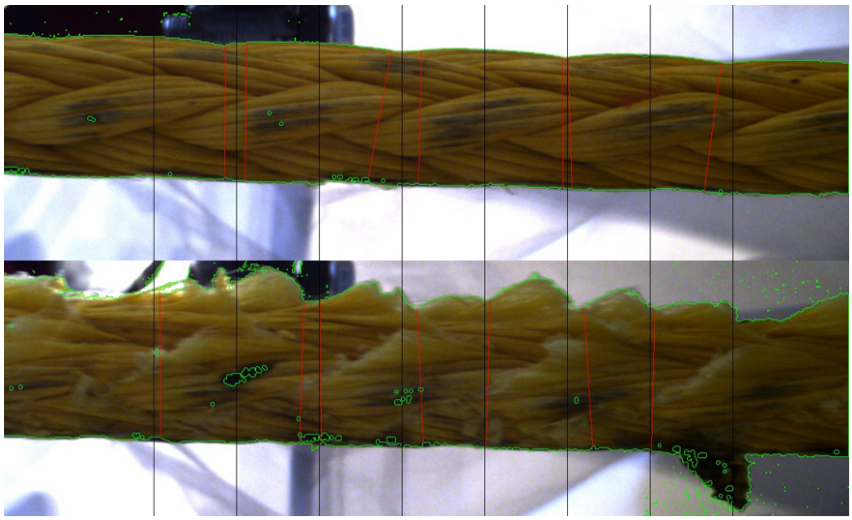

Figure C.19: Section of Rope 3 at the beginning of the test (top) and just before rupture, featuring extruded loops (bottom) as seen from camera 3.

Substantial movement of the rope could be a sign that significant deterioration or structural rearrangement has occurred during use. Monitoring these variations using this method can find use as an aid to decision making regarding discard or re-classification of the rope in use, as well as documenting the exact location of damage accumulation along the rope. Using the applied method it is straight-forward to gauge trends in width change and inspect the images that coincide with the measurements.

C.5.3 Thermal imaging

C.5.3.1 Findings

Thermal images are recorded as they indicate frictional and deformation work in the rope. Figures C.15 to C.16 show a distinct temperature measurement curve in each rope. However, within each recording there are distinct zones visible due to temperatures associated with the bending behaviour in each section. The first and second plateaus in the curves are associated with the SBZ and DBZ sections respectively.

After increasing from the beginning of the test, the average temperature in the DBZ section is shown to decrease as the rope heads toward rupture. This also coincides with lower maximum and minimum temperature at the DBZ section at the more advanced recording times during testing.

The varying temperatures in the sampling areas of the rope surface are given by the standard deviation. This follows the same "plateau" pattern as the temperatures. There are larger deviations recorded in the DBZ sections at the more advanced recording times in Ropes 4 and 7. However, the deviations are approximately the same in the SZ section for the recording times in Rope 4 but are larger in Rope 7. Additionally in the transfer points between the SZ and DBZ sections in Rope 7 show larger variations.

C.5.3.2 Uncertainties and error sources

The thermal camera is placed at approximately the same distance from the sheave entrance for each test but slight variations in distance from the rope are possible. The camera distance from the rope

is measured for each rope, and input to the camera software, so these movements do not influence the accuracy of the recorded temperatures.

Similar to the local length and width measurements, differences in the rope mounting can also lead to slight variation in values recorded. The temperatures are recorded from the portion of the rope visible in the defined ROI, therefore if noticeable twist is present, the displacement of the rope will result in slight differences in temperature recording.

Similar rope degradation and structural rearrangement will result in greater movement of the rope as the test progresses. The ROI is stationary and is chosen so that a portion of the rope will always be visible in the defined boundary. There is greater vertical movement in the rope towards the end of testing instead of the "smoother" transition of the rope portion visible in the ROI at the start of the test. It is possible this movement can give variation in the measurements.

Noticeable variations in temperature measurement were observed at the transfer points between the SZ to SBZ and SBZ to DBZ sections. The measurement ROI will contain portions from two different bending zones at the transition points and therefore a greater variation of temperatures. Additionally, the largest overall variations are observed at the latter stages of testing in the DBZ sections.

C.5.3.3 Application to condition monitoring

Thermal monitoring using an IR camera brings not only temperature measurements but can provide another useful visual aid to assess the rope surface. The method applied allows each specific bending zone to be scrutinised in detail and monitored over time. Moreover, the results found using the thermal camera in this study allow the physical changes of the rope to be compared concurrently with temperature. Monitoring of the average, maximum, minimum and variation by standard deviation gives information on changes into the physical structure of the rope.

The lower average, maximum and minimum temperatures that coincide with larger standard deviations at more advanced testing stages, particularly in the DBZ section, can be attributed to the increasing presence of structural degradation in the rope. As detected with the width measurement algorithm, the extruded loops and ruptured strands that are visible and more prevalent in the latter stages of testing via the thermal camera, which can be seen in Figure C.20. These degradation features are markedly cooler than the main body of the rope and contribute to the spread of measured temperature values.

The transfer points between the distinct bending zones are also worth investigation. As expected, heat generation will vary due to different bending regimes. The distinct shape indicates that the thermal conductivity in the rope is low and also that the effect of cooling by environment is negligible.

Visible deterioration of the rope will be noticeably more between the SZ and SBZ sections and the SBZ and DBZ sections respectively due to the differences in temperature between the zones. The increasing presence of these cooler temperatures through accumulated damage and effect on temperature measurements serves as an aid to find the exact positions and time for further inspection.

C.6 Future work

The physical properties of the rope have been measured during repeated deformations in a CBOS regime, thus monitoring the rope state change. For future testing, there is potential for more local length measurements throughout the SBZ and DBZ, with particular emphasis on applying markers to the same sub-rope through the test, rather than just the general area, to gain a better overview of localised changes in the rope condition. Additionally, the tests will make use of higher tensions in order to more accurately

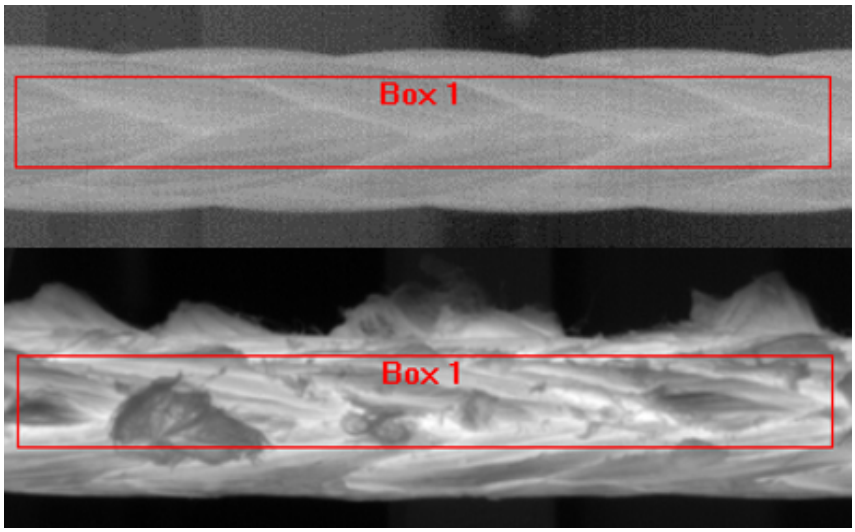

Figure C.20: An example of Rope 7 thermal images at the beginning of the test (top) and just before rupture, featuring extruded loops (bottom) and ruptured strands.

reflect safety factors used in industry. Monitoring at these conditions will also give useful insight into how the various condition indicators are influenced in different testing conditions. This will be performed on different types of rope to confirm applicability.

In real application, the same portion of the rope is not subject to constant repeated bending but rather distributed along the rope. This will also involve lifting operations with varying size of payloads instead of a constant applied tension. Additionally there will be differences in moisture and temperature, depending on vessel location and the surrounding environment. These are all factors that have to be considered to for testing and further assess the condition monitoring system effectiveness.

Increased understanding of the underlying physical mechanisms for the changes observed in local length, width and temperature is also required. Changes in the physical structure that occur as damage progresses and its subsequent effect on properties such as thermal conductivity in the rope and heat transfer to the environment require greater understanding. This would mean more informed decision making using the monitoring system and better interpretation of the trends observed in measurement changes.

In the same way inspectors are trained and build up experience by investigating for certain condition indicators during routine visual inspection of rope, there is potential to use machine learning algorithms to detect patterns in rope degradation that cannot be detected by normal visual inspection. The data shows that there are changes in the various measurements that coincide with the deterioration of the rope. These condition indicators can be extended to use as features for machine learning application. A proper understanding of these more subtle changes and identification of deterioration patterns has the potential to develop better RUL estimation for fibre ropes subject to CBOS regimes.

C.7 Conclusions

This paper presented results from a computer vision monitoring system, thermal camera and distance measuring laser to monitor the deterioration in ropes subjected to a CBOS regime. The computer vision algorithms presented are capable of detecting localised length changes subject to appropriate marking

in the rope, as well as detecting rope damage such as extruded loops and ruptured strands through cross width detection. The deterioration of the rope can also be monitored via thermal imaging, as it is capable of detecting temperature changes that coincide with structural deterioration in the latter stages of testing.

This combination of monitoring gives useful insight into fibre rope condition from different perspectives and emphasises the need for localised strand-level monitoring at specific sections in the rope. However, if longitudinal distortion is to be used, then a thorough and consistent account of the rope pattern and structure is needed, given the demonstrated potential for variations.

Ultimately, the detection of changes over time can be used as condition indicators and can be engineered into features in application of machine learning algorithms to classify damage and better gauge RUL for fibre rope subject to CBOS regimes.

C.8 Acknowledgements

The research presented in this paper has received funding from the Norwegian Research Council, SFI Offshore Mechatronics, project number 237896. The authors would also like to extend an extra special thanks to Benyamin Akdemir for his assistance in creating the experiment set up and his insight into the use of machine vision cameras and also to Yannick Bafanga for automating the task of retrieving the thermal image statistics.

Appendices

C.9 Instrumentation details

C.9.1 Optical camera

Table C.3: Optical camera specification

Maximum frame rate	169 fps
Resolution	1.3 MP
Pixels (H x V)	1280 x 1024
Pixel size	4.8 x 4.8 μm

C.9.2 Thermal camera

Table C.4: Thermal camera specification

Image acquisition	0.0015 Hz to 125 Hz
Temperature range	-20 °C to 350 °C
Pixels (H x V)	640 x 512
Accuracy	± 2 °C or ± 2 % of reading

C.9.3 Distance measuring laser

Table C.5: Distance measuring laser specification

Typical measuring tolerance	± 2.0 mm
Typical range	40 m

Paper D

Condition classification of HMPE rope during CBOS testing through supervised machine learning Methods

S. Falconer, P. Krause, T. Bäck, E. Nordgård-Hansen and G. Grasmo

This paper has been submitted as:

S. Falconer, P. Krause, T. Bäck, E. Nordgård-Hansen, G. Grasmo. Condition Classification of Fibre Ropes during Cyclic Bend over Sheave testing Using Machine Learning. *International Journal of Prognostics and Health Management*, Vol. 13, 1, 2022. doi: 10.36001/ijphm.2022.v13i1.3105

Condition Classification of Fibre Ropes during Cyclic Bend over Sheave testing Using Machine Learning

Shaun Falconer*, Peter Krause**, Thomas Bäck****, Ellen Nordgård-Hansen***, Geir Grasmo*

*Department of Engineering Sciences
University of Agder
NO-4876 Grimstad, Norway

**divis Intelligent Solutions GmbH
DE-44227 Dortmund, Germany

***NORCE Norwegian Research Centre AS
NO-4876 Grimstad, Norway

****Leiden Institute of Advanced Computer Science (LIACS)
Leiden University
NL-2333 CA Leiden, Netherlands

Abstract – Fibre ropes have been shown to be a viable alternative to steel wire rope for offshore lifting operations. Visual inspection remains a common method of fibre rope condition monitoring and has the potential to be further automated by machine learning. This would provide a valuable aid to current inspection frameworks to make more accurate decisions on re-certification or retirement of fibre ropes in operational use. Three different machine learning algorithms: decision tree, random forest and support vector machine are compared to classical statistical approaches such as logistic regression, k-nearest neighbours and Naïve-Bayes for condition classification for fibre ropes under cyclic-bend-over-sheave (CBOS) testing. By measuring the rope global elongation throughout the CBOS tests, a binary classification system has been used to label recorded samples as healthy or close to rupture. Predictions are made on one rope through leave-one-out cross validation. The models are then assessed through calculating the accuracy, probability of detection, probability of false alarm and Matthew's Correlation Coefficient, and ranked based on the results. The results show that both machine learning and classical statistical methods are effective options for condition classification of fibre ropes under CBOS regimes. Typical values for Matthews Correlation Coefficient (MCC) were shown to exceed 0.8 for the best performing methods.

D.1 Introduction

As offshore lifting operations move to deeper waters exceeding 3000 m, the possibility of implementing fibre ropes instead of steel wire ropes has shown to be a viable alternative. The benefits of fibre rope over steel ropes is well documented ([2], [3] and [4]) but condition monitoring and determination of retirement criteria remain issues. Machine learning is rapidly gaining traction as a condition monitoring method across a number of industries ([17], [16] and [147]). Due to improved monitoring methods and storage of

historical data, there has been a shift in research towards "intelligent maintenance systems" focusing on automatically determining the condition and detecting faults of engineering components with less human intervention. Condition monitoring for fibre ropes used for subsea deployment also has potential for further advancement with machine learning. Manual inspection methods detailed in industrial standards are still mainly used in condition classification and are still largely based on experience from mooring application ([6], [7] and [48]). Machine learning adaptation would serve as a useful aid to these methods and allow inspectors and operators to make a more informed decision on rope retirement or re-certification.

Fibre rope degradation mechanisms related to mooring and offshore lifting have been summarised in previous studies ([21], [22] and [11]). These include but are not limited to: creep, temperature, abrasion, tension fatigue and compression fatigue. These damage mechanisms and potential failure modes add difficulty in developing an all-encompassing method of monitoring fibre ropes. Therefore a combination of machine vision cameras, IR camera and a distance measuring laser were proposed for this study.

Machine learning methods have previously been applied to condition classification of steel wire ropes for hoisting in the mining sector. The use of k-nearest neighbours and artificial neural networks was adapted to classify the condition of balancing tail ropes in [112] and a type of support vector machine to classify rope faults based on vibration data in [111]. To the authors' knowledge there has been no publicly released research related to machine learning for condition classification of fibre ropes.

Condition monitoring for other engineering components benefits greatly form publicly available data sets, therefore allowing focus to be fully put on development for intelligent maintenance algorithms, rather than focusing on data recording. Fibre ropes for lifting operations do not benefit from this and major efforts are required to create these data sets. This article extends research on such condition monitoring methods performed at the University of Agder, Norway ([141], [148] and [149]) that make use of cyclic-bend-over-sheave (CBOS) tests monitored by both computer vision and thermal monitoring. The changes in geometry and temperature of the rope recorded during CBOS testing are used to create features that form the machine learning models.

In this study decision trees, random forest and support vector machines are compared to classic statistical methods such as k-nearest neighbours, logistic regression and Naïve-Bayes for binary classification of fibre rope condition. The methods chosen for application reflect current practice in machine learning for diagnostics of engineering components. An introduction to these methods is outlined in Section E.2 and the experimental set-up with associated data processing steps are summarised in Section **??**. The results of the classification models are presented in Section E.4, followed by discussion in Section E.5. Subsequently, the potential for industrial application of machine learning for fibre rope offshore construction cranes is discussed in Section E.6. Finally, conclusions are offered in Section E.7.

D.2 Methods

In this section, a brief overview of the methods that are applied in the present study is given.

D.2.1 Decision trees (DT)

This study applies the decision tree algorithm as detailed in [119], using the implementation in scikit-learn [120]. It comprises a flowchart that assigns each sample to one of two classes based on a condition selected from the features available. The samples are split based on an attribute selection measure, in this case the Gini index, which measures the impurity of a data split with respect to the classes available ([121] and [122]). This process is performed recursively until all samples are assigned to a class or there

are no more features available to make splits. The depth of the trees can also be limited to change the complexity of the model. For example, a deeper tree can lead to a more accurate result but has the risk of creating an overfitted model due to unrealistic complexity. Since there is a random element involved in the algorithm each tree configuration is repeated 20 times to assess the spread and confidence in the classification predictions.

D.2.2 Random forest (RF)

Random forest is an example of an ensemble learning method comprised of many decision trees. The method is described in detail in [123] and also implemented using scikit-learn [120]. A random forest is formed with a defined number of decision trees, where each individual tree is formed on a subset of samples and features created through random sampling with replacement. These multiple predictions are combined in the bagging phase [124], where the a class is assigned based on a majority vote by the individual trees in the random forest. Similar to the decision tree algorithm, the depth of the individual tree can also be controlled. The number of trees that make up the forest can also be adjusted. Each configuration is repeated 20 times to assess the variation in the predictions made by the model.

D.2.3 Support vector machines

Support vector machine has also found use for classification problems as defined in [125] and are implemented through scikit-learn [120]. The algorithm works by fitting a hyperplane that divides a set of instances into classes. The optimal solution is separated is where the margin that separates the instances has been maximised, with the instances used referred to as "support vectors" [126]. The generalisation to the nonlinear case is achieved by applying the so-called kernel trick, using nonlinear kernel functions for transforming the task into a higher-dimensional space, in which the number of possible linearly separating hyperplanes is larger than in the original space. In this study linear (SVM-linear), Sigmoid (SVM-Sigmoid) and radial basis function (SVM-RBF) models are applied to alter the hyperplane shape applied to the data. Each configuration is performed once and the performance of the kernels is compared.

D.2.4 Classical statistical methods

The machine learning models detailed previously are also compared and assessed along with classical statistical approaches such as k-nearest neighbours [127], Naïve-Bayes [128] and logistic regression [129]. These methods are also commonly used for classification problems as an alternative to machine learning. As this research is new use for machine learning, classical statistical methods are also investigated to assess if they are sufficient enough to achieve good classification results.

D.3 Experimental study

D.3.1 CBOS testing and data acquisition

Two different types of 28 mm diameter, 12-strand HMPE fibre rope (denoted "A" and "B") were tested in a CBOS test machine installed by DEP Engineering at the Mechatronics Innovation Lab (MIL) in Grimstad, Norway. The machine has two sheaves: a driving sheave and a test sheave. The test sheave is designed to be smaller than the driving sheave so that the rope break would occur there. The driving

sheave is controlled via a motor which instigates rope movement during testing. The test sheave is 800 mm diameter and made of 42CrNiMo4 steel with a U-groove profile, which equates to a D/d ratio of 28.6:1. It is attached to a portion of the machine which moves with the extension of a hydraulic cylinder. Tension in the rope is applied and maintained via this hydraulic cylinder, which will extend as the test progresses. Each rope is tested until failure, which can occur through rupture or accelerated extension of the rope detected by sensors in the cylinder. An overview of the machine is shown in Figure D.1. The safety factor (SF) of the each test is defined by expression A.1:

$$SF = \frac{MBL_{rope}}{T_{test}} \tag{D.1}$$

where MBL_{rope} is the rope minimum break load as specified by the manufacturer and T_{test} is the test tension exerted by the cylinder in the CBOS machine. The safety factors used in testing for data sets A and B are 11 and 8, respectively. Data set A contains five ropes and data set B contains four ropes.

Data is acquired from a set-up that includes: four machine vision cameras, a thermal camera and a distance measuring laser. The features used in model training are derived from the data acquired through the monitoring system. Algorithms developed in OpenCV [117] are used to extract local length and width data from the machine vision cameras. The change in these parameters as result of fatigue and abrasion during CBOS testing can be monitored. FLIR software with built-in features is used for thermal data [118] recorded with the IR cameras. This allows the temperature in each distinct bending zone to be monitored throughout testing. The distance measuring laser allows the global length to be continuously monitored and the effect of creep on elongation to be monitored. Further specific details related to data acquisition are available from previous work [149].

Figure D.2 shows a schematic of different bending zones measured throughout each experiment: the straight zone (SZ), single bend zone (SBZ) and double bend zone (DBZ). For each of the eight sections defined in Figure D.2, one length measurement and four width measurements are used as features. Each separate local length measurement equates to half a lay length. Computer vision data is recorded for 2000 images, corresponding to 13-15 complete cycles, every 1000 cycles. The values for each recording are thus aggregated to give median, maximum, minimum and standard deviations for these geometric features. The thermal camera was set to sample at 100 Hz for 2000 images, resulting in a 20 seconds video for each period. This was sufficient to record at least one full cycle in the CBOS test. Temperatures are only available for the lumped zone SZ, SBZ and DBZ and the temperature values within the rope part of each relevant image are aggregated as average, maximum, minimum and standard deviation. A complete list of features used in this study is shown in Table 1.

D.3.2 Data Pre-processing

After recording the data is treated for outliers and missing data. Outliers in the geometric measurements are handled using mean absolute deviation. This is due to the morphological operations in the width and length calculations occasionally detecting points outside of the rope region of interest in the images. Therefore, this is applied to both length and width measurements and will exclude outliers from the median, maximum, minimum and standard deviation calculations.

Missing data may occur as a result of instrumentation issues. The machine learning algorithms applied in this study omit the whole record if any feature has missing data, meaning useful data can also be left out. Therefore imputation of missing data points is done through interpolation.

After these steps, the raw measurements from the data acquisition phase are scaled by subtracting the mean value and dividing by the standard deviation. This done for each rope tested to improve

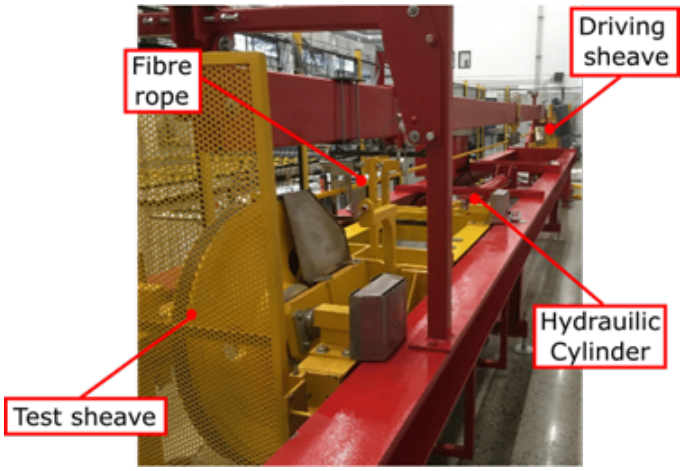

Figure D.1: Overview of CBOS machine at Mechatronics Innovation Lab, Grimstad, Norway.

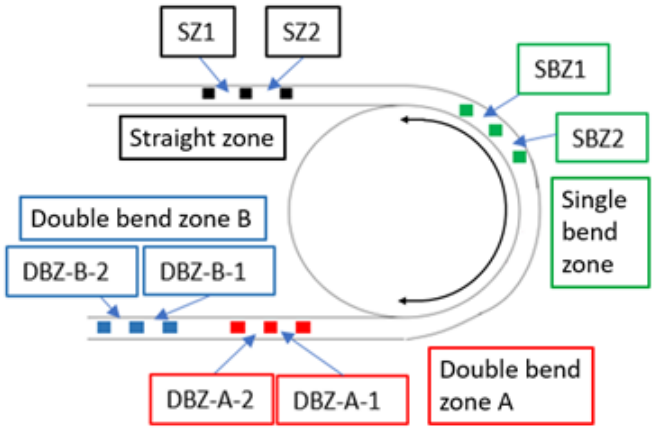

Figure D.2: Summary of bending zones monitored during CBOS testing.

comparability between the rope samples and is a standard step to prepare data for machine learning application.

D.3.3 Labelling

To perform classification predictions on the ropes, the records need to be appropriately labelled. This study is a binary classification problem, therefore the ropes can be considered either Healthy (HE) or Close To Rupture (CTR). The development of the global length resembles a creep curve with three distinct stages: primary, secondary and tertiary creep. The tertiary creep stage encompasses the accelerated creep phase after the transition point. Fitting the global length development to a polynomial allows a quantitative definition of the transition from secondary to tertiary creep, thereby labelling each sample as “HE” or “CTR”, as shown in Figure D.3. The “CTR” labelled examples equate to the accelerated creep phase. This labelling process allows an automated, quantitative definition of rope condition to be implemented.

Table D.1: List of features used for condition classification in data sets A and B.

Data type	Feature (zone)	Parameter
Geometric	Local length: SZ1, SZ2, SBZ1, SBZ2, DBZ-A-1, DBZ-A-2, DBZ-B-1, DBZ-B-2 Width: SZ1, SZ2, SBZ1, SBZ2, DBZ-A-1, DBZ-A-2, DBZ-B-1, DBZ-B-2	median, maximum, minimum, standard deviation
Thermal	Temperature: SZ, SBZ, DBZ	average, maximum, minimum, standard deviation

D.3.4 Model Training and Assessment

Leave one out cross validation (LOOCV) is performed on the CBOS data sets. A summary of the steps in the LOOCV process in this study are detailed in Figure D.4.

The results are shown through metrics that are derived from Confusion matrix description, which is shown in Figure D.5.

The correct predictions can be summarised as true positives (TP) and true negatives (TN) and the incorrect classifications are quantified as false positives (FP) and false negatives (FN). The negative and positive classes coincide with the HE and CTR classes, respectively. The metrics used for model assessment accuracy (ACC), probability of detection (POD), probability of false alarm (PFA) and Matthews correlation coefficient (MCC) are shown in Expressions D.2- D.5:

$$ACC = \frac{TP + TN}{TP + TN + FP + FN} \tag{D.2}$$

$$POD = \frac{TP}{TP + FN} \tag{D.3}$$

$$PFA = \frac{FP}{FP + FN} \tag{D.4}$$

$$MCC = \frac{TP \cdot TN - FP \cdot FN}{\sqrt{(TP + FP)(TP + FN)(TN + FP)(TN + FN)}} \tag{D.5}$$

ACC is the most general of the metrics presented in this section and simply takes into account the number of correct predictions across of the whole data set. The closer the value is to 1, the better the

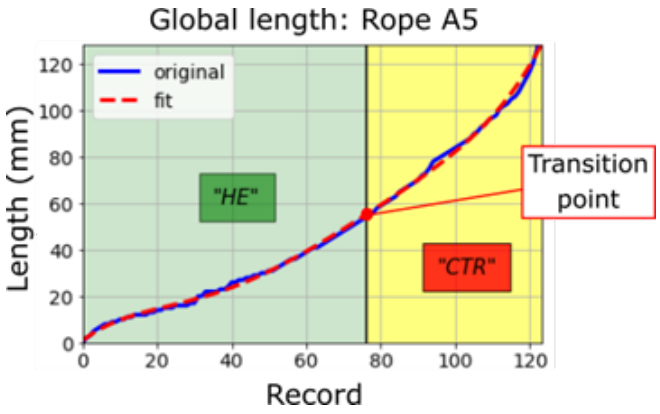

Figure D.3: Example of labelling process on rope A5 with transition point between both classes.

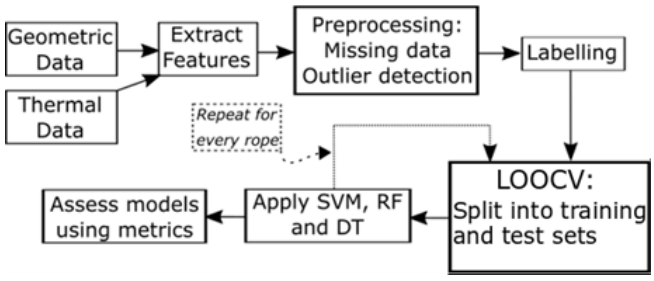

Figure D.4: Operations flowchart.

model is performing. However, this does not take into account the number of samples present in each class.

POD can be summarised as the likelihood of a CTR being correctly classified. The closer the metric is to 1, the better the model is deemed to have performed in this aspect. A model that fails to detect CTR samples runs the risk of allowing the rope to continue operation until it fails.

PFA is interpreted as the probability of an "HE" sample being mislabelled as "CTR". If a model has a higher tendency to classify samples as CTR when they are HE, it would lead to more false alarms during condition monitoring. This could potentially prove to be costly due to operational stoppages for inspection and therefore a lower value is preferred.

MCC takes into account all four values in the confusion matrix and provides a more balanced assessment regardless of whether one class is disproportionately over- or under-represented. A value close to 1 means that both classes are being predicted well and show that true and predicted classes are correlated.

However, none of the metrics give information about what specific samples have been misclassified. Figure D.8 shows an example the classifications predicted by the models at the various stages of the CBOS test. Separate results are presented for data sets A and B and the values of the metrics are averaged over the number of individual ropes in each data set. The algorithms are then ranked and compared based on the predictions made.

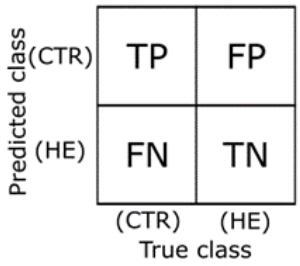

Figure D.5: Overview of confusion matrix.

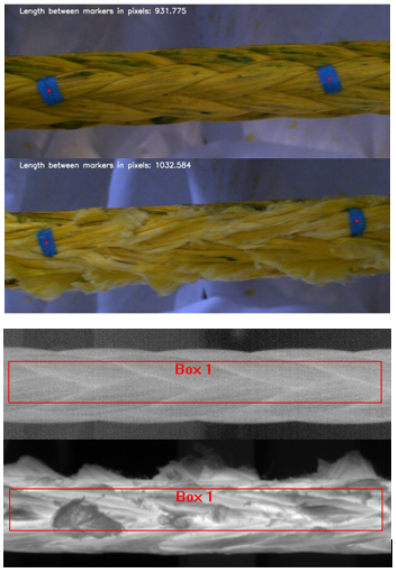

Figure D.6: Example of changes in rope in DBZ between the start and the end of a CBOS test.

D.4 Results

D.4.1 CBOS test results

Figure D.6 shows an example of changes observed in the rope from the start and end of the CBOS test. Using the images captured from the computer vision set-up (top image), it is possible to monitor changes in both local length and width. In this example there is significant localised increase in length, as well as the presence of ruptured strands and extruded loops. These defects can also be observed using the thermal monitoring set-up (bottom image). The ropes structure changes as the test progresses and the temperature difference between warmer compact core and the cooler ruptured strands is clearly visible.

The number of cycles each rope had at failure is summarised in Table 2. It can be seen that the number of cycles counted for data set B is fairly consistent, however there are slight variations with data set A. These "earlier" failures for ropes A1 and A4 are attributed to the splicing used in these rope samples. Due to experimental limitations, a portion of this splice was in contact with the driving sheave, resulting in failure there instead of at the test sheave.

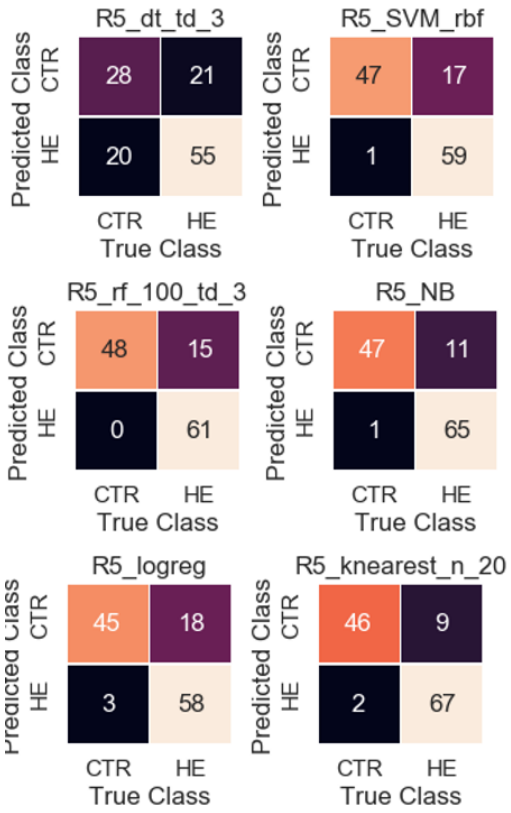

Figure D.7: Confusion matrices for results on rope A5 for six different algorithms.

D.4.2 Classification Comparison

Figure D.7 shows an example of confusion matrix results for the six different techniques applied to rope A5. Figure D.8 shows an qualitative example of the six different techniques applied and the results given for rope A5. The true transition point between the HE and CTR classes is highlighted by the vertical blue line.

It is shown that most models identify a too early transition between the classes. There are a substantial number of HE instances classified as CTR before the transition point indicated by the vertical blue line for every different model.

The decision tree is shown to have a particularly poor performance in comparison to the other algorithms. It misclassifies a significant number of both HE and CTR samples. Moreover, when a rope break is imminent it continues to classify the rope as safe for use.

k-nearest neighbor gives a lot more false alarms earlier in the CBOS test than the other algorithms. This could prove costly in terms of operation downtime, as a rope identified as potentially failing requires inspection and remedial actions to ensure continually safe use.

D.4.3 Average Metrics

The average results for metrics ACC, POD, PFA and MCC in data set A and B are shown in Figure D.9 to Figure D.12. The best performing configuration of each algorithm is presented and assessed for classification performance.

An ACC value that exceeds 90 % generally indicates a very good performance, as it measures how many correct classifications were made across all samples. Random forest and SVM-linear were shown

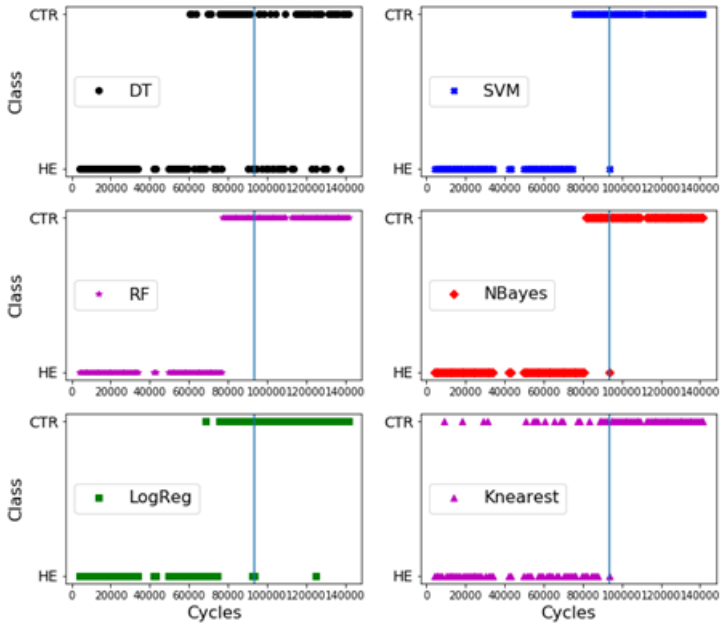

Figure D.8: Example of classification results on rope A5 for six different algorithms.

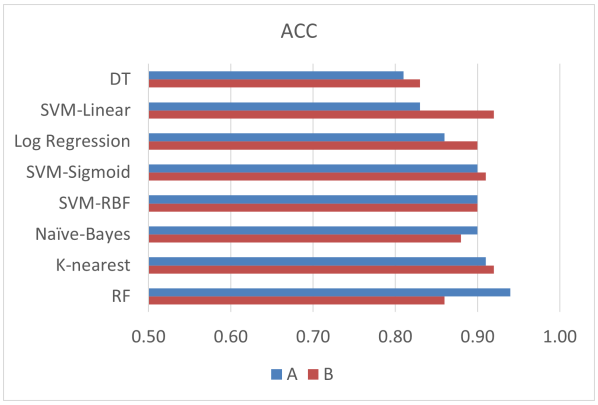

Figure D.9: ACC results for each algorithm compared between data set A and B.

to be best performing machine learning algorithms in data sets A and B respectively.

k-nearest was also shown to have similar scores in data set A to random forest, however as shown in Figure 9, this can be deceptive due to extensive mislabelling of HE samples as CTR in the earlier portions of the rope test time. These misclassification are reflected by the higher PFA score, indicating that there is around a 10 % probability of a HE sample being misclassified as CTR. These types of misclassification could prove costly due to increased down time for inspections.

Similarly, POD above 90 % also indicates a very good performance as this assesses how effective the model at classifying the CTR class. This was shown to drop between data sets A and B, indicating that the data used in B was to the detriment of successfully classifying the CTR class.

Generally, a lower PFA score indicates better performance. PFA is shown to decrease dramatically between data set A and B. From the outset a zero PFA score is ideal, however in the case of Naïve-Bayes, random forest and decision tree in data set B this indicates the models were biased towards predicting the majority of the samples as HE. There was no misclassification of HE samples as CTR but they failed to identify a number of CTR samples. These models could lead to dangerous operation as a rope that is

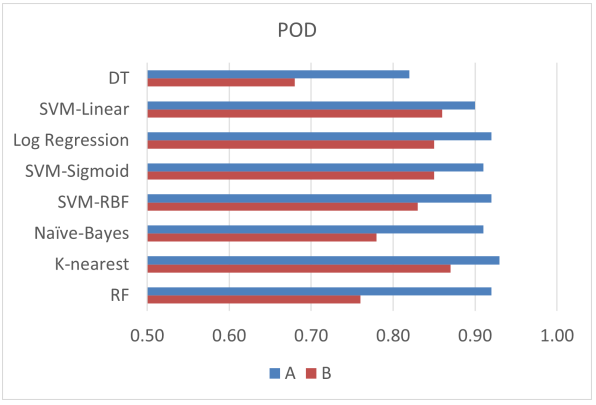

Figure D.10: POD results for each algorithm compared between data set A and B.

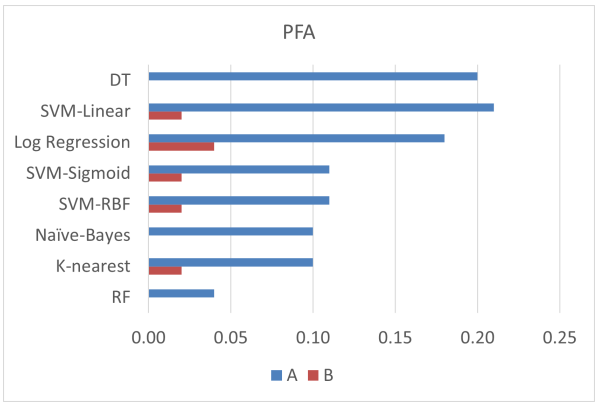

Figure D.11: PFA results for each algorithm compared between data set A and B.

nearing the end of its usage could potentially be classified as being safe to continue.

SVM linear increases dramatically in performance from A to B. This is reflected in the increase in scores for both MCC and ACC between A and B, indicating that the algorithm was able to better predict both classes with the change in data used.

Generally the ACC, POD, PFA and MCC show distinct groupings in data set A. When only assessing ACC and POD, the best performing algorithms could be interpreted as performing at the same level. However, when considering PFA and MCC scores, there is a clearer separation between the algorithms indicating that these metrics have to be used in combination to properly assess a model.

D.5 Discussion

The performance of each method is assessed and discussed individually in the following sections. Then the performance of the machine learning algorithms against the classical statistical methods is also considered and discussed. Despite discrepancies between the rope lifetimes, it is possible to achieve good condition classification results using both machine learning and statistical approaches with all the viable data from the zones outlined in Figure D.2.

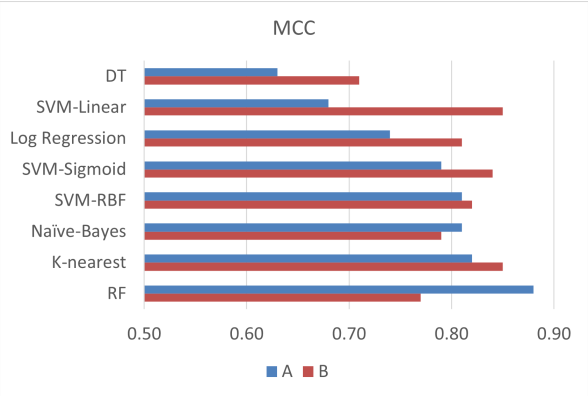

Figure D.12: MCC results for each algorithm compared between data set A and B.

D.5.1 Decision Tree

The decision tree method implemented in this study performed worse than all other algorithms, both machine learning and statistical based. Decision tree is an example of a heuristic algorithm and will classify instances based on the feature that has the lowest Gini index value. This approach causes the results of individual trees to vary, as a feature may produce the same "impurity" but the resulting segmentation point could classify samples differently. Unless explicitly programmed to make consistent data splits on the same features, the decision tree will produce variation in results.

The method is however shown to be useful for exploratory analysis of the features best suited to distinguishing between the two classes established in this study. For fibre rope condition monitoring of CBOS testing it highlights that the features derived from the SBZ and DBZ are more relevant than those from the SZ section. This is as expected, since more bending occurs in these zones leading to greater deformation and more variation in width, length and temperature to form data splits. The method should not be used as a stand-alone classification method but can be used as a technique for feature reduction before repeating the modelling process with other machine learning or statistical approaches.

D.5.2 Random Forest

Random forest was the most effective method for data set A but performed worse than all other algorithms apart from decision tree in data set B. Data set B had less data than data set A, so therefore the decrease in the amount of data to split the records contributes to the detriment in performance. This is due to the model not being able to achieve the same model complexity at shallow tree depths with fewer samples. This highlights the importance of having an extensive data set to make predictions when using random forest as indicated in data set A.

The technique is robust due to the properties of the algorithm, with random sampling with replacement and the majority vote system of trees contributing to more stable predictions. It is also possible to achieve excellent predictions with shallow tree depths, which limits the need for excessive computer capacity. However again, both of these characteristics are reliant on substantial and good quality data to achieve the model complexity needed to give the good results achieved through random sampling and the majority vote system.

D.5.3 Support Vector Machine

The linear kernel was not as effective in data set A, however was the best performing machine learning algorithm in data set B. The linear kernel is the simplest implementation of SVM, which puts a straight hyperplane in the higher dimensional space to separate the samples into classes. In data set A, there is lower temperatures in the bending zones during the experiment compared to data set B. Features with measurements that change little contribute noise to the process of finding the optimal hyperplane. In data set B there were larger temperature differences between the bending zones due to greater tension, allowing a more optimal split to be found due to more distinctly scaled values.

SVM using both the radial basis function and sigmoid kernels performed to more or less the exact same levels in both data sets, indicating the hyperplane shapes imposed were more adaptable to the differences between data sets A and B. While the linear kernel is limited in the separating hyperplane it can impose for class separation, the other kernels presented here can form a more complex hyperplane that can serve to separate the classes more effectively. Compared to decision tree and random forest, the SVM is a much more adaptable and consistent algorithm as reflected in the results presented.

D.5.4 Machine Learning and Statistical Methods Comparison

Both the machine learning and classical statistical approaches were shown to be valid methods for classifying condition of fibre ropes during CBOS testing. The k-nearest neighbours algorithm was shown to perform just as well or slightly worse than the best performing machine learning algorithm when assessed using only metrics. However, Figure D.8 demonstrates that there is a possibility that k-nearest neighbours produces a substantial amount of false alarms at earlier stages of testing. The false alarms for random forest occur closer to the transition point between classes and avoid very early stoppages.

However, the results presented in this paper show that there is merit in applying machine learning for fibre rope condition monitoring. In a machine learning application, the models created can only perform if there is enough data available. In situations where data is limited a classical statistical approach can suffice, as shown by the robust performance of logistic regression and k-nearest neighbours across both data sets. Logistic regression was also shown to be less hampered by smaller data sets as reflected by the stronger performance in data set B than in data set A. Some machine learning algorithms in this study, such as decision tree and random forest, performed worse in data set B than in data set A and failed to adapt to the smaller data set. Also SVM-linear showed an increase in performance with a smaller data set.

This also highlights the adaptability of different machine learning models for different circumstances. In situations where there is both enough and good quality data, machine learning should be used as the approach for condition classification. However, in situations where there is a smaller data set, a classical statistical approach could be more appropriate before attempting machine learning to find potential improvements in condition classification.

D.6 Future Work and Adaptation for Field Deployment

Further work is required to develop machine learning applied to fibre rope condition monitoring. There is a possibility of improving on the current feature set by considering the time each rope spends at

Table D.2: List of cycles at failure during CBOS testing in data sets A and B.

Data type	SF	Rope ID	No. cycles at failure
A	11	A1	73,324
		A2	122,368
		A3	120,430
		A4	87,314
		A5	143,374
B	8	B1	14,948
		B2	13,883
		B3	13,901
		B4	13,998

elevated temperatures, which could give further insight into rope lifetime. Moreover, embedded magnetic or electric threads could be weaved into the rope, which would allow additional data processing techniques to assess rope degradation. Combining these techniques with the features outlined in this paper can also improve prediction results.

Another potential improvement could be through limiting the number of features used for training. Features that vary very little throughout the experiments essentially contribute noise to machine learning models and hamper classification performance. This can be done by assessing the difference between using only geometric data and comparing it to using both geometric and thermal data. There is also the possibility to test the effect of limiting features from certain bend zones on performance and focusing only on features related to the SBZ and DBZ. The sensitivity of classification results to data loss can be further explored. The effect of using only visual features or temperatures can be further explored to assess the effect on what type of data is the best for achieving the best classification results.

In this study, the two different data sets are tested independently of one another. Combining data from two different rope types can also be assessed to see if it improves algorithm performance. With respect to field application, this would be useful as an industry-wide approach, where different sizes of cranes would use potentially several different diameters and types of rope in the same fleet of ships. Implementing the sensors detailed in this paper at a location near one of the main sheaves would give insight into how the measurements fluctuate during a real offshore lifting operation. Additionally, the rope sections would have to be properly tracked and marked, as different parts of the rope could be subject to extended bending periods and heat build up due to active heave compensation during lifting operations. The historical data could then be used to analyse the measurements and assess for patterns. Predictions on ropes in use can be continually updated as ropes are maintained or replaced based on the historical data from other equipment.

Data availability is also highlighted as an important factor in algorithm performance. Due to lack of operational data for fibre ropes of offshore lifting, CBOS testing is chosen as the approach to simulate similar forces and movements in a laboratory environment. However, CBOS testing is a long and expensive process to perform, so therefore robust intelligence maintenance algorithms that work would be of great advantage. Data recording was limited during these experiments, in particular for data set B, which highlighted the need for more frequent data recording to create larger data sets.

Furthermore, there are other machine learning approaches that can be implemented for classification problems. Neural networks are a suitable candidate as a machine learning technique, in addition to the algorithms presented in this paper. Similar to the techniques used previously, there is potential to use and adapt different network architectures and configurations for different data sets, such as the fibre rope measurements presented in this paper.

In addition to condition classification, the algorithms can also be adapted for remaining useful life estimation. Rather than simply assessing a class, a continuous variable could be developed to give a more accurate number or fraction which predicts the rope lifetime.

D.7 Conclusion

The research in this paper has indicated that both machine learning and classical statistical approaches based on computer vision and thermal monitoring are viable methods for condition classification in fibre ropes. Both were shown to effectively classify fibre rope condition during CBOS testing. However, it has also highlighted the need for a greater amount of data to truly gain advantage from different machine learning approaches. This was shown by the inconsistent performance of random forest between both data sets presented.

Ultimately, the methods proposed in this paper have the potential to be developed further for condition classification in fibre ropes. Additionally, with an established framework for machine learning there is further possibility to adapt these methods for remaining useful life estimation in fibre ropes subject to CBOS regimes.

Acknowledgment

The research presented in this paper has received funding from the Norwegian Research Council, SFI Offshore Mechatronics, project number 237896. Special thanks are given to Benyamin Akdemir for valuable help in setting up the equipment and the monitoring software, and to Yannick Bafanga for making Matlab code for pre-processing the thermal data.

Paper E

Remaining useful life estimation of HMPE rope during CBOS testing through machine learning

Shaun Falconer, Ellen Nordgård-Hansen and Geir Grasmo

This paper has been published as:

S. Falconer, E. Nordgård-Hansen, G. Grasmo. Remaining useful life estimation of HMPE rope during CBOS testing through machine learning. *Journal of Ocean Engineering*, 238(1), 2021. doi: 10.1016/j.oceaneng.2021.109617

Remaining useful life estimation of HMPE rope during CBOS testing through machine learning

Shaun Falconer*, Ellen Nordgård-Hansen**, Geir Grasmo*

*University of Agder
Department of Engineering Sciences
Jon Lilletunsvei 9, NO-4876 Grimstad, Norway

**NORCE Norwegian Research Centre AS
Jon Lilletuns vei 9 H, NO-4876 Grimstad, Norway

Abstract – Fibre rope use in cranes for offshore deployment and recovery has significant potential to perform lifts with smaller cranes and vessels to reach depths limited by weight of steel wire rope. Current condition monitoring methods based on manual inspection and time-based and reactive maintenance have significant potential for improvement coupled with more accurate remaining useful life (RUL) prediction. Machine learning has found use as a condition monitoring approach, coupled with vast improvements in data acquisition methods.

This paper details data-driven RUL prediction methods based on machine learning algorithms applied on cyclic-bend-over-sheave (CBOS) tests performed on two fibre rope types until failure. Data extracted through computer vision and thermal monitoring is used to predict RUL through neural networks, support vector machines and random forest. Random forest and neural networks methods are shown to be particularly adept at predicting RUL compared to support vector machines . Additionally, improved RUL predictions can be achieved by combining data from distinct rope types subject to different test conditions.

E.1 Introduction

Fibre ropes are increasingly used for lifting operations, however there are still issues related to the implementation. The material advantages of fibre rope are well documented [2, 22], as well as issues inhibiting their immediate implementation connected to creep, thermal response during cyclic-bend-over-sheave and lack of available data regarding their implementation in offshore construction cranes. To be able to exploit this potential fully, more advanced maintenance routines must be established to challenge the status quo of manual inspection [6]. There is significant potential and benefits with regards to avoiding premature retirement and reducing the chance of failure during operation through the development of intelligent maintenance methods for fibre ropes. Automation of manual processes and structured data-driven approaches to quantify historical health data, damage progression and physical measurements can lead to more informed decisions regarding rope condition and remaining useful life (RUL) through more frequent documented state observation. Establishing and verifying these methods would also signal a shift from time-based maintenance and reactive maintenance strategies to condition-based and predictive maintenance approaches. Positive implications of this include: preventing failure of rope during operation from an undetected fault; decreasing operation downtime for routine inspections; and avoiding retiring ropes with substantial remaining useful life .

Other sectors have implemented approaches for RUL estimation based on machine learning, with several reviews available detailing specific implementations [16, 107, 108, 15, 17, 109]. However, this study will focus on the use of data-driven approaches through machine learning applied to fibre rope condition monitoring data for RUL prediction from cyclic-bend-over-sheave (CBOS) testing.

While the application of machine learning for prognostics and health management in fibre rope condition monitoring is not as established in the publicly accessible research domain, these applications have seen successes in other fields. Much like other engineering components, fibre ropes have damage mechanisms and physical changes that can be detected by sensors, which can be used in machine learning approaches. Offshore fibre rope use in particular is concerned with RUL related to time, tension and temperature as advocated by industry standards [8, 48]. Previous studies into rope behaviour detailing CBOS testing also advocated acquiring this data [20]. Moving rope inspection from manual visual methods to computer vision opens up possibilities in machine learning and intelligent data-driven assessment of fibre rope condition.

In terms of previous work on RUL prediction related directly to fibre rope, extensive CBOS testing is normally performed, with Davies et all detailing an empirical model for High Modulus Polyethylene (HMPE) rope based on a linear regression fit to experimental results [47]. Nuttall detailed a modified version of the Feyrer model for fibre ropes in lifting operations in conjunction with CBOS testing [94]. There has also been other modelling approaches related to CBOS motion in rope [90, 95, 96]. Other model-based and experimental approaches to estimate service life have also been applied to HMPE ropes, under tension-tension regimes as seen in mooring [30]. In the context of lifting operations, machine learning has been applied for prognostics and health management in steel ropes with a focus on mining hoists. Onur et al used neural networks to predict RUL of steel wire rope in CBOS testing and compared the performance to Feyrer models at different loads and diameter ratios [110]. Xue et al used a form of support vector machines to classify steel wire rope condition based on vibration data [111] and Zhou et al used convolutional neural networks (CNN) applied to images for classifying faults in balancing tail ropes for mine shaft hoisting operations [112]. Finally, Huang also applied a CNN approach and computer vision techniques that detect surface damage in steel wire ropes [113].

The contribution of the present article can be summarised as follows: machine learning - based methods are presented for RUL prediction of fibre rope during CBOS testing. The methods comprise neural networks (NN), support vector machines (SVM) and random forest (RF), which are applied to data extracted from computer vision and thermal monitoring. All approaches predict a target variable, known as the RUL factor (R_f), which is based on the number of cycles left to failure occur during testing. The various model performances are then assessed for their effectiveness based on both qualitative and quantitative means. Conditions that are assessed to find the best methods for RUL assessment include: variation of hyperparameters in the models, and variations in the variables included in training the models. The approach of combining data from two rope types under different test conditions for training and RUL prediction is also explored. To the authors' knowledge, there is no publicly available detailed study into the application of machine learning for RUL prediction specifically for fibre ropes intended for offshore lifting until now.

The paper is organised as follows: The machine learning frameworks and how their performance is assessed in this context are detailed in Section E.2. The experimental study and data sets are summarised in Section E.3 and the results of the various approaches are shown in Section E.4. The results are then discussed in Section E.5 before further work is considered and conclusions are offered.

E.2 Applied methods

E.2.1 Target variable - RUL factor

A target variable is required for regression analysis in ML and will act as the value to be predicted based on training data used in the modelling process. The target variable used in this study is hereby referred to as the RUL factor (Rf), a fraction defined by equation E.1.

$$Rf = \frac{CTF_t}{CTF_{test}} \tag{E.1}$$

Where R_f denotes the RUL factor, CTF_t is the number of cycles to failure at the time of measurement and CTF_{test} is the amount of cycles at failure in each individual test where the measurements are made. This produces a value that starts at 1 representing start of life and ends at 0 representing end of life respectively (i.e 100% and 0%). Figure E.1 shows an example of damage progression in a section from a rope (A5) at various R_f , with the different stages highlighted by decreasing R_f from (a) through to (d). The images show that as R_f decreases the subsection becomes longer and there is more visible wear, as shown by by ruptured strands and extruded loops. The errors of the predictions made by the various approaches will be based on comparison to the R_f .

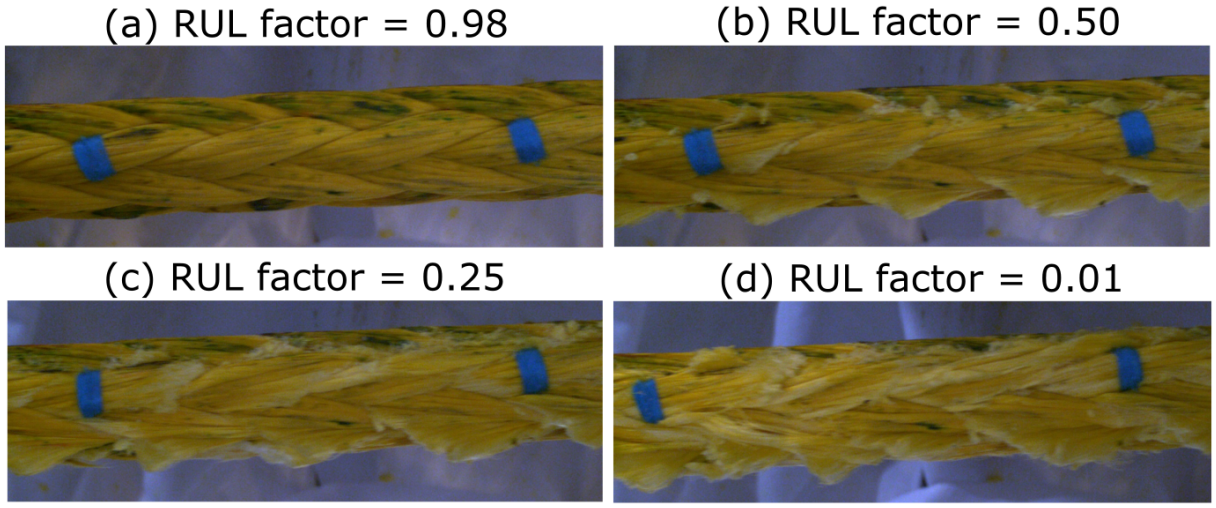

Figure E.1: Example of degradation in rope A5.

E.2.2 Neural networks

The NN structures, designated as NN1 and NN2, used in this study are detailed in Tables E.1 and E.2, and are implemented using the Keras library [130] with a Tensorflow backend [131]. The number of inputs in the input layer for both architectures correspond to the number of features, N_{feats}, used from the data extracted from the ropes during CBOS testing. The hidden layers are of a dense layer type with a specified number of neurons and a Rectified Linear Unit (ReLU) activation function that introduces non-linearity to the data. Both architectures use dropout layers that will randomly prevent 20 % of the neuron outputs from proceeding through the network. This is a regularisation technique used to prevent overfitting. The final output layer consists of one neuron coupled with a Sigmoid activation function that produces a value between 0 and 1 as a result. This is done to reflect the previously described R_f in Section E.2.1.

Table E.1: NN architecture 1 (NN1) used to predict R_f .

Layer	Type
1	Input layer, N_{feats} inputs
2	Dense layer, 100 neurons, activation function – 'ReLU'
3	Dropout layer – 20 %
4	Dense layer, 50 neurons, activation function – 'ReLU'
5	Dropout layer – 20 %
6	Output, Dense layer, 1 neuron, activation function – 'Sigmoid'

Table E.2: NN architecture 2 (NN2) used to predict R_f .

Layer	Type
1	Input layer, N_{feats} inputs
2	Dense layer, 100 neurons, activation function – 'ReLU'
3	Dropout layer – 20 %
4	Dense layer, 100 neurons, activation function – 'ReLU'
5	Dropout layer – 20 %
6	Dense layer, 50 neurons, activation function – 'ReLU'
7	Dropout layer – 20 %
8	Output, Dense layer, 1 neuron, activation function – 'Sigmoid'

The Adam optimisation function was used for both network architectures specified in Tables E.1 and E.2 to update the weight values associated with the input features. The inputs are fed forward and backpropagated through the networks for 50 epochs, with the model that produces the lower mean square error (MSE) on the test data being saved as the best model used for predictions. Each configuration is simulated 20 times to account for randomness in the weights assigned in the neural network and give a more robust value for model output. The average prediction calculated from these instances is used to compare to the ground truth R_f measured from the CBOS tests and provide a confidence interval.

E.2.3 Support vector machine

SVM was first used for classification [125] and was later adapted for regression problems [132]. To predict the R_f in this context, the latter approach is adopted which has also been applied in other studies related to RUL prediction [133]. Essentially, the data is separated by a hyperplane in a higher vector space. This plane can be formed by use of a kernel. In a classification implementation, this line is used to separate the measured vectors into classes, but for the regression analysis it will be used to predict a continuous variable for the other instances in the data set.

To compare to the performance of the NN, it is chosen to use an SVM framework adapted for regression analysis from scikit-learn [120]. Linear and Gaussian kernels are used to form the fit to the data and to compare their relative accuracy to R_f are compared to other methods.

E.2.4 Random Forest

RF is an example of an ensemble method which utilises a user-specified number of decision trees created by bootstrapping data from features and data available from a training pool [123][134]. The models

created will assign RUL values to the test samples in each individual tree and an average RUL value will be calculated.

The RF algorithm for regression analysis from scikit-learn [120] is used for R_f prediction. The configurations for RF implementation in each data set are specified in Table E.3 for data sets A and B. Different tree depths are chosen due to the difference in number of measurements available between the different data sets and to prevent overfitting. The differences between the data sets are highlighted in Table E.5.

Table E.3: Configurations used for RF to predict R_f for data sets A and B

Data set A		Data set B	
Tree depth	1-4	Tree depth	1-2
Number of trees	50, 100, 200	Number of trees	50, 100, 200

E.3 Experimental study

Figure E.2 details the flowchart of operations implemented in the ML process from beginning to final output and performance assessment. Specific details related to (a) test methods and (b) data acquisition are summarised in Section E.3.1 and the subsequent pre-processing techniques applied to the data for ML application in Section E.3.2. Then in Sections E.3.3 and E.3.4 the (c) training and RUL estimation stages and (d) model assessment are detailed.

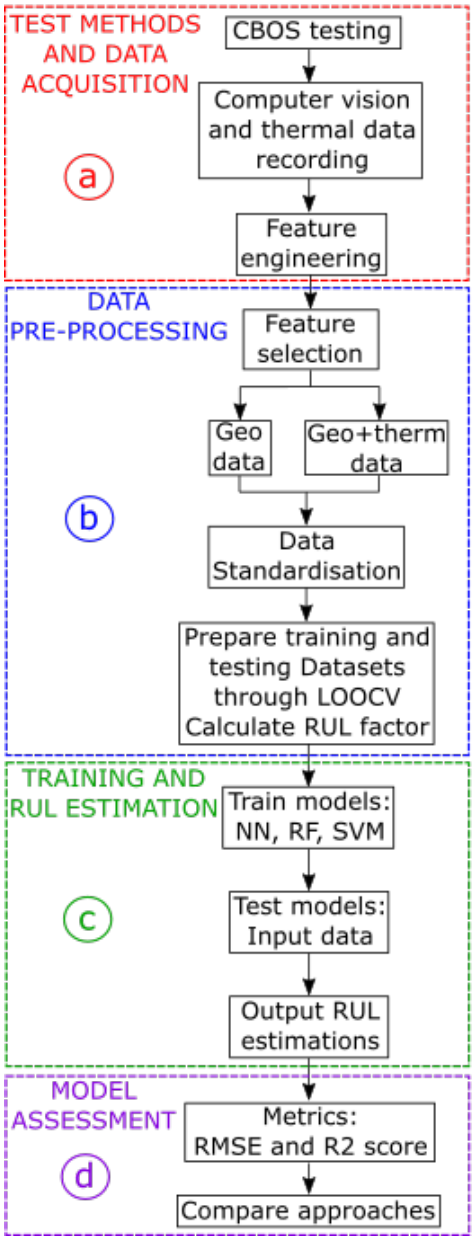

Figure E.2: Flowchart of operations detailing steps implemented in (a) data acquisition, (b) data pre-processing, (c) training and estimating RUL and (d) model assessment.

E.3.1 Test methods and data acquisition

The data sets were recorded from CBOS experiments performed at the Mechatronics Innovation Lab in Grimstad, Norway. Computer vision data is extracted via algorithms developed in OpenCV [117] and thermal data is extracted using FLIR ResearchIR 4 software [118]. Specific details of the various operations the algorithms use to extract data are summarised in previous work detailing the various CBOS testing campaigns [149].

The fibre ropes used in testing were 12-strand braided ropes with nominal diameter of 28 mm. The two types used were Dyneema DM20 XBO and Samson AmSteel Blue which are designated as separate campaigns A and B, respectively. Additionally, A is tested at safety factor (SF) 11 and B is tested at SF 8. This equates to average tensions of 1/11 and 1/8 of each rope type's max tensile capacity.

Features are engineered from data recorded during CBOS testing and the ropes were separated into different zones that reflect the distinct bending regimes during CBOS testing, as highlighted in Figure E.3. These are the positions in the rope where the rope is bending and unbending due to the cyclic movement of the sheaves. No bending occurs in section SZ, a single bend occurs during each cycle in SBZ and two bends occur in the DBZ during one cycle. Data designated as "geo" includes geometric measurements such as length and width, which were derived from the data recording from computer vision and global length from a distance measuring laser. The "therm" data represents thermal measurements taken from a FLIR A6753sc thermal camera. A list of features and their respective bending zones are summarised in Table E.4.

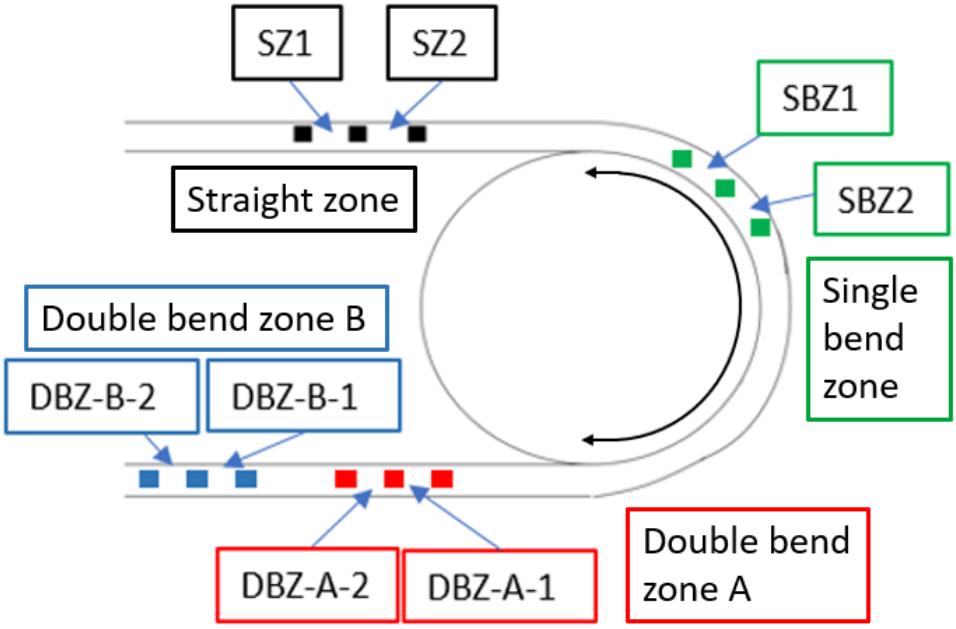

Figure E.3: Summary of different rope bending zones where the features are derived from.

E.3.2 Data pre-processing

The data sets are separated into "geo" and "geo_therm" feature sets based on data type to assess the effect of adding thermal features to the ML model. The data set compositions are summarised in Table E.5. The records are the number of data samples recorded by the data acquisition set up mentioned in Section E.3.1.

Table E.4: List of features created from data acquisition process.

Rope campaign	Feature (zone)	Data type	Statistical parameter
A	Local length (SZ1, SZ2, SBZ1, SBZ2, DBZ-A-1, DBZ-A-2, DBZ-B-1, DBZ-B-2)	geo	Median, max, min, stdev
A	Width (SZ1, SZ2, SBZ1, SBZ2, DBZ-A-1, DBZ-A-2, DBZ-B-1, DBZ-B-2)	geo	Median, max, min, stdev
A	Global length	geo	N/A
A	Temperature (SZ, SBZ, DBZ)	therm	Average, max, min, stdev, range
A	Temperature (SBZ-DBZ)	therm	Ratio
B	Local length (SZ1, SZ2, SBZ1, SBZ2, DBZ-A-1, DBZ-A-2, DBZ-B-1, DBZ-B-2)	geo	Median, max, min, stdev
B	Width (SZ1, SZ2, SBZ1, SBZ2, DBZ-A-1, DBZ-A-2, DBZ-B-1, DBZ-B-2)	geo	Median, max, min, stdev
B	Global length	geo	N/A
B	Temperature (SZ, SBZ, DBZ)	therm	Average, max, min, stdev, range
B	Temperature (SBZ-DBZ)	therm	Ratio

The ropes used in campaign B were tested at a higher tension and failed sooner than those in campaign A, hence the lower number of records in B compared to A.

Table E.5: Data set summary for 28 mm ropes

Data set ID	A_geo	A_geo_therm	B_geo	B_geo_therm
Data type	geo	geo + therm	geo	geo + therm
Features	161	177	161	177
Ropes	5	5	4	4
Records	509	509	103	103
Manufacturer	Dyneema	Dyneema	Samson	Samson
Rope type	DM20 XBO	DM20 XBO	Amsteel Blue	Amsteel Blue
SF	11	11	8	8

The raw measurements from the data acquisition phase are subject to pre-processing, where the data from the various features is standardised. The data was scaled using the approach detailed in equation E.2:

$$z_i = \frac{y_i - \bar{y}}{\sigma_y} \tag{E.2}$$

Where z_i is the individual standardised value, y_i is the individual raw value, $\bar{y}$ is the average of all readings for the specific feature in the rope sample and σ_y is the standard deviation of all readings for the specific feature in the rope sample. This is done for each rope in the data set to increase comparability between the different samples and is a standard pre-processing step to prepare data for ML application.

E.3.3 Training and RUL estimation

The models are tested through leave one out cross validation (LOOCV), where R_f predictions made on a single rope will be made using models trained with the remaining ropes in the data set. This process is done separately for both ropes in campaign A and campaign B and as a combined data set with both A and B together.

In addition to investigating the effect of only geometric and combined geometric and thermal measurements as outlined in Table E.5, different combinations of features from the various bending zones detailed in Figure E.3 are also trained and tested. This includes: testing using all zones; using only SBZ and DBZ measurements; and finally, using only DBZ measurements.

E.3.4 Model assessment

The metrics used for model assessment are root mean square error (RMSE) and R^2 score (R^2):

$$\text{RMSE} = \sqrt{\frac{1}{N}\sum_{n=1}^{N}(y_i - \hat{y}_i)^2} \tag{E.3}$$

$$R^2 = 1 - \frac{SS_{res}}{SS_{tot}} \tag{E.4}$$

Where N is the number of measurements made for each rope sample, y_i is the observed R_f at instance i, $\hat{y}_i$ is the predicted R_f at instance i, SS_{res} is the sum of squares of residuals and SS_{tot} is the total sum of squares.

RMSE in this context will give an insight into how concentrated the R_f predictions are around the R_f ground truth using each algorithm configuration outlined in Section E.2. Additionally, the R^2 score gauges the correlation R_f predictions have with the ground truth R_f using the input variables outlined in Table E.4.

The performance of the models is assessed through the use of R_f graphs and residual analysis. The R_f graphs will include the ground truth from the observed experimental measurements and tolerance bounds at ±20% based on this data. The average R_f prediction and a ±95% confidence interval of the repeated simulations of each distinct configuration are compared to the ground truth and tolerance bounds.

The residual values, e are calculated using equation E.5:

$$e = y_i - \hat{y}_i \tag{E.5}$$

where y_i are the RUL values from CBOS testing and $\hat{y}_i$ are the predictions made by each respective model. The analysis includes plotting the residual values against the predicted R_f values, the actual R_f value against the predicted R_f value and finally a histogram analysis accounting for the numerical

spread of the residual values. This provides further information about the model ability to predict R_f , potential model bias and where overestimation and underestimation in rope health occurs.

E.4 Results

E.4.1 Experimental results

The amount of cycles at failure for all ropes in campaigns A and B are summarised in Table E.6. It is noted that there is a wider spread of values in A than B. Ropes A1 and A4 were shown to fail at lower amounts of cycles compared to the other ropes in campaign A. This is owed to the rope failing at the driving sheave, rather than the test sheave. Due the the method used, parts of the splice were in contact with the sheave during testing and lead to premature failure of the rope samples. Rope A5 completed a greater number of cycles than the rest of the ropes in campaign A. This particular sample included an attempt to embed thermocouples within the strands of the rope and therefore could have contributed to slight discrepancy in the results.

Some halts in logging occurred sporadically during CBOS testing for campaign A, meaning data acquisition equipment had to be restarted occasionally. Furthermore, features for Rope B1 were recorded every 1000 cycles and has less data compared to the other campaign B ropes, which were recorded every 500 cycles. This change was made as a reaction to the comparatively shorter test times for campaign B than campaign A.

Table E.6: List of cycles at failure for ropes in campaigns A and B.

Rope	No. of cycles at failure	SF
A1	75,324	11
A2	122,368	11
A3	120,430	11
A4	87,314	11
A5	143,374	11
B1	14,948	8
B2	13,883	8
B3	13,901	8
B4	13,998	8

E.4.2 Average metrics

A quantitative assessment of R_f prediction is performed by calculating the average $RMSE$ and R^2 scores in each data set using different feature sets. Better performance is reflected by lower and higher values for $RMSE$ and R^2, respectively. The results for different feature combinations are compared for both A and B rope datasets and ranked by performance of the algorithm on only using geometric features (i.e A geo with A model and B geo with B model). The results using the various feature combinations cross validated on a combined A and B rope data set are also presented.

Figure E.4 gives an overview of each algorithm performance based on different feature sets and training model composition. It is seen that both configurations of RF performed best, followed by NN and finally SVM based on producing the lowest $RMSE$ scores. Introducing thermal features generally either changes nothing or leads to detriment in performance when only A ropes are used as training data, which is particularly noticeable in both NN and SVM. When the combined A and B model is used there

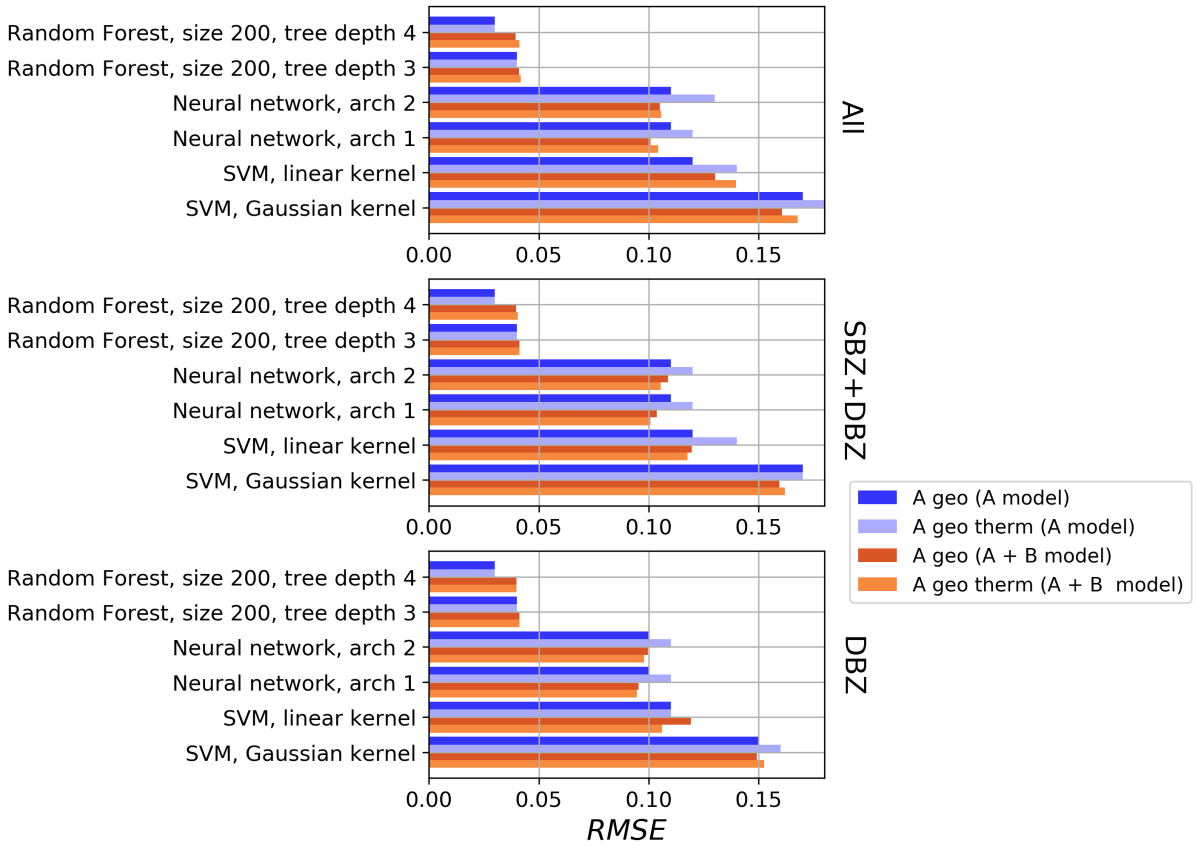

Figure E.4: Average RMSE values per algorithm for A ropes.

is shown to be a slight improvement in performance when thermal features are introduced for NN when the SBZ+DBZ and DBZ feature sets are considered. There is also shown to be a general reduction of $RMSE$ as the number of zones used in the training are decreased.

This performance is also reflected in the R^2 values as shown in Figure E.5. As seen with the $RMSE$, data types, feature sets and model compositions influenced the algorithms differently. The R^2 values for both RF configurations are shown to be the highest, followed by NN and SVM. The high values recorded for R^2 indicate that the features used to create the RF models better explain the changes in R_f . It is seen that by using both A and B data to train the NN configurations, that a higher R^2 is achieved than by only using A, indicating that the same feature with enhanced data from different ropes better explain the changes in R_f . This is also seen for both SVM configurations but had little impact on RF.

The $RMSE$ values for data set B are shown in Figure E.6. Both configurations of NN were shown to perform best when only B data is considered. A noticeable difference in the B data is that for both NN and SVM, the thermal data led to significantly better predictive performance as indicated by lower $RMSE$. Using the combined A and B data set also improved performance of NN with the exception of the NN2 configuration in the SBZ+DBZ feature set. The combined A and B data set has a detrimental impact on the RF configuration with depth one.

The R^2 scores for the same algorithms using the B rope data set are shown in Figure E.7. The highest R^2 values are achieved with NN, with improvements being shown when thermal data is introduced. It is noted that higher R^2 is recorded using A and B data for training when only geometric features are considered but similar values are seen for B only and A and B combined when thermal features are introduced. RF is shown to have similar R^2 values no matter what features are used. There is also a

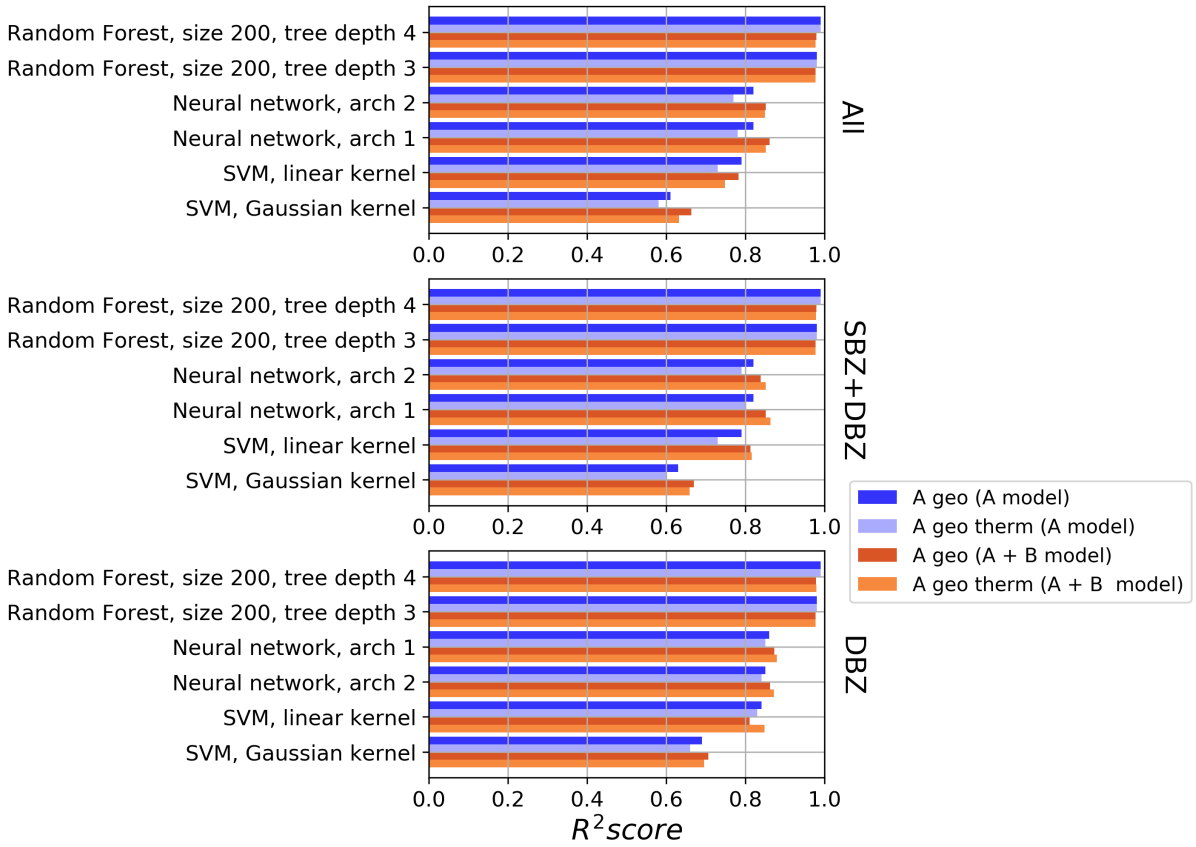

Figure E.5: Average R^2 values per algorithm for A ropes.

noticeable increase in R^2 for SVM Gaussian when the combined A and B data set is considered.

E.4.3 RUL graphs

A qualitative assessment of the algorithm performance during cross validation is given through plotting the predicted R_f at various cycles throughout each test. It is possible to gain a general idea of algorithm performance from the graphs, but they can also reveal at which times in the test both the best and worst predictions are made. The results of cross validation predictions made only using the single and combined data sets is also considered. Selected RUL prediction results from both A and B data sets are shown in Figures E.8, E.9, E.10 and E.11.

Figure E.8 shows the results of R_f prediction using NN2 for geometric features from all bending zones for rope A4. By using the combined A and B data set, the predictions in the first half of the test are shown to be closer to the ground truth, as well as showing a reduction in the "peak" seen in the middle of the A ropes model.

Figure E.9 presents the results for R_f prediction for rope A3 using RF at tree depth 4 using geometric features from all bend zones. As shown in the previous $RMSE$ results for RF, the combined A and B training data performed either the same or to slight decrease in performance, which is reflected in the R_f graphs. Additionally, both models have very small confidence intervals compared to the NN configurations.

Figure E.10 considers the predictions by NN2 on rope B2 when both geometric and thermal features from the DBZ are considered. The confidence interval in the prediction is significantly reduced and almost

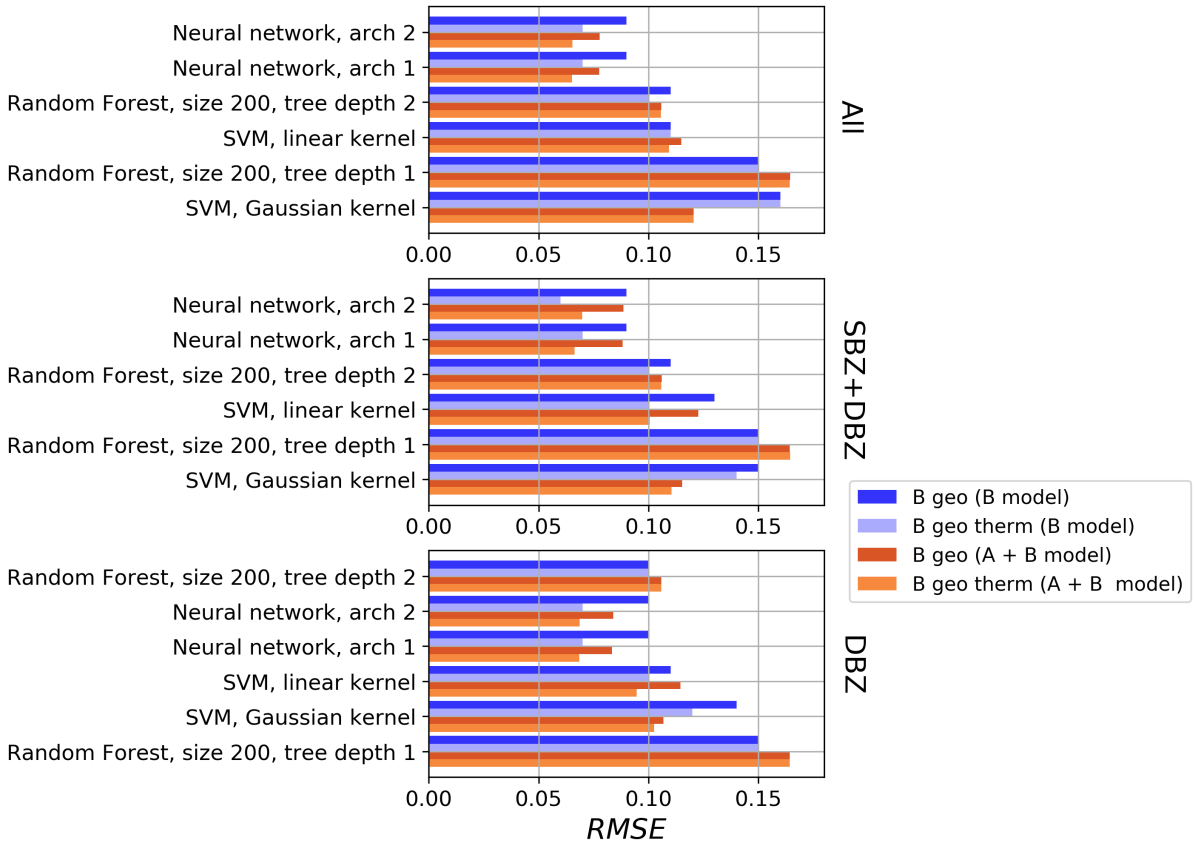

Figure E.6: Average RMSE values per algorithm for B ropes.

totally confined to the tolerance bounds. This is seen at the majority of test times with the exception of between 0 to 40,000 test cycles.

Figure E.11 shows the R_f prediction results of using SVM with a linear kernel when using geometric and thermal features from the DBZ. The model trained using the B ropes data is shown to significantly overestimate rope health after around 11,000 cycles but when the A and B data is included, this period of R_f predictions is corrected, albeit with some underestimation after 12,000 cycles.

E.4.4 Residual analysis

A residual analysis is performed to further investigate R_f predictions and to compare the differences in results depending on algorithm, features and training data used.

Figure E.12 shows the residual analysis comparison of using RF with tree depth 4 and NN2 predictions for rope A2 using only geometric features from all bend zones. In this specific case, both models were trained using only the A rope data. The RF model produces low residual values indicating closer agreement with the ground truth, while NN2 prediction are shown to both overestimate and underestimate as indicated by the spread of residual values.

Figure E.13 presents the residual analysis comparison of using geometric and the combined geometric and thermal features. This is done for rope B3 predictions made using NN2 with features from the DBZ. By including thermal data, the magnitude of all residuals is reduced to be within 0.1 of the R_f ground truth. When comparing predicted and actual R_f values, predictions are more effective generally but there is little effect on improving the predictions at the end of the test.

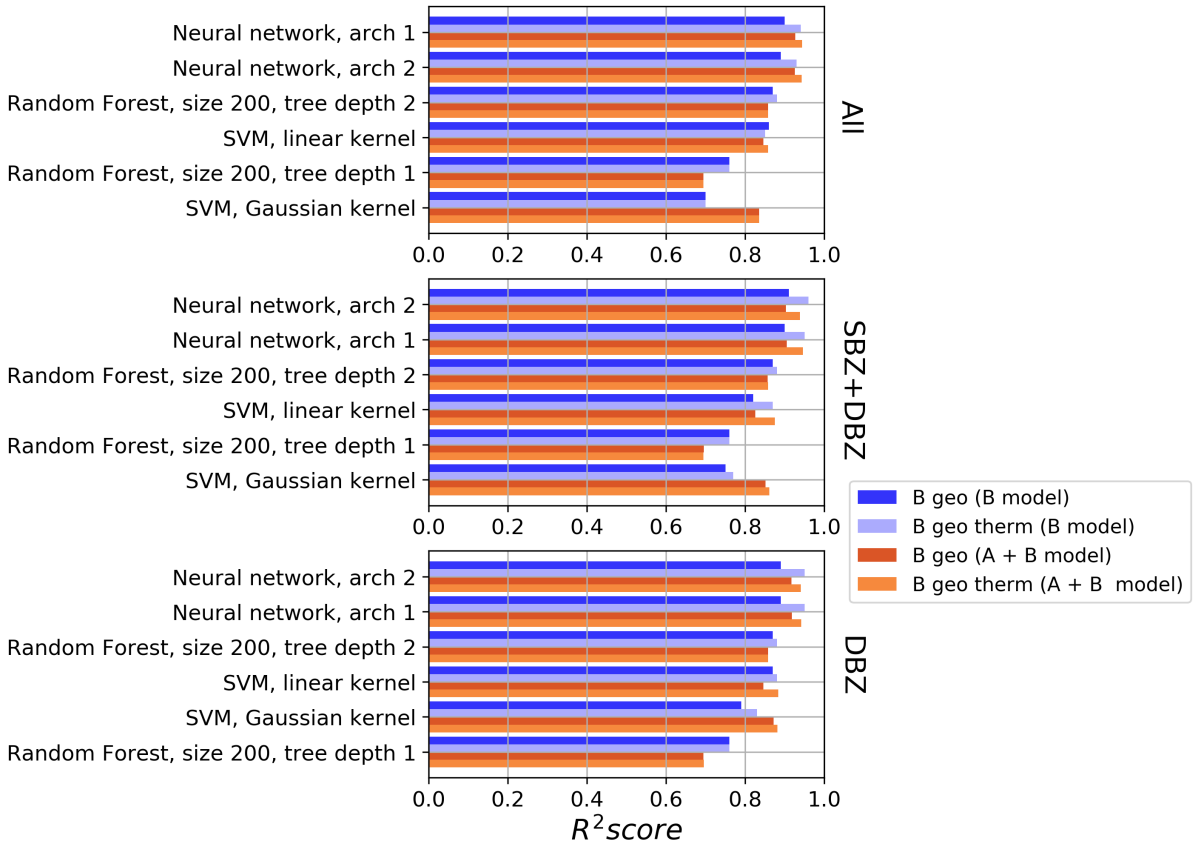

Figure E.7: Average R^2 values per algorithm for B ropes.

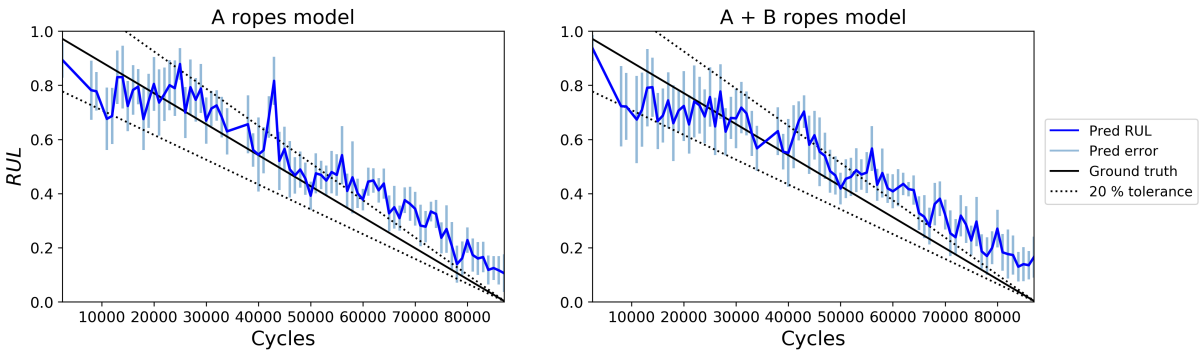

Figure E.8: R_f prediction using NN2 for rope A4, using geometric features from all bend zones.

Figure E.14 provides analysis of improvements that are possible by combining the A and B rope data sets in model training. This is presented for rope A1 with NN2 using combined geometric and thermal data from all bend zones. An improvement with the combined training set is observed, with magnitude of the outermost outliers being reduced. Rope A1 completed the least amount of cycles at failure when compared to the other ropes in the A data set and showed poor prediction results on models trained on this data set.

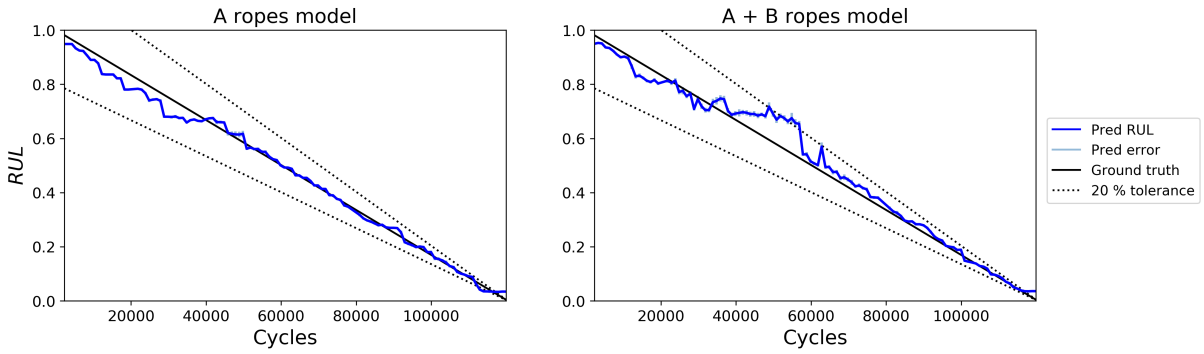

Figure E.9: R_f prediction with RF, forest size 200, tree depth 4 for rope A3, using geometric features from all bend zones.

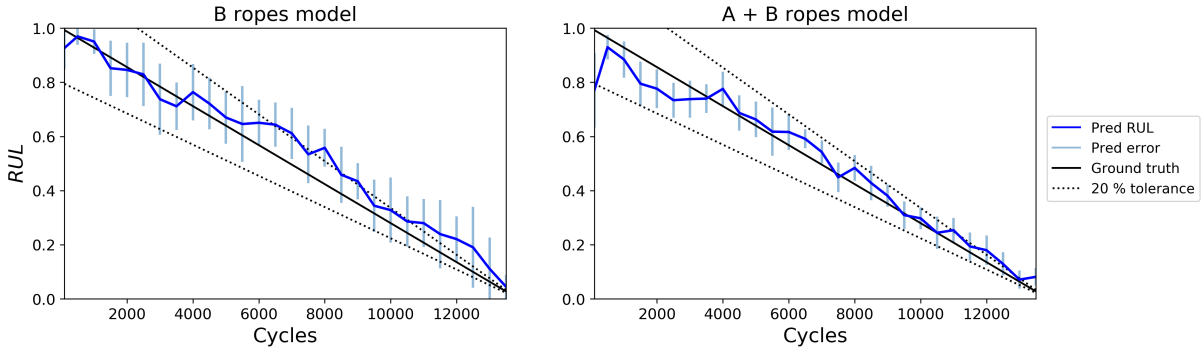

Figure E.10: R_f prediction using NN2 for rope B2, using geometric and thermal features from DBZ.

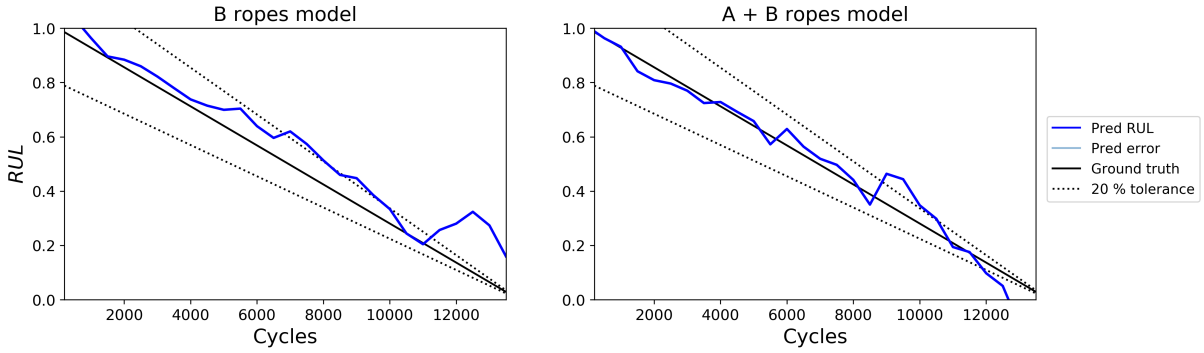

Figure E.11: R_f prediction using SVM, linear kernel for rope B3, using geometric and thermal features from DBZ.

E.5 Discussion

Model performance varied depending on the algorithm and the data set used. A major difference shown was that RF performs better than NN for campaign A but NN performs better than RF in campaign B. Differences in performance can be explained by the training data used, the size of the data set, and algorithm mechanisms.

Previous work on the same data sets as a classification problem indicated that SVM with a linear

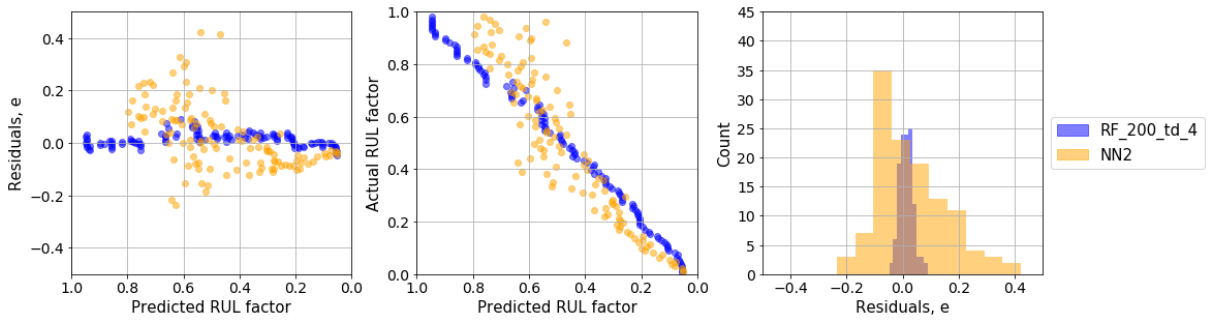

Figure E.12: Residual analysis and comparison for rope A2 predictions made by NN2 and RF, with 200 trees and depth 4 with all features. Both models are trained using only A data.

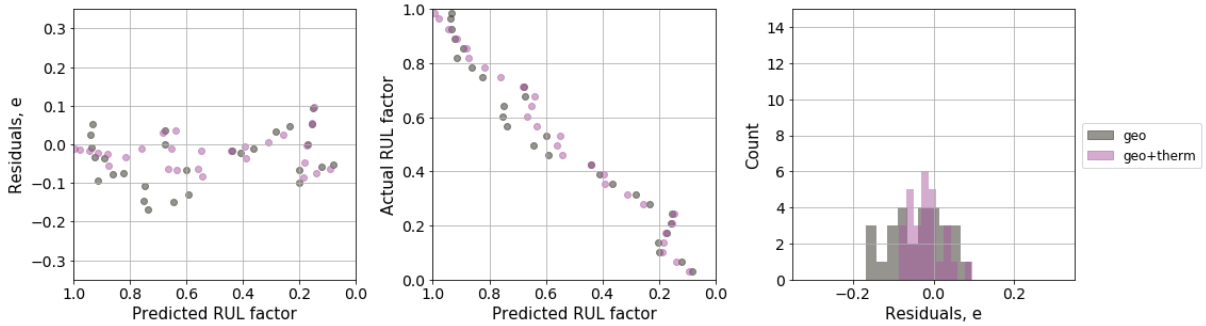

Figure E.13: Residual analysis and comparison for rope B3 predictions by NN2 using geo and geo+therm data, using DBZ features. Both models are trained using only B data.

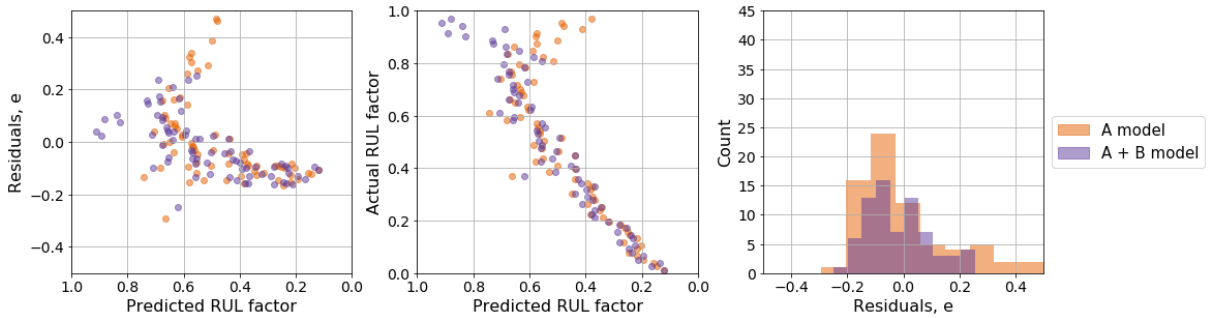

Figure E.14: Residual analysis and comparison for A1 predictions with geo + therm features from all zones by NN2, using models trained with A data set and combined A + B data set.

kernel was the most effective algorithm for classification [150]. However, the previous study did not include global elongation as a feature for training and prediction purposes, hence the different results in this study for RF and the implementation of NN are new additions to this study.

E.5.1 Random forest

RF is formed of several individual decision trees, where data is separated based on feature values that give the purest split. The global elongation shows a steady increase during testing, and it will therefore create one of the best splits in the decision trees of the RFs. However, this feature will not be available to all trees in the forest, due to feature bagging. Still, the averaging over 200 trees will ensure its contribution to the overall forests.

In general, increased tree depth increases random forest accuracy and improvements by increasing forest size tend to plateau. In campaign B, each rope had fewer records than in campaign A. To avoid overfitting, the result was shallower trees for this campaign, giving less accurate RF results. The data is split by random feature sampling in each tree, there would be slightly more variation in the quality of fits due to data splits made on less suitable features. This leads to less accurate RUL predictions as indicated by the higher RMSE and lower R^2 values.

E.5.2 Neural networks

The NN algorithms performed better in campaign B than campaign A. All input variables are considered when using NN and depending on the neurons that randomly dropout the network through regularisation, this can influence the model. A feature that varies very little during the testing only contributes noise to a model and impacts performance negatively. A clear example is comparing the use of geometric and the combined geometric and thermal feature sets for campaign A, where thermal features lead to a higher $RMSE$. At the lower test tensions the temperatures do not vary significantly throughout the CBOS tests, but reach a steady temperature until failure, thus contributing noise to a potential model formulation. However, the temperatures recorded in campaign B are noticeably higher and have more variation between the SBZ and DBZ in line with the decreasing R_f , therefore contributing to a better model. Due to campaign B having both less data coupled with more variation in measurements leads to NN finding a better model than developed for campaign A.

Generally, it is noted that despite inconsistent numbers of test cycles in campaign A, it is still possible to achieve acceptable results within the range of $\pm$ 20 % of the RUL ground truth. Additionally, NN is shown to struggle with predicting RUL in the earlier stages of the testing in particular for some ropes in the data set. Initially, the various widths, lengths and temperatures monitored will not change until later in the test and therefore the networks struggles to predict the distinct R_f values at this testing stage.

E.5.3 Support vector machine

The SVM algorithms performed poorly compared to the other algorithms applied in this study. If the hyperplane fit to the data is poor and non-representative, it will in turn have a detrimental impact on R_f prediction using the algorithm. As with NN, the presence of noise via lack of variation in certain features will negatively influence this fit. This is particularly prevalent in campaign A, however it is noticed that SVM performed slightly better in campaign B due to the greater variation in values measured. It is also shown that the fit created by the linear kernel suits this rope test data set better than the Gaussian kernel.

Potential improvements for SVM could be reducing the number of features used to create a simpler model. There is also further potential in hyperparameter optimisation for both linear and Gaussian kernels that can contribute to improve models.

E.5.4 Feature selection

Creating models from different feature sets consisting of the different bending zones features also influences algorithm performance. During CBOS testing, the SBZ and DBZ are subject to substantially more bending, whereas there is none present in the SZ. Therefore, in line with what was previously stated about NN, measurements from the SZ essentially contribute noise in the modelling process. As only the features that give the best splits in the data are considered from the random subsets in RF, the likelihood that features from SZ will be consistently picked as splitting criteria in individual trees is extremely low, hence minimal effect on both $RMSE$ and R^2 values.

However, limiting the features used to only those from the DBZ is shown to improve algorithm performance for both NN and SVM. There was very little difference between the results from models that used all features and the combination of SBZ and DBZ features but the most accurate results for SVM were achieved by reducing to only training with DBZ features. More frequent repeated bending will cause more accumulated damage and variation in these features will relate better to the associated RUL value.

E.5.5 Combining data sets

Combining the two data sets for predictions based on cross validation had both a positive and negative impact depending on the algorithm considered. The main benefactors of this approach were the NN configurations, as shown by improved results in average $RMSE$ and R^2 for both the A and B ropes. Introducing thermal features for A rope predictions led to decreased performance when only considering the A data set, but improved for the cases where SBZ+DBZ and DBZ features are used with models trained using the A and B ropes. This can be attributed to the different thermal behaviour in each data set, with the thermal information from the B ropes contributing to better predictions. From a B ropes prediction perspective, combining the A and B data sets creates a larger training data set and improves estimations from both NN and SVM. This suggests that simply increasing the amount of training data with slightly different feature behaviours will benefit model fitting in these cases. The observations support the finding from this study that unique rope types subject to different relative test tensions can be combined to produce more accurate results.

E.6 Future work and adaptation for field deployment

From the perspective of RUL prediction in CBOS testing, the effectiveness of ML approaches is influenced by the quality and quantity of data recorded. Though good prediction results are achieved at two safety factors, further ML application to CBOS test sets performed at a wider range of lower safety factors is needed. These further tests would also benefit from more frequent data recording, that would give a more rounded picture of the performance of a specific rope type. This would be beneficial for methods such as RF, which gave excellent results in campaign A but had its performance inhibited by the limited tree depths in campaign B. Furthermore, it is shown that these further enhanced data sets can be combined into a common training data pool that can be used to make predictions on new test data from distinct rope types from various test conditions.

Data availability is another limiting factor to further development of ML algorithms for application to fibre ropes. Other engineering components such as bearings and motors benefit from publicly available datasets and can therefore specifically focus on further development of prognostics methods, rather than the condition monitoring framework for data acquisition.

This study provides an overview of the main ML techniques used for RUL prediction, but each algorithm mentioned has potential for further exploration. This was done on tabular data that dealt with measurable physical quantities such as width, length and temperatures but there are still further opportunities for enhancement by using CNN to quantify damage in the rope condition directly from visual and thermal images.

However, there is further work required to fully adapt the ML approach usage in offshore construction cranes. Firstly, CBOS testing is an example of a run-to-failure test where a constant tension is applied at the same rope sections. In real practice, it will be different sections of the rope that will be subject to bending depending on lift depth and sea state during operations. Other factors such as payload size, the temperature at lift location and the operation time will also influence rope longevity. Data from potential lifting campaigns would have to be recorded as part of a wider rope condition monitoring system, where data is continually added to form a model with historical data. Generalising the findings from this study of different ropes at different relative test tensions, it is shown there is potential in using data from a fleet of fibre rope cranes performing different lifting operations to validate the condition of an individual fibre rope crane.

Intelligent prognosis techniques would then be applied to assess this data and establish what are the most relevant features to be monitored in practice and further develop a retirement criteria based on informed data-driven methods for condition based maintenance, rather than manual inspection geared towards reactive and time-based maintenance practices. In this study it is shown that there are benefits from monitoring the length, both locally and globally, and the temperature in different bend zones. Such measurements would be made from sensors collecting visual and IR data, ideally from a location near the main sheave, from a rope that has clearly defined sections. The global rope length measurement would also have to be incorporated through some form of embedded sensor measurements within the rope structure to monitored continually during use.

E.7 Conclusion

Several approaches for RUL prediction in fibre ropes during CBOS testing are discussed in this work. The algorithms in this study are capable of predicting a continuous target variable, known as R_f , for ropes using features derived from an experimental set-up that uses computer vision and thermal monitoring.

In this investigation machine learning methods, such as neural networks, random forest and support vector machine were applied for prognostics for two sets of CBOS test data at different safety factors. For data set A, random forest showed the most promise as a RUL prediction method, while NN was the best performing algorithm in data set B. The benefit of combining data from different types of ropes for training data for RUL prediction is also demonstrated for NN and SVM. RF has been shown to be the most effective in this study, particularly in cases where larger amounts of data are available, allowing a suitably complex model to be developed based on features selected by the algorithm. NN is also shown to be useful, but slightly less effective compared to RF. If large amounts of data are not available, then NN application with more focus in including only relevant features is a useful fall-back solution.

E.8 Acknowledgements

The research presented in this paper has received funding from the Norwegian Research Council, SFI Center for Offshore Mechatronics, project number 237896.

Special thanks are given to Nadia Saad Noori for valuable discussions and advice related to the application of neural networks in this context, Benyamin Akdemir for help in setting up the equipment and the monitoring software, and to Yannick Bafanga for making Matlab code for pre-processing the thermal data.